

**Effect of broadband excitation ions in the
luminescence of Ln³⁺ doped SrF₂ nanophosphor for
solar cell application**

by

Mubarak Yagoub Adam Yagoub
(M.Sc)

A thesis submitted in fulfilment of the requirements for the degree of

PHILOSOPHIAE DOCTOR

in the

Faculty of Natural and Agricultural Sciences

Department of Physics

at the

University of the Free State

Republic of South Africa

Promoter: [Dr. E. Coetsee](#)

Co-Promoter: [Prof. H. C. Swart](#)

June 2015

**This thesis is dedicated to my lovely son, Zahid. I look forward
to watching you grow and achieve your goals.**

Acknowledgements

I would like to thank the following individual and institutions:

- Dr. E Liza Coetsee for being my promoter, her help, guidance and suggestions throughout this study, and especially for her confidence in me.
- Special thanks goes to Prof. HC Swart for giving me this opportunity to be part of the department of physics family and for his guidance and professional suggestions throughout this thesis as my co-promoter.
- Dr. MM Duvenhage for her fruitful discussions and for carefully reviewing the manuscript, and for her help with TOF-SIMS data.
- Prof. P Bergman and Prof. HC Swart for their help with luminescence decay time measurements at University of Linköping, Sweden.
- Prof. RE Kroon for his assistance with PL laser measurements and fruitful discussions.
- Staff and students at the department of Physics for discussion and encouragement “we have been together like a family for long”.
- Dr. LL Noto for his useful discussion and helping with some measurements and analyses.
- I am indebted to my lovely family, my parents for their support, encouragement, love and constant assistance throughout my life, to my sisters and brothers for their respect, appreciation, encouragement and constant love. Special thanks goes to my second mom, Noon for her support.
- Special thanks to my wife, Ibtihal for her love and constant support, for all the late nights and early mornings, and for not been close for sometimes. But most of all, thank you for being my best friend.

- **National Research Foundation (NRF), South African Research Chairs Initiative (SARChI) chair and the cluster program of the University of the Free State for financial support.**
- But above all, I would like to thank the Almighty Allah for everything that he has given to me, for his blessing and guidance to finish this work.

Abstract

$\text{SrF}_2:\text{Pr}^{3+}\text{-Yb}^{3+}$ phosphor powder was previously investigated for down-conversion application in solar cells. The first surface, structural and optical characterization results indicated that the $\text{Pr}^{3+}\text{-Yb}^{3+}$ couple requires a sensitizer for effective enhancement in energy conversion. Broadband excitation ions of Ce^{3+} and Eu^{2+} , that could be used as sensitizers, were therefore doped and co-doped in the SrF_2 crystal. Detailed characterizations and investigations were then done on the surface, structure and optical aspects to see the effect on the energy conversion.

Initially, the influence of different synthesis techniques on the surface, structure and concentration quenching of Pr^{3+} doped SrF_2 was studied. The singly doped $\text{SrF}_2:\text{Pr}^{3+}$ was prepared by the hydrothermal and combustion methods. Scanning electron microscope (SEM) images showed different morphologies which was an indication that the morphology of the $\text{SrF}_2:\text{Pr}^{3+}$ phosphor strongly depended on the synthesis procedure. Both the $\text{SrF}_2:\text{Pr}^{3+}$ samples exhibited blue-red emission under a 439 nm excitation wavelength at room temperature. The emission intensity of Pr^{3+} was also found to be dependent on the synthesis procedure. The dipole-dipole interaction was found to be responsible for the concentration quenching effects at high Pr^{3+} concentration in both methods.

$\text{SrF}_2:\text{Eu}$ nano-phosphors were successfully synthesized by the hydrothermal method. The crystalline size of the phosphors was found to be in the nanometre scale. The photoluminescence and high resolution x-ray photoelectron spectroscopy (XPS) results indicated that the Eu was in both Eu^{2+} and Eu^{3+} valance states. The presence of Eu^{2+} and Eu^{3+} in the system largely enhanced the response of the Eu^{3+} under ultra-violet excitation. Time of flight secondary ion mass spectrometry (tof-SIMS) results suggested that the energy transfer between these two ions was likely occurred. The relative photoluminescence intensity of the Eu^{2+} rapidly decreased with an increasing laser beam irradiating time. This result would make the current Eu^{2+} doped SrF_2 samples unsuitable candidates for several applications, such as white light-emitting diodes and wavelength conversion films for silicon photovoltaic cells.

The effect of Ce^{3+} ions on the $\text{SrF}_2:\text{Eu}$ nano-phosphor was also studied. Ce^{3+} largely enhanced the Eu^{3+} emission intensity via energy transfer mechanism. The calculated energy transfer efficiency was relatively efficient at high Eu concentration. The results suggested that Ce^{3+} may therefore be used as an efficient sensitizer to feed the Eu ions in SrF_2 host.

Eu^{2+} co-doped Pr^{3+} , Yb^{3+} and $\text{Pr}^{3+}-\text{Yb}^{3+}$ couple in SrF_2 were successfully prepared. XPS confirmed that all Eu contents were in Eu^{2+} oxidation states. Initially, Eu^{2+} co-doped $\text{SrF}_2:\text{Pr}^{3+}$ was studied. From PL and decay curve results, an efficient energy transfer was demonstrated in $\text{SrF}_2:\text{Eu}^{2+}$, Pr^{3+} phosphors. The energy transfer process was effective until a concentration quenching between Pr^{3+} ions occurred. The results proposed that Eu^{2+} could be a good sensitizer for absorbing the UV photons and hence efficiently enhancing the Pr^{3+} emission intensity.

$\text{SrF}_2:\text{Eu}^{2+}$ (1.5 mol%) co-doped with Na^+ (0.5 mol%) and various concentrations of Yb^{3+} were also investigated. XRD results showed a mixture of the cubic SrF_2 and NaYbF_4 phases. The NaYbF_4 phase gradually formed with increasing Yb^{3+} doping concentration. Emission spectra and the fluorescence decay curve measurements were utilized to demonstrate the cooperative energy transfer. Energy transfer occurred subsequently from Eu^{2+} to Yb^{3+} followed by intense NIR emission. The energy transfer was completed at high concentrations but the Yb^{3+} emission intensity was reduced as a result of concentration quenching. In addition, from the photoluminescence data it was evident that Na^+ induced significant change to NIR emission.

The possibility of using the broadband absorption of Eu^{2+} to sensitize the $\text{Pr}^{3+}-\text{Yb}^{3+}$ down-conversion couple in SrF_2 matrix was also investigated. The energy transfer process was demonstrated by the decrease of Eu^{2+} and Pr^{3+} related photoluminescence and lifetime with increasing Yb^{3+} concentration. Upon 325 nm excitation into the 5d levels of Eu^{2+} , the samples yield intense near infrared emission corresponding to $\text{Pr}^{3+}:4f-4f$ and $\text{Yb}^{3+}:4f-4f$ transition. Yb^{3+} emission was clearly observed only at high Yb^{3+} concentrations after the emission intensity of Pr^{3+} was quenched. The PL lifetime results of Eu^{2+} confirmed the the second-order cooperative energy transfer also occurred between Eu^{2+} and Yb^{3+} ions.

Contents

List of figures	ix
List of tables	xvi
1 Introduction	1
1.1 General overview	1
1.2 Definition of the research problem	3
1.3 Research aims	4
1.4 Thesis organization	5
References	6
2 Background information	8
2.1 Solar radiation	8
2.2 Solar cells	10
2.3 Solar cell conversion efficiency limits	11
2.4 Photon conversion processes	13
2.5 Luminescent materials	15
2.6 Lanthanide ions	15
2.7 Energy transfer between lanthanide ions	20
2.8 Down-conversion	22
2.9 Downshifting	25
2.10 Crystal structure of SrF ₂ and dopant defects	27
References	30
3 Characterization techniques	33

3.1	UV-Vis spectroscopy	33
3.2	Photoluminescence spectroscopy (PL)	35
3.3	X-ray diffraction (XRD)	37
3.3.1	Introduction	37
3.3.2	Bragg's law	38
3.4	X-ray photoemission spectroscopy (XPS)	40
3.5	Auger electron spectroscopy (AES)	43
3.6	Time-of-flight secondary ion mass spectrometry (ToF-SIMS)	45
3.7	Scanning electron microscopy (SEM)	48
	References	50
4	Concentration quenching, surface and spectral analyses of SrF₂:Pr³⁺ prepared by different synthesis techniques	53
4.1	Introduction	53
4.2	Experimental	54
4.3	Results and Discussion	55
4.4	Conclusions	65
	References	66
5	The effects of Eu-concentrations on the luminescent properties of SrF₂:Eu downshifting nanophosphor	68
5.1	Introduction	68
5.2	Experimental setup	69
5.3	Results and discussion	71
5.3.1	Structure and morphology analysis	71
5.3.2	Photoluminescence spectroscopy	74

5.3.3	XPS analysis	77
5.3.4	TOF-SIMS analysis	79
5.3.5	Luminescence decay curves	80
5.4	Conclusions	83
	References	84
6	Surface characterization and an efficient energy transfer in Ce³⁺ co-doped SrF₂:Eu downshifting nano-phosphor	87
6.1	Introduction	87
6.2	Experimental section	88
6.3	Results and discussion	89
6.3.1	Structure and surface analysis	89
6.3.1.1	XRD analysis	89
6.3.1.2	AES analysis	90
6.3.1.3	XPS analysis	91
6.3.1.4	TOF-SIMS analysis	94
6.3.2	Photoluminescence spectroscopy	96
6.3.2.1	SrF ₂ :Ce ³⁺	96
6.3.2.2	SrF ₂ :Ce,Eu	98
6.3.2.3	Decay curve analysis	104
6.4	Conclusions	107
	References	108
7	Eu²⁺ enhanced Pr³⁺ photoluminescence by energy transfer in SrF₂ phosphor	111
7.1	Introduction	111

7.2	Experimental section	112
7.3	Results and Discussion	113
7.4	Conclusions	126
	References	127
8	NIR quantum cutting of Na⁺ and Eu²⁺-Yb³⁺ couple activated SrF₂ crystal	129
8.1	Introduction	129
8.2	Experimental	130
8.3	Results and discussion	131
8.4	Conclusions	140
	References	141
9	Eu²⁺ sensitized Pr³⁺-Yb³⁺ quantum cutting couple in a SrF₂ crystal	143
9.1	Introduction	143
9.2	Experimental	143
9.3	Results and discussion	144
9.4	Conclusions	153
	References	154
10	Conclusions and future work	156
10.1	Conclusions	156
10.2	Future work	158
A	Publications	160
A.1	Conference proceedings:	160
A.2	Presentations at national and international conferences/workshops:	161

List of Figures

1.1	Energy-loss processes in a single-junction solar cell: (1) lattice thermalization losses; (2) transparency loss; (3) recombination loss; (4) junction loss; (5) contact voltage loss.	2
2.1	The global spectral solar spectrum on the earth for air mass (AM) = 0 to 9. It can be seen that the AM0 spectra closely matches the black-body radiation.	9
2.2	Schematic diagram showing the calculation of the air mass (AM).	10
2.3	A typical normalized spectral response of a c-Si solar cell [4].	11
2.4	Schematic diagram showing the photon conversion processes.	13
2.5	Spectral conversion design for PV applications including downshifting (Ds), down-conversion (DC) and up-conversion (UC) luminescent materials.	14
2.6	Splitting of the $\text{Ln}^{3+}:4f^n$ electronic configuration due to atomic and crystal field forces.	16
2.7	Dieke diagram for energy-levels of Ln^{3+} ions.	18
2.8	Schematic diagram showing the influence of the crystal field (Δ) on the emission of the $4f^7$ and $4f^65d^1$ levels in Eu^{2+} ion.	19
2.9	Schematic diagram of four different basic energy transfer processes between two ions [16].	21
2.10	Schematic diagram of typical mechanisms of NIR quantum cutting. (a) NIR quantum cutting on a single ion by the sequential emission of two NIR photons, (b-d) NIR quantum cutting due to resonant energy transfer from donor to an acceptor and (e) NIR quantum cutting due to cooperative energy transfer.	23

2.11 (a) Energy levels and quantum cutting mechanism for Pr ³⁺ -Yb ³⁺ couple in SrF ₂	24
2.12 Emission of the Eu ³⁺ ion in SrF ₂ under 318 nm excitation wavelength.	26
2.13 A schematic diagram of the pure SrF ₂ structure, which shows that each second simple cubic of the F ⁻ sublattice contains a Sr ²⁺ ion (the other are empty).	28
2.14 Some common structure defects involving Ln ³⁺ ions.	29
3.1 Schematic diagram showing the incident and transmittance light as it passes through a transparent material.	34
3.2 Schematic diagram of the key components of a typical dual-beam UV-vis spectrometer.	35
3.3 Schematic illustration of the basic components of a spectrofluorometer.	36
3.4 Schematic diagram showing Bragg's law and scattering from the atoms.	38
3.5 Schematic diagram of a x-ray diffractometer. The photo shows the Bruker AXS D8 advance x-ray diffractometer used to collect the XRD data of this study.	39
3.6 Characteristic emission of Cu x-rays without a filter and with Nickel filter.	40
3.7 Schematic diagram of the energy distribution involved in photoemission spectroscopy.	42
3.8 Calculated and experimental XPS binding energies of C 1s in a range of molecules via Koopman's theorem. These two values differ by 15 eV as indicated by the straight line.	43
3.9 Schematic diagram showing the decay of ionized atoms by emission of the KL _{2,3} L _{2,3} Auger electron.	44
3.10 A typical Auger spectrum for the SrF ₂ :Ce,Eu phosphor material.	45
3.11 Schematic diagram of Time-of-Flight Secondary Ion Mass Spectrometry (TOF-SIMS).	46

3.12	SIMS 5 TOF-SIMS instrument based on department of physics, UFS.	47
3.13	Schematic diagram of a scanning electron microscopy system with other signals that can be produced during electrons bombardment.	48
4.1	(a) XRD patterns of SrF ₂ :Pr ³⁺ phosphors; (b) Williamson-Hall plots for Pr ³⁺ doped SrF ₂ samples for both the hydrothermal and combustion methods.	56
4.2	SEM images of SrF ₂ :Pr ³⁺ phosphors prepared by different synthesis methods (a) combustion and (b) hydrothermal.	57
4.3	High resolution XPS peaks of (a) Sr 3d, (b) F 1s, (c) Pr 3d _{3/2} , and (d) survey scan for SrF ₂ :Pr ³⁺ phosphors.	59
4.4	Excitation and emission spectra of SrF ₂ :Pr ³⁺ at different synthesis methods, (a) excitation and (b) emission spectrum for combustion method, (c) emission spectrum for hydrothermal method. The inset shows the weak ³ P ₀ - ¹ G ₄ transition band of Pr.	61
4.5	Variation of the Pr ³⁺ emission intensity as a function of Pr ³⁺ concentration for hydrothermal and combustion methods. The vertical lines represent the error bars. (Note: The comparison were only made for the optimum Pr ³⁺ doping concentration between the two synthesis methods. The excitation slit width was different for the two methods during the measurements).	63
4.6	The curve of log(<i>I/C</i>) vs. log(<i>C</i>) in SrF ₂ :Pr ³⁺ phosphors.	64
5.1	XRD pattern of (a) SrF ₂ and (b) SrF ₂ :Eu 3.0 mol% samples. The vertical lines are the standard data of SrF ₂ from the 00-086-2418 card.	72
5.2	SEM images of undoped (a, c) and 5 mol% of Eu doped (b, d) SrF ₂ at low and high magnification, respectively, (e) HRTEM image of the Eu 5 mol% SrF ₂ sample and (f) EDS spectrum of the Eu doped SrF ₂ samples.	73

5.3	Excitation and emission spectra of SrF ₂ :Eu ³⁺ (a) $\lambda_{exc} = 394$ nm and (b) $\lambda_{exc} = 318$ nm using a xenon lamp. The inset graph presents the variation of the Eu ³⁺ emission intensity as a function of the Eu concentration.	75
5.4	PL spectra of Eu doped SrF ₂ using the He-Cd laser system with a 325 nm excitation wavelength.	76
5.5	Eu 3d high resolution XPS spectrum of Eu doped SrF ₂	78
5.6	High resolution XPS peak of Sr 3d and Eu 4d in SrF ₂	79
5.7	TOF-SIMS spectra showing EuF ⁺ and EuF ²⁺ peaks at different concentrations of Eu doped SrF ₂ nanophosphor (a) 1.0 mol% Eu and (b) 10.0 mol% Eu.	80
5.8	(a) Relative PL intensity of the Eu ²⁺ emission band (416 nm) with time and (b) decay curves for the ⁵ D ₀ → ⁷ F ₁ transition (591 nm) of the Eu ³⁺ .	81
5.9	Schematic diagram of the proposed energy transfer mechanism between Eu ²⁺ and Eu ³⁺ ions.	82
6.1	XRD patterns of pure and doped SrF ₂ crystal.	90
6.2	Auger spectrum of Ce and Eu co-doped SrF ₂	91
6.3	High resolution XPS peaks of (a) Sr 3d, (b) F 1s, (c) Eu 3d, and (d) Ce 3d for SrF ₂ :Ce, Eu phosphors powder.	93
6.4	(a and b) Positive and (c) negative TOF-SIMS spectra of SrF ₂ :Ce,Eu nanophosphor powder.	95
6.5	TOF-SIMS correlation analysis using three-colour overlay image showing Eu and Ce dopants distribution in SrF ₂ for an area of 100 μ m × 100 μ m.	96
6.6	Excitation and emission spectra of the SrF ₂ :Ce ³⁺ (0.7 mol%) nanophosphor. The inset shows the 5d-4f transition's emission intensity as a function of Ce ³⁺ concentration.	97

6.7	(a) Photoluminescence spectra of SrF ₂ : Ce ³⁺ (0.7 mol%), xEu excited by laser system with 325 nm excitation wavelength and (b) Eu ³⁺ : ⁵ D ₀ - ⁷ F ₁ emission intensity (= 591 nm) of Eu singly and Ce co-doped Eu in SrF ₂ matrix as function of Eu concentration excited by 394 nm using the xenon lamp.	99
6.8	PL emission spectra of (a) Ce ³⁺ (b) Eu ³⁺ and (c) Ce ³⁺ and Eu ²⁺ with different Eu doping concentration excited by an excitation wavelength of 295 nm. The inset in (b) is the emission of Eu ³⁺ in SrF ₂ :Eu (1 mol%) without Ce ³⁺ ions and the inset in (c) is the Eu ²⁺ emission from SrF ₂ :Ce ³⁺ (0.7 mol%), Eu (5.0 mol%).	101
6.9	Spectral overlap between (a) Ce ³⁺ emission and Eu ²⁺ excitation and (b) the Eu ²⁺ emission and Eu ³⁺ excitation (SrF ₂ :Ce ³⁺ (0.7 mol%), Eu (0.6 mol%)).	102
6.10	Excitation spectra of SrF ₂ :Ce ³⁺ (0.7 mol%), Eu (0.6 mol%) nano-phosphors measured at an emission wavelength of 416 nm and 591 nm. The inset shows the enlarged Ce ³⁺ excitation part of the spectrum.	103
6.11	The decay lifetime of Ce ³⁺ ions in the SrF ₂ host with an increase in Eu concentration. The inset graph shows the decay curve of 0.7% Ce ³⁺ in SrF ₂ fitted to a single-exponential fitting function.	105
6.12	Schematic energy level diagram of Ce ³⁺ and Eu with a possible energy transfer between the Ce ³⁺ and Eu ions.	106
7.1	XRD pattern of the SrF ₂ :Eu ²⁺ (1.5 mol%), Pr ³⁺ (10 mol%) phosphor powder and the standard data (card No. 00-086-2418).	114
7.2	(a) SEM image and (b) EDS spectrum of SrF ₂ :Eu, Pr phosphor powder.	115
7.3	XPS high resolution peaks for the (a) Pr 3d and (b) Eu 3d ions in the SrF ₂ phosphor powder.	117
7.4	Excitation spectrum (dotted line) and emission spectrum (solid line) of SrF ₂ :Pr ³⁺ 0.3 mol% excited with 439 nm to the ³ P ₂ energy level.	118

7.5	Excitation spectrum (dotted line) and emission spectrum (solid line) of SrF ₂ :Eu ²⁺ 1.5 mol% excited by 332 nm.	118
7.6	Spectral overlap between Eu ²⁺ emission and Pr ³⁺ excitation in the SrF ₂ crystal structure.	119
7.7	a) Emission spectra of the 1.5 mol% Eu ²⁺ in SrF ₂ with varied Pr ³⁺ concentration, (b) emission spectra of Pr ³⁺ in codoped samples with increasing Pr ³⁺ concentration and (c) a comparison between Pr ³⁺ singly doped (α) and codoped (β) ions in SrF ₂ . The inset graph in (b) is a variation of Pr ³⁺ (³ P ₀ - ³ H ₄) emission intensity as a function of the Pr ³⁺ concentration for SrF ₂ containing 1.5 mol%Eu ²⁺	121
7.8	PLE spectra of the SrF ₂ :0.3 mol% Pr ³⁺ and SrF ₂ :1.5 mol%Eu ²⁺ , 0.3 mol%Pr ³⁺ samples.	123
7.9	Decay curves of (a) Eu ²⁺ 5d (monitoring 416 nm emission) under 355 nm excitation and (b) Pr ³⁺ : ³ P ₀ - ³ H ₄ (monitoring 488 nm emission) under 375 nm excitation.	124
7.10	Simplified energy level diagram of Eu ²⁺ and Pr ³⁺ showing a possible energy transfer between Eu ²⁺ and Pr ³⁺ ions, and a possible cross-relaxation mechanism between the Pr ³⁺ ions.	125
8.1	XRD patterns of the SrF ₂ :Eu ²⁺ (1.5 mol%) crystals and a mixture of the SrF ₂ and NaYbF ₄ XRD patterns obtained after co-doping with high Yb ³⁺ concentration (0.5 mol% Na). The peaks marked with a triangle refer to the cubic-phase of NaYbF ₄ . The SrF ₂ and NaYbF ₄ standard XRD patterns are also shown.	132
8.2	(a) A pure SrF ₂ structure showing that every second simple cubic of the F ⁻ sub-lattice contains a Sr ²⁺ ion, (b) Schematic pictures of some Yb ³⁺ ions' charge compensation pairs (i.e. both the Na substitutional sites and the F interstitial sites).	133

8.3	Diffuse reflectance spectra of Eu^{2+} and Yb^{3+} ions co-doped in SrF_2 : 0.5 mol% Na^+ with 15 and 30 mol% Yb^{3+} ions' concentrations.	134
8.4	(a) Eu^{2+} emission intensity as a function of Yb^{3+} concentration, and (b) NIR emission spectra as a function of Yb^{3+} concentration excited by a He-Cd laser system with a 325 nm excitation wavelength.	135
8.5	Normalized decay curves of the Eu^{2+} emission at 416 nm as a function of the Yb^{3+} concentration.	138
8.6	Schematic energy level diagrams of Eu^{2+} and Yb^{3+} in SrF_2 and possible energy transfer process between Eu^{2+} and Yb^{3+}	139
9.1	Diffuse reflectance spectra of the Eu^{2+} sensitized Pr^{3+} - Yb^{3+} couple in SrF_2 with different Yb^{3+} concentrations.	145
9.2	Visible emission of Eu^{2+} and Pr^{3+} ions in the SrF_2 host excited by the He-Cd laser system with 325 nm excitation wavelength.	146
9.3	Visible PL emission of (a) Eu^{2+} and (b) Pr^{3+} as a function of Yb^{3+} concentration, excited by 332 nm.	147
9.4	NIR emission spectra of Eu^{2+} and the Pr^{3+} - Yb^{3+} couple as a function of Yb^{3+} concentration. The 10 % Yb spectrum is drawn with a different scale.	149
9.5	(a) Normalized decay curves of the Eu^{2+} emission at 416 nm of $\text{SrF}_2:\text{Eu}^{2+}$, $\text{SrF}_2:\text{Eu}^{2+}$, Pr^{3+} and $\text{SrF}_2:\text{Eu}^{2+}$, Pr^{3+} , Yb^{3+} . (b) Normalized decay curves of the Pr^{3+} emission at 488 nm for $\text{SrF}_2:\text{Eu}^{2+}$, Pr^{3+} and with 0.5 and 1 mol% Yb^{3+}	150
9.6	(Color online) schematic diagram energy level and down-conversion mechanism for the Eu^{2+} sensitized Pr^{3+} , Yb^{3+} couple. The diagram shows the cooperative energy transfer and first-order energy transfer between the Pr^{3+} and Yb^{3+}	152

List of Tables

4.1	The estimated average crystallite size (S) of the particles using the William-Hall and the well-known Debye-Scherrers equations.	56
5.1	Calculated particle size of the undoped and Eu doped SrF ₂ using Sherer's equation.	72
5.2	Calculated intensity ratio between Eu ³⁺ /Eu ²⁺ as a function of Eu concentrations. The emission intensity of ⁵ D ₀ → ⁷ F ₁ transition was taken for Eu ³⁺ and 5d-4f transition centered at 415 nm for Eu ²⁺	76
5.3	Deconvolution parameters for Eu 3d from fig. 5.5. The energy separations ΔE and intensity ratio were fixed and are underlined.	78
6.1	XPS peak position, area distribution and chemical bonding of as-prepared SrF ₂ :Ce,Eu phosphors powder.	94
6.2	Lifetime of the 5d-4f transition of Ce ³⁺ (330 nm) and the Ce ³⁺ -Eu energy transfer efficiency (η_{ET}) in SrF ₂ matrix.	105
8.1	The average decay lifetime (τ (nm)) of the 5d-4f transition of Eu ²⁺ (416 nm) and the Eu ²⁺ -Yb ³⁺ energy transfer efficiency ($\eta_{ET,x\%Yb}$).	138

Chapter 1

Introduction

In this chapter the general overview on the research done on the possibility of using the photon conversion processes in solar cells application is given.

1.1 General overview

In many parts of the world, the sun delivers an abundant source of energy, which can be utilized to generate sufficient and clean energy. It has been shown that the sunlight that reaches the earth's surface provides about 10 000 times more energy than what we consume at the moment [1]. As a result, it is expected that by using solar energy it can increase the potential to meet a large portion of future energy consumption requirements [2].

Recently, many researchers have devoted their attentions to use the sunlight efficiently to increase the performance of the solar cell [2–6]. Solar cells are devices that convert solar energy into electrical energy by using the photovoltaic effect [7, 8]. The most commonly used state-of-the-art solar cell material is crystalline silicon (c-Si), which efficiently absorbs photons in the near infrared (NIR) region ($E_g = 1.12$ eV, ~ 1000 nm), and has energy efficiency around 25% [9, 10]. Efficiency is defined as the ratio of incident energy converted to useful energy. This means that the silicon solar cell can only convert a small part of the solar radiation energy into electrical energy. Fig. 1.1 shows a schematic diagram of the mechanisms responsible for the energy-loss that limits the efficiency of single junction solar cells [6]. The recombination loss (3) depends on the electron-hole lifetime and it can be minimized by controlling the carrier lifetime in the semiconductor. The major energy loss mechanisms are related to processes (1) and (2). The absorption of high energy photons (higher than the band-gap (E_G) of the solar cell) generate heat into the solar cell lattice due to the thermalization process. Lower energy photons transmit through the band-gap of the solar cell, which

is called the transparency or transmission loss and therefore they do not take part in the energy conversion process. The transmission loss and thermalization loss are the two major energy-loss mechanism in the energy conversion process. Both these mechanisms thus relate to the spectral mismatch of the energy distribution of photons in the solar spectrum and the band-gap of a semiconductor material [2–6, 11].

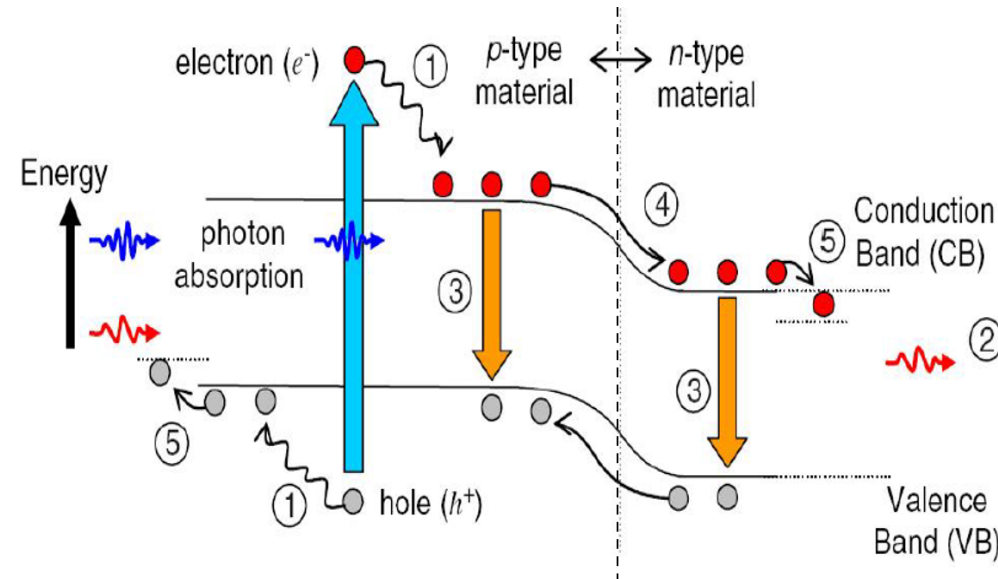


Fig. 1.1: Energy-loss processes in a single-junction solar cell: (1) lattice thermalization losses; (2) transparency loss; (3) recombination loss; (4) junction loss; (5) contact voltage loss. Adapted from Richards [6].

It is possible to use sub band-gap photons that cannot be absorbed by the solar cell to generate high energy photons that can be absorbed. This process is called up-conversion and it can boost the solar cells' conversion efficiency [9]. Up-conversion therefore can be used to reduce the transparency losses. Two mechanisms were proposed to minimize the thermalization loss, namely, down-conversion (also known as quantum cutting) and downshifting. Downshifting is a process of shifting one higher energy photon into a lower energy photon [12]. In the downshifting mechanism, the external quantum efficiency cannot exceed unity and therefore the solar cell system will not be able to overcome the Shockley-Queisser limit [13]. Down-conversion is a process in which one high energy photon cuts into two lower-energy photons. Both these lower energy photons can be absorbed by the solar cell. The external quantum efficiency in down-

conversion therefore exceeds unity [14]. More detail on the photon conversion process can be found in chapter 2.

Most down-converting materials for solar cell application are based on a combination of lanthanide (Ln^{3+}) and Ytterbium (Yb^{3+}) ions. Different down-conversion materials have been investigated by different researchers. Various rare earth couples $\text{Ln}^{3+}\text{-Yb}^{3+}$ ($\text{Ln} = \text{Pr}, \text{Er}, \text{Nd}, \text{Ho}, \text{Dy}, \text{Tb}$ and Tm) were doped in different hosts in which the Ln^{3+} ions act as the absorption centers [14–20]. Absorption of a photon by the Ln^{3+} ions results in feeding two Yb^{3+} ions, which turns out to emit two near infrared photons that can be used for creating two electron-hole pairs (more detail will follow in chapter 2). A combination of Pr^{3+} and Yb^{3+} ions in SrF_2 was reported as one of the best quantum cutting couple with an external quantum efficiency of close to 200% [14]. A theory has predicted that $\sim 39\%$ energy efficiency can be achieved by combining a down-conversion layer with a c-Si solar cell, [3, 4]. Practical realization of such higher efficiency is however still far away and requires further research.

1.2 Definition of the research problem

As it is mentioned previously $\text{SrF}_2\text{:Pr}^{3+}\text{-Yb}^{3+}$ is a suitable candidate for c-Si solar cells application. Ideal NIR down-converting materials for silicon based solar cells however should efficiently convert the broadband UV-Vis part of the solar spectrum into the range where the spectral response of Si is high (red-NIR photons). A prime limitation in the use of the $\text{Pr}^{3+}\text{-Yb}^{3+}$ ions couple in solar cell application is its 4f-4f absorption cross-section. The forbidden 4f-4f transitions of the Pr^{3+} ion is characterized by a low absorption cross-section [3]. A suggestion to this limitation is to add a third sensitizer [3]. Such a sensitizer must have dipole-allowed 4f-5d transitions, which is characterized by a strong absorption cross-section. The 4f-5d transitions of broadband ions strongly depend on the crystal field of the host [14, 21–23]. This property makes such ions good candidates in energy transfer processes. This is because efficient first-order energy transfer between a sensitizer and an acceptor can occur only when the emission band of the sensitizer overlaps the excitation band of the acceptor.

Another problem that needs to be addressed is concentration quenching that mostly occur at high dopant concentration. Energy transfer between the Pr^{3+} and Yb^{3+} ions efficiently occurs at high Yb^{3+} -concentrations. In order to solve this problem the choice of a suitable host lattice and optimization of synthesis conditions may reduce concentration quenching to acceptable levels [3].

Detailed investigation on the application of Eu^{3+} ion as a downshifting layer for solar cells can be found in literature [12, 24]. Emission of the Eu^{3+} ion mainly originates from the 4f-4f transition. In order to enhance the 4f-4f absorption strength of the Eu^{3+} ion, a sensitizer with a high absorption coefficient is also required. Many reports can also be found in literature regarding the synthesis of new dye Eu^{3+} complexes and broadband ions to enhance the spectral response of Eu^{3+} ion [25, 26].

This study focuses on the possibility of using some of the broadband excitation ions to improve the NIR emission of the Pr^{3+} - Yb^{3+} down-conversion couple as well as the red emission of the Eu^{3+} doped SrF_2 crystal. In addition, we also studied the effect of different synthesis techniques on the concentration quenching of the Pr^{3+} ion doped SrF_2 crystal. The decision to use the $\text{SrF}_2:\text{Pr}^{2+}$ - Yb^{3+} structure for this study is motivated by the high quantum cutting efficiency (close to 200%) that can be utilized for creating two electron-hole pairs [14]. The SrF_2 host has been characterized to induce clustering of the dopant ions, which is required in energy transfer processes. Both Eu^{2+} and Ce^{3+} ions however showed a broadband transition from allowed electric-dipole transitions that could make them suitable for this study.

1.3 Research aims

The aim of this study is clearly stated in the following points:

- Synthesising SrF_2 phosphor powder doped and co-doped broadband excitation ions and Ln^{3+} by using different preparation techniques.
- Using different characterization techniques to investigate the influence of broadband excitation ions (as sensitizers) on the luminescence of Ln^{3+} in SrF_2 crystal

for use in solar cell application namely; Eu^{2+} as a sensitizer for Pr^{3+} - Yb^{3+} quantum cutting couple and Ce^{3+} as sensitizer for Eu^{3+} .

- Study the effect of different synthesis techniques on the concentration quenching of the Pr^{3+} ion doped SrF_2 crystal by using different surface, structural and optical characterization techniques.

1.4 Thesis organization

This thesis consists of ten chapters. Chapter 1 contains the introduction that gives a general overview and definitions regarding the research problem. In chapter 2, the basic concepts that are necessary to understand the background information of this research study were briefly discussed. It is followed by a brief description of the theory and experimental procedures of the techniques that were used in this study, chapter 3. The effect of different synthesis techniques on the morphology and concentration quenching of Pr^{3+} doped SrF_2 is given in chapter 4. Chapter 5 provides a detailed description of the possibility of using the Eu ions as a downshifting layer for a solar cell application. The effect of the Ce^{3+} ions on the structure and optical properties of SrF_2 :Eu downshifting nano-phosphor is outlined in chapter 6. Chapter 7 focuses on the possibility of using the Eu^{2+} ion as a sensitizer to the Pr^{3+} ion in the SrF_2 crystal. In chapter 8, the influence of Na^+ ions on the photoluminescence of SrF_2 : Eu^{2+} - Yb^{3+} is studied for possible down-conversion mechanism. Chapter 9 investigates the effect of Eu^{2+} on the NIR emission of Pr^{3+} - Yb^{3+} quantum cutting couple in SrF_2 crystal. In chapter 10, conclusions and planned future work are given. Appendix A contains the published papers and conference presentations of this work.

References

- [1] H. Aguas, S. K. Ram, A. Araujo, D. Gaspar, A. Vicente, S. A. Filonovich, E. Fortunato, R. Martins and I. Ferreira, *Energy Environ. Sci.*, **4** (2011) 4620-4632.
- [2] X. Huang, S. Han, W. Huang and X. Liu, *Chem. Soc. Rev.*, **42** (2013) 173-201.
- [3] B. M. Van der Ende, L. Aarts and A. Meijerink, *Phys. Chem. Chem. Phys.*, **11**(2009) 11081-11095.
- [4] T. Trupke, M. A. Green and P. Würfel, *J. Appl. Phys.*, **92** (2002) 1668-1674.
- [5] Q. Y. Zhang and X. Y. Huang, *Prog. Mater. Sci.*, **55** (2010) 353-427.
- [6] B. S. Richards, *Sol. Energy Mater. Sol. Cells*, **90** (2006) 2329-2337.
- [7] J. Nelson, *The Physics of Solar Cell*, Imperial College Press, UK, (2003).
- [8] M. A. Green, *Solar Cell: Operating Principles, Technology, and System Application*, Prentice-Hall, Englewood Cliffs, (1982).
- [9] B. Ahrens, *Down- and Up-Conversion in Fluorozirconate-Based Glasses and Glass Ceramics for Photovoltaic Application*, University of Paderborn, PhD Thesis, (2009).
- [10] M. A. Green, K. Emery, Y. Hishikawa and W. Warta, *Prog. Photovolt: Res. Appl.*, **16** (2008) 435-440.
- [11] Solar cell conversion-efficiency limit; available from:
<http://aerostudents.com/files/solarCells/CH5SolarCellConversionEfficiencyLimits.pdf>, (Accessed on 18.12.2014).
- [12] E. Klampaftis, D. Ross, K. R. McIntosh and B. S. Richards, *Sol. Energy Mater. Sol. Cells*, **93** (2009) 1182-1194.
- [13] W. Shockley and H. J. Queisser, *J. Appl. Phys.*, **32** (1961) 510-519.
- [14] B. M. Van der Ende, L. Aarts and A. Meijerink, *Adv. Mater.*, **21** (2009) 3073-3077.

-
- [15] B. Fan, C. Point, J. L. Adam, X. Zhang, X. Fan and H. Ma, *J. Appl. Phys.*, **110** (2011) 113107-113114.
- [16] J. M. Meijer, L. Aarts, B. M. van der Ende, T. J. H. Vlugt and A. Meijerink, *Phys. Rev., B* **81** (2010) 035107-035116.
- [17] L. Guo, Y. Wang, J. Zhang, Y. Wang and P. Dong, *Nanoscale Res. Lett.*, **7** (2012) 636-642.
- [18] Z. Bai, M. Fujii, T. Hasegawa, K. Imakita, M. Mizuhata and S. Hayashi, *J. Phys. D: Appl. Phys.*, **44** (2011) 455301-455305.
- [19] X. Zhou, Y. Wang, G. Wang, L. Li, K. Zhou and Q. Li, *J. Alloys Compd.*, **579** (2013) 27-30.
- [20] J. Guicheng, W. Xianta, C. Yonghu, D. Changkui and Y. Min, *J. Rare Earth*, **31** (2013) 27-31.
- [21] A. Guille, A. Pereira, G. Breton, A. Bensalah-ledoux and B. Moine, *J. Appl. Phys.*, **111** (2012) 043104-043108.
- [22] Q. Yan, J. Ren, Y. Tong and G. Chen, *J. Am. Ceram. Soc.*, **96** (2013) 1349-1351.
- [23] Y. Teng, J. Zhou, X. Liu, S. Ye and J. Qiu, *Opt. Express*, **18** (2010) 9671-9676.
- [24] D. Gao, H. Zheng, X. Zhang, Z. Fu, Z. Zhang, Y. Tian and M. Cui, *Opt. Express*, **98** (2011) 011907-011909.
- [25] O. Moudam, B. C. Rowan, M. Alamiry, P. Richardson, B. S. Richards, A. C. Jones and N. Robertson, *Chem. Commun.*, (2009) 6649-6651.
- [26] E. Klampaftis, M. Congiu, N. Robertson and B. S. Richards, *IEEE J. Photovolt.*, **1** (2011) 29-36.

Chapter 2

Background information

In this chapter the basic concepts that are necessary to understand the theory of this study are reviewed and explained.

2.1 Solar radiation

The sun emits a nearly continuous spectrum ranging from ultraviolet, visible and infrared parts of electromagnetic radiation. The distribution of electromagnetic radiation as a function of wavelength is called the solar spectrum or solar radiation. Fig. 2.1 shows the solar irradiance as a function of wavelength (λ).

The electromagnetic radiation emitted by the sun resembles a black-body radiation at 5760 K. The spectral photon flux $\beta_s(E, s, \theta, \phi)$ (number of photons with energy in the range E and $E + dE$ emitted through an unit area per unit solid angle per unit time) at a point s on the surface of the black-body is given by [1]

$$\beta_s(E, s, \theta, \phi)d\Omega.dS.dE = \frac{2}{h^3c^2} \left(\frac{E^2}{e^{\frac{E}{k_B T_s}} - 1} \right) d\Omega.dSdE, \quad (2.1)$$

where dS is the element of the surface area s and $d\Omega$ is the unit of solid angle. Integrating β_s over the solid angle and resolved along dS gives the emitted flux normal to the surface $b_s(E, s)$

$$b_s(E, s) = \int_{\Omega} \beta_s(E, s, \theta, \phi) \cos \theta d\Omega.dS.dE = \frac{2F_s}{h^3c^2} \left(\frac{E^2}{e^{\frac{E}{k_B T_s}} - 1} \right) dSdE, \quad (2.2)$$

Assuming the temperature of all the points on the surface of the black-body is the same, the spectral photon flux normal to the surface is written as

$$b_s(E) = \frac{2F_s}{h^3c^2} \left(\frac{E^2}{e^{\frac{E}{k_B T_B}} - 1} \right), \quad (2.3)$$

where F_s is a geometrical factor. In general $F_s = \pi \sin^2 \theta_{\text{sun}}$. Whereas, at the surface of the sun and because of the hemispheric nature $F_s = \pi$.

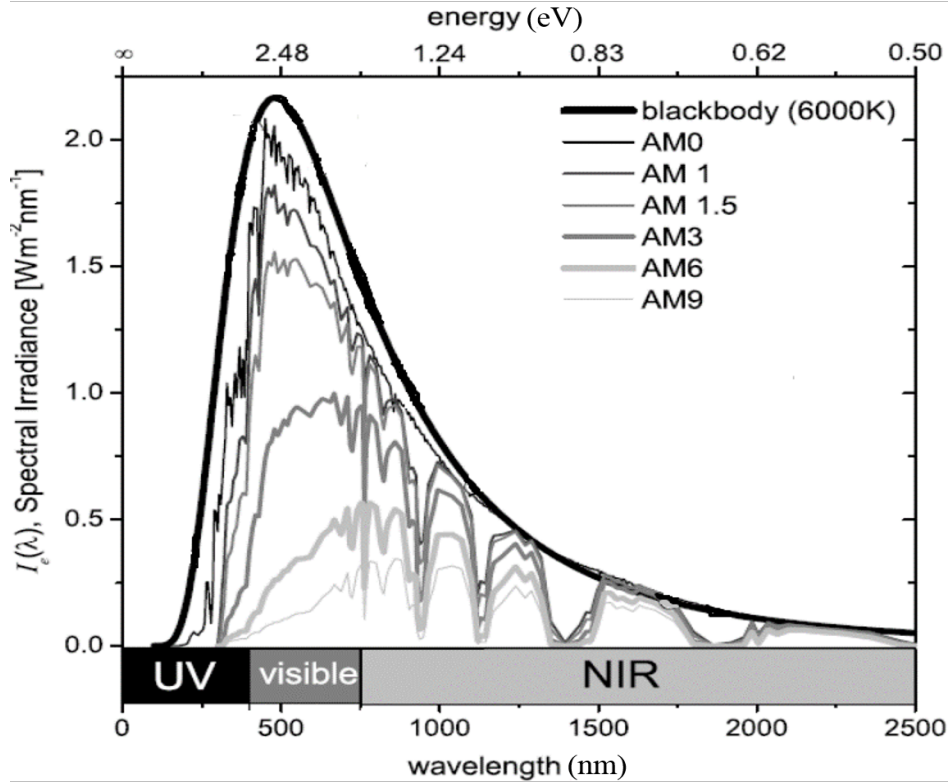


Fig. 2.1: The global spectral solar spectrum on the earth for air mass (AM) = 0 to 9. It can be seen that the AM0 spectra closely matches the black-body radiation. Adopted from A. Shalav [2].

The emitted energy flux or irradiance on the earth's surface is defined as

$$I(E) = Eb_s(E), \quad (2.4)$$

Integrating Eqn. 2.4 gives the total intensity per meter square incident on the earth, which is equal to σT , where σ is the Stefan-Boltzmann's constant [1, 2]. At the sun's surface this value is 62 MW m^{-2} . At a point just outside the earth surface, the total intensity value is reduced to 1376 W m^{-2} . This value corresponds to the air mass zero (AM0) solar spectrum and is used for calibration of solar cell performance in space. The AM measures the path length of radiation relative to the length of the direct beam path through the atmosphere and is given by $1/\cos(\theta)$ (fig. 2.2). The AM0 value rapidly decreases when the sun light passes through the earth's atmosphere or with increasing the air mass (AM). The journey of the solar radiation through the earth's atmosphere causes the attenuation of the solar radiation due to scattering

and absorption by atmospheric gases [2]. Fig. 2.1 shows the influence of the earth's atmosphere on the solar radiation with increasing AM values.

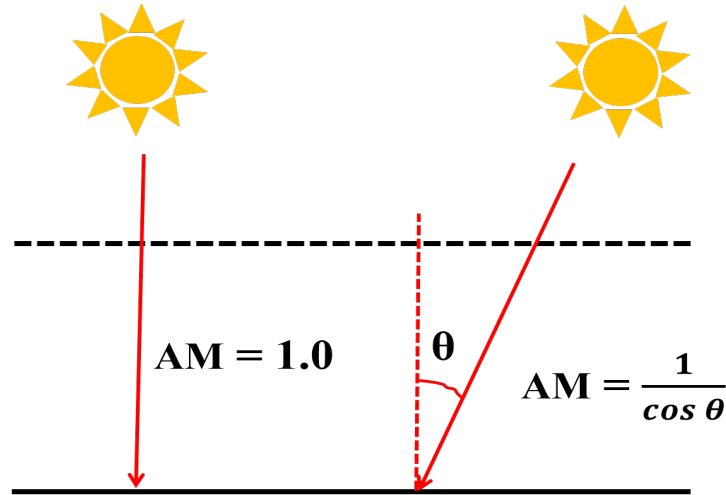


Fig. 2.2: Schematic diagram showing the calculation of the air mass (AM).

The standard solar spectrum for temperature latitude is AM1.5 corresponding to $\theta = 48.2^\circ$. The terrestrial solar spectrum has been normalized so that the integrated irradiance is 1000 W m^{-2} . Actual irradiances clearly differ with account to seasonal and daily variations in the position of the sun, orientation of the earth and condition of the sky [1].

2.2 Solar cells

Solar cells are semiconductor devices that convert solar energy to electrical energy [1]. When the sunlight interacts with a solar cell, the photons promote the electrons in the cell into the conduction band from where these electrons can then be utilized to generate electric current. In a solar cell the absorber layer is a very important part. It absorbs the incident photons that cause the e-h pairs to be created [3]. A typical semiconductor solar cell composes of two layers. One is doped with positive charge carriers (p-type) and the other with negative charge carriers (n-type). A p-n junction is then produced on the boundary of the layer. The conversion efficiency is one of the most significant factors that determine PV's performance. The bandgap of the

semiconductor plays a fundamental role in the solar cell's conversion efficiency. Today the crystalline, polycrystalline and amorphous solar cells occupy more than 90% of the world's solar energy production [1]. The c-Si solar cell only achieves a maximum energy conversion efficiency of $\sim 25\%$ [4].

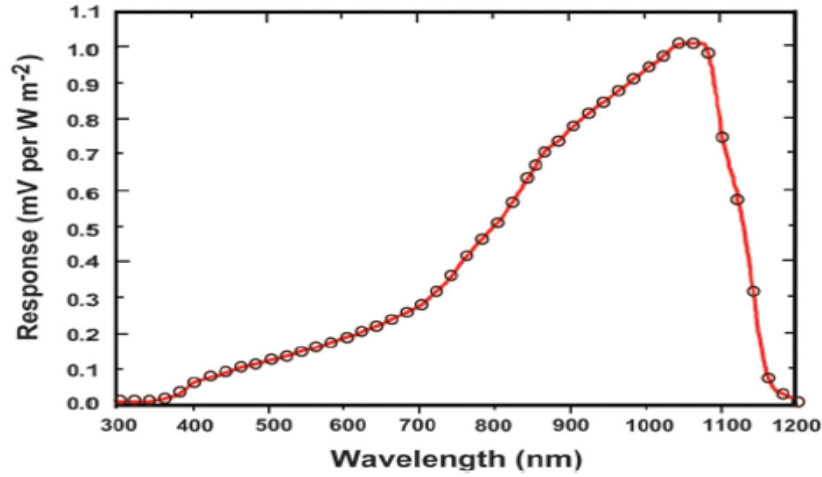


Fig. 2.3: A typical normalized spectral response of a c-Si solar cell [4].

The c-Si solar cells efficiently absorb light in the range of 950-1100 nm, but they show very low spectral response in the short-wavelength range, see fig. 2.3. The decrease of the spectral response of the c-Si solar cells at the shorter wavelength is one of the reasons that limits the energy conversion efficiency.

2.3 Solar cell conversion efficiency limits

The maximum conversion efficiency (η) of a solar cell is defined as the ratio of maximum power (P_m) generated by a solar cell to the incident power (P_{in}). The incident power is normally equal to the AM1.5 irradiance spectrum, which is also equal to the total optical density (power per unit area) incident on the solar cell. P_m is defined as the voltage at the point of maximum power (V_m) multiplied by the maximum current density at that point [2, 3]

$$\eta = \frac{P_m}{P_{in}} = \frac{J_m V_m}{P_{in}} = \frac{J_{sc} V_{oc} FF}{P_{in}}, \quad (2.5)$$

where J_{sc} and V_{oc} are the short-circuit current density and open circuit voltage, respectively. FF is the fill factor describing the ‘squareness’ of the IV curve. Low band-gap materials have high thermalization losses (giving low V_{oc} and V_m), whereas high band-gap materials have low J_m and J_{sc} due to their maximum sub-bandgap losses [2]. The incident power can be calculated from the spectral power density, $P(\lambda)$, using the following equation [3]:

$$P_{in} = \int_0^{\infty} \phi(\lambda) \frac{hc}{\lambda} d\lambda, \quad (2.6)$$

where $\phi(\lambda)$ is the photon flux density and $P(\lambda) = \phi(\lambda) \frac{hc}{\lambda}$, c is the speed of light and h is Plank’s constant.

In principle, only photons with energy higher than the semiconductor energy band-gap (E_G) are utilized to generate e-h pairs. The fraction of incident energy that is absorbed by the single junction solar cell, used in energy conversion, is given by

$$P_{abs} = \frac{\int_0^{\lambda_G} \phi(\lambda) \frac{hc}{\lambda} d\lambda}{\int_0^{\infty} \phi(\lambda) \frac{hc}{\lambda} d\lambda}, \quad (2.7)$$

where λ_G is the wavelength of photons that corresponds to the bandgap energy of the absorber of the solar cell. A part of the absorbed energy, the excess photon energy, is lost due to the thermalization at the edge of the conduction and valance bands of the absorber material. The fraction of the absorbed energy that the solar cell utilized as useful energy, P_{use} , is given by

$$P_{use} = \frac{E_G \int_0^{\lambda_G} \phi(\lambda) d\lambda}{\int_0^{\lambda_G} \phi(\lambda) \frac{hc}{\lambda} d\lambda}, \quad (2.8)$$

Therefore, we can write the conversion efficiency limited by the spectral mismatch as [2, 3]

$$\eta = P_{abs} P_{use} = \overbrace{\frac{\int_0^{\lambda_G} \phi(\lambda) \frac{hc}{\lambda} d\lambda}{\int_0^{\infty} \phi(\lambda) \frac{hc}{\lambda} d\lambda}}^1 \overbrace{\frac{E_G \int_0^{\lambda_G} \phi(\lambda) d\lambda}{\int_0^{\lambda_G} \phi(\lambda) \frac{hc}{\lambda} d\lambda}}^2. \quad (2.9)$$

where the first part (1) is the transmission loss and the second part (2) is the thermalization loss. These losses are known as spectral mismatch losses [2]. The thermalization loss is dominant in solar cells with a small bandgap. The transmission loss is substantial in semiconductors with a wider bandgap. According to the detailed balance model

developed by Shockley and Queisser [5], the theoretical conversion efficiency limit for a single-junction solar cell with energy gap 1.1 eV is 30%. The spectral mismatch losses account for 70% of the total conversion efficiency limit [6].

Proposals are therefore needed to raise the existing solar cells beyond the Shockley-Queisser limit. One approach was theoretically developed to adapt the solar spectrum. The approach is to convert the high and low energy photons (thermalization and transmission losses) to the energy range where the spectral response of the solar cells is high by using the concept of photon conversion processes. The basic concepts of the photon conversion processes will be discussed in the next section (2.4).

2.4 Photon conversion processes

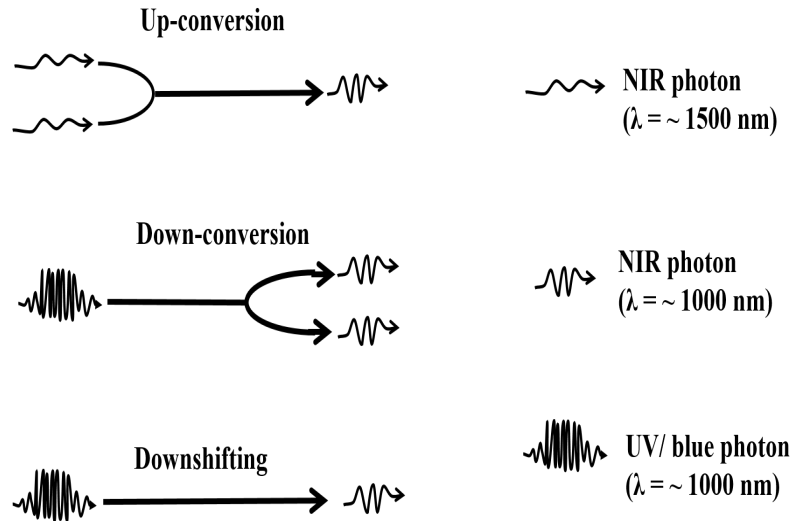


Fig. 2.4: Schematic diagram showing the photon conversion processes.

Photon conversion processes aim to adapt the solar spectrum to better match the absorption properties of the solar cell device via luminescence. This is in contrast to the other concepts which all concern to develop a semiconductor device to better match the solar spectrum such as space-separated quantum cutting and multiple exciton generation [7, 8]. There are three photon conversion processes, namely, down-shifting, down-conversion and up-conversion. These processes are illustrated schematically in fig. 2.4. Up-conversion is where two lower energy photons combine to give one higher

energy photon. The sum of the absorbed photons energies must be greater or equal to the emitted photons energies. Up-conversion is an anti-Stokes shifts since Stokes law states that the wavelength of the emitted light should be greater than the wavelength of the exciting spectrum. For solar cell application, an up-converter material could be placed behind a bifacial solar cell to convert the sub band-gap photons to higher energy photons back to the solar cell where they can be absorbed (fig. 2.5). The up-conversion processes can occur through three different mechanisms, namely excited state absorption, direct two photon absorption, and energy transfer up-conversion [9]. A detailed description of the up-conversion process and its history can be found elsewhere [4, 6, 9]. Down-conversion is where one high energy photon (i.e. UV/visible photon) splits into two low energy photons. Whereas, downshifting is a process of shifting one higher energy photon into one lower energy photon. Both down-conversion and downshifting layers should be placed on top of a bifacial single-junction solar cell to convert the high energy photons to lower energy photons where the spectral response of the solar cell is high and hence minimize the thermalization loss (fig. 2.5).

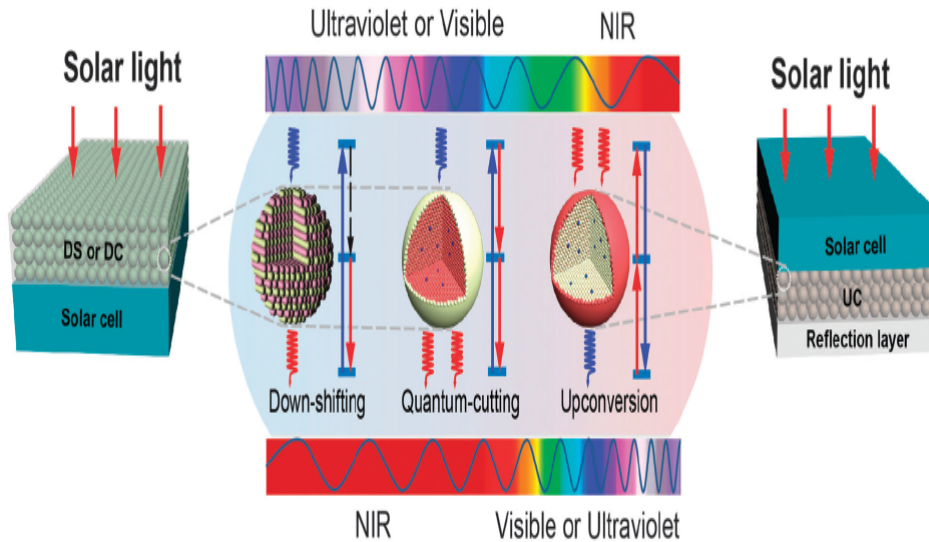


Fig. 2.5: Spectral conversion design for PV applications including downshifting (Ds), down-conversion (DC) and up-conversion (UC) luminescent materials [4].

Luminescent materials provide the most vital options for photon conversion processes. This project focused on the possibility of using broadband excitation ions to en-

hance the spectral response of luminescent materials based on downshifting and down-conversion. Luminescence materials will therefore be discussed in the next sections.

2.5 Luminescent materials

Luminescence is the emission of light by a material when exposed to an external energy excitation [4]. Different excitation sources can be used in luminescence, including electromagnetic radiations, electric fields, x-rays, etc. The excitation source type determines the type of the luminescence, which are generally indicated by a prefix, i.e. in the case of where the excitation source is photons, this luminescence is called photoluminescence. Luminescence is divided into two categories, namely fluorescence and phosphorescence, depending on the nature of the excited state. Fluorescence has fast emission rates. The emission rates of fluorescence are typically 10^8 s^{-1} , so that a typical fluorescence lifetime is near 10 ns. Phosphorescence emission arises from triplet excitation states in which the electron in the excited state has the same spin orientation as the ground state electron. Such transition are forbidden and the emission rates are slow.

Inorganic solids that give luminescence are called phosphors or luminescent materials [4, 10]. Luminescent materials generally require a host that form the bulk of the phosphors [10]. The characteristic luminescence properties of the phosphor are often obtained by doping the host material with a relatively small amount of foreign ions. The host is necessary to optimize the distribution of the activators and prevent the occurrence of rapid non-radiative processes. The dopant ions substitutionally replace the host ions in the host lattice. In this project SrF_2 is used as a host matrix, see section 2.10. Lanthanide ions are usually used as dopant ions to induce the luminescence.

2.6 Lanthanide ions

Although the lanthanide ions maybe find in different forms, the trivalent form is abundant. The trivalent form of the lanthanide (Ln^{3+}) ions have electronic configuration of

$4f^n 5s^2 5p^6$ where n is the number of electrons (from 0 to 14). The partly filled 4f level is important in the optical and magnetic properties of the lanthanides. The number of 4f orbital configurations for n electrons is given by $(14!/[n!(14-n)!])$, and each configuration can have a specific energy. Shielding of the 4f orbital by the filled 5s and 5p outer electrons makes the 4f electrons weakly affected by the ligand ions in the crystal. As a result the lanthanide 4f-4f electronic transitions exhibit relatively narrow lines in the luminescence and absorption spectra. Such transitions are forbidden by the Laporte selection rule, which states that “the states with even parity can only be connected by electric dipole transitions with states of odd parity, and odd states only with even ones” [11]. The transitions within the 4f shell are forbidden in terms of electric dipole transitions, but allowed for magnetic dipole or electric quadrupole radiation. Although an electric dipole transition is forbidden it may occur but with a low probability [11].

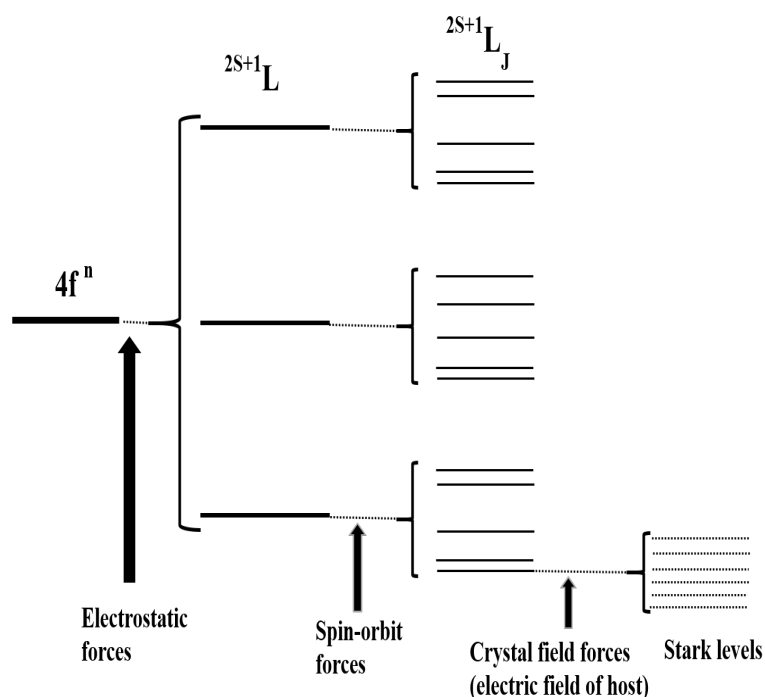


Fig. 2.6: Splitting of the $\text{Ln}^{3+}:4f^n$ electronic configuration due to atomic and crystal field forces.

The weak interactions of the 4f electrons in the crystals perturbs the $^{2s+1}L_J$ states of the Ln^{3+} ions and causes additional splitting (Stark splitting). The stark splitting is typically smaller than the spin-orbit splitting. As a result, the optical emission

and absorption of a Ln^{3+} ion are typically similar to that of free ions. The atomic interactions and energy level splitting are depicted in fig. 2.6. The fact that the Stark splitting is smaller than the spin-orbit splitting, the free ion Hamiltonian can be written as [11]

$$H_F = -\frac{\hbar^2}{2m} \sum_{i=1}^N \nabla_i^2 - \sum_{i=1}^N \frac{Ze^2}{r_i} + \sum_{i<j}^N \frac{Ze^2}{r_{ij}} + \sum_{i<1}^N \xi(r_i)(s_i \cdot L_i), \quad (2.10)$$

The first term is the sum of the kinetic energies of all the electrons of the 4f ion and the second term is the potential energy of all the electrons in the field of the nucleus. The third term is the repulsive Coulomb potential of the interactions between pairs of electrons and the last term is the spin-orbit interaction, which accounts for coupling between the spin angular momentum and the orbital angular momentum, see fig. 2.6. In the free atom, the spherical symmetry of each level is reduced to $(2J+1)$ degeneracy. When the ion is placed in a crystal field the spherical symmetry is reduced to the point symmetry at the ion site. Hence, the perturbed free ion Hamiltonian for an ion in a crystal is written as

$$H = H_F + V_{CF} \quad (2.11)$$

where V_{CF} is the perturbation Hamiltonian due to the the crystal field around the ion, which is responsible for the Stark splitting. From fig. 2.6 the smaller forces V_{CF} split the free ion (spin-orbit) levels into a collection of Stark levels.

Dieke et al. [12] studied the energy of the 4f electrons of the Ln^{3+} ions. Their calculation results is shown in a diagram known as the Dieke diagram, shown in fig. 2.7. Nowadays, it is a common reference that is used to estimate the low-lying f^n levels of the Ln^{3+} ions. In the Dieke diagram the thickness of the level indicates the degree of the crystal field splitting and the location of the free ion $^{2s+1}L_J$ approximated from the center of the multiplet level. The energy splitting slightly changes when the Ln^{3+} ions are incorporated into different crystals, but the dominant spectral features remain unchanged [2].

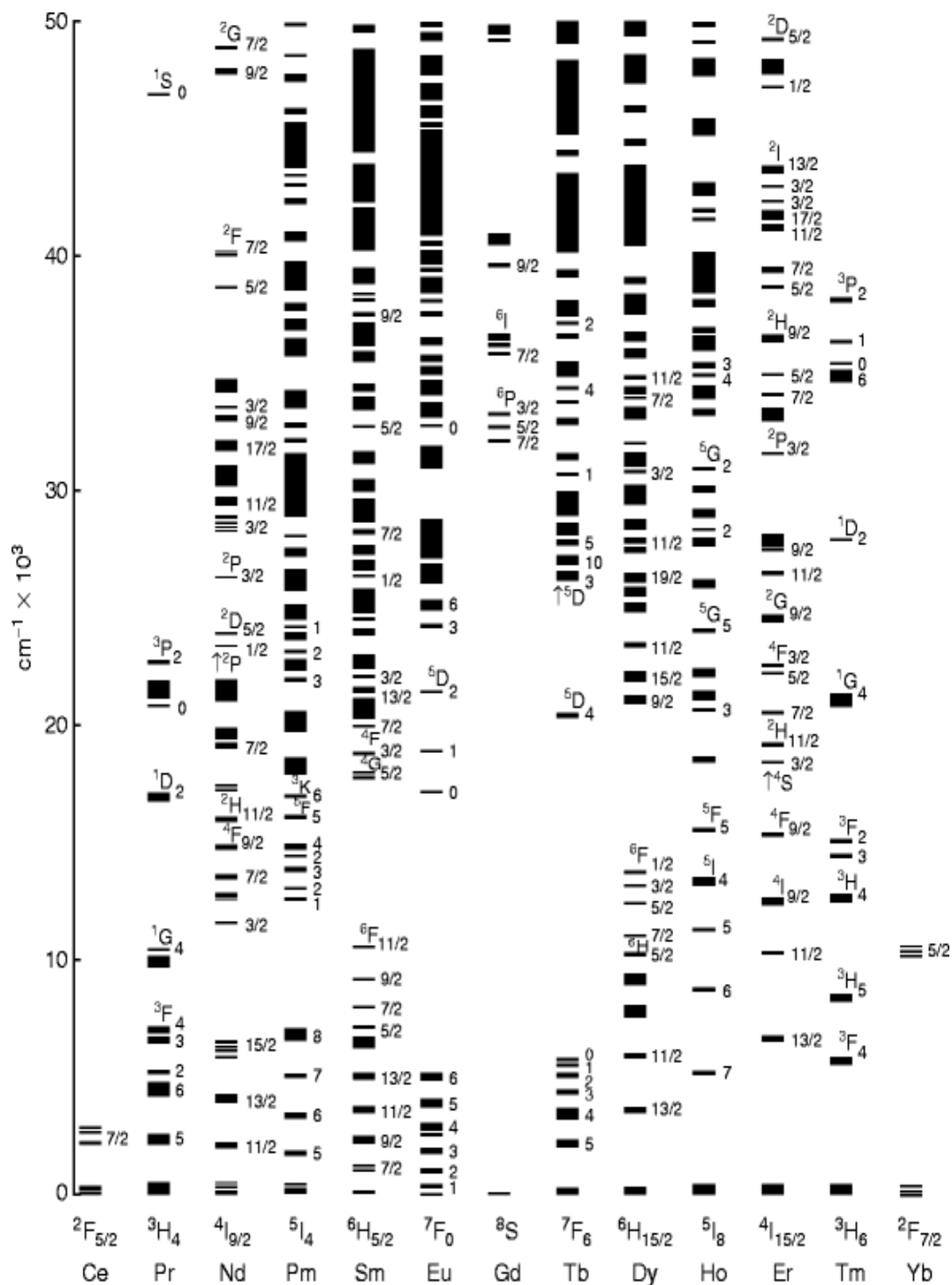


Fig. 2.7: Dieke diagram for energy-levels of Ln^{3+} ions [13].

In contrast to the 4f orbital, the crystal field in the 5d orbital is large compared to the spin-orbit interaction. The interaction of the 5d level with the neighboring anion ligands (the crystal field interaction) degenerate the 5d levels of the free ion and shifts the whole 5d configuration (centroid shift) towards lower energy. The 5d splitting depends on the site symmetry. Both the crystal field splitting and the centroid shift lowers the lowest 5d level, which is known as the redshift or depression D [14]. The value of D determines the emission color and excitation wavelength of the 4f-5d transitions. A good example of 4f-5d transition is related to the Ce^{3+} ion. The ground state of Ce^{3+} ion consists of an optically active electron in the 4f shell. Its 5d excited state is strongly effected by the crystal environment. The crystal environment can split the 5d level by as much as 25000 cm^{-1} , depending on the host material. In SrF_2 , Ce^{3+} emits broadband emission centered at 330 nm that originates from the 5d-4f transitions.

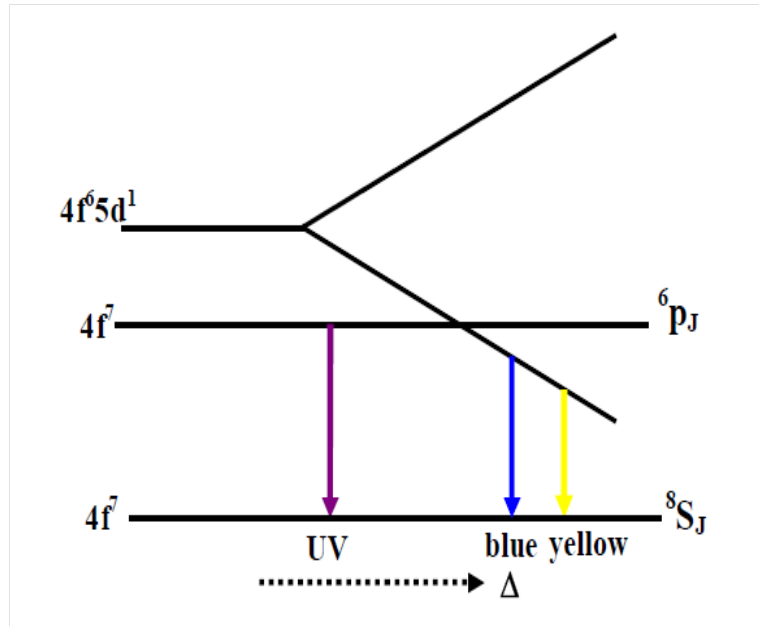


Fig. 2.8: Schematic diagram showing the influence of the crystal field (Δ) on the emission of the $4f^7$ and $4f^6 5d^1$ levels in Eu^{2+} ion [15].

Divalent rare earth ions also have similar $4f^n$ outer electronic configurations but with one more electron. In contrast to the Ln^{3+} ions, the $4f^{(n-1)}5d$ configuration of the divalent rare earth ions is situated close to the $4f^n$ fundamental configuration. As a result, the transition of $4f^n \rightarrow 4f^{(n-1)}5d$, for the divalent rare earth ions in most cases is dominant over the 4f-4f transitions. This leads to intense (parity-allowed

transitions) and broad absorption and emission bands [15]. The Eu^{2+} is an example of such an ion. Its emission bands are usually broad due to the f-d transitions. The wavelength positions of these broad emission bands strongly depend on the host's crystal field. It changes from the near-UV to the red colour, as shown schematically in fig. 2.8. Increasing the crystal field strength tends to shift the emission bands to longer wavelengths.

2.7 Energy transfer between lanthanide ions

Energy transfer is a process where the excitation energy is absorbed by a luminescent centre called a donor and then transferred to another luminescence centre called an acceptor. The acceptor may then release the energy as a photon.

There are different mechanisms involved in the energy transfer processes between Ln^{3+} ions namely, (a) resonant radiative transfer through emission of the donor and re-absorption by the acceptor, (b) non-radiative transfer associated with resonance between the absorber and emitter, (c) phonon-assisted energy transfer, and (d) cross-relaxation between two identical ions [16], see fig. 2.9. The resonant radiative transfer from the emission of the donor (fig. 2.9(a)) requires a significant spectral overlap between the donor's emission region and the absorption region of the acceptor [16, 17]. When the radiative energy transfer dominates in the system the decay time of the donor does not change with the acceptor concentration. In the case of non-radiative energy transfer (fig. 2.9(b)), the energy transfer would lead to a significant decrease in the decay time of the donor ion with an increase in the acceptor concentration. In most inorganic systems the radiative energy transfer can usually be neglected [16, 17]. A resonant condition is required for the energy transfer to occur between a donor and an acceptor. This condition is what the energy difference between the ground and the excited states of the donor, which should be equal to that of the acceptor. There will then exist a suitable interaction, either an exchange interaction or a multipolar interaction between the donor and the acceptor [16, 17]. The exchange interaction (Dexter energy transfer) relies on the overlap of the wave function and thus only exists

over very short distances. The multipolar interaction (Föster energy transfer) depends on the strength of the optical transitions involved and can occur over relatively large distances.

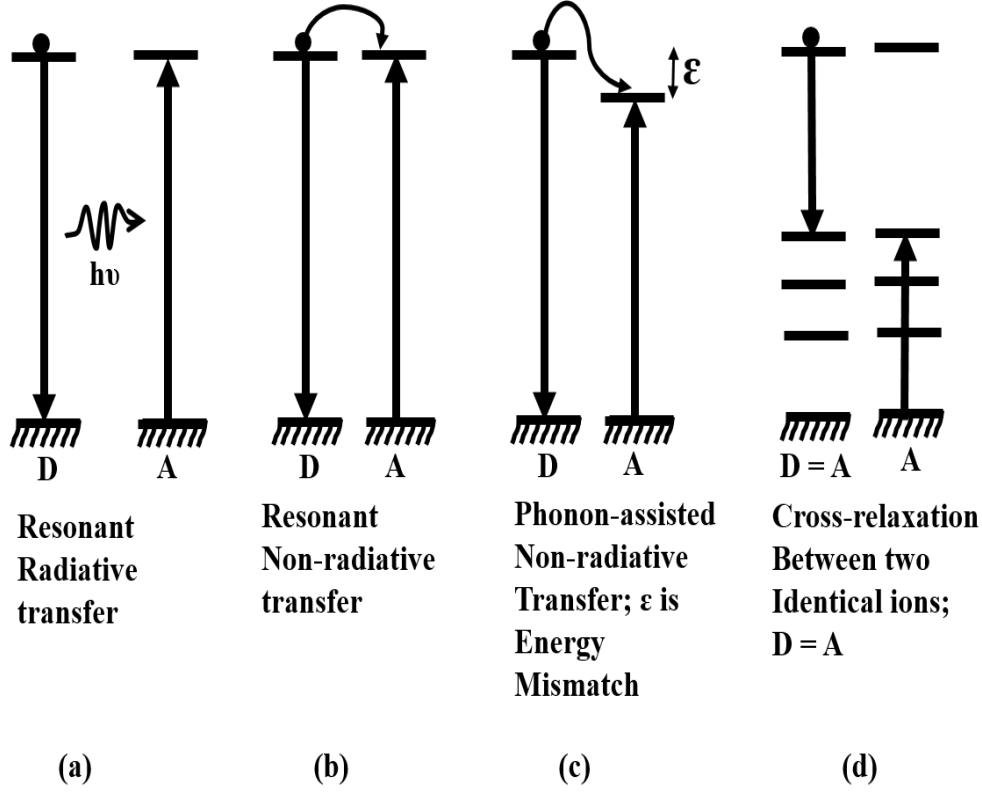


Fig. 2.9: Schematic diagram of four different basic energy transfer processes between two ions [16].

The Dexter energy transfer from a donor to an acceptor is generally approximated as follow

$$W_{DA} = \frac{2\pi}{\hbar} | \langle DA^* | H_{DA} | D^*A \rangle |^2 \int g_D(E) g_A(E) dE \quad (2.12)$$

where $\langle DA^* |$ and $|D^*A \rangle$ are the final and initial states, respectively. The integral represents the spectral overlap between the donor's emission spectrum and the acceptor's absorption spectrum. The factors $g_D(E)$ and $g_A(E)$ represents the normalized shape of the donor's emission and acceptor's absorption spectra, respectively. Eqn. 2.12 shows that the energy transfer probability should drop to zero when the overlap integral vanishes. The square of the matrix element in Eqn. 2.12 is expressed in

terms of the distance-dependent energy transfer probability between the donor and acceptor. The distance dependence of the transfer rate varies with the type of interaction. For exchange interaction the distance dependence is exponential, while for electric multipolar interaction the distance dependence is given by R^{-n} ($n = 6, 8, 10$ for electricdipole-electricdipol interaction and electricdipole-electricquadrupole interaction, respectively) [4].

In the case where the resonance condition is not well met between the donor and the acceptor, the energy transfer might occur through a phonon, which is known as phonon-assisted energy transfer (fig. 2.9(c)). According to the Miyakawa-Dexter theory [18] the probability of phonon-assisted transfer is given by

$$P_{PA}(\Delta E) = P_{PAT}(0)e^{-\beta\Delta E} \quad (2.13)$$

where ΔE is the energy gap between the electronic levels of the donor and the acceptor ions, β is a parameter that depends on the energy occupation number of the participating phonons and $P_{PAT}(0)$ is equal to the resonant transfer probability given by Eqn. 2.12. In the cross-relaxation energy transfer process the donor and an acceptor is the same ion. Fig. 2.9(d) shows that the cross-relaxation may lead to the diffusion process between activators when the levels involved are identical or lead to self quenching if the levels are different [17]. Energy transfer between the Ln^{3+} ions is the heart of the down-conversion process.

2.8 Down-conversion

A down-conversion or quantum cutting material offers such a process could have a quantum efficiency of more than a 100% [4]. Quantum cutting can occur by photon cascade emission from a single lanthanide ion or by energy transfer through different centers of lanthanide ions [19, 20]. Nowadays, down-conversion is investigated to convert high energy photons before entering a solar cell and therefore minimize lattice thermalisation losses as well as to enhance the solar cell efficiency [4, 6]. A theory has predicted that an energy efficiency of 38.6% can be achieved by using a down-conversion layer in conjunction with a Si solar cell [21].

Different mechanisms that demonstrate NIR quantum cutting are shown in fig. 2.10. Quantum cutting can occur with only one optically active center ion or with a combination of different ion centers. The single quantum cutting process consists of one ion with more than two energy levels. Excitation into the highest excited state yields two photons due to stepwise relaxation to the ground state, see fig. 2.10(a). This was demonstrated in Er^{3+} and Ho^{3+} where upon absorption of an UV/Vis photon two NIR photons are produced [22, 23]. A major problem of using single ion based quantum cutting is however the recombination of both unwanted UV/Vis and non-radiative emissions that compete with the desired emission of the two NIR photons [4].

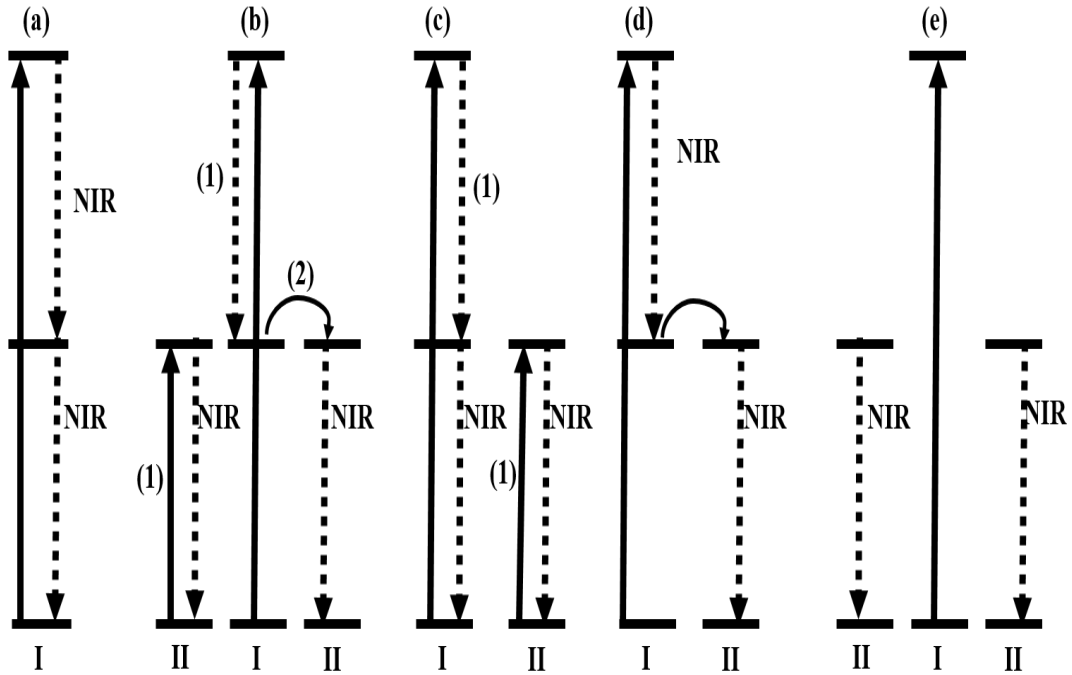


Fig. 2.10: Schematic diagram of typical mechanisms of NIR quantum cutting. (a) NIR quantum cutting on a single ion by the sequential emission of two NIR photons, (b-d) NIR quantum cutting due to resonant energy transfer from donor to an acceptor and (e) NIR quantum cutting due to cooperative energy transfer. Adapted from X. Huang et al. [4].

Another possibility is that quantum cutting occurs within more than one ion (summarized in fig. 2.10(b-e)) through cross-relaxation or resonant energy transfer between the ions. The energy resonance condition needs to be fulfilled. Quantum cutting can

also occur by the use of three optically active centers. Fig. 2.10(b) shows the emission of two photons from ion pairs via cross-relaxation between the donor and acceptor ions followed by the emission from the acceptor ions. There are some cases where quantum cutting may occur through cooperative energy transfer where the emission of the donor ion simultaneously excite two nearby ions through a cooperative process. The energy resonance must be fulfilled, so the energy difference for the energy transfer transitions in both ions must be equal.

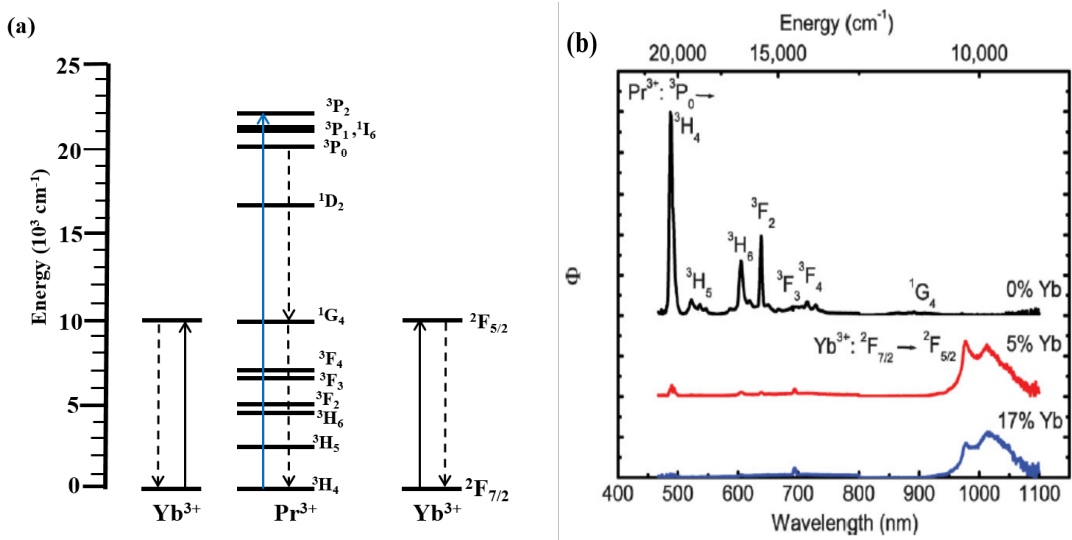


Fig. 2.11: Energy levels and quantum cutting mechanism for $\text{Pr}^{3+}-\text{Yb}^{3+}$ couple in SrF_2 and (b) Emission spectra for $\text{SrF}_2:\text{Pr}^{3+}-\text{Yb}^{3+}$ through quantum cutting process (excitation wavelength is 441 nm) [24].

$\text{Pr}^{3+}-\text{Yb}^{3+}$ in different crystal field hosts is the most studied quantum cutting couple [24–26]. Two energy transfer mechanisms have been assigned for quantum cutting in the $\text{Pr}^{3+}-\text{Yb}^{3+}$ couple, (i) second-order cooperative energy transfer where one Pr^{3+} ion feeds two different Yb^{3+} ions [26] and (ii) first-order resonant energy transfer [24, 25]. The 1st mechanism is where the $\text{Pr}^{3+}:^3\text{P}_0$ level (see fig. 2.11(a)) is situated at about twice the energy level of the $^2\text{F}_{5/2}$ level of Yb^{3+} . The $\text{Pr}^{3+}:^3\text{P}_0 \rightarrow ^3\text{H}_4$ transition can therefore excite two Yb^{3+} ions. The 2nd mechanism consists of two steps of resonance energy transfer as shown in fig. 2.11(a). If a blue photon is absorbed (441 nm excitation wavelength) into the $^1\text{I}_6$ - and $^3\text{P}_j$ ($j = 0, 1, 2$) levels, depopulation from the $^1\text{I}_6$ - and $^3\text{P}_{1,2}$ energy levels occurs to the metastable $^3\text{P}_0$ level. Resonance energy transfer will

then occur with two steps between Pr^{3+} and Yb^{3+} with ${}^1\text{G}_4$ acting as the intermediate level: $\text{Pr}^{3+}: [{}^3\text{P}_0-{}^1\text{G}_4, {}^1\text{G}_4-{}^3\text{H}_4] \rightarrow 2 \times \text{Yb}^{3+}: [{}^2\text{F}_{5/2}-{}^2\text{F}_{7/2}]$. It results in feeding two Yb^{3+} ions which gives rise to the emission of two near infrared photons.

The energy transfer process in quantum cutting systems can be investigated by steady-state and time-resolved luminescence spectroscopy [27]. The energy transfer (η_{ET}) and quantum efficiency (η_{QE}) is usually calculated from the luminescence decay curves by using the following equations:

$$\eta_{ET} = \eta_{x\%Acc} = 1 - \frac{\int I_{x\%Acc} dt}{\int I_{0\%Acc} dt} = 1 - \frac{\tau_{x\%Acc}}{\tau_{0\%Acc}} \quad (2.14)$$

$$\eta_{QE} = \eta_{Don}(1 - \eta_{ET}) + 2\eta_{ET} \quad (2.15)$$

where I and τ represent the intensity and the lifetime, respectively, $x\%Acc$ stands for the acceptor concentration and η_{Don} represents the quantum efficiency for the donor and is set to 1 [4]. The relative quantum efficiency can also be determined through careful comparison of integrated areas from the emission spectra [24]. This can be done by calculating the ratio of the integrated emission intensity of the donor ion in the absence of the Yb^{3+} ion to the integrated Yb^{3+} ion emission intensity in co-doped systems. To apply this method it is important to measure the emission spectra under identical conditions. An example of this method has recently been applied on the Pr^{3+} - Yb^{3+} couple co-doped SrF_2 host [24]. The corrected emission spectra for SrF_2 : Pr^{3+} , Yb^{3+} are shown in fig. 2.11(b) under 441 nm excitation wavelength. The emission of Yb^{3+} was quenched at high Yb^{3+} doping concentration due to concentration quenching between the Yb^{3+} ions. The conversion efficiency for the Pr^{3+} and Yb^{3+} doped SrF_2 samples reached 140% until the conversion efficiency decreased at higher Yb^{3+} doping due to concentration quenching.

2.9 Downshifting

Downshifting is a single photon process of shifting one higher energy photon into one lower energy photon. In a typical downshifting process and is upon excitation with a high-energy photon non-radiative relaxation occurs followed by radiative relaxation.

The result is the emission of a lower energy photon. This fulfils the shifted wavelength between the absorption spectrum and emission spectrum, which is known as the Stokes shift. Luminescent downshifting can be used in many devices that show poor spectral response to short-wavelength light. The downshifting materials absorb the short wavelength light and re-emit at a longer wavelength where the external quantum efficiency of the device is high. Ideal downshifting materials exhibit good external quantum efficiency, close to unity, and large Stokes shifts. A major advantage of downshifting for solar cell devices the thermalization loss during the absorption of high energy photons is minimized.

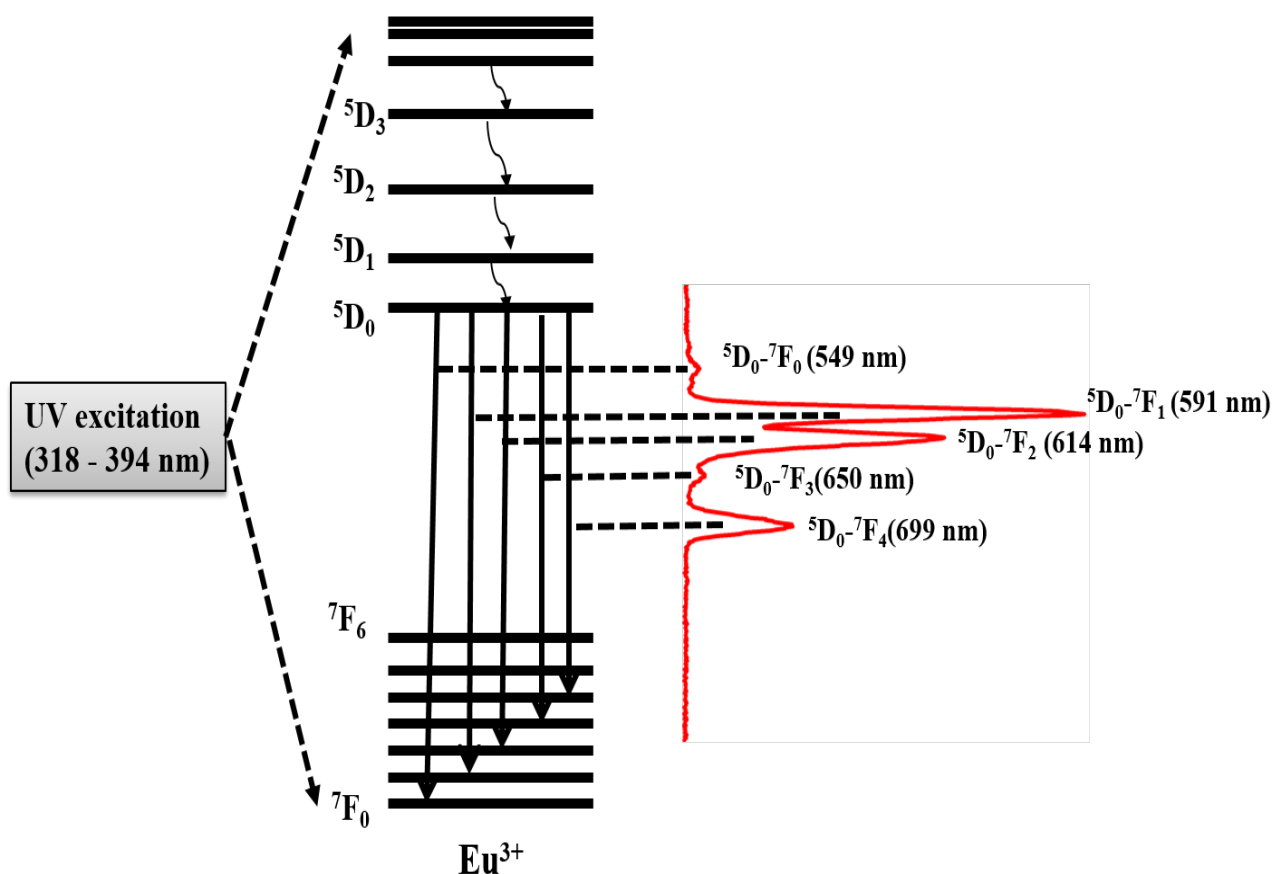


Fig. 2.12: Emission of the Eu^{3+} ion in SrF_2 under 318 nm excitation wavelength.

A good example of a downshifting ion is Eu^{3+} which emits red light and exhibits large Stokes shifts (>150 nm) [28–30]. The luminescence from Eu^{3+} mainly consists of narrow lines in the red spectral region. Such transitions are parity forbidden which is characterized by a weak absorption cross-section. Most of the lines' emission originate

from the transitions of the 5D_0 level to the 7F_j ($j = 0, 1, 2, 3, 4, 5, 6$) levels, although transitions from other 5D -levels are often observed. Fig. 2.12 shows the transition and luminescence of Eu^{3+} in a fluoride crystal. The 5D_0 - 7F_j transitions are ideally appropriate to determinate the lattice site symmetry of the Eu^{3+} ion [15]. The electric dipole transitions between the 4f levels are strictly forbidden. The electric dipole transitions, without inversion symmetry, become allowed and some transitions appear and dominate the spectrum for even small deviations from inversion symmetry [15]. In this respect, the 5D_0 - 7F_1 emission (around 591 nm in fig. 2.12) is due to the magnetic dipole transition which is insensitive to the site symmetry. Whereas the 5D_0 - 7F_2 emission (around 615 nm) is due to the electric dipole transition that is induced by the lack of inversion symmetry at the Eu^{3+} site. In the SrF_2 crystal, the 5D_0 - 7F_1 emission is much stronger than that of the 5D_0 - 7F_2 transition (see fig. 2.12).

2.10 Crystal structure of SrF_2 and dopant defects

SrF_2 is an ionic crystal with a molecular weight of 125.62 atomic units and a melting temperature of 1477 °C. It has a face centered cubic (fcc) structure and a space lattice of symmetry O_h with a lattice constant of 5.798 Å [31]. The crystal consists of a simple cubic lattice of F^- anions with Sr^{2+} cations occupying every second cube formed by the F^- lattice. This results in six interstitial sites or empty cubes surrounding each Sr^{2+} ion (see fig. 2.13). The existence of vacant cubic sites that is equal in number to the occupied cation sites, enables the SrF_2 crystal to host a large number of anion F^- interstitials.

SrF_2 is an insulator and is optically transparent. It consists of quite a large band-gap of around 11 eV. Thermal excitation may however lead to anion Frenkel defects [32]. This makes SrF_2 a weak ionic conductor at room temperature. The cation Frenkel defects in SrF_2 have large formation energy and therefore their effect on the structure is small. SrF_2 may undergo a superionic phase transition close to melting temperature where a sudden increase of anion Frenkel defects occurs and the material becomes a superconductor. The anion sublattice basically melts whereas the cation lattice remains

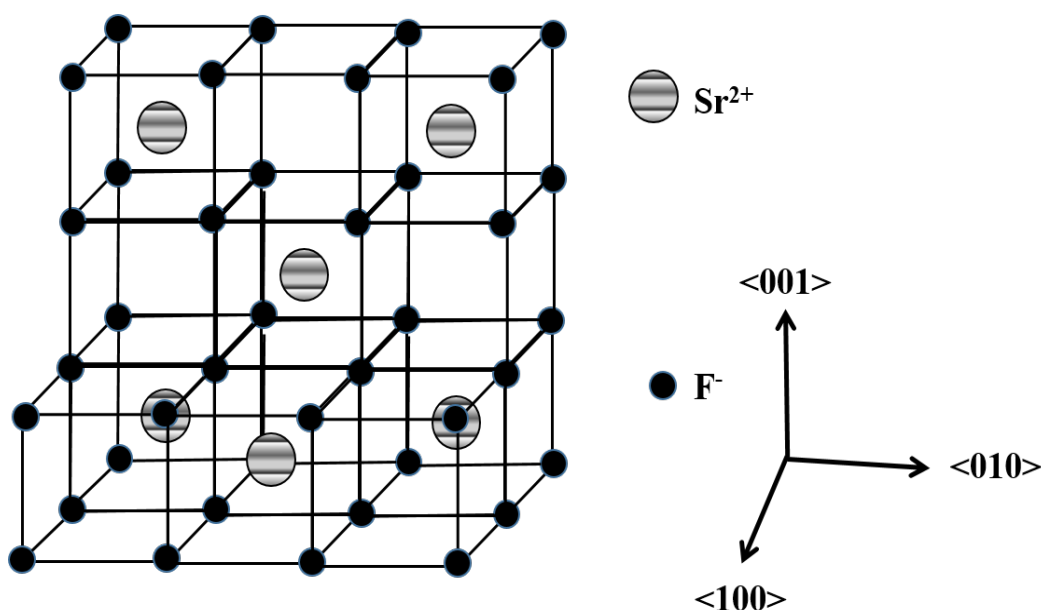


Fig. 2.13: A schematic diagram of the pure SrF_2 structure, which shows that each second simple cubic of the F^- sublattice contains a Sr^{2+} ion (the other are empty).

relatively stable [32].

The dopant ions are most often Ln^{3+} ions. The divalent ions (Ln^{2+}) simply substitute Sr^{2+} ions in the crystal to form crystal defects with cubic symmetry. Up to 40% of the Ln^{3+} ions may replace the Sr^{2+} ions leaving the structure without significant change [32]. When Ln^{3+} ions are doped in SrF_2 the extra positive charge relative to the Sr^{2+} ion makes some type of charge-compensation mechanism necessary, which is required to maintain the electrical neutrality of the crystal.

A number of crystal defects (or crystal field effects) can be formed when Ln^{3+} ions are doped in SrF_2 , see fig. 2.14. The simplest defect has a cubic symmetry which consists of a single substitutional Ln^{3+} ion. In this case the F^- anion charge is situated elsewhere in an interstitial site of the lattice and compensates for the Ln^{3+} extra charge.

Different types of crystal defects form with dipole formation. One common dipole defect has tetragonal or C_{4v} symmetry. In this defect the anion F^- ion is located in one of the six interstitial sites, closest or nearest-neighbour (nn), to the Ln^{3+} ion. Such defect has a net dipole moment type along a $\langle 100 \rangle$ direction [32–34]. In a trigonal or C_{3v} symmetry, the F^- ion is located in one of the eight interstitial sites next-next-

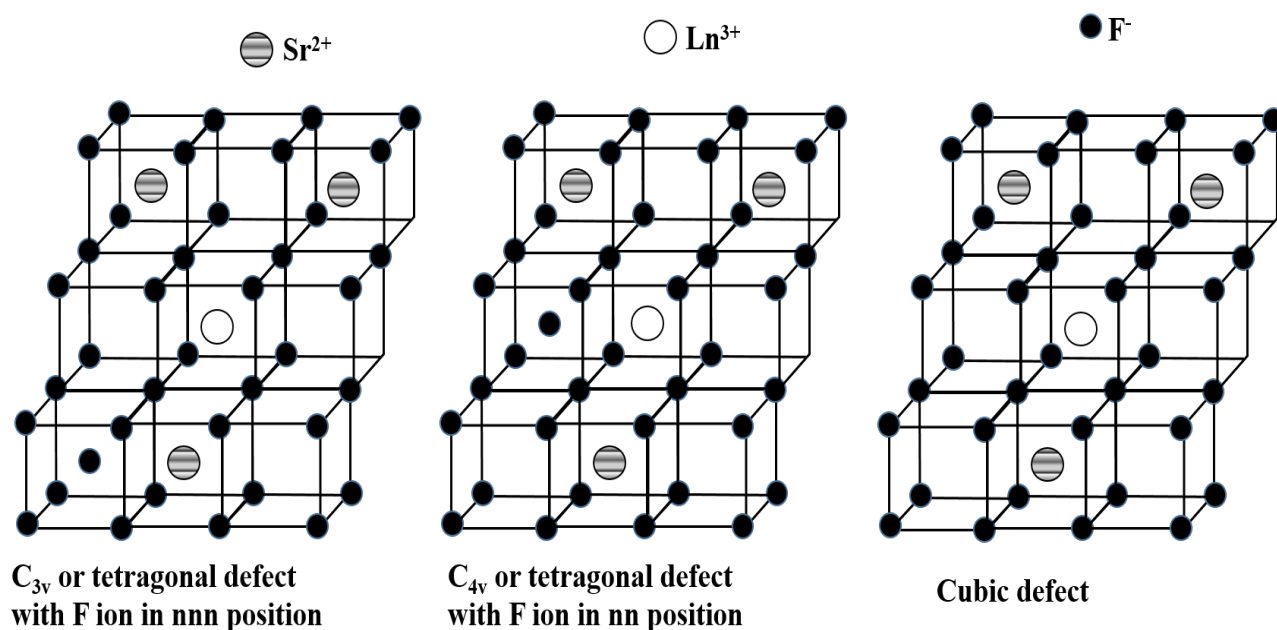


Fig. 2.14: Some common structure defects involving Ln³⁺ ions.

neighbor (nnn) to the Ln³⁺ ion. The resulting net dipole moment then occur along a $\langle 111 \rangle$ direction [32, 34], see fig. 2.14.

Other defects result from Ln³⁺ ions clustering. The clusters likely tend to form with high dopant concentration but they may also form at relatively small concentrations due to unfamiliar interactions of a certain ion with the lattice [32]. These kind of defects are found to cluster in two dipole (dimers) and three dipole (trimers) [32, 35]. These dipole clusters may also “gattered”. In this type of clusters the clustering capture an extra interstitial F⁻ ion from the lattice [32, 36]. The dimer clustering consists of two Ln³⁺ ion and two F⁻ ion either all on nn or all on nnn sites.

References

- [1] J. Nelson, *The Physics of Solar Cell*, Imperial College Press, UK, (2003).
- [2] A. Shalav, *Rare-Earth Doped Up-converting Phosphors For an Enhanced Silicon Solar Cell Response*, University of New South Wales, PhD Thesis, (2006).
- [3] Solar cell conversion-efficiency limit; available from:
<http://aerostudents.com/files/solarCells/CH5SolarCellConversionEfficiencyLimits.pdf>, (Accessed on 18.12.2014).
- [4] X. Huang, S. Han, W. Huang and X. Liu, *Chem. Soc. Rev.*, **42** (2013) 173-201.
- [5] W. Shockley and H. J. Queisser, *J. Appl. Phys.*, **32** (1961) 510-519.
- [6] B. M. Van der Ende, L. Aarts and A. Meijerink, *Phys. Chem. Chem. Phys.*, **11**(2009) 11081-11095.
- [7] D. Timmerman, I. Izeddin, P. Stallinga, I. N. Yassievich and T. Gregorkiewicz, *Nat. Photonics*, **2** (2008) 105-108.
- [8] R. D. Schaller, V. M. Agranovich and V. I. Klimov, *Nat. Phys.* **1** (2005) 189-195.
- [9] B. Ahrens, *Down- and Up-conversion in Fluorozirconate-Based Glasses and Glass Ceramics for Photovoltaic Application*, University of Paderborn, PhD Thesis, (2009).
- [10] C. Feldmann, T. Justel, C. R. Ronda and P. J. Schmidt, *Adv. Funct. Mater.*, **13** (2003) 511-516.
- [11] Judd-Ofelt theory: principles and practices; available from:
<http://link.springer.com/chapter/10.1007/1-4020-4789-4-21page-1>, (Accessed on 19.12.2014).
- [12] G. H. Dieke and H. M. Crosswhite, *Appl. Opt.*, **2** (1963) 675-686.
- [13] J. Chen, W. Cranton, M. Fihn (eds.), *Handbook of Visual Display Technology*, Springer-Verlag, Germany, (2012).

- [14] J. G. Sole', L. E. Bausa and D. Jaque, An Introduction to the Optical Spectroscopy of Inorganic Solids, John Wiley and Sons Ltd, England, (2005).
- [15] B. D. Bem, Thermal, Structural and Luminescent Properties of Long After-Glow $\text{MAl}_x\text{O}_y:\text{Eu}^{2+}, \text{Dy}^{3+}$ (M: Sr, Ba) Phosphors, University of the Free State, PhD Thesis (2010).
- [16] G. Liu and B. Jacquier, Spectroscopic Properties of Rare Earth in Optical Materials, Springer, China, (2005).
- [17] Q. Y. Zhang and X. Y. Huang, Prog. Mater. Sci., **55** (2010) 353-427.
- [18] T. Miyakawa and D. L. Dexter, Phys. Rev. B, **1** (1970) 2961-2969.
- [19] A. M. Srivastava and S. J. Duclos, Chem. Phys. Lett., **275** (1997) 453-456.
- [20] R. T. Wegh, E. V. D. van Loef and A. Meijerink, J. Lumin., **90** (2000) 111-122.
- [21] T. Trupke, M. A. Green and P. Würfel, J. Appl. Phys., **92** (2002) 1668-1674.
- [22] M. Miritello, L. R. Savio and P. Cardile and F. Priolo, Phys. Rev. B, **81** (2010) 041411-041414.
- [23] D. C. Yu, X. Y. Huang, S. Ye, M. Y. Peng, Q. Y. Zhang and L. Wondraczek, Appl. Phys. Lett., **99** (2011) 161904-161906.
- [24] B. M. Van der Ende, L. Aarts and A. Meijerink, Adv. Mater., **21** (2009) 3073-3077.
- [25] J. T. Van Wijngaarden, S. Scheidelaar, T. J. H. Vlugt, M. F. Reid and A. Meijerink, Phys. Rev. B, **81** (2010) 155112-155117.
- [26] Q. Y. Zhanga, G. F. Yang and Z. H. Jiang, Appl. Phys. Lett., **91** (2007) 051903-051905.
- [27] J. Zhou, Y. Teng, G. Lin and J. Qiu, J. Non-Cryst. Solids, **357** (2011) 2336-2339.
- [28] M. Dejneka, E. Snitzer and R. E. Riman, J. Lumin., **65** (1995) 227-245.
- [29] Y. Hu, W. Zhuang, H. Ye, D. Wang, S. Zhang and X. Huang, J. Alloys Compd., **390** (2005) 226-229.

-
- [30] Y. Li, Y. Chang, Y. Lin, Y. Chang and Y. Lin, *J. Alloys Compd.*, **439** (2007) 367-375.
- [31] Strontium Fluoride; available from: <http://www.americanelements.com/srf.html>, (Accessed on 25.02.2015).
- [32] F. T. Charnock, Dynamic of Dipolar Defect in Rare Earth Doped Alkaline-Earth Fluoride Crystal, Wake Forest University, PhD Thesis, (1999).
- [33] P. J. Bendall, C. R. A. Catlow, J. Corish and P. W. M. Jacobs, *J. Solid State Chem.*, **51** (1984) 159-169.
- [34] J. Corish, C. R. A. Catlow, P. W. M. Jacobs and S. H. Ong, *Phys. Rev. B*, **25** (1982) 6425-6438.
- [35] H. W. Den Hartog, *Radiat Eff. Defects Solids*, **139** (1996) 125-145.
- [36] C. G. Andeen, J. J. Fontanella, M. C. Wintersgill, P. J. Welcher, R. J. Kimble and G. E. Matthews, *J. Phys. C: Solid State Phys.*, **14** (1981) 3557-3563.

Chapter 3

Characterization techniques

The powder samples used in this work were characterized by several surface, structural and optical techniques. The optical spectroscopic techniques provide various optical information on the luminescent materials. These techniques are usually designed for measuring the absorption, scattering and emission of light from the materials. The surface and structural techniques are basically modelled to study the materials' structure and chemical composition of the investigated materials. All these techniques can provide qualitative and in certain cases quantitative analysis of the materials. This chapter therefore provides a brief description of the theory and experimental procedures of the techniques that were used in this study.

3.1 UV-Vis spectroscopy

This technique measures the absorption of light by the electronic transitions of the material. The electronic absorption is often called UV-visible or UV-Vis spectroscopy because the electronic transitions of the material require wavelengths typically in the UV and visible region of the electromagnetic radiation. The transmission or absorption measurements technique is however designed to measure the transmitted or absorbed light from liquid samples as the light passes through. For solid or powder samples however the diffuse reflectance measurements is a suitable technique.

Fig. 3.1 shows a schematic diagram of attenuation of a monochromatic beam of light passing through a transparent material. Different mechanism can occur when light of intensity I_0 strike a transparent material including absorption, transmittance, scattering and reflection. The transmittance (T) is defined as the ratio between the transmitted light (I) and the incident light I_0

$$T = \frac{I}{I_0}, \quad (3.1)$$

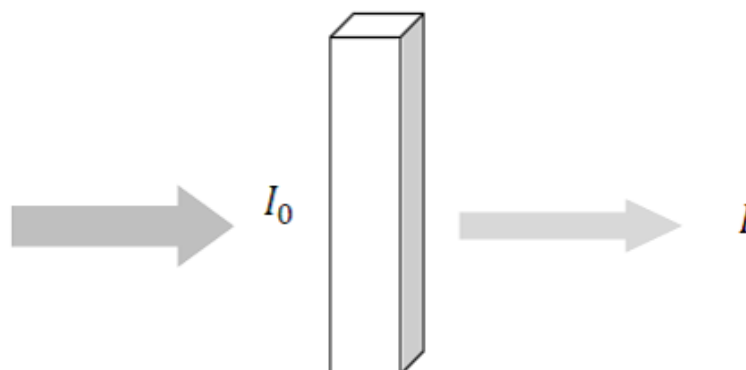


Fig. 3.1: Schematic diagram showing the incident and transmittance light as it passes through a transparent material.

According to Beer's law the absorbance (A) is defined as

$$A = \log \frac{I_0}{I} = \epsilon lc = \alpha c \quad (3.2)$$

where c is the sample concentration, l is the length of the sample, α is the absorption coefficient and ϵ is the molar absorptivity. Both I_0 and I can be measured experimentally and thus A can be determined. The absorption coefficient is wavelength dependent and a plot of α as a function of the wavelength is known as the absorption spectrum [1]. The spectrum represents the characteristic of a measured sample and hence it reflects the fundamental electronic properties of the sample.

Fig. 3.2 represents the schematic diagram of a UV-Vis instrument. The main parts of a UV-Vis instrument are the source, a monochromator and a detector. The deuterium lamp is usually used as light source for UV measurement and a tungsten lamp for visible measurement [2]. The monochromator is used to generate monochromatic beam (single wavelength) radiation selected from a wide range of wavelengths. After the light passed through the transparent sample, the light intensity is measured by a a detector, e.g. photodiode, photomultiplier tube (PMT) or a charge coupled device (CCD) detector [1]. Absorption of some of the wavelengths by the sample reduces the transmitted light and vice versa. The measurement range of most spectrometers

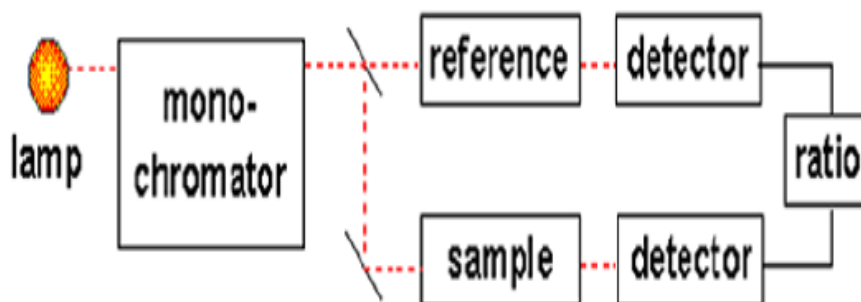


Fig. 3.2: Schematic diagram of key components of a typical dual-beam UV-Vis spectrometer [2].

ranges from about 200 nm to 800 nm. Measurement beyond 800 nm is also possible but different light source, optics, and detectors are required.

The diffuse reflectance measurements instrument usually is used to measure the reflected light from the powder samples. The reflectance spectrum represent the reflected light as a function of the wavelength. Diffuse reflectance instrument is equipped with an integrating sphere coated with a white standard to collect the light reflected by the standard and the sample [3]. Modern double-beam spectrophotometers provide holders in which the powder sample and the white standard are tightly packed. In this study, the diffuse reflectance spectra were recorded by a Lambda 950 UV-Vis spectrophotometer with an integrating sphere that exhibits reflectance close to 100% reflectance in the wavelength range from near UV to the near IR (spectralon saw used as the standard).

3.2 Photoluminescence spectroscopy (PL)

PL spectroscopy is a technique that is capable to measure the emission and excitation as well as the luminescence lifetime of a luminescent material. PL spectroscopy measurements are divided into the steady-state and time-resolved PL. In the steady-state PL the information is normally extracted from the emission and the excitation spectra. In time-resolved measurements the decay curve is used to extract the information.

A typical PL spectrum is a distribution of the emission intensity as a function of the wavelength measured at a fixed excitation wavelength. A photoluminescence excitation spectrum is a measurement of the emission intensity at a single emission wavelength as a function of excitation wavelength. The photoluminescence excitation spectrum, to a good approximation, is identical to the absorption spectrum if there is no multiple overlapping of excited states [1].

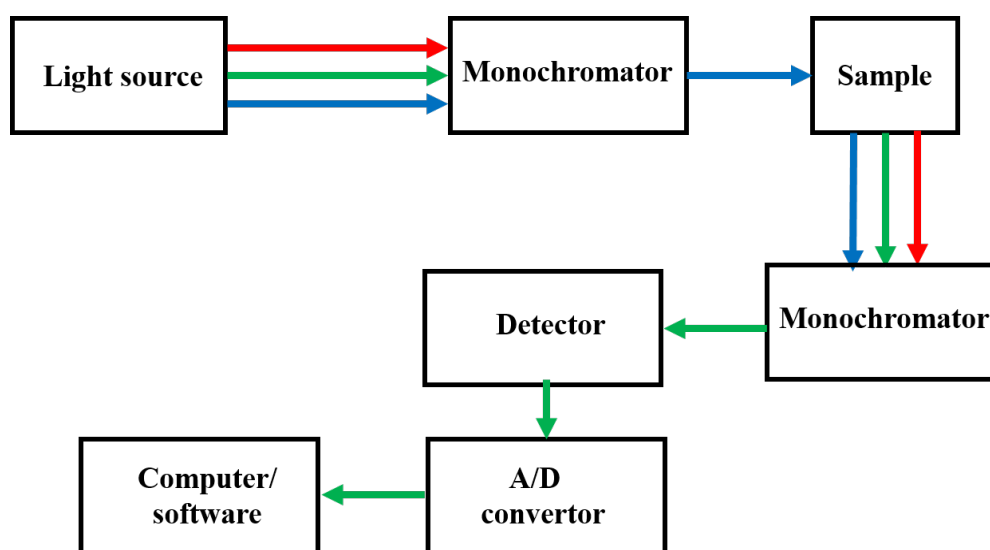


Fig. 3.3: Schematic illustration of the basic components of a spectrofluorometer.

Fig. 3.3 schematically shows the basic components of the PL spectrofluorometer. Light photons, generated by the source, enter a monochromator that selectively transmit a specific excitation wavelength that is used to excite the sample. The emitted light is directed by lenses, dispersed by another monochromator and then collected by a detector, i.e. PMT, photodiode or a CCD. The analog to digital convertor converts the electrical signal that is generated by the photo detector into a digital signal. The digital signal is then processed by software on a computer [1]. In this study two systems were used to collect our PL data including the Cary Eclipse fluorescence spectrophotometer and the 325 nm He-Cd laser PL system. The Cary Eclipse is equipped with PMT detector and a xenon lamp that exhibits a wide excitation spectrum range between 200 and 1100 nm. The monochromator generally produces good monochromatic light. The laser PL often produces some lines with 325 nm, therefore, a narrow filter was used instead of an excitation monochromator. The NIR PL measurements were collected

with a He-Cd laser PL system with a 325 nm excitation wavelength and a 2 mm InGaAs photodiode detector.

Photoluminescence is a very sensitive technique to study the optical properties of materials. The time-dependent nature of photoluminescence can also be used to better understand the chemical and physical information [4]. A pulsed excitation source and a fast detector are required in time-resolved photoluminescence measurements. Today lifetime as short as 10 femtoseconds can readily be detected. Time-resolved photoluminescence provides better information on the chemical surrounding of the material. Therefore, time-resolved measurements can be used to investigate the energy transfer and dynamic quenching that can occur on the system [5–8]. The time-resolved instrument is basically the same as the photoluminescence measurements [4]. The only difference is that in the time-resolved instrument a pulsed source is included instead of a continuous light source. The luminescence decay curves on this study were recorded under pulsed excitation (HORIBA scientific) with a NanoLED diode and pulsed excitation using a diode pumped YAG laser with a 335 nm excitation wavelength, power of 1.3 milliwatt and a SR430 Multichannel scaler photomultiplier (Linköping, Sweden).

3.3 X-ray diffraction (XRD)

3.3.1 Introduction

XRD is a technique that gives information on the degree of crystallinity, phase identification, lattice parameters and grain sizes of the materials [9, 10]. The basic idea of the XRD mechanism is the diffraction of waves from the periodic arrays of atoms in solids [9, 11]. About 95% of all solid materials can be described as crystalline materials. The wavelengths of the x-rays are between 0.7 and 2.3 Å, which is approximately close to the interplanar spacing of most crystalline materials. This makes x-rays a suitable source for diffraction application. The x-ray wave scatter and interfere when it approaches an atom due to its interaction with the atom's electrons. In a crystal the scattering produces a diffraction pattern with sharp maxima (peaks) at certain an-

gles. The peaks in the x-ray diffraction pattern are directly related to the interatomic distances [11].

3.3.2 Bragg's law

The law was derived by Sir W.H. Bragg and his son Sir W.L. Bragg in 1913 [9]. Bragg's law explicitly explains why the cleavage faces of crystals appear to reflect x-ray beams at certain angles of incidence. Using this law it is possible to make accurate qualification and quantification analysis of the experimental results. A schematic diagram of Bragg's law in two dimensions is presented in fig. 3.4.

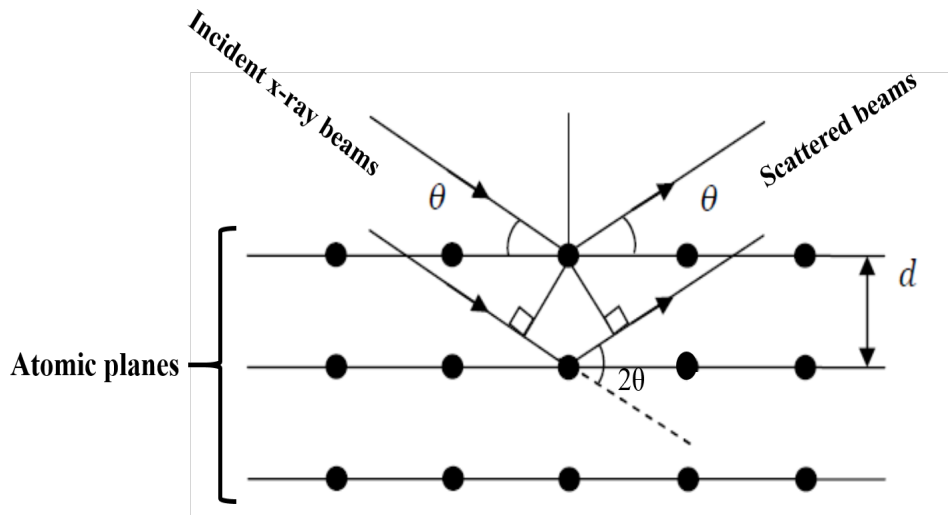


Fig. 3.4: Schematic diagram showing Bragg's law and scattering from the atoms.

From fig. 3.4 it can be seen that an x-ray which reflects from the plane in the surface of the crystal has traveled less distance than the x-ray that reflects from the atoms' planes inside the crystal. The distance travelled relies on the separation of the layers and the angle at which the x-ray entered the material. For the wave reflected from the atom's plane inside the crystal to be in phase with that reflected from the surface, it needs to have travelled a whole number of wavelengths inside the material. Bragg expressed this in an equation now known as Bragg's Law:

$$n\lambda = 2d \sin \theta, \quad (3.3)$$

This law relates the angle at which there is a maximum in diffracted intensity to the wavelength (λ) of x-rays and the inter-layer distance d between the planes of atoms, ions or molecules in the lattice. n is an integer that represents the order of the diffraction peak. The angle between the diffracted and transmitted beams is always equal to 2θ because of the geometry of the Bragg's condition. The 2θ angle is easily obtained in experimental situations and the results of x-ray diffraction are therefore given in terms of 2θ .

Normally a diffractometer is used to record the XRD pattern. The schematic diagram that presents the essential features of a diffractometer is shown in fig. 3.5. It consists of an x-ray tube (generating monochromatic x-rays of known wavelength), a detector and a sample holders. The x-ray are directed onto the samples at a specific angle θ while the detector records the intensity of the diffracted x-rays that are scattered at an angle of 2θ .

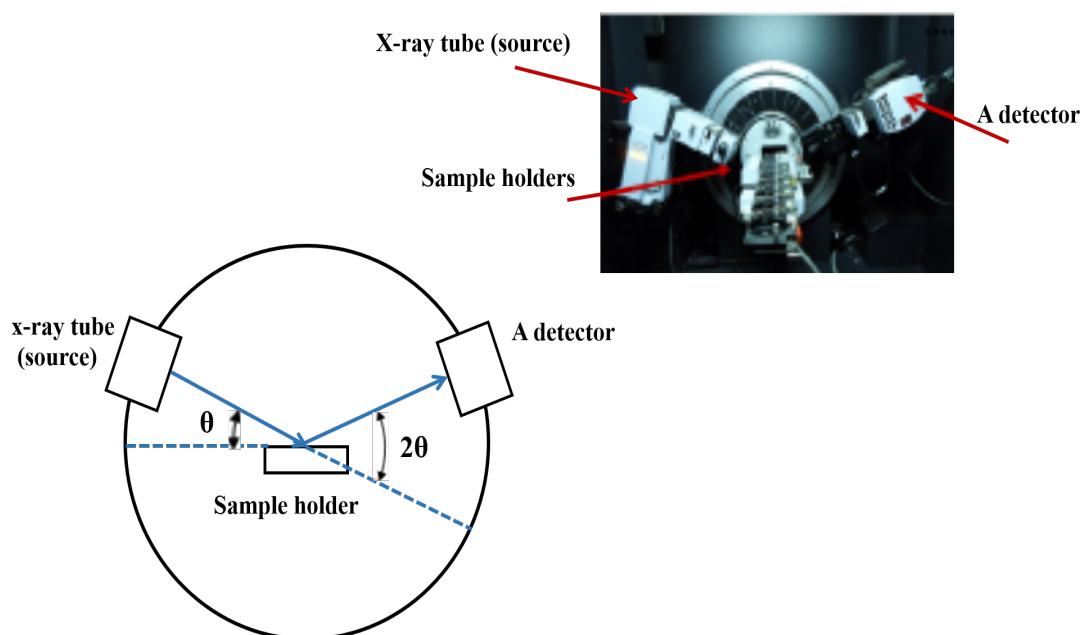


Fig. 3.5: Schematic diagram of a x-ray diffractometer. The photo shows the Bruker AXS D8 advance x-ray diffractometer used to collect the XRD data of this study.

The mean crystallite sizes can be calculated from the XRD pattern. The idea was first investigated by Paul Scherrer who examined the effect of limited particle size on x-ray

diffraction patterns and it is known as the Scherrer's equation [12],

$$S = \frac{K\lambda}{\beta \cos \theta}, \quad (3.4)$$

S is the mean crystallite size which may be smaller or equal to the grain size, K is the shape factor, β is the line broadening at half the maximum intensity (FWHM) in radians and θ is the Bragg's angle.

The XRD data of this study were collected by using a Bruker D8 Advance diffractometer equipped with a copper anode ($\lambda = 0.154$ nm), operating at a voltage of 40 kV and a current of 40 mA. Moreover, the Nickel was used as a filter for the monochromatic x-rays as it absorbs the x-ray waves below a wavelength of 0.154 nm (see fig. 3.6).

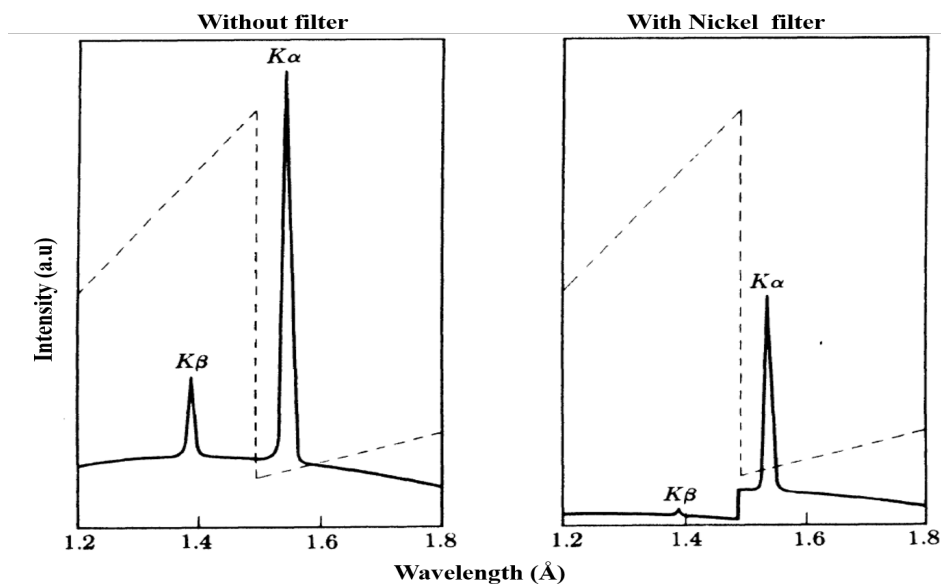


Fig. 3.6: Characteristic emission of Cu x-ray emission without a filter and with a Nickel filter. Adapted from [9].

3.4 X-ray photoemission spectroscopy (XPS)

Photoemission spectroscopy (also known as Electron Spectroscopy for Chemical Analysis (ESCA)) extensively been used to investigate the chemical composition of the surface

of solid materials [13–17]. A detailed description of the photoemission process and its history can be found in various textbooks [18–23].

The basic idea of the XPS mechanism is based on the photoelectric effect where photoelectrons can be released when the solid is excited with sufficient photon energy ($\hbar\nu$) [24]. The kinetic energy of the ejected electrons is then given by [18]

$$E_k = \hbar\nu - E_B - \Phi, \quad (3.5)$$

where E_k is the kinetic energy of the ejected electron, E_B is the binding energy (BE) of the state from which the electron is ejected, and Φ is the sample's work-function¹. In the photoemission process the counting rate of the photoelectrons (the photoemission intensity $I(E_k)$) can be expressed as a function of binding energy by

$$I(E_k) = \text{DOS}(\hbar\nu - E_B - \Phi), \quad (3.6)$$

where $\text{DOS}(E)$ is the density of states as a function of the binding energy. Hence, in the simplest case, the photoemission spectrum should therefore represent the energy distribution of the electron states in a solid (see fig. 3.7) [25].

During the experimental procedure both the sample and analyser are grounded together, so their Fermi levels are aligned. It is therefore convenient to write the kinetic energy, measured from the Fermi energy level, E_F as [25]

$$E_k = \hbar\nu - E_B - \phi_{sp}, \quad (3.7)$$

where (ϕ_{sp}) is the spectrometer work-function. The binding energy is characteristic to the core electrons for each element and plays a crucial role in interpreting the XPS spectra. In the simplest case, the binding energy is determined by the electrostatic attraction of electrons to the nucleus. The energy level of the core electrons depend slightly on the chemical state of the atom. One can gain valuable information about the system if the binding energy of XPS data is determined correctly. It is necessary to understand the binding energy of XPS to distinguish between initial and final state

¹The minimum amount of energy needed to remove an electron from the metal corresponds to the work-function [21].

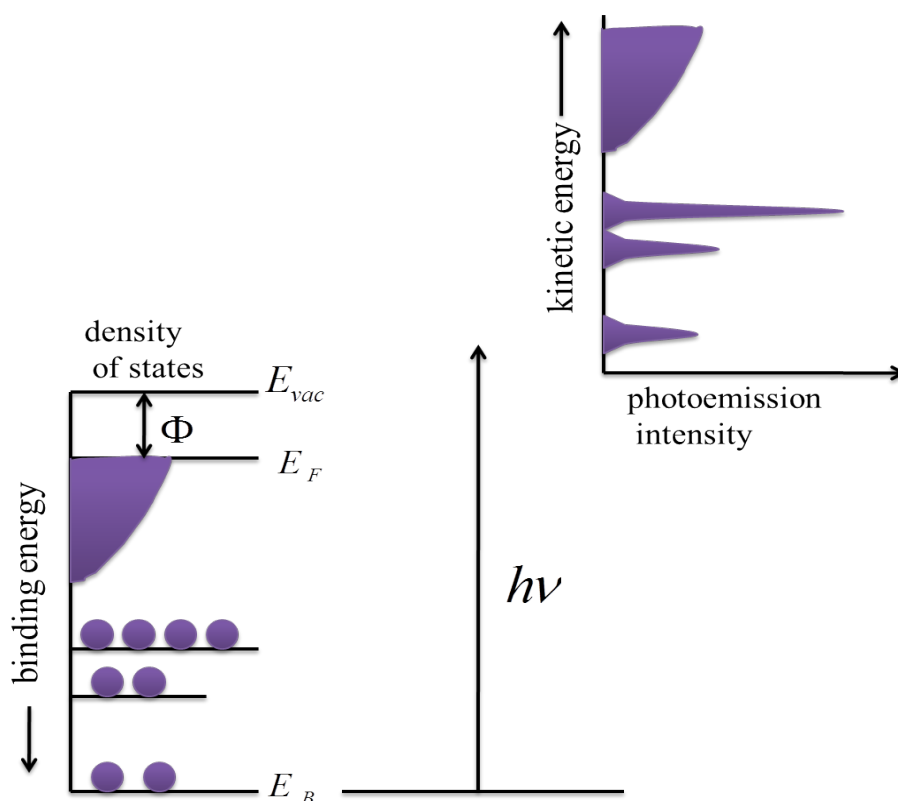


Fig. 3.7: Schematic diagram of the energy distribution involved in photoemission spectroscopy.

effects. The final state effects occur due to the photoemission event itself and due to the nature of the final state. In general the binding energy depends on the oxidation states. The binding energy increases with increasing oxidation states. The measured and calculated binding energies of the C 1s level in different chemical environments are shown in fig. 3.8. XPS can therefore give information about atomic compositions and about the chemical states of the elements.

The XPS results in this study were obtained with a PHI 5000 Versaprobe system. A low energy Ar⁺ ion gun and low energy neutralizer electron gun were used to minimize charging on the surface. A 100 μm diameter monochromatic Al K_α x-ray beam ($h\nu = 1486.6$ eV) generated by a 25 W, 15 kV electron beam was used to analyze the different binding energy peaks. The pass energy was set to 11 eV giving an analyzer resolution ≤ 0.5 eV. Multipack version 8.2 software was utilized to analyze the spectra to identify the chemical compounds and their electronic states using Gaussian-Lorentz fits.

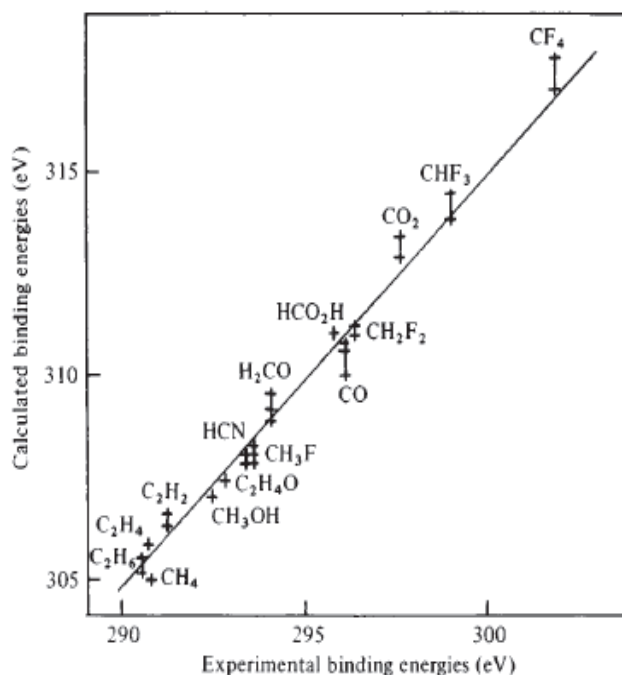


Fig. 3.8: Calculated and experimental XPS binding energies of C 1s in a range of molecules via Koopman's theorem [21]. These two values differ by 15 eV as indicated by the straight line.

3.5 Auger electron spectroscopy (AES)

The AES technique is used for surface analysis almost similar to XPS. The Auger effect was discovered by Pierre Auger in 1923. He observed that the detected electron with kinetic energies were independent from incident electron beam. The mechanism originates in an atom with a hole in the core level K. When this hole is filled with an electron in level L_1 the remaining energy causes an electron to be released from level $L_{2,3}$. In other words, Auger electrons are generated when incident radiations interact with an atom and subsequently provides secondary electron. The process is schematically shown in fig. 3.9. The kinetic energy of ejected Auger electron is given by

$$E_{kin} = E_K - E_{L_1} - E_{L_{2,3}} - \phi, \quad (3.8)$$

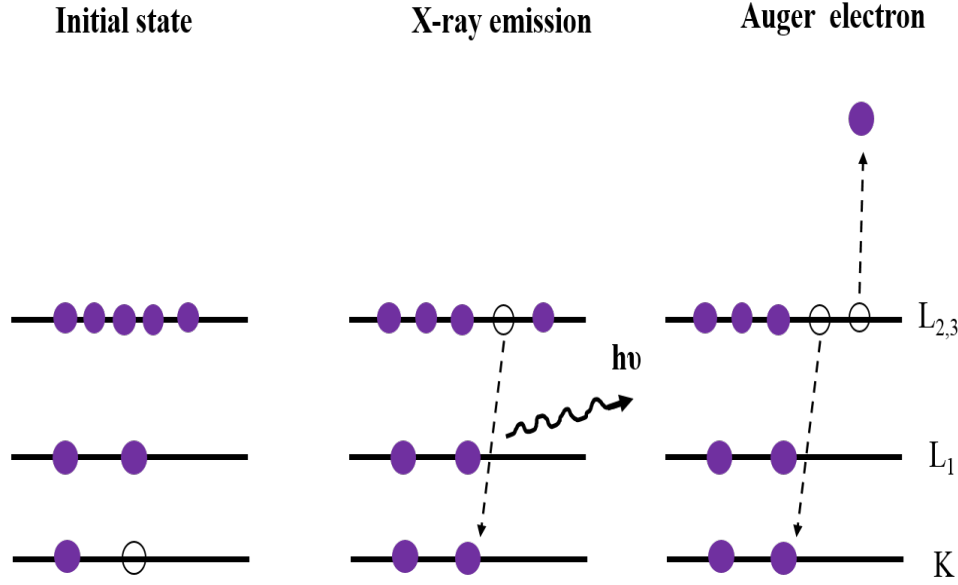


Fig. 3.9: Schematic diagram showing the decay of ionized atoms by emission of the $KL_{2,3}L_{2,3}$ Auger electron.

where ϕ is the workfunction of the analyzer. The notation K is the initial state and L_1 and $L_{2,3}$ represent the final state transitions. Eqn. 3.8 is an approximate formula for the Auger electron's kinetic energy. It does not take account for the difference between a one-hole binding energy state and a two-hole binding energy state. One very approximate method to account for this was developed by Jenkins and Chung [26] (the revised form of Eqn. 3.8) is therefore

$$E_{kin} = E_K^z - \frac{1}{2} [E_{L_1}^z + E_{L_1}^{z+1}] - \frac{1}{2} [E_{L_{2,3}}^z + E_{L_{2,3}}^{z+1}] - \phi \quad (3.9)$$

where z is the atomic number of the atom involved. AES provides element-specific information on the surface region. AES is therefore a very surface sensitive technique. This is because of the relatively short inelastic mean free path for Auger electrons. AES can detect all elements except H and He. Fig. 3.10 shows a typical Auger spectrum for the Ce and Eu doped SrF_2 phosphor material. Peaks that are related to the Ce, Eu, F and Sr Auger peaks and peaks related to C and O contaminations of the surface are clearly shown. PHI 700 scanning Auger nanoprobe were used to collect the Auger measurements in this study. The AES surveys were done with a 25 kV and 10 nA

electron beam.

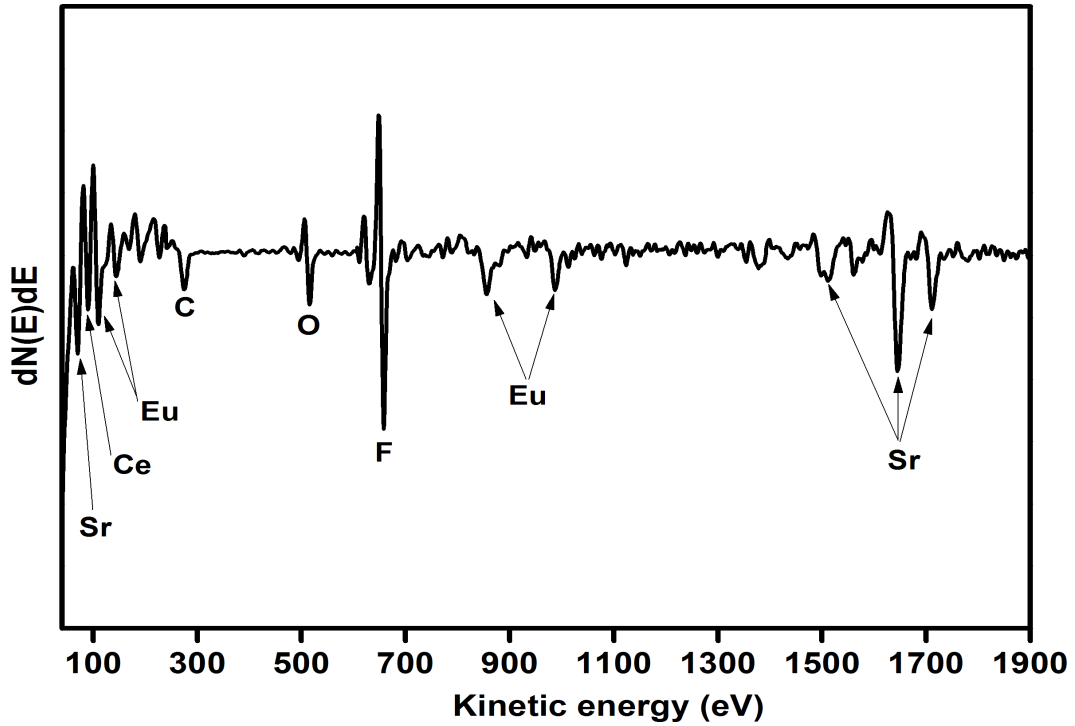


Fig. 3.10: A typical Auger spectrum for the $\text{SrF}_2:\text{Ce},\text{Eu}$ phosphor material.

3.6 Time-of-flight secondary ion mass spectrometry (ToF-SIMS)

TOF-SIMS is an analytical surface technique that provides elemental, compositional, chemical and molecular information from the surface of the solid state sample by bombarding the surface with a pulsed ion beam (Cs, Bi or microfocused Ga). Fig. 3.11 illustrates the basic principles of TOF-SIMS technique. When the primary ion beam hits the surface sample it causes secondary ion and ion clusters to be emitted from the sample's surface. The secondary ions with specific polarity are then accelerated into a field-free drift region with kinetic energy given by

$$E_{kin} = zU_0 = \frac{mv^2}{2}. \quad (3.10)$$

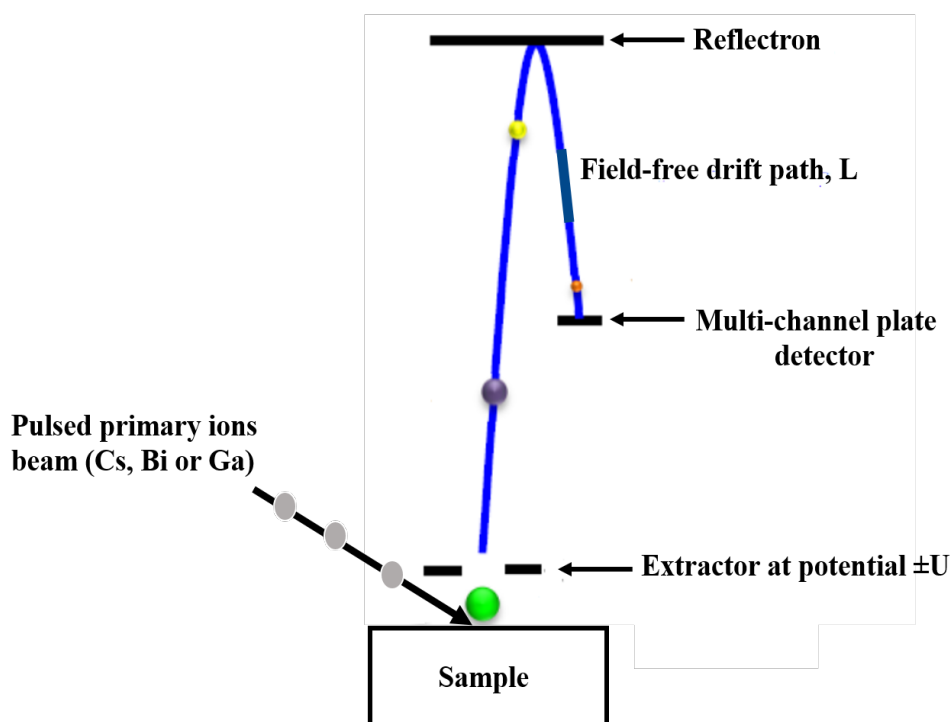


Fig. 3.11: Schematic diagram of Time-of-Flight Secondary Ion Mass Spectrometry (TOF-SIMS).

z is the charge of the secondary ion, ν its velocity, m its mass and U_0 is the accelerating voltage. In this study, the potential U_0 is kept at ± 2000 volts, depending on the ion species. A negative voltage is preferred to be used for species with positive ions and a positive voltage is suitable for negative ions. Ions with different masses travel with different velocities and hence the mass separation can be obtained in the flight time (t). The flight time is given by

$$t = \frac{L}{\nu} = L\sqrt{\frac{m}{2zU_0}}, \quad (3.11)$$

where L is the effective length of the mass spectrometer. The mass to charge ratio measured is given by

$$\frac{m}{z} = \frac{2U_0t^2}{L^2}. \quad (3.12)$$

Mass resolution is important for accurate identification of the peaks in a ToF-SIMS spectrum. The mass resolution represents to what extent the ionic mass of interest can be distinguished from other interfering masses (a high value indicates a good

distinction). The mass resolution $(\frac{\Delta m}{m})^{-1}$ of the TOF-SIMS system is given by

$$\frac{m}{\Delta m} \cong \frac{t}{2\Delta t}, \quad \text{where} \quad \Delta t = \sqrt{\Delta t_p^2 + \Delta t_D^2 + \Delta t_A^2}, \quad (3.13)$$

Δm is the peak width, Δt_p is the duration of the primary ion pulse, Δt_D is the time resolution of the detector system (rise and deadtime in the detector and its electronics) and Δt_A is due to time focusing aberrations in the analyser [27]. The mass resolution can also be calculated from the spectrum as the mass of the highest peak intensity divided by the peak width at full width half maximum (FWHM),

$$\frac{m}{\Delta m} = \frac{\text{mass at highest energy}}{\text{peak width}}. \quad (3.14)$$



Fig. 3.12: SIMS 5 TOF-SIMS instrument based on department of physics, UFS.

In principle ToF-SIMS is a very simple analysis technique but it is not always so straightforward to interpret the mass spectrum due to the number of information obtained when a spectrum is acquired. TOF-SIMS is the most sensitive technique for elemental analysis and is therefore used for numerous information including the chemical structure of the surface. The mass spectrum of ToF-SIMS analysis scans all atomic

masses over a range of 0-10,000 amu (including single ions (positive or negative), individual isotopes, and molecular compounds). Maps of any mass of interest can also be produced by the rastered beam.

All the data in this work were collected by SIMS 5 TOF-SIMS instrument from ion-TOF (fig. 3.12). It is equipped with a Bi primary ion source and a dual column Oxygen (O^+) and Caesium (Cs^+) sputter source, acting as two active ion sources. The flight path is 2 m and it contains a multi channel plate analyzer with 2 million channels.

3.7 Scanning electron microscopy (SEM)

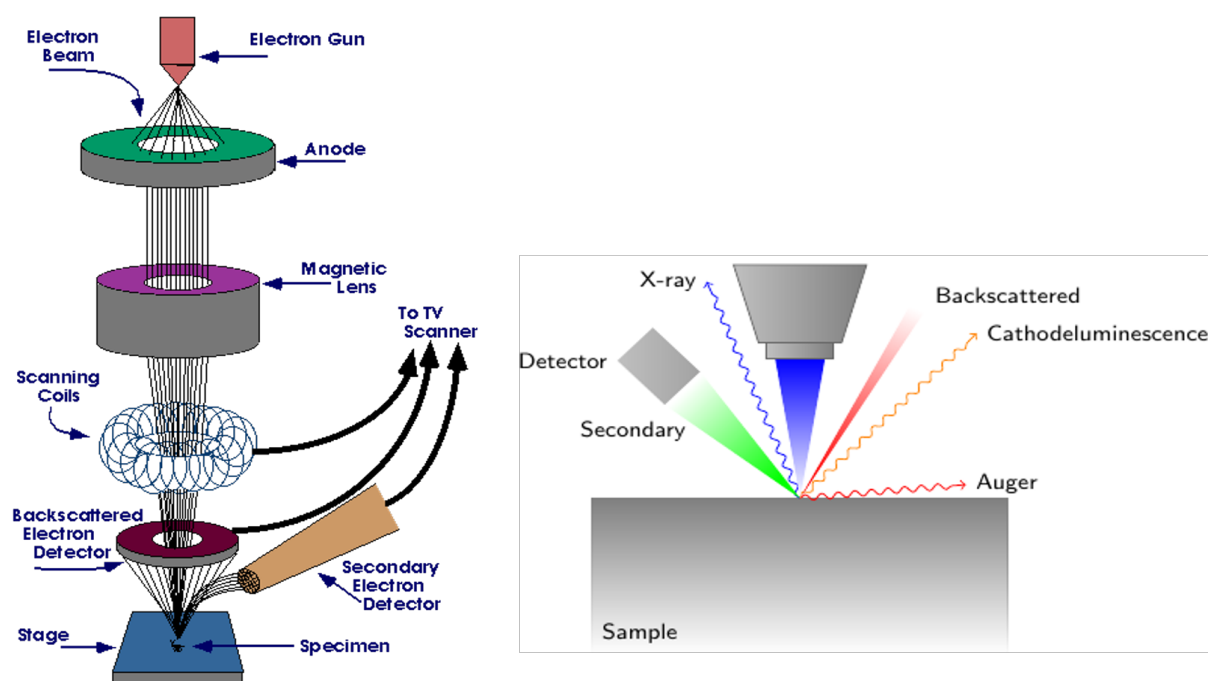


Fig. 3.13: Schematic diagram of a scanning electron microscopy system with other signals that can be produced during electrons bombardment [28].

SEM is a microscope that uses a focused electron beam to generate information from the surface of solid specimens. Topography (i.e. texture) and morphology (the shape and size of surface's particles) of a sample can be revealed by SEM. SEM can also be used to perform energy-dispersive x-ray spectrometer (EDS) measurements to determine the chemical composition [28].

The principle of the SEM technique is governed by the interaction of the electron beam with a solid sample's surface. In a SEM instrument, electrons are generated from an electron gun and then focused and accelerated onto the sample's surface (fig. 3.13). When the electron beam hits the sample surface different kinds of signals are produced. These are including secondary electrons, backscattered electrons, x-ray photons, Auger electrons, diffracted backscattered electrons and heat. Secondary electrons and backscattered electrons are used to image the samples' surfaces. Secondary electrons provide information on the morphology and topography of the samples while backscattered electrons are used for illustrating contrasts in compositions in multi-phase samples (i.e. for rapid phase discrimination) [29]. The SEM images of this project are collected by using a Shimadzu Super-scan scanning electron microscope model ZU SSX-550 and JEOL JSM-7800F high field emission scanning electron microscope (FE-SEM) equipped with EDS.

References

- [1] J. Z. Zhang, Optical Properties and Spectroscopy of nanomaterials, World Scientific, Singapore, (2009).
- [2] Ultraviolet and Visible Absorption Spectroscopy; available from:
<http://www.files.chem.vt.edu/chem-ed/spec/uv-vis/uv-vis.html> (Accessed 27.02.2015).
- [3] H. A. A. Seed Ahmed, Luminescence from lanthanide ions and the effect of co-doping in silica and other hosts, University of the Free State, PhD Thesis, (2012).
- [4] Time-Resolved Fluorescence Spectroscopy; available from:
<http://content.piaction.com/Uploads/Princeton/Documents/Library/UpdatedLibrary/Time-resolved-fluorescence-spectroscopy.pdf> (Accessed 02.03.2015).
- [5] H. A. A. Seed Ahmed, O. M. Ntwaeaborwa and R. E. Kroon, *Curr. Appl. Phys.*, **13** (2013) 1264-1268.
- [6] R. E. Kroon, H. C. Swart, O.M. Ntwaeaborwa and H. A. A. Seed Ahmed, *Physica B*, **439** (2014) 83-87.
- [7] G. P. Morgan, D. L. Huber and W. M. Yen, *J. DE Physique*, **46** (1985) C7-25.
- [8] M. Ilhan, R. Samur, H. Demirer and F. Mindivan, *Metalurgija*, **54** (2015) 407-410.
- [9] B. D. Cullity, *Element of x-ray diffraction*, Addison-Wesley Publishing Company, Inc., USA, (1956).
- [10] X-ray Powder Diffraction (XRD); available from:
<http://serc.carleton.edu/research-education/geochemsheets/techniques/XRD.html> (Accessed on 06.03.2015).
- [11] Basics of X-ray diffraction; available online from:
<http://old.vscht.cz/clab/RTG/dokumenty/thermo/xrd/Introduction%20to%20powder%20diffraction.pdf> (Accessed 06.03.2015)
- [12] C. Oprea, V. Ciupina and G. Prodan, *Romanian J. Phys.*, **53** (2008) 223-230.

-
- [13] R. Vercaemst, D. Poelman, L. Fiermans, R. L. Van Meirhaeghe, W. H. Laflere and F. Cardon, *J. Electron. Spectrosc. Relat. Phenom.*, **74** (1995) 45-56.
- [14] C. Caspers, M. Muller, A. X. Gray, A. M. Kaiser, A. Gloskovskii, C. S. Fadley, W. Drube and C. M. Schneider, *Phys. Status Solidi RRL*, (2011) 1-3.
- [15] I. M. Nagpure, S. J. Dhoble, M. Mohapatra, V. Kumar, S. S. Pitale, O. M. Ntwaeaborwa, S. V. Godbolc and H. C. Swart, *J. Alloys Compd.*, **509** (2011) 2544-2551.
- [16] H. C. Swart, I. M. Nagpure, O. M. Ntwaeaborwa, G. L. Fisher and J. J. Terblans, *Opt. Express*, **20** (2011) 17119-17125.
- [17] H. Ogasawara, A. Kotani, R. Potze, G. A. Sawatzky and B. T. Thole, *Phys. Rev. B*, **44** (1999) 5465-5469.
- [18] S. Hüfner, *photoelectron Spectroscopy Principles and Application*, Springer, Berlin, Second Edition (1995).
- [19] D. W. Lynch and C. G. Olson, *Photoemission Studies of High-Temperature Superconductors*, Cambridge University Press, UK, (2005).
- [20] J. W. Niemantsverdriet, *Spectroscopy in Catalysis and An Introduction*, Wiley, Weinheim, (2000).
- [21] D. P. Woodruff and T. A. Delchar, *Modern Techniques of Surface Science*, Cambridge University Press, UK, Second Edition (1994).
- [22] F. de Groot and A. Kotani, *Core Level Spectroscopy of Solids*, CRC Press, New York, (2008).
- [23] J. M. Hollas, *Modern Spectroscopy*, Wiley, UK, (2004).
- [24] N. Zettili, *Quantum Mechanics Concepts and Application*, Wiley, UK, Second Edition (2009).
- [25] M. Y. A. Yagoub, *The Study of Molecules-Metal interfaces: Structure and Electronic Properties*, University of Johannesburg, MSc Thesis, (2013).

-
- [26] L. H. Jenkins and M. F. Chung, *Surf. Sci.* ,**28** (1971) 409-422.
- [27] U. Bexell, *Surface Characterisation Using ToF-SIMS, AES and XPS of Silane Films and Organic Coatings Deposited on Metal Substrates*, Uppsala University, PhD thesis, (2003).
- [28] Scanning Electron Microscopy (SEM); available from:
<http://serc.carleton.edu/research-education/geochemsheets/techniques/SEM.html> (Accessed 04.03.2015).
- [29] Scanning Electron Microscope; available from:
<http://www.purdue.edu/ehps/rem/rs/sem.htm> (Accessed 04.03.2015).

Chapter 4

Concentration quenching, surface and spectral analyses of $\text{SrF}_2:\text{Pr}^{3+}$ prepared by different synthesis techniques

The luminescent and surface properties of $\text{SrF}_2:\text{Pr}^{3+}$ powder prepared by different synthesis techniques are outlined in this chapter. It was studied to investigate the effect of different synthesis techniques on the concentration quenching.

4.1 Introduction

Pr^{3+} is an interesting ion because it has multiple transitions that allows for detailed studies of both radiative and non-radiative mechanisms. Pr^{3+} doped materials have been extensively investigated due to its potential use in a variety of applications [1–5]. For phosphor applications, the 4f-4f transitions are the most relevant, especially the $^1\text{D}_2$ - $^3\text{H}_4$ red emission from Pr^{3+} doped oxide materials [6, 7]. Recently, the Pr^{3+} ion was found to be a promising co-doped ion in the lanthanide-based luminescent materials to be used for quantum cutting with the Yb ion, which can be used to enhance the solar cell efficiency [1, 8]. Quantum cutting with Pr^{3+} requires a host material with a lower vibrational energy. SrF_2 has very small cut-off phonon energy ($\sim 350 \text{ cm}^{-1}$) and was found to be a good host for the quantum cutting application [1, 8].

The $\text{SrF}_2:\text{Pr}^{3+}$ system has been investigated by several researchers [5, 9, 10] and the majority reported the photon emission cascade and energy transfer mechanism in SrF_2 doped with Pr^{3+} ions (with the main focus on the $4f^n-4f^{n-1}5d$ emission). The 4f-4f transitions have also been studied, but most of these results have been devoted to the red emission from Pr^{3+} doped oxide materials [6, 7, 11]. On the other hand, it has been shown that the probability of the multi-phonon relaxation between $^3\text{P}_0$ and $^1\text{D}_2$ levels of Pr^{3+} significantly decreases as the phonon energy of the host decreased [12]. It has also been observed that the emission intensity of the $^3\text{P}_0$ state of the Pr^{3+} doped host with a small phonon energy decreased with increasing the Pr^{3+} concentration. This

was attributed to cross-relaxation processes [12–15]. This behavior normally occurs at the smaller average interionic distances between the Pr^{3+} ions.

Most investigations on the concentration quenching of Pr^{3+} doped crystals have been studied in oxide hosts. The different pathways by which cross-relaxation can take place makes Pr^{3+} a challenging ion to study. The low phonon energy of the SrF_2 host may play a key role on the optical properties of the dopant ion. Furthermore, the emission intensities of lanthanide ions in a host were found to be strongly dependent on the condition of the synthesis procedure [8]. This was observed on Pr^{3+} co-doped Yb^{3+} in SrF_2 where the concentration quenching of both ions at small concentrations reduced the near infrared emission intensity and prevented more quantitative assessment of the quantum cutting efficiency. The $\text{SrF}_2:\text{Pr},\text{Yb}$ quantum cutting samples were synthesised by solid state reaction [8]. It is therefore quite meaningful to study the effect of different synthesis techniques on the concentration quenching of Pr^{3+} in SrF_2 phosphor. In this chapter, the surface and spectral investigation of Pr^{3+} doped SrF_2 phosphor powders prepared by using both the hydrothermal and combustion methods are studied. The concentration quenching of Pr^{3+} for both methods was investigated.

4.2 Experimental

Cubic SrF_2 nanocrystals doped with Pr^{3+} were prepared using hydrothermal and combustion synthesis procedures, as previously described [16, 17]. For the hydrothermal synthesis, analytical grade of $\text{Sr}(\text{NO}_3)_2$, $\text{Pr}(\text{NO}_3)_3 \cdot 6\text{H}_2\text{O}$, NH_4F , sodium oleate, oleic acid and ethanol were used without further purification. For a typical synthesis of $\text{SrF}_2:\text{Pr}^{3+}$, ethanol, sodium oleate and oleic acid were added simultaneously to an aqueous solution containing $\text{Sr}(\text{NO}_3)_2$, NH_4F and $\text{Pr}(\text{NO}_3)_3 \cdot 6\text{H}_2\text{O}$. After 10 min of stirring the milky colloidal solution was transferred to a 125 ml autoclave lined with teflon and heated at 180 °C for 24 h. The product was collected by centrifugal and washed with water and ethanol. Finally, the product was dried for 24 h in an oven at 80 °C. The as-prepared $\text{SrF}_2:\text{Pr}^{3+}$ samples did not emit, therefore, they were sintered for 2 h at 450 °C.

In the combustion synthesis, an aqueous solution of NH_4F was added drop-wise to a mixture of $\text{Sr}(\text{NO}_3)_2$, $\text{Pr}(\text{NO}_3)_3 \cdot 6\text{H}_2\text{O}$ and urea, which was used as fuel. The milky solution was collected after thoroughly stirring. Then, the obtained solution was transferred into a porcelain crucible and placed in a furnace at $500\text{ }^\circ\text{C}$ until the ignition occurred. Finally, the as-prepared powder was sintered for 2 h at $700\text{ }^\circ\text{C}$.

The phosphors were characterized by XRD (Bruker Advance D8 diffractometer with $\text{Cu K}\alpha$ radiation ($\lambda = 0.154\text{ nm}$)) to identify the crystalline structure of the powder. PL and PLE spectra were collected using a Cary Eclipse fluorescence spectrophotometer and Horiba scientific (Fluorolog-3) spectrofluorometer equipped with a xenon lamp. The surface morphology was recorded using a Shimadzu Supers-can scanning electron microscope model ZU SSX-550. High resolution XPS was obtained with a PHI 5000 Versaprobe system. A low energy Ar^+ ion gun and low energy neutralizer electron gun were used to minimize charging on the surface. A $100\text{ }\mu\text{m}$ diameter monochromatic $\text{Al K}\alpha$ x-ray beam ($h\nu = 1486.6\text{ eV}$) generated by a 25 W, 15 kV electron beam was used to analyze the different binding energy peaks. The pass energy was set to 11 eV giving an analyzer resolution $\leq 0.5\text{ eV}$. Multipack version 8.2 software was utilized to analyze the spectra to identify the chemical compounds and their electronic states using Gaussian-Lorentz fits. All measurements were performed at room temperature.

4.3 Results and Discussion

Fig. 4.1(a) depicts the XRD patterns of $\text{SrF}_2:\text{Pr}^{3+}$ prepared by the hydrothermal and combustion method as well as the standard data for SrF_2 (card No. 00-086-2418). The strong diffraction peaks indicate that the samples powder is fully crystallized (face-centred cubic with space group: $\text{Fm}\bar{3}\text{m}$). The patterns for doped samples with Pr^{3+} are similar to those from the pure SrF_2 matrix. This indicates that there is no obvious influence of the dopants on the crystalline structure of the host. It can, however, be noticed that doping of Pr^{3+} in both methods causes a slight shift to a higher angle with comparison to the standard data (fig. 4.1(a)). This can be attributed to the radius difference between Pr^{3+} (0.099 nm) and Sr^{2+} (0.126 nm) ions, which confirms

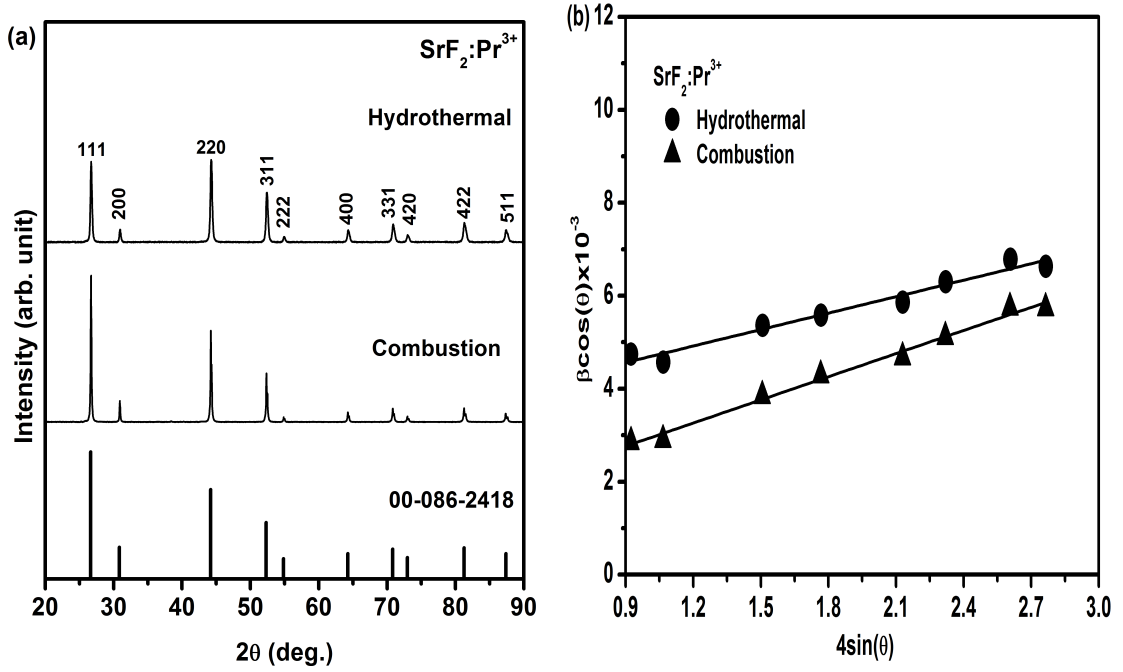


Fig. 4.1: (a) XRD patterns of SrF₂:Pr³⁺ phosphors; (b) Williamson-Hall plots for Pr³⁺ doped SrF₂ samples for both the hydrothermal and combustion methods.

that Pr³⁺ ions are incorporated into the SrF₂ lattice. The sintering temperature of the as-prepared hydrothermal samples caused a slight variation in the XRD intensities. The reason might be that, the orientation growth of the particles occurred in certain directions. The calculated SrF₂ lattice parameter is $(5.778 \pm 0.0025) \text{ \AA}$ and $(5.775 \pm 0.0054) \text{ \AA}$ for the samples prepared by the combustion and hydrothermal methods, respectively. These results agreed well with reported values [17].

	S using Debye-Scherrers equation (nm)	S using William-Hall equation (nm)
hydrothermal	37-41	36
combustion	56-62	69

Table 4.1: The estimated average crystallite size (**S**) of the particles using the William-Hall and the well-known Debye-Scherrers equations.

Fig. 4.1(b) shows Williamson-Hall plots for the combustion and hydrothermal samples, where the peak broadening is dependent on both crystallite size and microstrain. The Williamson-Hall equation is given by $\beta \cos \theta = K\lambda/S + 4\epsilon \sin \theta$, where λ is the wave-

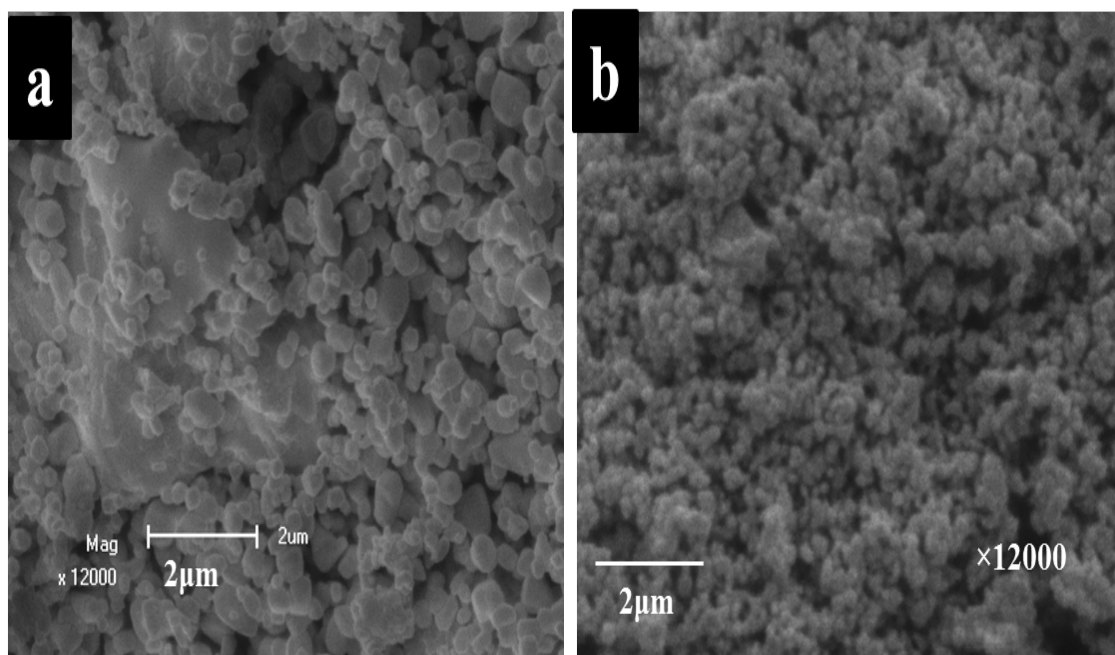


Fig. 4.2: SEM images of $\text{SrF}_2:\text{Pr}^{3+}$ phosphors prepared by different synthesis methods (a) combustion and (b) hydrothermal.

length of the x-rays (0.154 nm) and β is the full-width at half maximum of the x-ray peak at the Bragg angle θ , K is a shape factor taken as 0.9, S is the crystallite size and ϵ is the microstrain [18]. The slope of this equation is equal to the microstrain and the crystallite size can be calculated from the intercept ($K\lambda/S$). The microstrain of both the hydrothermal and combustion samples has values approximately of 0.0012 (0.12%) and 0.0017 (0.17%), respectively, showing only very small amount of microstrain in this produced materials. The bigger strain was produced by combustion synthesis, which might be true as the combustion technique requires a higher temperature. The estimated average crystallite size (S) of the particles was calculated from both the slope of the William-Hall equation and from the well-known Debye-Scherrers equation [19]. These are tabulated in table 4.1, which show that the hydrothermal method produced a smaller particle size.

SEM images were obtained in order to investigate the surface morphology of the synthesized phosphors. Fig. 4.2 represents the SEM images that were taken from the powders that were prepared by the different synthesis methods ((a) combustion and (b) hydrothermal). The results indicate different types of morphology. The combustion

synthesis produced large number of particles and voids, which may be due to the high temperature reaction during the combustion process. In hydrothermal synthesis fluffy type morphology was formed. These results suggested that the synthesis procedure strongly change the morphology of the $\text{SrF}_2:\text{Pr}^{3+}$ phosphor.

XPS measurements have been done in order to investigate the chemical, composition and bonding state of the $\text{SrF}_2:\text{Pr}^{3+}$ phosphors. There was no difference observed in the XPS spectra of the two synthesis methods. Fig. 4.3 shows the peak fits for the (a) Sr 3d, (b) F 1s and (c) Pr 3d high resolution XPS peaks and (d) the survey scan for $\text{SrF}_2:\text{Pr}^{3+}$. The results confirmed the presence of Sr, F, and Pr to their corresponding binding energies. In addition C and O were also observed. The C contamination is attributed to adventitious hydrocarbons which are known to be always present [20]. In a fluoride compound oxygen is considered to be a common impurity [21]. In fact the presence of the O in the sample did not change the structure of the sample (see fig. 4.1(a)). Therefore, the O contamination was due to adventitious impurity species in the surface rather than oxygen impurity in the SrF_2 matrix. During the peak fit procedure, the C 1s peak at 284.8 eV was taken as a reference for all charge shift corrections. This is done because the C 1s peak resulted from hydrocarbon contamination and its binding energy generally remains constant, irrespective to the chemical state of the sample. In the peak fit procedure, all the Gaussian percentages were assumed to have a combined Gaussian-Lorentzian shape. The high resolution XPS peak for the Sr 3d showed two individual peaks. These two peaks are assigned to Sr 3d in SrF_2 that originate from the spin-orbit splitting $3d_{5/2}$ (133.52 eV) and $3d_{3/2}$ (135.30 eV), while the F 1s peak is situated at 684.67 eV. The Pr $3d_{5/2}$ signal was comparatively low, which is due to a very low doping concentration of Pr. The high resolution XPS for Pr $3d_{5/2}$ peak consists of two individual peaks, which are assigned to the Pr^{3+} peak in $\text{SrF}_2:\text{Pr}^{3+}$ and a shake-down (s) peak that is always present in the Pr 3d spectra [22, 23]. These results not only approved the formation of the SrF_2 matrix, but also confirm the presence of the Pr dopant in the material.

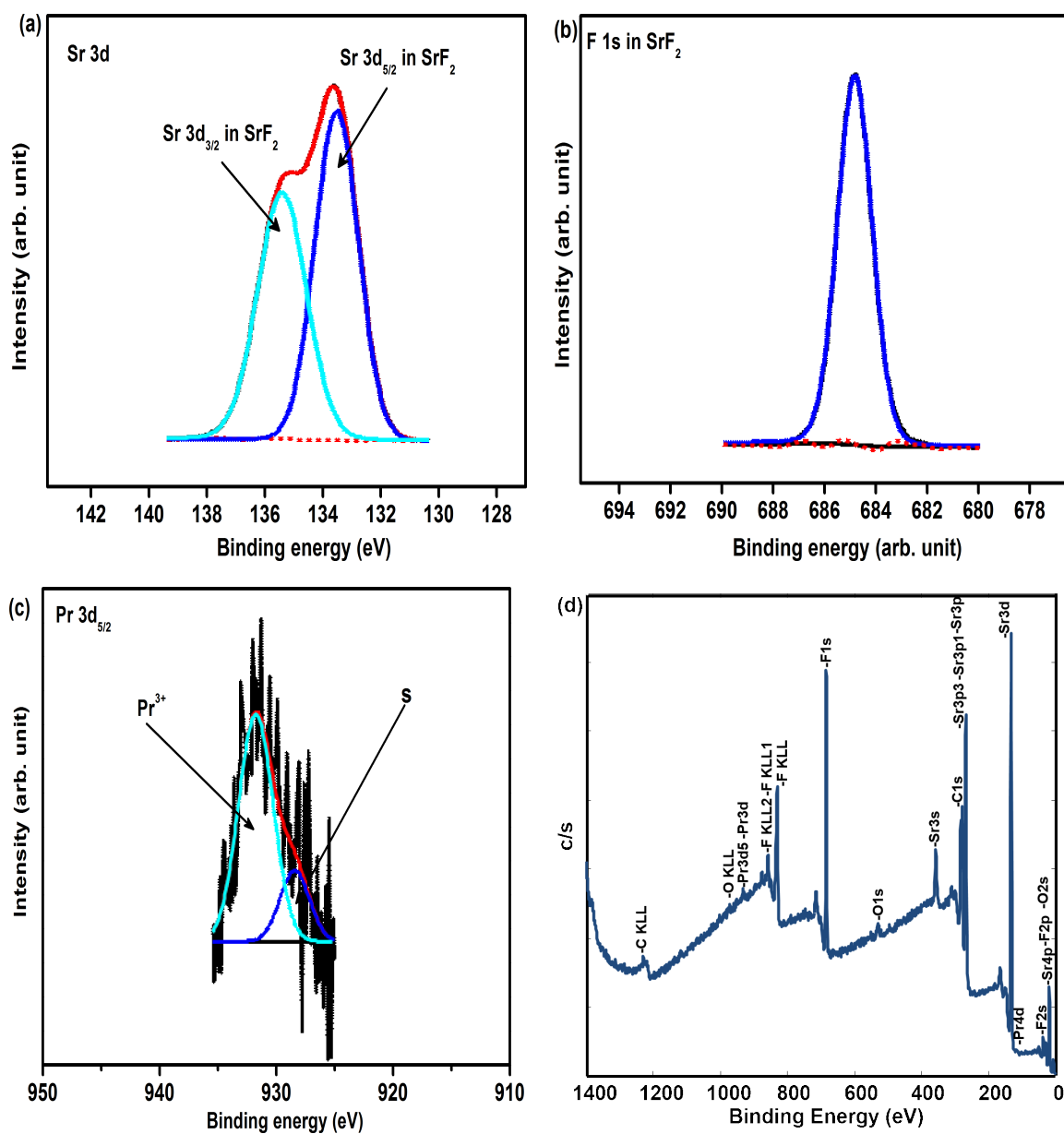


Fig. 4.3: High resolution XPS peaks of (a) Sr 3d, (b) F 1s, (c) Pr 3d_{3/2}, and (d) survey scan for SrF₂:Pr³⁺ phosphors.

Fig. 4.4(a), (b) and (c) show the excitation and emission spectra of the SrF₂ phosphor doped with Pr³⁺ ions that were prepared by the combustion and the hydrothermal methods. The extra charge of Pr³⁺ doped SrF₂ was compensated locally by F⁻ ions. All observed excitation and emission bands are similar in both synthesis methods. The excitation spectrum of SrF₂:Pr³⁺ (fig. 4.4(a)) was obtained by monitoring the emission centered at 488 nm (³P₀-³H₄ transition). The observed excitation bands are similar in both synthesis, which are corresponding to the transitions of ³H₄-³P_{*j*} (*j*=0, 1, 2) and ¹I₆. All these bands occurred within the 4f-4f transitions of the Pr³⁺ ion [11]. The metastable ³P₀ energy level depopulated through non-radiative relaxation when any level above ³P₀ is optically excited. Upon excitation with 439 nm (into the ¹I₆ and ³P_{*j*}, *j* = 0, 1, 2), depopulation from the ¹I₆ and ³P_{1,2} energy bands occurred to the metastable ³P₀ energy band. Both samples exhibit blue-red emission from the ³P₀ level. There are at least six luminescent bands that correspond to relaxation from the ³P₀ emission energy band. These six bands are centered at 488, 524, 605, 638, 715 and 730 nm, which are assigned to the ³P₀-³H₄, ³P₀-³H₅, ³P₀-³H₆, ³P₀-³F₂, ³P₀-³F₃ and ³P₀-³F₄ transitions, respectively [8]. This demonstrates that the dominant transition in SrF₂ is the ³P₀ transition. There is also a small peak marked with (S) around 879 nm (fig. 4.4(b) and (c)), which is assigned to the second order observation of the excitation wavelength. This band has been previously assigned to the ³P₀-¹G₂ transitions [8], but in this work, we observed that its position changes with the excitation wavelength, which is exactly twice of the excitation wavelength (λ_{exc}). The second order observation of the Pr³⁺ system has also been previously reported on Pr³⁺ doped YF₃ [2]. The actual peak of ³P₀-¹G₄ transition in SrF₂ host is very much weaker and can be clearly seen in the inset of fig. 4.4(c). Its position in the fluoride hosts was found around 974 nm, which is well in agreement with our results [24].

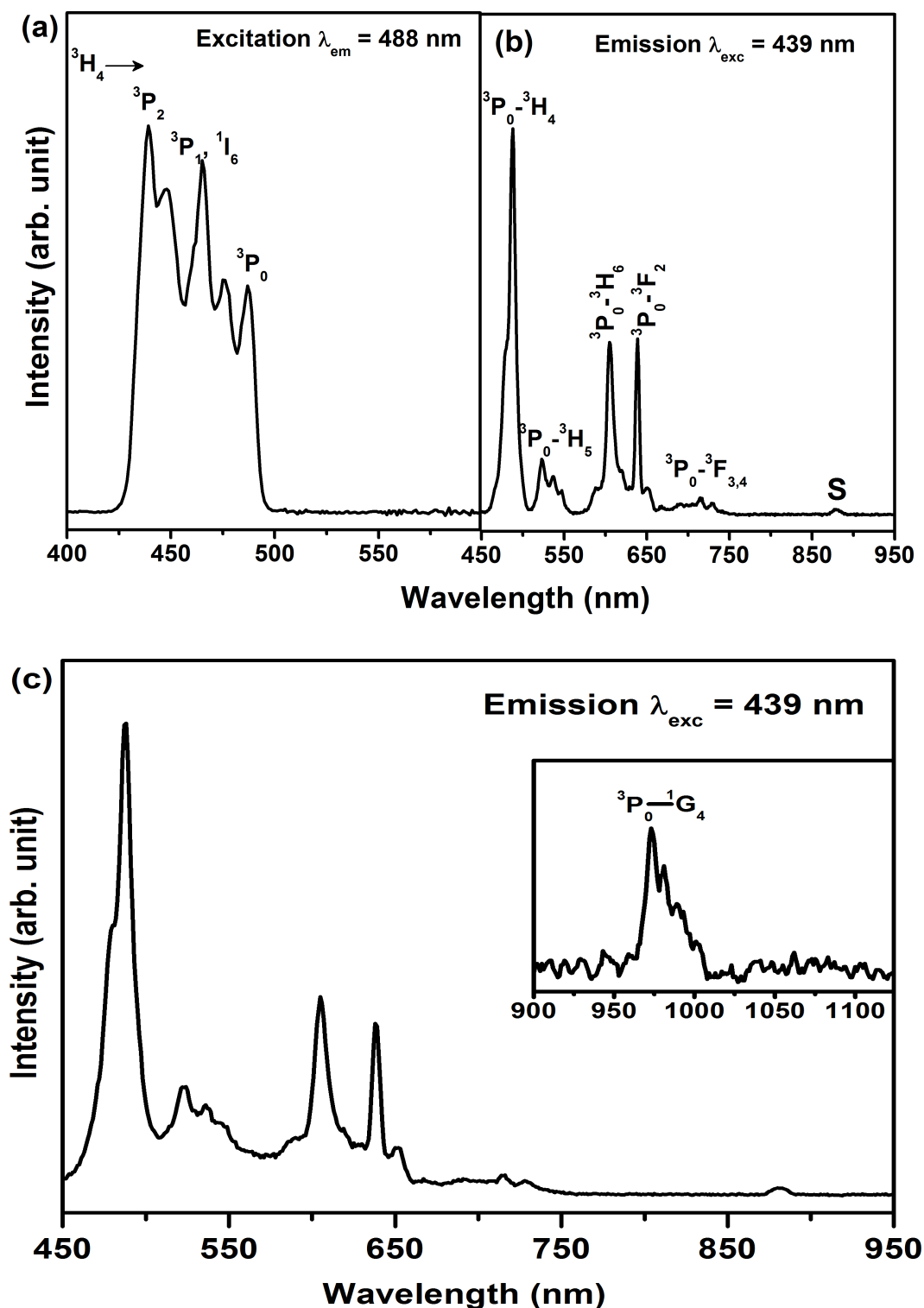


Fig. 4.4: Excitation and emission spectra of $\text{SrF}_2:\text{Pr}^{3+}$ at different synthesis methods, (a) excitation and (b) emission spectrum for combustion method, (c) emission spectrum for hydrothermal method. The inset shows the weak $^3P_0-^1G_4$ transition band of Pr.

Concentration quenching is considered to be a common energy loss mechanism for dopant ions. We therefore have prepared the SrF₂ phosphors doped with different concentrations of Pr³⁺ ions. Fig. 4.5 shows the ³P₀-³H₄ emission intensity variation as a function of Pr³⁺ concentration for combustion and hydrothermal methods. It is worth mentioning that all the samples were carefully synthesized and measured under the same condition for each preparation method so that the Pr³⁺ ion emission intensity can be compared. In the combustion method, the PL intensity of the ³P₀ emission increased until around 0.2 mol% Pr³⁺ concentration, whereas in the hydrothermal method it increased from 0.1 up to around 0.4 mol% Pr³⁺ concentrations. It then started to decrease systematically as the Pr³⁺ concentration increased. This demonstrates that the optimum Pr³⁺ doping for maximum luminescence of Pr³⁺ doped SrF₂ was about 0.2 and 0.4 mol% for the combustion and hydrothermal samples, respectively. The same behaviour was also observed for the other emission bands. When the Pr³⁺ ions concentration increases, the Pr³⁺-Pr³⁺ distance decreases, which give rise to non-radiative energy transfers between Pr³⁺ ions. This causes non-radiative energy transfer between Pr³⁺ ions. Therefore, the emission intensity strongly depends on the distance between Pr³⁺ ions. Thus, the difference in the intensity optimization between the synthesis methods can be associated to the distance between nearby Pr³⁺ ions. This assumption is drawn from the knowledge that the lanthanide ions form clusters in SrF₂ because charge compensation is required when Sr²⁺ is substituted by Pr³⁺ ions [25, 26]. The Pr³⁺ ions form less clustering in the hydrothermal samples relative to that in the combustion samples. This makes the energy transfer between Pr³⁺ ions in combustion samples more effective than in hydrothermal samples. However, the non-radiative emission from ³P₀ level normally occurs through two different processes: relaxation by multi-phonon emission to the ¹D₂ level, or cross-relaxation between Pr³⁺ pairs. As it is mentioned earlier the probability of the multi-phonon process significantly reduces as the phonon energy of the host decreases [12]. The energy difference between ³P₀ and ¹D₂ is around 3500 cm⁻¹ and the energy cut-off of the SrF₂ is about 350 cm⁻¹. This means that ten phonons are required to bridge the energy gap. It is well known that when the number of required phonons exceeded 5, the possibility of multi-phonon relaxation to occur is low. Hence, the multi-phonon relaxation processes

for the 3P_0 and 1D_2 levels can be considered negligible. Therefore, the 3P_0 emission quenching might occur due to the cross-relaxation interaction between the nearby Pr^{3+} ions as a results of clustering effects.

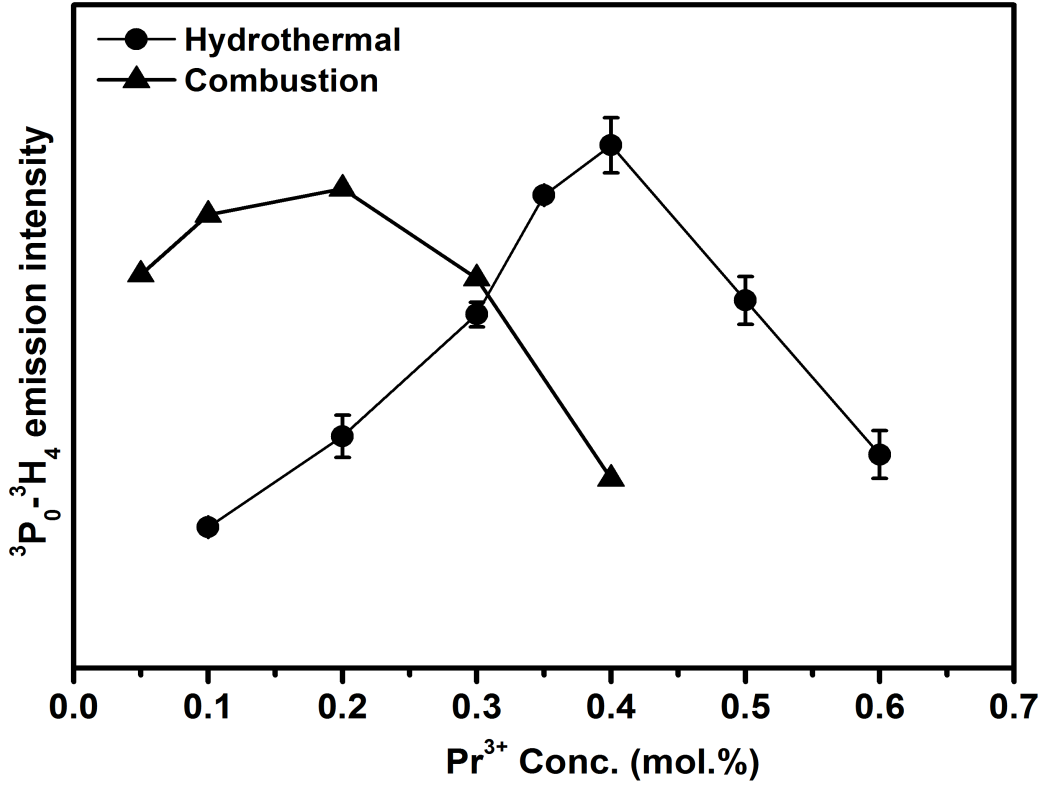


Fig. 4.5: Variation of the Pr^{3+} emission intensity as a function of Pr^{3+} concentration for hydrothermal and combustion methods. The vertical lines represent the error bars. (**Note:** The comparison were only made for the optimum Pr^{3+} doping concentration between the two synthesis methods. The excitation slit width was different for the two methods during the measurements).

It is necessary to describe the type of interaction that is responsible for the non-radiative energy transfer process between the Pr^{3+} ions. According to Dexter's theory [27], if the energy transfer occurs between the same sorts of activators, the strength of the multipolar interaction can be determined from the change of the emission intensity with concentration ions as follow:

$$\frac{I}{C} = \kappa(1 + \beta(C)^{Q/3})^{-1}, \quad (4.1)$$

where C is the activator concentration; $Q = 6, 8, 10$ for dipole-dipole, dipole-quadrupole,

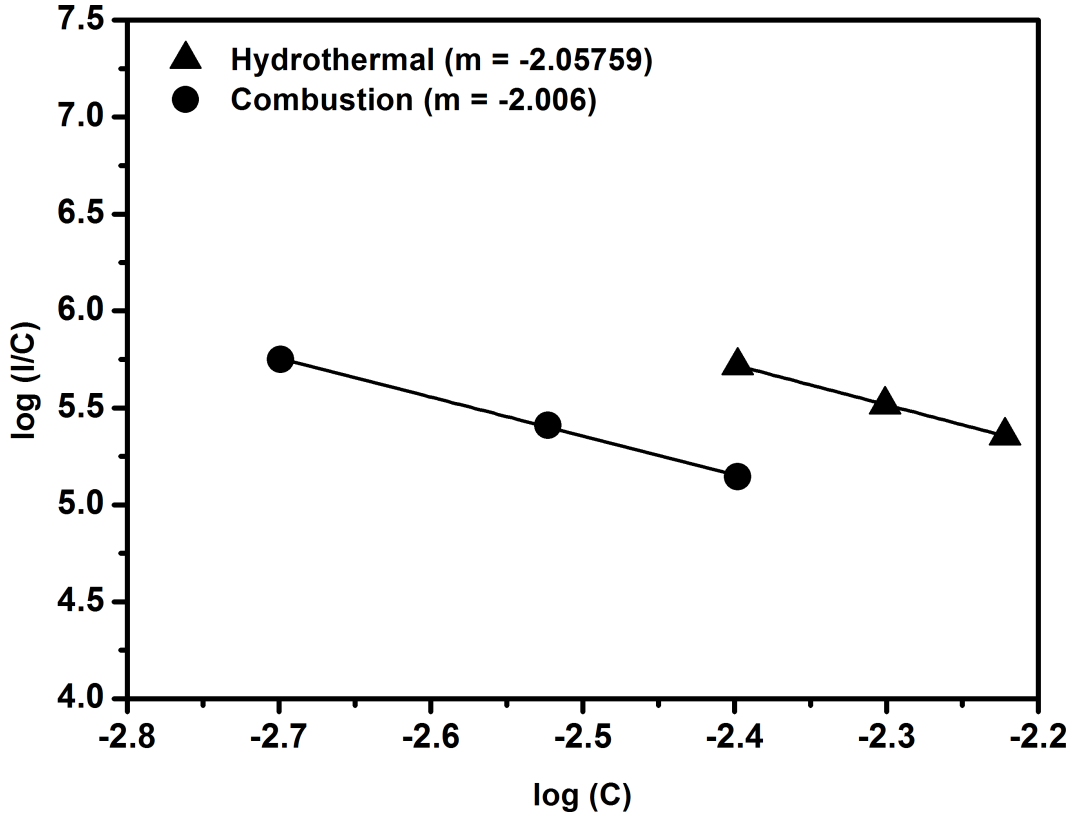


Fig. 4.6: The curve of $\log(I/C)$ vs. $\log(C)$ in $\text{SrF}_2:\text{Pr}^{3+}$ phosphors.

quadrupole-quadrupole interactions, respectively; and κ and β are constant for the same excitation conditions for a given host material.

At a concentration C higher than the critical quenching concentration C_c , Eqn. 4.1 can be approximated to Eqn. 4.2 below for $\beta(C)^{Q/3}$ [28];

$$\frac{I}{C} = \frac{\kappa'}{\beta(C)^{Q/3}} \quad (4.2)$$

where κ' is constant and C is the activator concentration greater than C_c . Fig. 4.6 represents $\log I/C$ as a function of $\log C$. It can be seen that the dependence of $\log I/C$ versus $\log C$ is linear for both techniques and the line slopes are -2.006 and -2.05759 for the combustion and hydrothermal, respectively. Therefore the value of Q for both techniques is approximately equal to 6, which indicates that the dipole-dipole interaction between Pr^{3+} ions is the mechanism that is responsible for the concentration quenching in the $\text{SrF}_2:\text{Pr}^{3+}$ phosphor. The dipole-dipole interactions have also been reported previously to describe the interaction between Pr^{3+} ions in LaF_3 and BaTa_2O_6 crystals [29, 30]. Such information could be important for the optimization of the Pr^{3+}

concentration in nano-crystalline materials for certain applications.

4.4 Conclusions

The $\text{SrF}_2:\text{Pr}^{3+}$ powder was prepared by hydrothermal and combustion methods. The XRD patterns showed strong and sharp diffraction peaks for both samples, which indicate that the powders were completely crystallized with a pure face-centred cubic (space group: $\text{Fm}\bar{3}\text{m}$) structure. A comparison between these two methods showed that the calculated particle sizes are smaller for the hydrothermal technique. XPS confirms the presence of Sr, F and Pr materials on the host matrix. It was found that both samples exhibit blue-red emission under 439 nm from 4f-4f excitation at 425 to 500 nm. The optimum Pr^{3+} doping level for maximum emission intensity was 0.4 and 0.2 mol% for the hydrothermal and combustion samples, respectively. The reduction of Pr^{3+} emission intensity was a result of the Pr^{3+} clustering in SrF_2 due to charge compensation. The dipole-dipole interactions between the nearby Pr^{3+} ions is responsible for the concentration quenching of Pr^{3+} intensity in the $\text{SrF}_2:\text{Pr}^{3+}$ crystal.

References

- [1] B. M. Van der Ende, L. Aarts and A. Meijerink, *Phys. Chem. Phys. Chem.*, **11** (2009) 11081-11095.
- [2] A. Srivastava and S. J. Duclos, *Chem. Phys. Lett.*, **275** (1997) 453-456.
- [3] M. A. Gusowski, H. C. Swart, L. S. Karlsson and M. G. Trzebiatowska, *Nanoscale*, **4** (2012) 541-546.
- [4] A. I. Voloshin, N. M. Navaleev and V. P. Kazakov, *J. Lumin.*, **93** (2001) 199-204.
- [5] N. Kristianpoller, D. Weiss and R. Chen, *Radiat. Meas.*, **38** (2004) 719-722.
- [6] P. Boutinaud, M. Dubois, A. P. Vink and R. Mahiou, *J. Lumin.*, **111** (2005) 69-80.
- [7] P. J. Deren, R. Pazik, W. Streck, P. Boutinaud and R. Mahiou, *J. Alloys Comp.*, **451** (2008) 595-599.
- [8] B. M. Van der Ende, L. Aarts and A. Meijerink, *Adv. Mater.*, **21** (2009) 3073-3077.
- [9] E. Radzhabov, *J. Lumin.*, **129** (2009) 1581-1585.
- [10] R. Shendrik and E. Radzhabov, *IEEE Trans. Nucl. Sci.*, **59** (2012) 2089-2094.
- [11] L. L. Noto, S. S. Pitale, M. A. Gusowki, J. J. Terblans, O. M. Ntwaeaborwa and H. C. Swart, *Powder Technol.*, **237** (2013) 141-146.
- [12] R. Naccache, F. Vetrone, A. Speghnini, M. Bettinelli and J. A. Capobianco, *J. Phys. Chem. C*, **112** (2008) 7750-7756.
- [13] R. Balda, J. Fernandez, I. S. Ocariz, M. Voda and A. J. Garcia, *Phys. Rev. B*, **59** (1999) 9972-9980.
- [14] Q. J. Chen, W. J. Zhang, X. Y. Huang, G. P. Dong, M. Y. Peng and Q. Y. Zhang, *J. Alloys Comp.*, **513** (2012) 139-144.
- [15] J. Collins, M. Geen, M. Bettinelli and B. Di Bartolo, *J. Lumin.*, **132** (2012) 2626-2633.

- [16] J. Sun, J. Xian and H. Du, *Appl. Surf. Sci.*, **257** (2011) 3592-3595.
- [17] N. Rakov, R. B. Guimaraes, D. F. Franceschini and G. S. Maciel, *Mater. Chem. Phys.*, **135** (2012) 317-321.
- [18] W. A. I. Tabaza, H. C. Swart and R. E. Kroon, *J. Lumin.*, **148** (2014) 192-197.
- [19] C. Oprea, V. Ciupina and G. Prodan, *Romanian J. Phys.*, **53** (2008) 223-230.
- [20] R. E. Kroon, H. C. Swart, O.M. Ntwaeaborwa and H. A. A. Seed Ahmed, *Physica B*, **439** (2014) 83-87.
- [21] J. T. van Wijngaarden, S. Scheidelaar, T. J. H. Vlugt, M. F. Reid and A. Meijerink, *Phys. Rev. B*, **81** (2010) 155112-155117.
- [22] H. Ogasawara, A. Kotani, R. Potze, G. A. Sawatzky and B. T. Thole, *Phys. Rev. B*, **44** (1999) 5465-5469.
- [23] J. Gurgul, M. T. Rinke, I. Schellenberg and R. Pottgen, *Solid State Sci.*, **17** (2013) 122-127.
- [24] A. Guille, A. Pereira, G. Breton, A. Bensalah-ledoux and B. Moine, *J. of Appl. Phys.*, **111** (2012) 043104-043108.
- [25] P. J. Bendall, C. R. A. Catlow, J. Corish and P. W. M. Jacobs, *J. Solid State Chem.*, **51** (1988) 159-169.
- [26] D. R. Tallent, D. S. Moore and J. C. Wright, *J. Chem. Phys.*, **67** (1977) 2897-2907.
- [27] D. L. Dexter, *J. Chem. Phys.*, **21** (1953) 836-850.
- [28] D. Wang, Q. Yin, Y. Li and M. Wang, *J. Lumin.*, **97** (2002) 1-6.
- [29] G. P. Morgan, D. L. Huber and W. M. Yen, *J. DE Physique*, **46** (1985) C7-25.
- [30] M. Ilhan, R. Samur, H. Demirer and F. Mindivan, *Metalurgija*, **54** (2015) 407-410.

Chapter 5

The effects of Eu-concentrations on the luminescent properties of SrF₂:Eu downshifting nanophosphor

This chapter studied the effect of Eu-concentration on the Eu emission in SrF₂ crystal. The investigation was done to study the possibility of using the Eu ions as a downshifting layer for a solar cell application.

5.1 Introduction

Lanthanide ions including europium (Eu) ion are trivalent in most of their compounds, whereas in certain compounds Eu shows two oxidation states (trivalent (Eu³⁺) and divalent (Eu²⁺)) [1, 2]. These two oxidation states have also been identified in certain hosts at high temperature treatment in a reducing atmosphere (such as H₂/Ar, H₂/N₂) or air condition [3–5]. The presence of these oxidation states has caused detailed theoretical and experimental measurements by various workers [1, 6, 7].

It is well known that Eu³⁺ ion doped materials emits red light and exhibits large Stokes shifts (>150 nm), which makes it a suitable ion in various applications [8–10]. The emission of Eu³⁺ is mainly originated from the 4f-4f transition (more details in chapter 2). Such transition is parity forbidden, which is characterized by weak absorption cross-section. In some applications, high or suitable absorption cross-section is needed. One of these applications is the use of Eu³⁺ as a downshifting layer to enhance the response of photovoltaic cells [11, 12]. In order to enhance the 4f-4f absorption strength of Eu³⁺, a sensitizer with a high absorption coefficient is required. This sensitizer can efficiently absorb all the light in the ultraviolet (UV) part of the solar spectrum and transfers its energy to the downshifting ion (Eu³⁺). A number of researches reported on the synthesis of new dye Eu³⁺ complexes to enhance the spectral response of Eu³⁺ [13, 14]. However, Eu²⁺ ion showed a broadband that originated from the 4f⁶5d¹-4f⁷ inter-configuration fully allowed transition [15]. Thus, the presence of Eu²⁺ and Eu³⁺ in a

host is very crucial in down-shifting applications.

SrF₂ is one of the most widely used optical materials due to its optical properties (wide bandgap and low phonon energy) as well as physical properties (low refraction index, high radiation resistance, mechanical strength and low hygroscopicity) [16]. The Eu doped as-prepared SrF₂ phosphor has been studied by different researchers [17, 18]. In 2008, Y. Jin et al. [17] reported that Eu³⁺ emits visible light dominated by a narrow band situated at 591 nm upon UV irradiation. The optimal Eu³⁺ doping for maximum luminescence of Eu³⁺ doped SrF₂ nanospheres was reported to be about 2 mol%. This demonstrates that the sample exhibited only the Eu³⁺ oxidation state of the Eu compound in SrF₂. A study by S. Kurosawal et al. [18] demonstrated that the Eu doped as-prepared SrF₂ revealed both the emissions from the Eu oxidation states (Eu³⁺ and Eu²⁺). The light output of the SrF₂:Eu scintillator was significantly enhanced. In fact, Eu³⁺ is more stable than Eu²⁺ in material scintillators. Therefore, the presence of both Eu oxidation states gave rise to better scintillation properties [18]. It is therefore quite meaningful to investigate the Eu doped SrF₂ for its application in photovoltaic cells.

In this chapter, the potential application of a Eu doped SrF₂ nano-phosphors as a possible downshifting phosphor is investigated. The surface and spectral analysis to study the effect of the Eu concentrations on the luminescent properties are presented.

5.2 Experimental setup

Eu doped and undoped SrF₂ phosphor samples were synthesised by the hydrothermal method. For the hydrothermal process, all chemical reagents were of analytical grade and were used without further purification. For a typical synthesis, 1 mmol of Sr(NO₃)₂ was first dissolved in 30 mL distilled water, followed by 5 mmol of C₁₀H₁₄N₂O₈·2H₂O (Na₂EDTA, ethylenediamine tetraacetic acid disodium salt) and 2 mmol of NaBF₄ under constant stirring. After further magnetic stirring for 10 min. the solution was transferred into a 125 ml autoclave lined with Teflon, heated at 160 °C for one hour and naturally cooled down to room temperature [19]. The product was collected by centrifugal and washed with water and ethanol. Finally, the product was dried for

10 hours in an oven at 60 °C. Eu doped SrF₂ samples were prepared by the same hydrothermal technique, Eu(NO₃)₃·(H₂O)₅ was used as source for the Eu dopant.

The phosphors were characterized by XRD (Bruker Advance D8 diffractometer with Cu K_α radiation ($\lambda = 0.154$ nm)) to identify the crystalline structure of the powder. PL spectra were collected using a Cary Eclipse fluorescence spectrophotometer equipped with a xenon lamp and also He-Cd laser PL system with a 325 nm excitation wavelength with 1 milliwatt power. The surface morphology was recorded using a Shimadzu Supers scanning electron microscope model ZU SSX-550. Transmission electron microscopy (TEM) specimen was prepared using a FEI Helios Nanolab 650 FIB. Initial milling of the TEM section was done with 30 keV Ga ions with a final polishing performed at 2 keV producing a near damage free TEM foil. Specimens were analysed (imaged in the high-angle annular dark field mode (HAADF)) using a JEOL ARM 200F transmission electron microscope operated at 200 kV with an Oxford X-Max 80 EDS detector. An IonTof time of flight secondary ion mass spectrometer instrument equipped with a Bi primary ion source was used to characterize the nanophosphor materials for their chemical composition. In spectroscopy mode, the system equipped with a DC current of 30 nA and a pulsed current of 1 pA at 30 kV with a heating current of 2.95 A and emission current of 0.8 μ A was used. High resolution XPS was obtained with a PHI 5000 Versaprobe system. A low energy Ar⁺ ion gun and low energy neutralizer electron gun were used to minimize charging on the surface. A 100 m diameter monochromatic Al K_α x-ray beam ($h\nu = 1486.6$ eV) generated by a 25 W, 15 kV electron beam was used to analyze the different binding energy peaks. The pass energy was set to 11 eV giving an analyzer resolution ≤ 0.5 eV. Multipack version 8.2 software was utilized to analyze the spectra to identify the chemical compounds and their electronic states using Gaussian-Lorentz fits. Luminescence decay curves were recorded by using a diode pumped YAG laser with a 335 nm excitation wavelength, power of 1.3 milliwatt and a SR430 Multichannel scaler photomultiplier. All measurements were performed at room temperature.

5.3 Results and discussion

5.3.1 Structure and morphology analysis

Fig. 5.1 shows the XRD patterns of undoped and doped SrF₂ as well as the standard data for SrF₂ (card No. 00-086-2418). The sharp and strong diffraction peaks indicate that the sample powder was fully crystallized (face-centered cubic with space group: Fm3m). Doping of Eu caused a slight shift to a higher angle with comparison to the undoped sample and standard data (see dashed line in fig. 5.1). This can be attributed to the radius difference between Eu (Eu²⁺ is 0.125 nm and Eu³⁺ is 0.107 nm) and Sr²⁺ (0.126 nm) ions, which confirms that Eu ions were successfully incorporated into the SrF₂ lattice. It should be mentioned that doping of Eu ions (up to 10 mol%) did not change the structure, morphology and crystallization of the SrF₂ host in this study. The calculated SrF₂ lattice parameter was 5.785 ± 0.0054 nm and this indicates a small reduction in the unit cell compared to the standard card (5.80 nm) [20].

The estimated particle size \mathbf{S} was calculated using the diffraction peaks and Scherrer's equation [21].

$$\mathbf{S} = \frac{0.9\lambda}{\beta \cos \theta} \quad (5.1)$$

where \mathbf{S} is the average size of SrF₂ particles, λ is the wavelength of the x-rays (0.154 nm) and β is the full-width at half maximum of the x-ray peak at the Bragg angle θ . The average crystallite sizes of the undoped and doped samples are tabulated in table 5.1. Doping with Eu ions tend to reduce the nano-particle size of the matrix. This result is in agreement with a study done by F. Wang et al. [22]. They have described a material system in which doping influences the growth process to give simultaneous control over the crystallographic phase, size and optical emission properties on the resulting nano-crystals. The system described was NaYF₄ nanocrystals and the results showed (specifically the XRD results) that the nanocrystals can be tuned in size (down to ten nanometres), phase and upconversion emission colour through the use of trivalent lanthanide dopant ions introduced at defined concentrations.

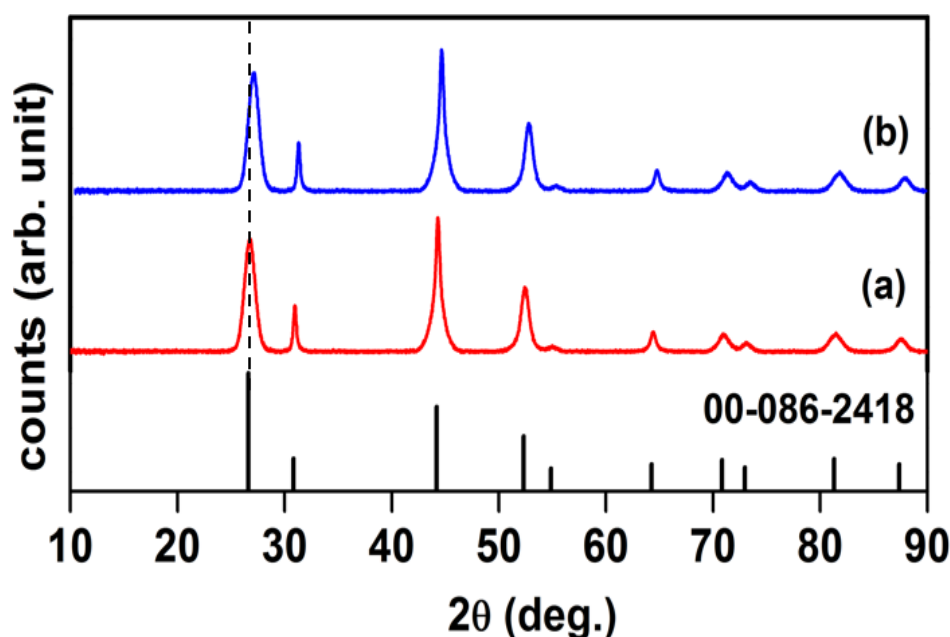


Fig. 5.1: XRD pattern of (a) SrF_2 and (b) $\text{SrF}_2:\text{Eu}$ 3.0 mol% samples. The vertical lines are the standard data of SrF_2 from the 00-086-2418 card.

Eu concentration (mol%)	particle size (nm)
host	7.6
1.5	7.3
3.0	6.8
10.0	4.5

Table 5.1: Calculated particle size of the undoped and Eu doped SrF_2 using Sherrer's equation.

The morphology of the as-prepared doped and undoped SrF_2 samples were characterized with SEM. Fig. 5.2 presents the SEM images of the as-prepared and 5 mol% of Eu^{3+} doped SrF_2 at low (a, b) and high (c, d) magnification, respectively. A large number of uniform microsphere agglomerated particles with a diameter of about 1.5-2.0 μm were formed in both the doped and undoped SrF_2 samples. These results confirm that doping with Eu ions does not change the structure and the morphology of the SrF_2 sample. In order to study the surface morphological features of the nanophosphor, HRTEM was performed. HRTEM image for the individual microsphere particles are shown in fig. 5.2(e), which reveals that the microsphere particles consists of dense

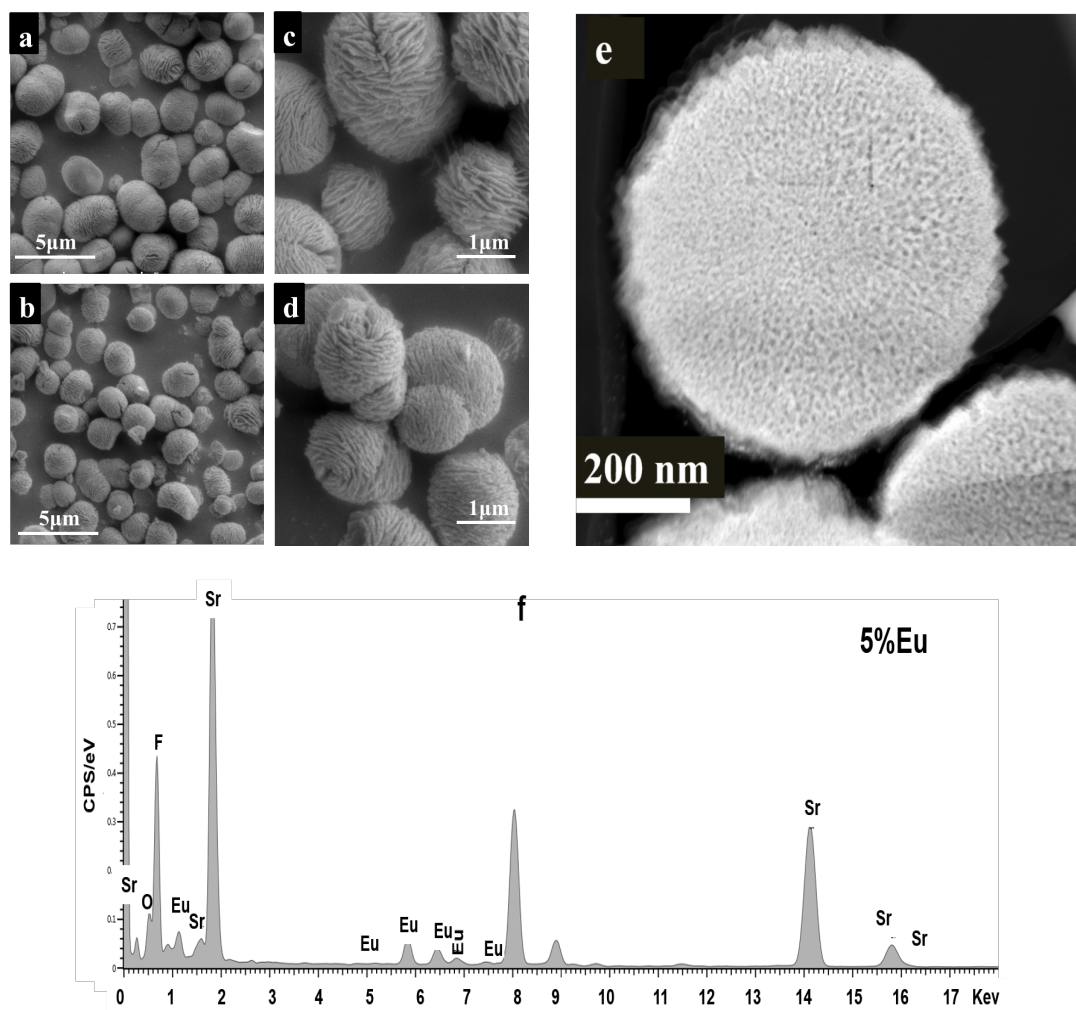


Fig. 5.2: SEM images of undoped (a, c) and 5 mol% of Eu doped (b, d) SrF₂ at low and high magnification, respectively, (e) HRTEM image of the Eu 5 mol% SrF₂ sample and (f) EDS spectrum of the Eu doped SrF₂ samples.

particles in the nano-structure size 5-7 nm range. These results are in good agreement with the estimated crystallite sizes obtained by Scherrers equation from the XRD peak broadening. Fig. 5.2(f) depicts the elemental analysis of the samples using EDS. Representative peaks associated to F, Eu and Sr elements are clearly identified. The unlabelled peaks are due to system peaks such as the copper grid and sample holder, etc. The Sr:F ratio indicating a 1:2 atomic ratio and the Eu about 5-6 % with very little oxygen.

5.3.2 Photoluminescence spectroscopy

Fig. 5.3 shows the excitation and emission spectra of the Eu^{3+} doped SrF_2 (1 mol%) excited by the xenon lamp at room temperature. The excitation spectrum of $\text{SrF}_2:\text{Eu}^{3+}$ (fig. 5.3(a)) was obtained by monitoring the emission centred at 591 nm (${}^5\text{D}_0 \rightarrow {}^7\text{F}_1$ transition). There are at least seven excitation bands in the range 300 to 550 nm that correspond to the transitions of ${}^7\text{F}_0 \rightarrow {}^5\text{H}_6$ (319 nm), ${}^7\text{F}_0 \rightarrow {}^5\text{D}_4$ (360 nm), ${}^7\text{F}_0 \rightarrow {}^5\text{L}_7$ (381 nm), ${}^7\text{F}_0 \rightarrow {}^5\text{L}_6$ (394 nm), ${}^7\text{F}_0 \rightarrow {}^5\text{D}_3$ (416 nm), ${}^7\text{F}_0 \rightarrow {}^5\text{D}_2$ (465 nm) and ${}^7\text{F}_0 \rightarrow {}^5\text{D}_1$ (525 nm). All these seven bands occur within the 4f-4f transitions of the Eu^{3+} ion [10, 23]. The metastable ${}^5\text{D}_0$ energy level depopulated through non-radiative relaxation when any level above ${}^5\text{D}_0$ is optically excited. The emission spectra exhibited orange-red emission bands from 550 to 710 nm that is attributed to the ${}^5\text{D}_0 \rightarrow {}^7\text{F}_j$ transitions ($j = 1, 2, 3, 4$). The red peak centered at 615 nm associated with the ${}^5\text{D}_0 \rightarrow {}^7\text{F}_2$ transition is a parity forbidden electric dipole transition, which is very sensitive to the environment around the Eu^{3+} ion, see chapter 2. The emission of ${}^5\text{D}_0 \rightarrow {}^7\text{F}_1$ transition is a parity allowed magnetic dipole transition, which is insensitive to the site symmetry [9, 17]. The strong emission from ${}^5\text{D}_0 \rightarrow {}^7\text{F}_1$ only occurs when Eu occupied non-inversion symmetry sites. In the spectra, the strongest emission is from the ${}^5\text{D}_0 \rightarrow {}^7\text{F}_1$ transition and the ${}^5\text{D}_0 \rightarrow {}^7\text{F}_0$ (550 nm) transition is hardly observed.

Concentration quenching is considered to be a common energy loss mechanism for dopant ions. We therefore have prepared the SrF_2 nanophosphor doped with different concentrations of Eu ions. The inset graph in fig. 5.3 presents the ${}^5\text{D}_0 \rightarrow {}^7\text{F}_1$ emission intensity variation as a function of Eu concentration in SrF_2 . It is worth mentioning that all the samples were carefully synthesized and measured under the same condition so that the Eu^{3+} emission intensity can be compared. At low Eu concentrations (< 5 mol%), the PL intensity of the ${}^5\text{D}_0 \rightarrow {}^7\text{F}_1$ emission increased slightly after which it then increased dramatically. These results contradict the previous study by Y. Jin et al. [17] who demonstrated that the optimal concentration of Eu^{3+} ions in as-prepared SrF_2 nanosphere was about 2 mol% [17]. The sample however exhibited only one oxidation state of Eu. The presence of one oxidation state of Eu (i.e. Eu^{3+} ion) in as-prepared SrF_2 has also been reported by other groups [19, 24]. Eu that exhibits only

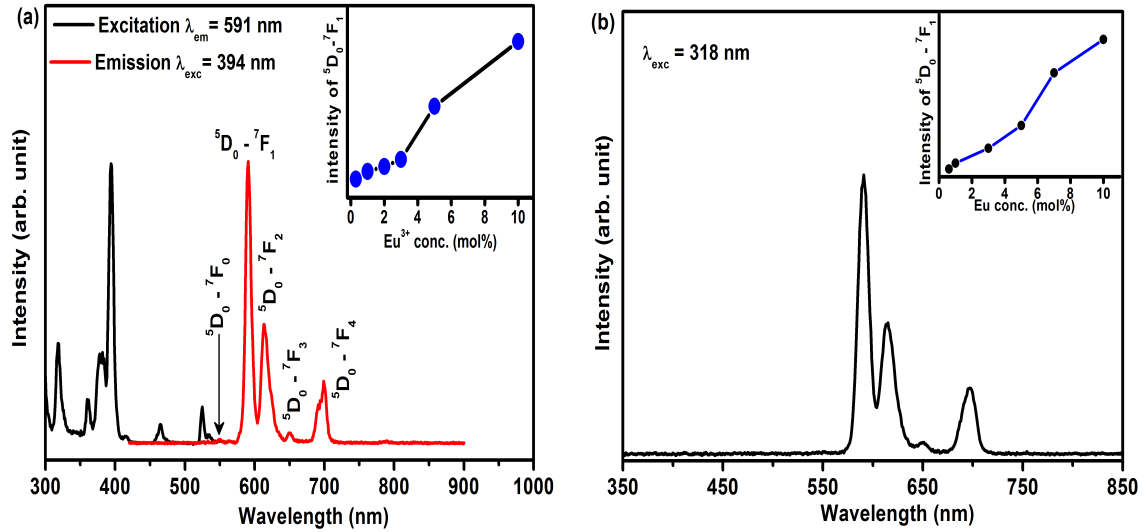


Fig. 5.3: Excitation and emission spectra of $\text{SrF}_2:\text{Eu}^{3+}$ (a) $\lambda_{exc} = 394$ nm and (b) $\lambda_{exc} = 318$ nm using a xenon lamp. The inset graph presents the variation of the Eu^{3+} emission intensity as a function of the Eu concentration.

one oxidation state (Eu^{3+}) has also been reported in other fluoride hosts [8, 25, 26]. A study that was done by S. Kurosawal et al. [18] showed that the $\text{SrF}_2:\text{Eu}$ sample exhibited both the Eu oxidation states' emissions. In fact, the increase in the PL intensity reflects the increase of the luminescent centres of Eu^{3+} with increasing the Eu concentration [27]. Therefore, we attribute the increase of the Eu intensity to the increase of the Eu luminescent centres that might be originated from the presence of both oxidation state of Eu. Hence, more measurements are needed to confirm the expectation.

Fig. 5.4 shows the PL emission spectra recorded using the He-Cd laser PL system with a 325 nm excitation source. It can be seen that at small Eu concentrations (up to 3 mol%), the spectra clearly consist of a broad emission band centred at 416 nm and very small narrow emission bands in the range of 550-710 nm. The broad emission band can be attributed to the inter-configuration $4f^65d^1-4f^7$ allowed transition of Eu^{2+} [18]; and the narrow emission bands to the Eu^{3+} emission. At high concentrations (i.e 10 mol%) the emission of Eu^{3+} became more significant. The emission intensity of Eu^{3+} has increased with an increase in Eu concentration. The exact $\text{Eu}^{3+}/\text{Eu}^{2+}$ ion ratio cannot be detected using the PL data but the PL intensity ratio between Eu^{3+} and

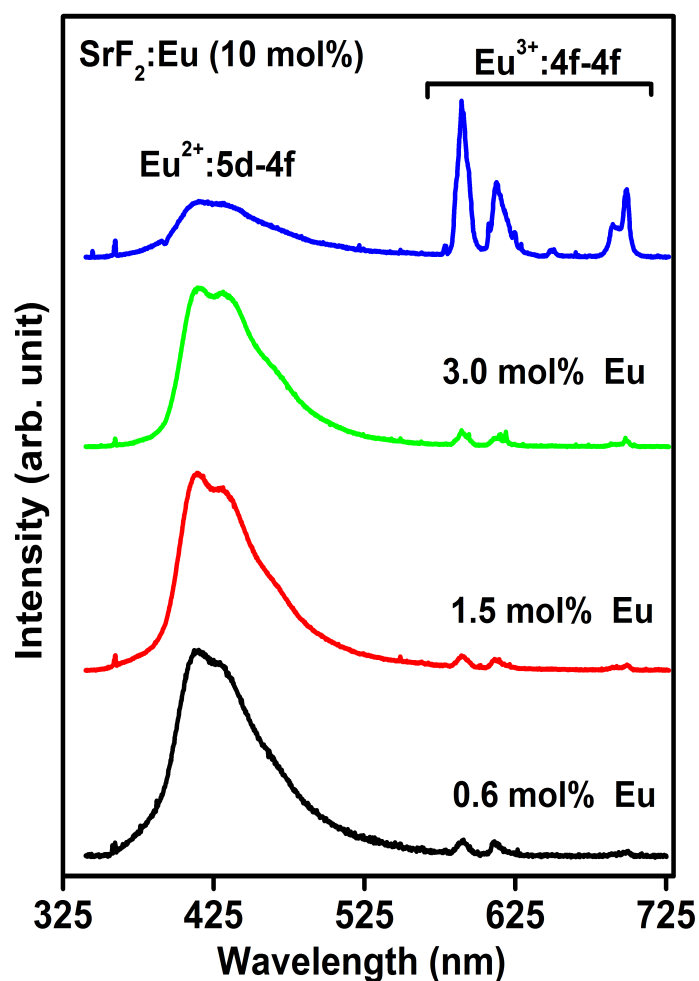


Fig. 5.4: PL spectra of Eu doped SrF_2 using the He-Cd laser system with a 325 nm excitation wavelength.

Eu concentration (mol%)	Intensity ratio ($\text{Eu}^{3+}/\text{Eu}^{2+}$)
0.6	0.083
1.5	0.095
3.0	0.111
10.0	2.743

Table 5.2: Calculated intensity ratio between $\text{Eu}^{3+}/\text{Eu}^{2+}$ as a function of Eu concentrations. The emission intensity of ${}^5\text{D}_0 \rightarrow {}^7\text{F}_1$ transition was taken for Eu^{3+} and 5d-4f transition centered at 415 nm for Eu^{2+} .

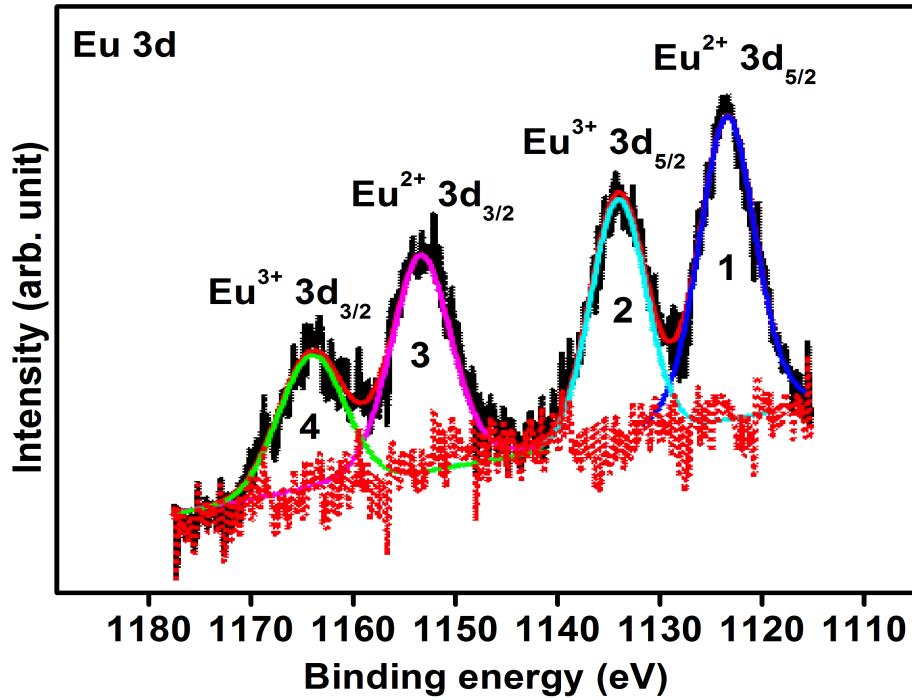
Eu^{2+} was calculated and shown in table 5.2. It was also observed that the intensity ratio increased with increasing Eu concentrations in the SrF_2 matrix. The increase of the Eu^{3+} emission intensity with an increase in the Eu concentration can be attributed to different factors: (1) an increase in the Eu^{3+} ions ratio; (2) the presence of energy transfer from Eu^{2+} ions to Eu^{3+} ions; and (3) a change in the local symmetry around the Eu^{3+} ions. The first possibility gives rise to a decrease in the number of Eu^{2+} ions. Whereas, in the case where the energy transfer takes place from Eu^{2+} to Eu^{3+} the $\text{Eu}^{3+}/\text{Eu}^{2+}$ ratio should remain constant. In both cases, the intensity emission of Eu^{2+} ($4f^65d^1-4f^7$ transition) should be decreasing with increasing the Eu concentrations.

Local symmetry adjustment through the presence of Eu^{2+} ions can also be verified by examining the intensity ratio of the $^5\text{D}_0 \rightarrow ^7\text{F}_1$ and $^5\text{D}_0 \rightarrow ^7\text{F}_2$ transitions. Since the $^5\text{D}_0 \rightarrow ^7\text{F}_2$ transition is sensitive to the local symmetry while the $^5\text{D}_0 \rightarrow ^7\text{F}_1$ is not. The difference in the intensity ratio between the $^5\text{D}_0 \rightarrow ^7\text{F}_1$ and $^5\text{D}_0 \rightarrow ^7\text{F}_2$ transitions (which is constant for all Eu concentration) for the measured samples (see fig. 5.3) correlates with where there is no variation in the local crystal symmetry. In this study, we proposed that there was an energy transfer between the two ions and these PL results showed that this could be true.

5.3.3 XPS analysis

XPS analysis was performed to investigate if Eu^{3+} and Eu^{2+} ions or maybe a defect could be found that could be responsible for the tunable luminescence of the Eu doped SrF_2 . Fig. 5.5 shows the peak deconvolution for the Eu 3d high resolution XPS peaks. The deconvolution parameters are summarized in table 5.3. The fixed parameters namely the energy separation and the intensity ratio between the photo-peaks 3, 4 and 1, 2 are underlined. In the deconvolution procedure, all the Gaussian percentages were assumed to have a combined Gaussian-Lorentzian shape. The four peaks as seen from fig. 5.5 can be attributed to Eu^{2+} and Eu^{3+} spin-orbit splitting $3d_{5/2}$ and $3d_{3/2}$ core level, respectively [28, 28–30]. Thus, the recorded Eu 3d XPS spectrum shows both the valence states of Eu (Eu^{2+} and Eu^{3+}) [3, 4, 30].

Fig. 5.6 shows a broad high resolution XPS peak for the Sr 3d and Eu 4d as the

Fig. 5.5: Eu 3d high resolution XPS spectrum of Eu doped SrF₂.

peak label	peak position (eV)	ΔE (eV)	relative to	intensity ratio	FWHM (eV)	Gauss (%)	interpretation
1	1123.36	-	-	-	6.45	80	Eu ²⁺ 3d _{5/2}
2	1133.05	-	-	-	7.35	100	Eu ³⁺ 3d _{5/2}
3	1153.22	29.96	1	0.66	6.45	80	Eu ²⁺ 3d _{3/2}
4	1163.01	29.96	2	0.66	7.35	100	Eu ³⁺ 3d _{3/2}

Table 5.3: Deconvolution parameters for Eu 3d from fig. 5.5. The energy separations ΔE and intensity ratio were fixed and are underlined.

energy ranges overlap. Peak deconvolution showed four individual peaks. Two of these peaks are assigned to Sr 3d in SrF₂ that originates from the spin-orbit splitting 3d_{5/2} (133.52 eV) and 3d_{3/2} (135.31 eV) [31]. It can clearly be seen that the other two peaks (labelled ⁷D and ⁹D) contradict the 3/2 intensity ratio expected when spin-orbit splitting is present. Therefore, the two peaks ⁷D and ⁹D are associated with the Eu 4d_{5/2} multiplet splitting due to the interaction with the 4f energy level, rather

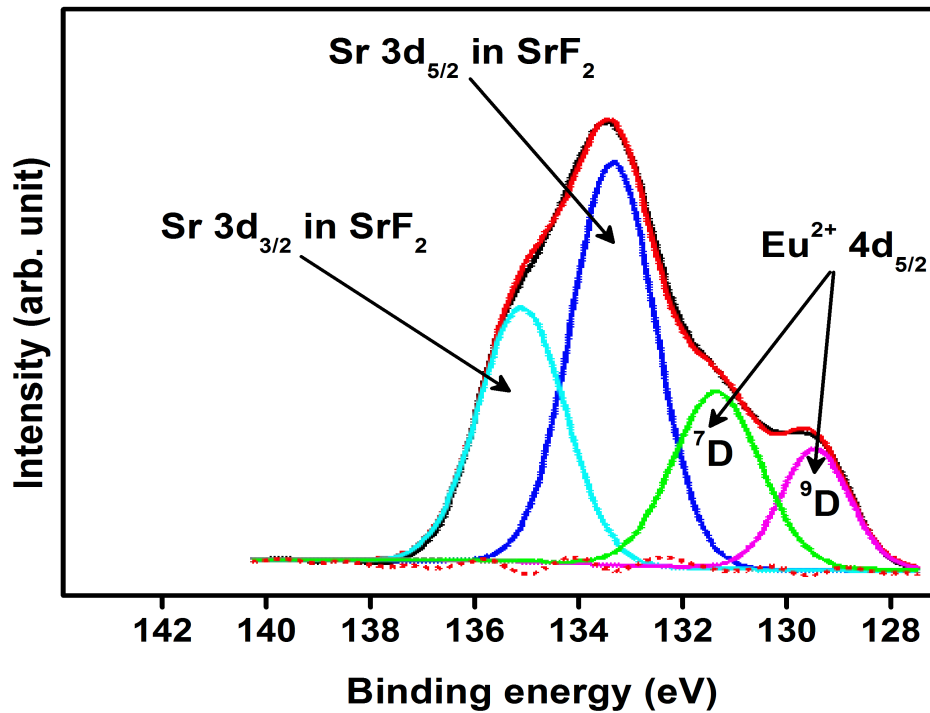


Fig. 5.6: High resolution XPS peak of Sr 3d and Eu 4d in SrF₂.

than spin-orbit splitting. Multiplet interaction arises between unpaired electrons (e.g. Eu²⁺ 4d¹⁰4f⁷) in the photoelectric process [28]. This process occurs when an electron from the 4d level is removed by photoionization and then a coupling between the unpaired electrons in the 4d energy level and the unpaired in the 4f energy level occurs. This can create a number of final states that can be seen in the spectrum. Multiplet splitting is more effective in a sub-shell with the same principle quantum number as the partially filled sub-shell [28]. This is because the overlap between such orbitals is more significant. Such interaction is therefore more active in the Eu 4d photo-peak than in the Eu 3d peak. The Eu 4d multiplet interactions normally show a strong 4d-4f interaction and a much weaker 4d spin-orbit splitting [2, 28]. Therefore, the 4d spectra cannot be separated into their 4d_{5/2} and 4d_{3/2} spin-orbit splitting components.

5.3.4 TOF-SIMS analysis

Further investigation to identify the presence of Eu oxidation states was performed by TOF-SIMS. It is worth mentioning that the SrF₂ nano-phosphor was doped with

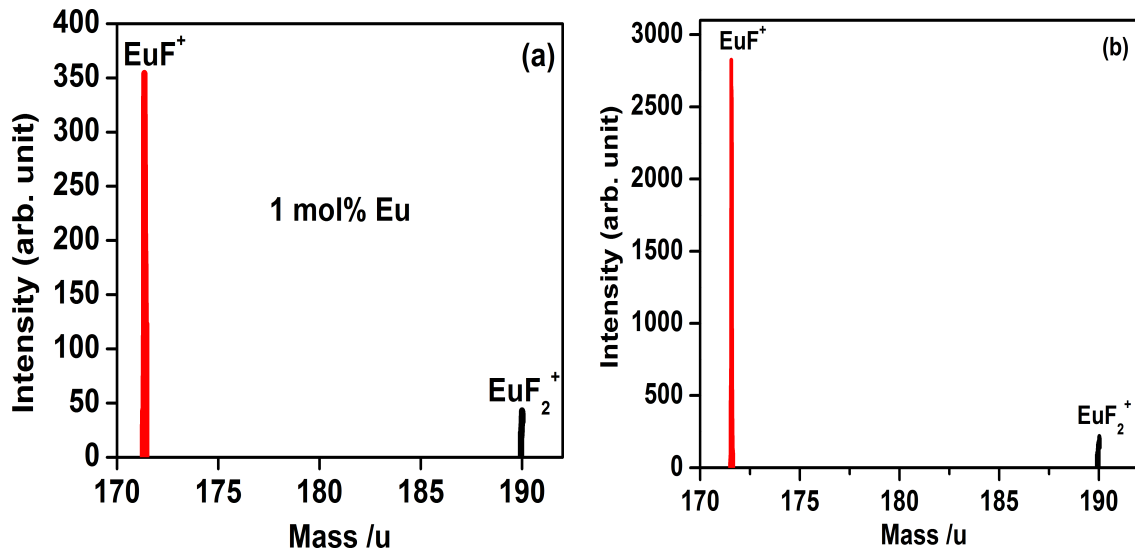


Fig. 5.7: TOF-SIMS spectra showing EuF^+ and EuF_2^+ peaks at different concentrations of Eu doped SrF_2 nanophosphor (a) 1.0 mol% Eu and (b) 10.0 mol% Eu.

Eu in the +3 oxidation state, Eu^{3+} . Based on the PL laser emission and XPS results of the phosphor, it can be seen that Eu dopant exhibited both oxidation state, Eu^{2+} and Eu^{3+} . In fact, it is very difficult to differentiate between the two oxidation states using TOF-SIMS, but the parallel detection capability of the technique gives rise to full molecular and isotopic characterization of the elemental chemistry [4]. The Eu oxidation states were detected by the EuF^+ and EuF_2^+ species, representing the Eu^{2+} and Eu^{3+} , respectively. Fig. 5.7 shows the mass spectra in the positive polarity mode where the peaks for EuF^+ and EuF_2^+ can be clearly observed. The peaks were detected at $m/z = 171.36$ and 190.05 corresponding to EuF^+ and EuF_2^+ respectively, in both concentrations. The count rate of EuF_2^+ in both the high and low concentration was low compared to that of EuF^+ . This also demonstrates that the $\text{Eu}^{2+}/\text{Eu}^{3+}$ ion ratio remained constant with increasing Eu concentration. These results therefore suggested that the energy transfer between the two ions is highly possible.

5.3.5 Luminescence decay curves

Fig. 5.8(a) shows the relative PL intensity of the Eu^{2+} ion while irradiated with the YAG laser at a 355 nm excitation wavelength. It can be seen that the PL intensity

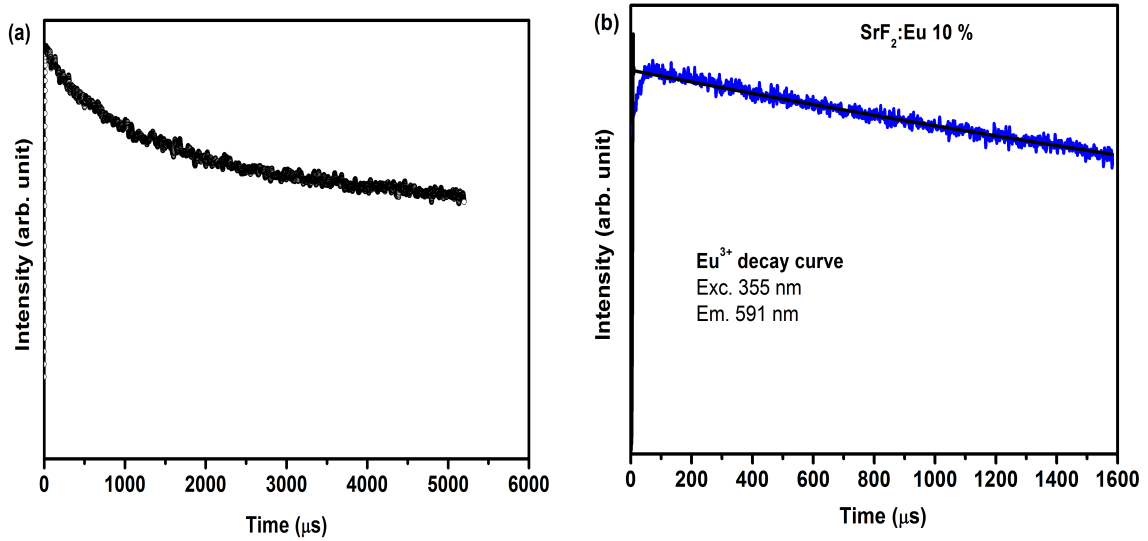


Fig. 5.8: (a) Relative PL intensity of the Eu^{2+} emission band (416 nm) with time and (b) decay curves for the ${}^5\text{D}_0 \rightarrow {}^7\text{F}_1$ transition (591 nm) of the Eu^{3+} .

of the sample rapidly decreased with increasing the irradiating time of the laser. In other words, the sample degraded to form non-luminescent species with the Eu^{2+} when irradiated by the YAG laser and therefore prevented us from measuring the Eu^{2+} decay time. This result is an indication that the molecular structure of the Eu^{2+} doped SrF_2 system was completely changed when exposed to the YAG laser. The sample was also exposed to oxygen in the open air during laser irradiation and this condition is also known to destroy the molecular structure of some compounds [32–35].

The luminescence decay curves of the 591 nm emission (${}^5\text{D}_0 \rightarrow {}^7\text{F}_1$ transition) of the Eu^{3+} ions in SrF_2 were also measured and can be seen in fig. 5.8(b). The decay curve for the Eu^{3+} ion can be fitted approximately by a single exponential function with a lifetime of 6.4 ms. This result is also in agreement with values reported in literature [36]. The single exponential decay curve was measured for 10 mol% of Eu^{3+} doped SrF_2 , which proved that there is no interaction between the Eu^{3+} ions.

The proposed energy transfer mechanism from the excited 4f5d states of Eu^{2+} to the Eu^{3+} ions is schematically shown in fig. 5.9. The energy absorbed when the system is excited at 325 nm is most likely transferred by non-radiative energy transfer via energy migration, from the Eu^{2+} ($4f^65d$) to Eu^{3+} ions. This process can enhance the emission

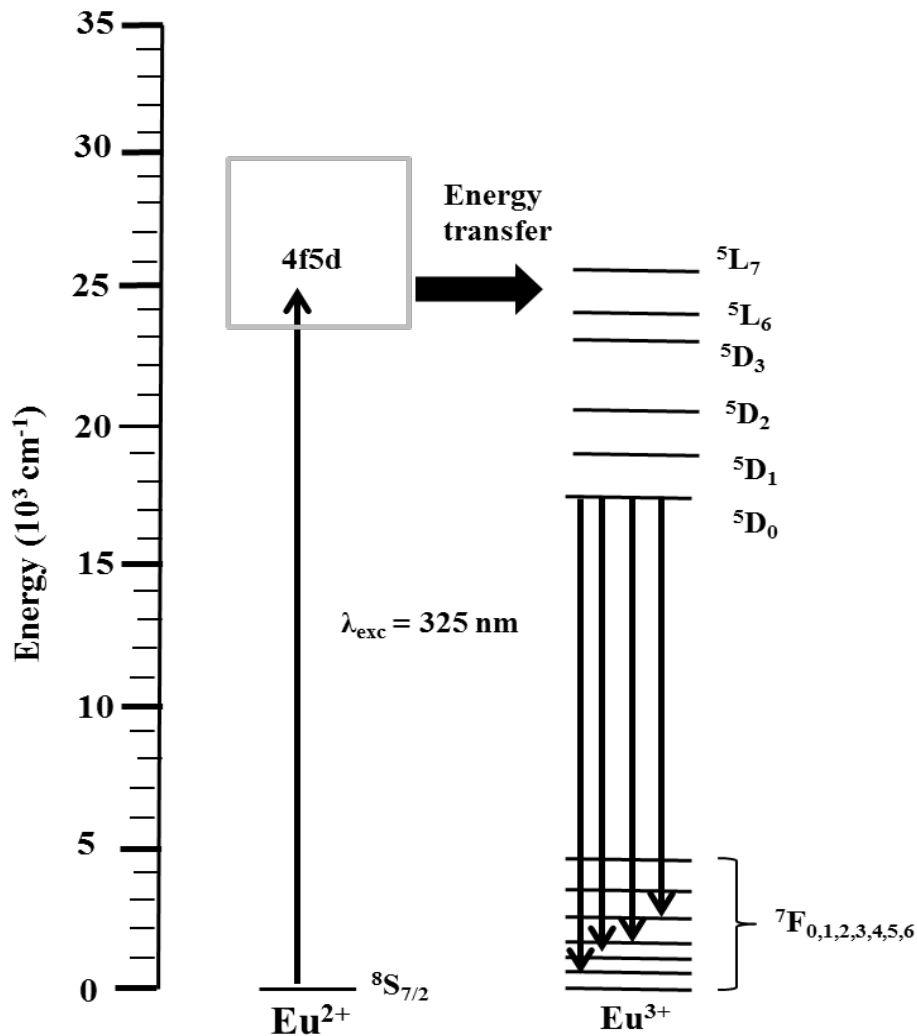


Fig. 5.9: Schematic diagram of the proposed energy transfer mechanism between Eu^{2+} and Eu^{3+} ions.

of the Eu^{3+} ions. Therefore the absorption and emission of the Eu^{3+} ions can strongly be enhanced due to the presence of both the Eu oxidation states. This energy transfer mechanism will result in a subsequent positive effect on spectral conversion.

The most interesting result of this study is that concentration quenching did not take place between the Eu^{3+} ions at high concentration as observed previously by Y. Jin et al. [17]. It is well known that the transition 4f-4f of the Eu^{3+} ion is parity forbidden and therefore, it has a low absorption cross-section. On the contrary, the 4f-5d transition of Eu^{2+} is a fully allowed transition. This makes the Eu^{2+} ions absorb most of the incident energy and therefore transfer their energy to the Eu^{3+} ions. The light yield

is then much more significant in the presence of both the Eu oxidation states than the Eu^{3+} singly doped systems. The idea of enhancing the excitation cross-section of Eu^{3+} has been reported by Z. Xia et. al. [37] for YVO_3 phosphor co-doped with Bi^{3+} . In their study the Bi^{3+} ions enhanced the emission intensities of ${}^5\text{D}_0 \rightarrow {}^7\text{F}_2$ electric dipole transition of Eu^{3+} at 615 nm upon 365 nm excitation. Results from our study showed that the as-prepared SrF_2 doped with Eu ions contained both the Eu oxidation states. Spectral conversion from 325-550 to 570-710 nm can be achieved at high doping concentrations, but the Eu^{2+} ion was unstable under the YAG laser irradiation. This would therefore make the sample not suitable for spectral conversion applications.

5.4 Conclusions

As-prepared $\text{SrF}_2:\text{Eu}$ nano-phosphors were successfully synthesised with the hydrothermal technique. The average crystalline size calculated using Scherrer's equation was found to be in nano-metre scale. The surface morphology of the samples was characterised by SEM. The samples composition consisted of spherical particles with a diameter of around 1.5-2 μm . From PL and XPS results, it was found that Eu was in both the Eu^{2+} and Eu^{3+} valance states. It is demonstrated that the presence of both Eu oxidation states significantly enhanced the absorption response of Eu^{3+} UV excitation. The results indicated that Eu concentration of more than 5 mol% of Eu were beneficial for improving fluorescence emission of Eu^{3+} and conversion efficiency under the broadband excitation. TOF-SIMS results suggested that the energy transfer from Eu^{2+} to Eu^{3+} is likely to be dominant. The Eu^{2+} ion was however found to be unstable when irradiated by the YAG laser. The Eu^{2+} ion's PL emission intensity rapidly decreased with time and this result make this $\text{SrF}_2:\text{Eu}$ nano-phosphor an unsuitable candidate for applications such as a downshifting layer to enhance the response of photovoltaic cells.

References

- [1] R. Vercaemst, D. Poelman, L. Fiermans, R. L. Van Meirhaeghe, W. H. Laflere and F. Cardon, *J. Electron. Spectrosc. Relat. Phenom.*, **74** (1995) 45-56.
- [2] C. Caspers, M. Muller, A. X. Gray, A. M. Kaiser, A. Gloskovskii, C. S. Fadley, W. Drube and C. M. Schneider, *Phys. Status Solidi RRL*, (2011) 1-3.
- [3] I. M. Nagpure, S. J. Dhoble, M. Mohapatra, V. Kumar, S. S. Pitale, O. M. Ntwaeaborwa, S. V. Godbolc and H. C. Swart, *J. Alloys Compd.*, **509** (2011) 2544-2551.
- [4] H. C. Swart, I. M. Nagpure, O. M. Ntwaeaborwa, G. L. Fisher and J. J. Terblans, *Opt. Express*, **20** (2011) 17119-17125.
- [5] F. H. Su, W. Chen, K. Ding and G. H. Li, *J. Phys. Chem. A*, **112** (2008) 4772-4777.
- [6] S. P. Kowalczyk, N. Edelstein, F. R. McFeely, L. Ley and D. A. Shirley, *Chem. Phys. Lett.*, **29** (1974) 491-495.
- [7] W. Burian, J. Szade, T. O'Keevan and Z. Celinski, *Phys. Status Solidi B*, **241** (2004) R15-R18.
- [8] M. Dejneka, E. Snitzer and R. E. Riman, *J. Lumin.*, **65** (1995) 227-245.
- [9] Y. Hu, W. Zhuang, H. Ye, D. Wang, S. Zhang and X. Huang, *J. Alloys Compd.*, **390** (2005) 226-229.
- [10] Y. Li, Y. Chang, Y. Lin, Y. Chang and Y. Lin, *J. Alloys Compd.*, **439** (2007) 367-375.
- [11] X. Huang, S. Han, W. Huang and X. Liu, *Chem. Soc. Rev.*, **42** (2013) 173-201.
- [12] E. Klampaftis, D. Ross, K. R. McIntosh and B. S. Richards, *Sol. Energy Mater. Sol. Cells*, **93** (2009) 1182-1194.
- [13] O. Moudam, B. C. Rowan, M. Alamiry, P. Richardson, B. S. Richards, A. C. Jones and N. Robertson, *Chem. Commun.*, (2009) 6649-6651.

- [14] E. Klampaftis, M. Congiu, N. Robertson and B. S. Richards, *IEEE J. Photovolt.*, **1** (2011) 29-36.
- [15] P. Dorenbos, *J. Lumin.*, **104** (2003) 239-260.
- [16] B. M. Van der Ende, L. Aarts and A. Meijerink, *Adv. Mater.*, **21** (2009) 3073-3077.
- [17] Y. Jin, W. Qin and J. Zhang, *J. Fluorine Chem.*, **129** (2008) 515-518.
- [18] S. Kurosawa, Y. Yokota, T. Yanagida and A. Yoshikaw, *Phys. Status Solidi C*, **9** (2012) 2275-2278.
- [19] J. Peng, S. Hou, X. Liu, J. Feng, X. Yu, Y. Xing and Z. Su, *Mater. Res. Bull.*, **47** (2012) 328-332.
- [20] N. Rakov, R. B. Guimaraes, D. F. Franceschini and G. S. Maciel, *Mater. Chem. Phys.*, **135** (2012) 317-321.
- [21] C. Oprea, V. Ciupina and G. Prodan, *Romanian J. Phys.*, **53** (2008) 223-230.
- [22] F. Wang, Y. Han, C. S. Lim, Y. Lu, J. Wang, J. Xu, H. Chen, C. Zhang, M. Hon and X. Liu, *Nature*, **463** (2010) 1061-1065.
- [23] S. Sasidharan, A. Jayasree, S. Fazal, M. Koyakutty, S. V. Nair and D. Menon, *Biomater. Sci.*, **1** (2013) 294-305.
- [24] S. Ugemugen, A. M. Muke, A. A. Muley, C. S. Gayner and S. V. Moharil, *Int. J. Knowl. Eng.*, **3** (2012) 67-68.
- [25] V. Sudarsan, F. C. J. M. van Veggel, R. A. Herring and M. Raudsepp, *J. Mater. Chem.*, **15** (2005) 1332-1342.
- [26] J. Labegueriea, P. Gredina, M. Mortierb, G. Patriarchec and A. de Kozaka, *Z. Anorg. Allg. Chem.*, **632** (2006) 1538-1543.
- [27] L. L. Noto, S. S. Pitale, M. A. Gusowki, J. J. Terblans, O. M. Ntwaeaborwa and H. C. Swart, *Powder Technol.*, **237** (2013) 141-146.

-
- [28] R. Vercaemst, D. Poelman, R. L. Van Meirhaeghe, L. Fiermans, W. H. Laflere and F. Cardon, *J. Lumin.*, **63** (1995) 19-30.
- [29] D. Lu, M. Sugano, X. Y. Sun and W. Su, *Appl. Surf. Sci.*, **242** (2005) 318-325.
- [30] J. Zhang, M. Yang, H. Jin, X. Wang, X. Zhao, X. Liu and L. Peng, *Mater. Res. Bull.*, **47** (2012) 247-252.
- [31] R. P. Vasquez, *Surf. Sci. Spectra*, **1** (1994) 24-28.
- [32] E. Kin, T. Fukuda, N. Kamata, H. Ohara, T. Yokoo and N. Kijima, *J. Light and Vis. Env.*, **33** (2009) 82-87.
- [33] T. Fukuda, S. Kato, S. Akiyama, Z. Honda and N. Kamata, *Opt. Mater.*, **35** (2012) 5-11.
- [34] M. Duvenhage, H. C. Swart, O. M. Ntwaeaborwa and H. G. Visser, *Opt. Mater.*, **35** (2013) 2366-2371.
- [35] H. C. Swart, J. J. Terblans, O. M. Ntwaeaborwa, R. E. Kroon and B. M. Mothudi, *Physica B*, **407** (2012) 1664-1667.
- [36] X. Wang, J. Chen, J. Li and H. Guo, *J. Non-Cryst. Solids*, **357** (2011) 2290-2293.
- [37] Z. Xia, D. Chen, M. Yang and T. Ying, *J. Phys. Chem. Solids*, **71** (2010) 175-180.

Chapter 6

Surface characterization and an efficient energy transfer in Ce^{3+} co-doped $\text{SrF}_2:\text{Eu}$ downshifting nano-phosphor

The effect of Ce^{3+} ion on the structure and optical properties of $\text{SrF}_2:\text{Eu}$ downshifting nano-phosphor is outlined in this chapter.

6.1 Introduction

SrF_2 is one of the most widely used optical materials because of its interesting luminescent, optical and physical properties. The photoluminescence properties of SrF_2 doped by Ln^{3+} ions have been extensively investigated in which charge compensation is required when Ln^{3+} ions substitute Sr^{2+} cation. This gives to a rich multisites structure. It has therefore been considered as a good phosphor host material that can be doped by a number of lanthanide ions for various luminescent applications [1–4]. SrF_2 host material doped with Ce^{3+} is extensively being investigated specifically for light amplification [5, 6]. Some of these light amplification studies proposed that the $\text{SrF}_2:\text{Ce}^{3+}$ phosphor material could be a promising scintillator [5]. Shendrik et al. [5] reported efficient scintillation light output of $\text{SrF}_2:\text{Ce}^{3+}$ with high temperature stability suggesting that this material can be applied in well-logging scintillation detectors. They have also reported that the optimal Ce^{3+} doping level for maximum luminescence was 0.3 mol% if prepared by the Stockbarger method. Ce^{3+} ions in SrF_2 showed a fully allowed broad band 4f-5d transition [5] and this transition strongly absorbs UV radiation that results in a high absorption coefficient.

In our previous investigation of $\text{SrF}_2:\text{Eu}$ nano-phosphors, chapter 5, Eu was found to exhibit two oxidation states (Eu^{2+} and Eu^{3+}) and the presence of both the oxidation states ions in the SrF_2 host greatly enhanced the emission intensity of Eu^{3+} at high concentrations. In this chapter, the effect of the Ce^{3+} ion on the structure and optical properties of $\text{SrF}_2:\text{Eu}$ downshifting nano-phosphor is outlined. Ce^{3+} singly and

co-doped Eu in SrF₂ were prepared by using the hydrothermal method. The phosphors were characterized by different surface and optical characterization techniques. Different luminescent aspects were investigated to see if the Ce³⁺ ion can efficiently enhance the emission intensity of Eu ions in the SrF₂ host.

6.2 Experimental section

SrF₂:Ce³⁺, Eu were synthesised by the hydrothermal techniques. Eu(NO₃)₃.5H₂O and Ce(NO₃)₃.6H₂O were used as sources for the Eu and Ce dopants, respectively. The details description of the hydrothermal process was described in chapter 5.

The structure of the nano-phosphors powder were characterized by XRD (Bruker Advance D8 diffractometer with Cu K α radiation ($\lambda = 0.154$ nm)). Auger spectra were collected with a PHI 700 Scanning Auger Nanoprobe equipped with a scanning Auger microscope (SAM). The field emission electron gun used for the SAM analyses was set at: 2.34 A filament current; 4.35 kV extractor voltage and 381.4 μ A extractor current. With these settings a 25 kV, 10 nA electron beam was obtained for the Auger analyses. The electron beam diameter was about 10 nm. An IonTof time of flight secondary ion mass spectrometer instrument equipped with a Bi primary ion source was used to characterize the nano-phosphor materials for their chemical composition and dopants distribution. In spectroscopy mode, the system equipped with a DC current of 30 nA and a pulsed current of 1 pA at 30 kV with a heating current of 2.95 A and emission current of 0.8 μ A was used. High resolution XPS was obtained with a PHI 5000 Versaprobe system. A low energy Ar⁺ ion gun and low energy neutralizer electron gun were used to minimize charging on the surface. A 100 μ m diameter monochromatic Al K α x-ray beam ($h\nu = 1486.6$ eV) generated by a 25 W, 15 kV electron beam was used to analyze the different binding energy peaks. The pass energy was set to 11 eV giving an analyzer resolution ≤ 0.5 eV. Multipack version 8.2 software was utilized to analyze the spectra to identify the chemical compounds and their electronic states using Gaussian-Lorentz fits. PL spectra were collected using a Cary Eclipse fluorescence spectrophotometer equipped with a xenon lamp and also with a He-Cd laser PL system

with a 325 nm excitation wavelength. Luminescence decay curves were recorded by using a NanoLED with a 335 nm excitation wavelength and repetition rate of 1 MHz. All measurements were performed at room temperature.

6.3 Results and discussion

6.3.1 Structure and surface analysis

6.3.1.1 XRD analysis

Fig. 6.1 shows the XRD patterns of un-doped and doped SrF₂ as well as the standard data for SrF₂ crystal from card 00-086-2418. Doping with Ce- or Eu ions as well as the co-doped systems result in a small shift to higher angles with comparison to the un-doped sample and the standard data. This can be attributed to the radius difference between Eu (Eu²⁺ is 0.125 nm, Eu³⁺ is 0.107 nm), Ce³⁺ (0.114 nm) and Sr²⁺ (0.126 nm) ions, which confirms that Eu- and Ce ions are successfully incorporated into the SrF₂ lattice. It should be mentioned that doping with Eu- and Ce ions (up to 10 mol%) does not change the structure of the SrF₂ host in this study. The calculated SrF₂ lattice parameter is found to be 5.785 ± 0.005 Å and this agreed well with the reported value of (5.7996 ± 0.0001) Å [7].

The estimated average crystallite size (**S**) for pure and doped SrF₂ is calculated by using the diffraction peaks and Scherrer's equation [8], $\mathbf{S} = 0.9\lambda/\beta \cos \theta$. λ is the wavelength of the x-rays (0.154 nm) and β is the full-width at half maximum of the x-ray peak at the Bragg angle θ . The average crystallite size of the pure SrF₂ was found to be 7.6 nm. The XRD peaks broaden with increasing the dopants ions (see fig. 6.1). The broadening of the XRD peaks were also observed by other groups [9, 10]. H. A. A. Seed Ahmed et al. [9] attributed the XRD peak broadening to impurity broadening. Whereas, F. Wang et al. [10] assigned the XRD peak broadening to reduction in the nano-particle size of the matrix. In our previous investigation of Eu doped SrF₂ samples, we assigned the XRD broadening as a result of a decrease in particle size of the matrix, which agreed well with F. Wang et al. [11]. Therefore, in the current study we can also assign these

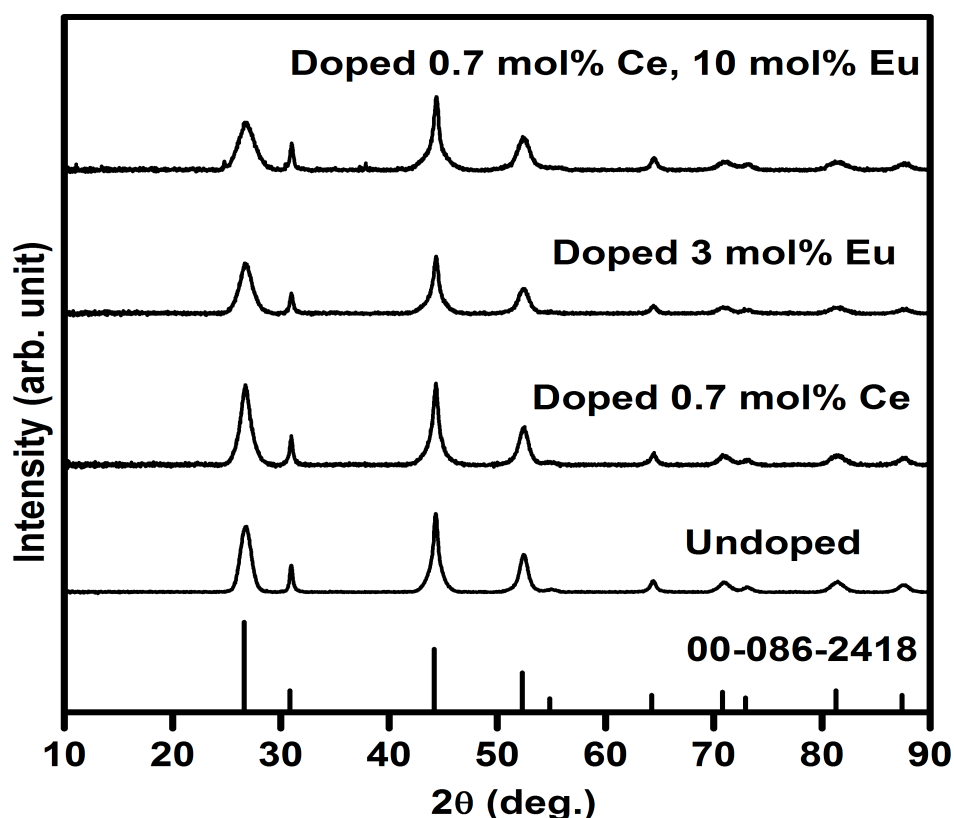


Fig. 6.1: XRD patterns of pure and doped SrF_2 crystal.

peaks' broadening to reduction in particle size of the matrix. The particle size reduced up to 3.9 nm for SrF_2 sample that doped with 0.7 mol% Ce^{3+} and 10 mol% Eu.

6.3.1.2 AES analysis

An Auger profile of Ce and Eu co-doped SrF_2 was done to identify the samples composition. The Auger spectrum of the $\text{SrF}_2:\text{Ce}^{3+}$, Eu is presented in fig. 6.2. The Auger peaks at 71, 1515, 1644 and 1713 eV are assigned to Sr while the F peak is situated at 656 eV [12]. The Auger spectrum not only confirmed the formation of the host matrix, but also showed the presence of the dopants. The Eu peaks were at 111, 142, 853 and 985 eV, while the peak at 89 eV corresponds to Ce. In addition C and O were also observed. The C contamination is attributed to adventitious hydrocarbons and the oxygen is considered to be a common impurity in a fluoride compound [12, 13]. The presence of the oxygen in the sample did not change the structure of the sample

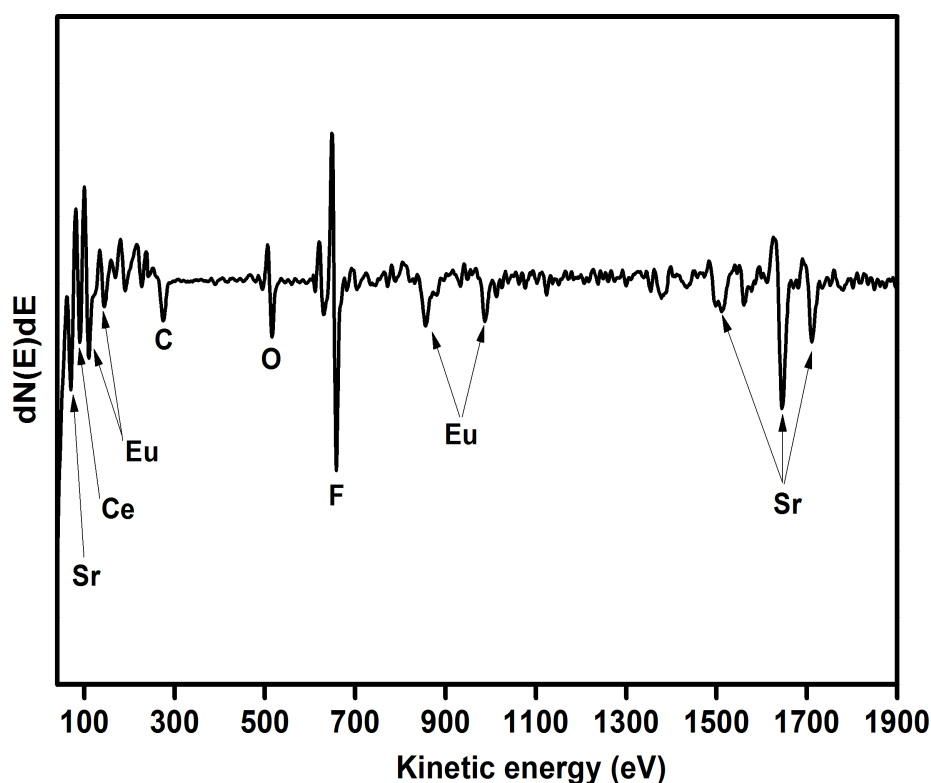


Fig. 6.2: Auger spectrum of Ce and Eu co-doped SrF_2 .

(see fig. 6.1). Therefore, the oxygen contamination was due to adventitious impurity species in the surface rather than oxygen impurity in the SrF_2 matrix.

6.3.1.3 XPS analysis

XPS measurements have been done in order to investigate the chemical composition and bonding state of the $\text{SrF}_2:\text{Ce},\text{Eu}$ phosphor powders. A higher dopant concentration (5 mol% for both Eu and Ce) was used in order to obtain a reasonable signal from the dopants. Fig. 6.3 shows the peak fits for the (a) Sr 3d, (b) F 1s, (c) Eu 3d and (d) Ce 3d high resolution XPS peaks. The results also confirmed the presence of the host matrix elements (Sr and F) as well as the dopants (Eu and Ce) to their corresponding binding energies. During the peaks fit procedure, the C 1s peak at 284.8 eV was taken as a reference for all charge shift corrections. This is done because the C 1s peak resulted from hydrocarbon contamination and its binding energy generally remains constant, irrespective to the chemical state of the sample. In addition to that, all the Gaussian

percentages were assumed to have a combined Gaussian-Lorentzian shape. The high resolution XPS peak for the Sr 3d showed two individual peaks. These two peaks are assigned to Sr 3d in SrF₂ that originate from the spin-orbit splitting 3d_{5/2} (133.5 eV) and 3d_{3/2} (135.3 eV), while the F 1s peak is situated at 684.7 eV. The spin-orbit splitting of Sr 3d is about 1.78 eV, it is in a good agreement with reported value of 1.75 eV [14].

The peak deconvolution for the Eu 3d high resolution XPS peaks are shown in fig. 6.3(c). The 3d level of Eu ion is composed of four peaks. These four peaks can be attributed to Eu³⁺ and Eu²⁺ spin-orbit splitting 3d_{5/2} and 3d_{3/2} core level, respectively [15–18]. The spin-orbit splitting for both oxidation states Eu³⁺ and Eu²⁺ is about 29.96 eV. The Eu 3d results showed good agreement with our previous XPS investigation of SrF₂:Eu phosphors powder where Eu composed of its two oxidation states (Eu²⁺ and Eu³⁺) [11].

The Ce 3d high resolution peak is shown in fig. 6.3(d). The strong peaks correspond to the photoemission from the Ce³⁺ 3d state. Due to the spin-orbit interaction, the Ce³⁺ 3d photoemission peak consisted of two peaks that are assigned to the 3d_{3/2} and 3d_{5/2} peaks with 4f¹ final states, with an intensity ratio $I(3d_{5/2})/I(3d_{3/2}) = 3/2$ [18–20]. The spin-orbit splitting value (~ 18.15 eV) is in good agreement with the estimated value (~ 18.10 eV). The energy peaks labelled SD are due to the strong Coulomb interaction between photoemission in the 3d level and electrons located near the Fermi level. These peaks originate from the screening of the 3d level by valence band electrons to the 4f states [20]. This is possible due to hybridization of the Ce 4f level with the conduction band states [20]. In the photoemission nomenclature, these peaks are a result from what is called, shake-down process [18]. The 3d shake-down peaks behave the same as the 3d spin-orbit splitting peaks but they are a result from the 3d⁹f² final state. Therefore, the SD peaks can be assigned to the 3d_{3/2} and 3d_{5/2} XPS peaks with 4f² final states and this is in accordance with previous work done in Ce [19, 20]. The shoulder peaks marked as A is related to the F KLL Auger electron peak. The XPS peak positions, area distributions and chemical bonding for all the peaks in as-prepared SrF₂:Ce,Eu are tabulated in table 6.1.

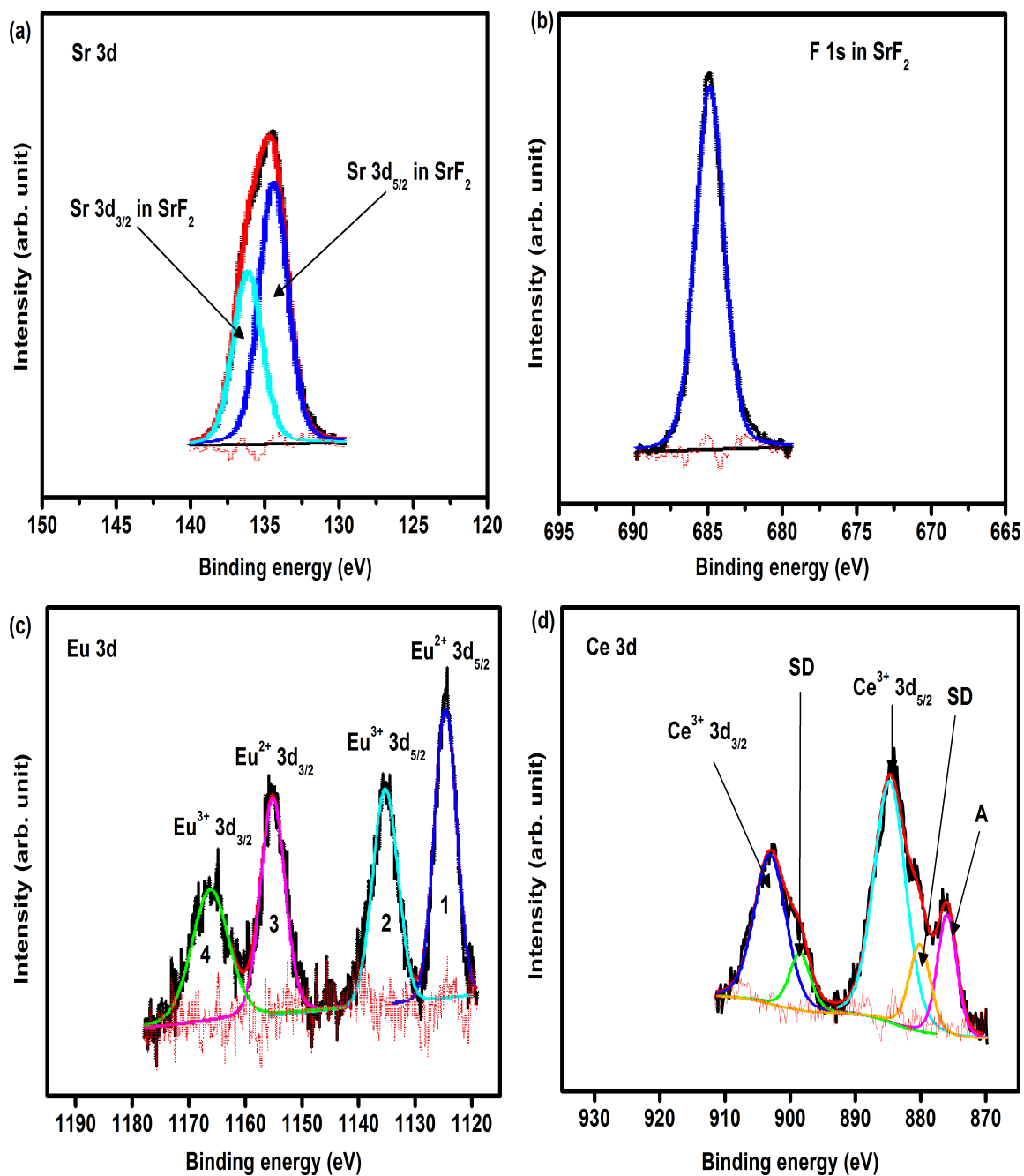


Fig. 6.3: High resolution XPS peaks of (a) Sr 3d, (b) F 1s, (c) Eu 3d, and (d) Ce 3d for SrF₂:Ce, Eu phosphors powder.

Element	B.E (± 0.1 eV)	Area distribution	Interpretation
F1s	7684.7	2688	F in SrF ₂
Sr3d	133.5	1986	Sr 3d _{5/2} in SrF ₂
	135.3	1311	Sr 3d _{3/2} in SrF ₂
Eu3d	1123.3	1613	Eu ²⁺ 3d _{5/2} in fluoride
	1133.05	1372	Eu ³⁺ 3d _{5/2} in fluoride
	1153.2	1064	Eu ²⁺ 3d _{3/2} in fluoride
	1163.0	905	Eu ³⁺ 3d _{3/2} in fluoride
Ce3d	880.3	1296	shake-down satellite
	884.8	5141	Ce ³⁺ 3d _{5/2} in fluoride
	898.5	855	shake-down satellite
	903.0	3393	Ce ³⁺ 3d _{3/2} in fluoride
	8761	1592	FKL ₁ L ₁ Auger electron peak

Table 6.1: XPS peak position, area distribution and chemical bonding of as-prepared SrF₂:Ce,Eu phosphors powder.

6.3.1.4 TOF-SIMS analysis

The compositional identification, the presence of the dopant and the doping distribution in the SrF₂ crystal lattice were also investigated by using TOF-SIMS. Fig. 6.4 shows the mass spectra of the sample in positive and negative polarity modes. It is worth mentioning that the nanophosphor matrix only consists of Sr⁺ and F⁻ ions in the form of SrF₂. In TOF-SIMS, the Sr⁺ can be detected in positive polarity mode while F⁻ in negative polarity mode. Fig. 6.4(a) shows a very strong peak for ⁸⁸Sr in the positive polarity mode and the ¹⁰⁷SrF peak, while the ¹⁹F peak together with C and O peaks (detected in the negative polarity mode) are shown in fig.6.4(c). The count rates of both the Sr and F peaks were high, which confirm the formation of the host matrix. It is mentioned previously that the presence of C and O is due to adventitious impurity species in the surface rather than oxygen impurity in the SrF₂ matrix. These results not only confirm the formation of the SrF₂ matrix, but also the presence of

the dopants in the material. Fig.6.4(b) presents the mass spectra in positive polarity mode where the ^{140}Ce isotope and ^{153}Eu isotope including ^{159}CeF and ^{172}EuF peaks can clearly be seen. The ^{140}Ce signal was comparatively low, which is due to a very low doping concentration of Ce (0.7 mol%) [21]. The peak position of ^{153}Eu was situated at $m/z = 152.918$ amu, which is in agreement with the value reported in literature [21].

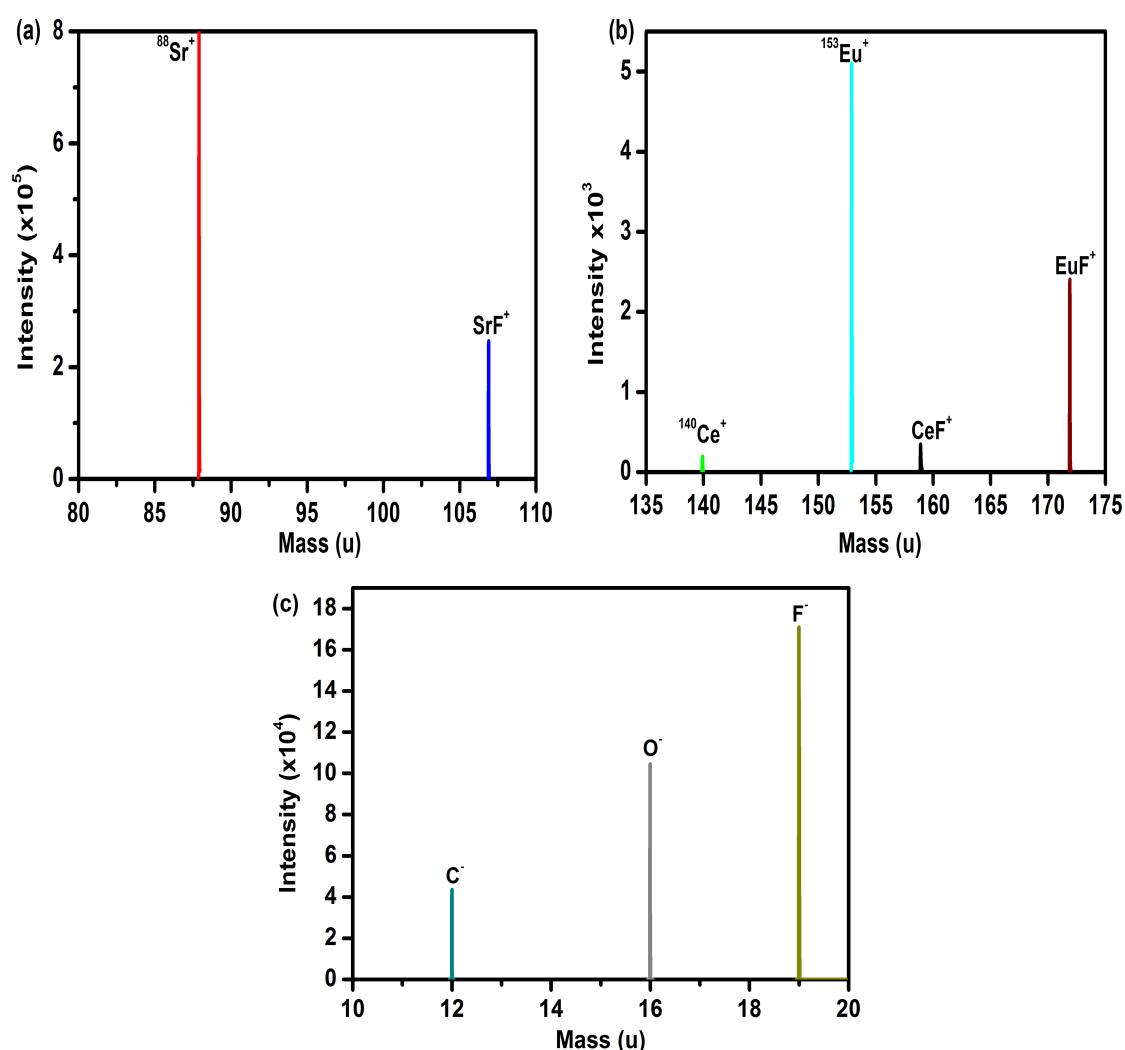


Fig. 6.4: (a and b) Positive and (c) negative TOF-SIMS spectra of $\text{SrF}_2:\text{Ce},\text{Eu}$ nanophosphor powder.

The dopant distributions in SrF_2 nano-phosphors were investigated with the TOF-SIMS chemical imaging technique. The chemical images for Sr, Ce and Eu ions were collected in positive polarity mode. Fig. 6.5 shows the three colour overlay of an area of

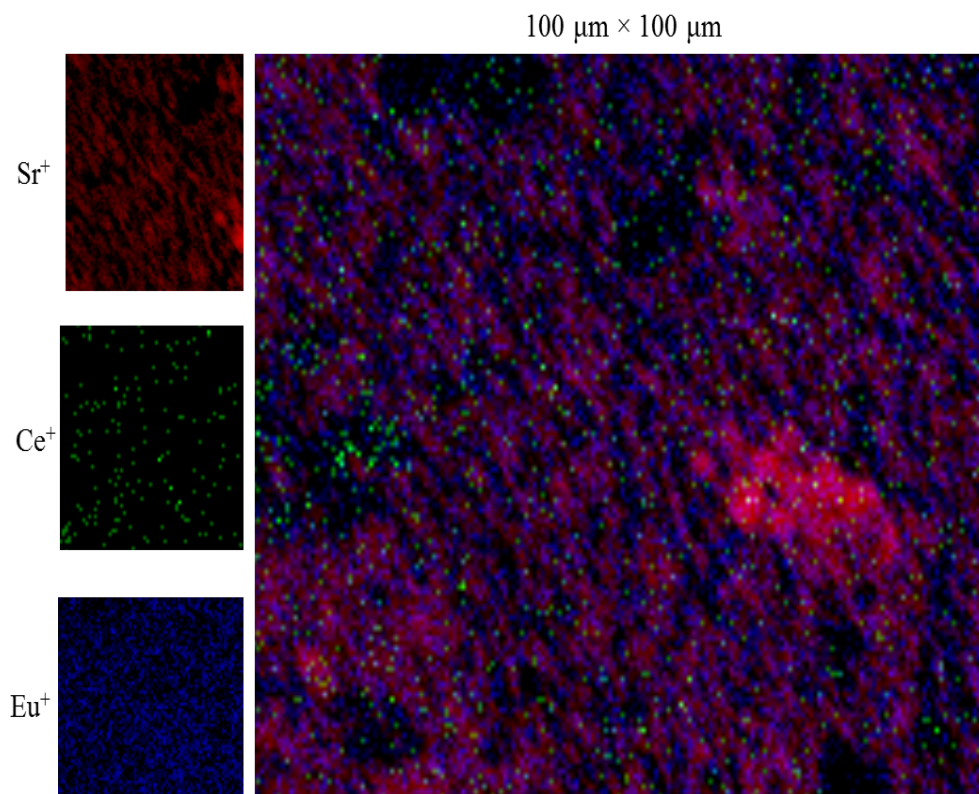


Fig. 6.5: TOF-SIMS correlation analysis using three-colour overlay image showing Eu and Ce dopants distribution in SrF_2 for an area of $100\ \mu\text{m} \times 100\ \mu\text{m}$.

$100\ \mu\text{m} \times 100\ \mu\text{m}$. It can clearly be seen that both the Ce and Eu ions' colours are distributed quite homogeneously over the entire area. This indicates that the dopants were uniformly distributed in the SrF_2 matrix during the hydrothermal synthesis method.

6.3.2 Photoluminescence spectroscopy

6.3.2.1 $\text{SrF}_2:\text{Ce}^{3+}$

The emission and excitation spectra of the Ce^{3+} singly doped SrF_2 nano-phosphor are shown in fig. 6.6. The excitation spectrum consists of a prominent peak that is centred at 295 nm. This peak has been previously assigned to $\text{Ce}^{3+}:4f-5d$ excitation transition in SrF_2 [22]. By exciting the samples by 295 nm, a broad band emission peak is observed, which is attributed to the inter-configuration $5d^1-4f^1$ allowed transition of

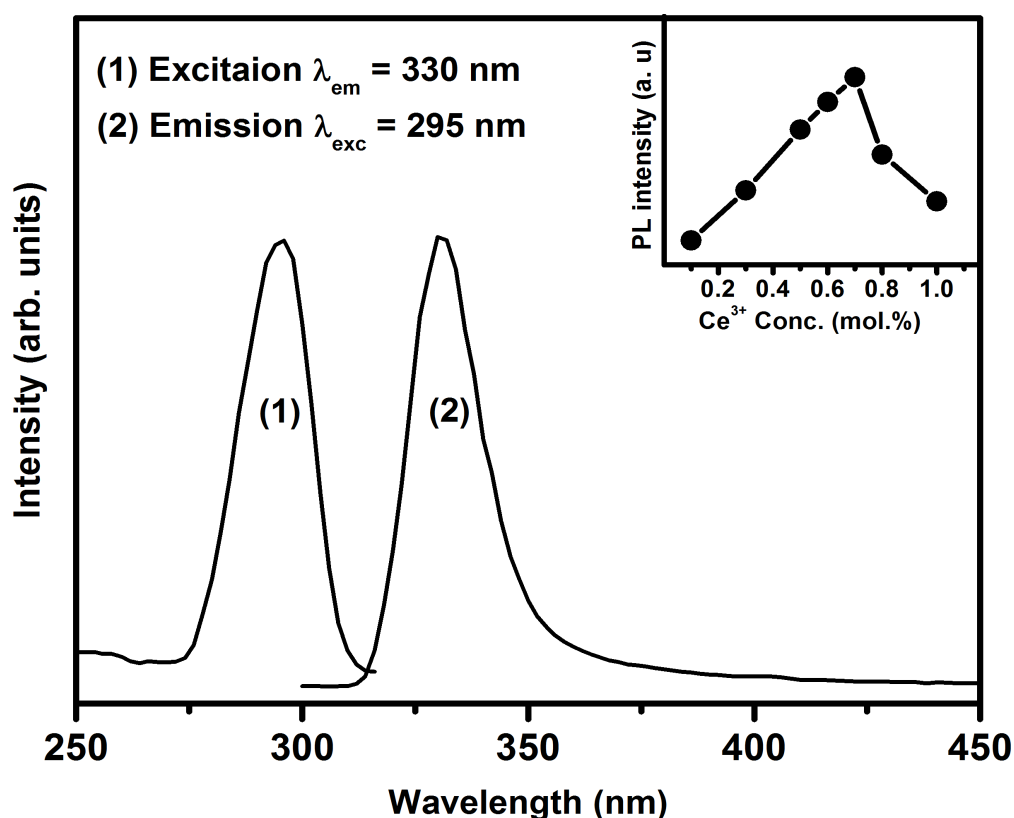


Fig. 6.6: Excitation and emission spectra of the SrF₂:Ce³⁺ (0.7 mol%) nano-phosphor. The inset shows the 5d-4f transition's emission intensity as a function of Ce³⁺ concentration.

Ce³⁺ ions. The inset graph in fig. 6.6 shows the emission intensity variation as a function of the Ce³⁺ concentration. The maximum luminescence intensity occurred for the sample doped with 0.7 mol% and a further increase in concentration resulted in a decrease in Ce³⁺ emission intensity. A previous study done by R. Shendrik et al. [5] on the SrF₂:Ce³⁺ sample reported that Ce³⁺ has a broad emission band that consist of two emission peaks (Ce³⁺ 5d to 4f ground state (²F_{7/2} and ²F_{2/2})) and the maximum luminescent intensity of Ce³⁺ was 0.3 mol%. In this study, the peaks were broadened and they fully overlap, which might be the reason why only one broad peak was observed.

6.3.2.2 SrF₂:Ce,Eu

Fig. 6.7(a) depicts the PL emission spectra of Ce³⁺ (0.7%) co-doped SrF₂:xEu (where x = 0.2, 0.6, 5 and 10%) excited with the He-Cd laser system with a 325 nm wavelength. The spectra also consisted of both the Eu²⁺ and Eu³⁺ emissions. The spectra clearly consist of a broad emission band that is centred at 416 nm with narrow bands in the range of 550-710 nm. The broad emission band is assigned to the inter-configuration 4f⁶5d¹-4f⁷ allowed transition of Eu²⁺ [23–25] and the narrow emission bands to the Eu³⁺ emission originating from 4f-4f transition [26]. The Eu³⁺ emission consists of orange-red emission bands that is attributed to the ⁵D₀-⁷F_{*j*} transitions (*j* = 1, 2, 3, 4). A shoulder peak (marked with a dollar sign (\$)) at a lower wavelength only appeared in small dopant concentrations' (0.2 and 0.6 mol%). This shoulder (\$) is assigned to the 4f-5d emission of Ce³⁺, which is completely quenched at high Eu concentration. The Eu³⁺ emission band at small Eu concentration (i.e 0.2 and 0.6 mol% see fig. 6.7(a)) cannot be clearly observed if compared to the Eu singly doped SrF₂ system (see chapter 5, fig. 5.4). The emission of Eu³⁺ dramatically increased at high Eu doping concentrations. This can clearly be seen in fig. 6.7(b) where the Eu³⁺ (⁵D₀-⁷F₁) emission intensity is plotted as function of Eu concentration for both the Eu singly and co-doped Ce³⁺ system. It can be noticed that Ce³⁺ co-doped SrF₂:Eu greatly enhanced the Eu³⁺ ions emission intensity at high Eu concentration. Whereas, when the Eu concentration was smaller than the Ce³⁺ concentration (Eu concentration < 0.7 mol% of Ce³⁺) the Eu³⁺ (⁵D₀-⁷F₁) emission intensity in the singly doped system was stronger than that of the co-doped system with Ce³⁺. This can be attributed to the energy transfer between Ce³⁺ and Eu ions. In the SrF₂ crystal, the Sr²⁺ ion is located at the body centre of a cube of eight F ions. The trivalent Ln³⁺ ions normally replace the Sr²⁺ cation. The extra charge of Ln³⁺ ions is compensated by F⁻ anion charges situated elsewhere in an interstitial site. With increasing Ln³⁺ concentration, some kind of structural deformation occurs. The Ln³⁺-F dipoles couple to dimers, trimers and higher aggregates. The interstitial F⁻ ions and vacancies on the normal F⁻ site compose cuboctahedral clusters [27, 28]. Since the exact nature of the Ce³⁺-Eu clusters cannot be inferred from our optical data, different kinds of small clusters in which the

Ce^{3+} and Eu ions can be imagined in the SrF_2 lattice. At small Eu concentration, it could therefore be that the clusters were not completely formed which makes the atomic distance between Eu^{2+} and Eu^{3+} ions bigger than the energy transfer distance. We assumed that energy transfer could only occur between Ce^{3+} and Eu^{2+} and that there is no direct energy transfer between Ce^{3+} and Eu^{3+} . It might also be that the Ce^{3+} ions are situated between the Eu^{2+} and Eu^{3+} ions, resulting in no direct interaction between the Eu^{2+} and Eu^{3+} ions. The Ce^{3+} ion would therefore only efficiently transfer its energy to the Eu^{2+} ions. This causes only the Eu^{2+} ions to emit at low concentration, whereas at high Eu concentration (bigger than Ce^{3+} concentration) the situation would change where the clustering could increase and therefore direct interaction between the Eu^{2+} and Eu^{3+} ions is possible.

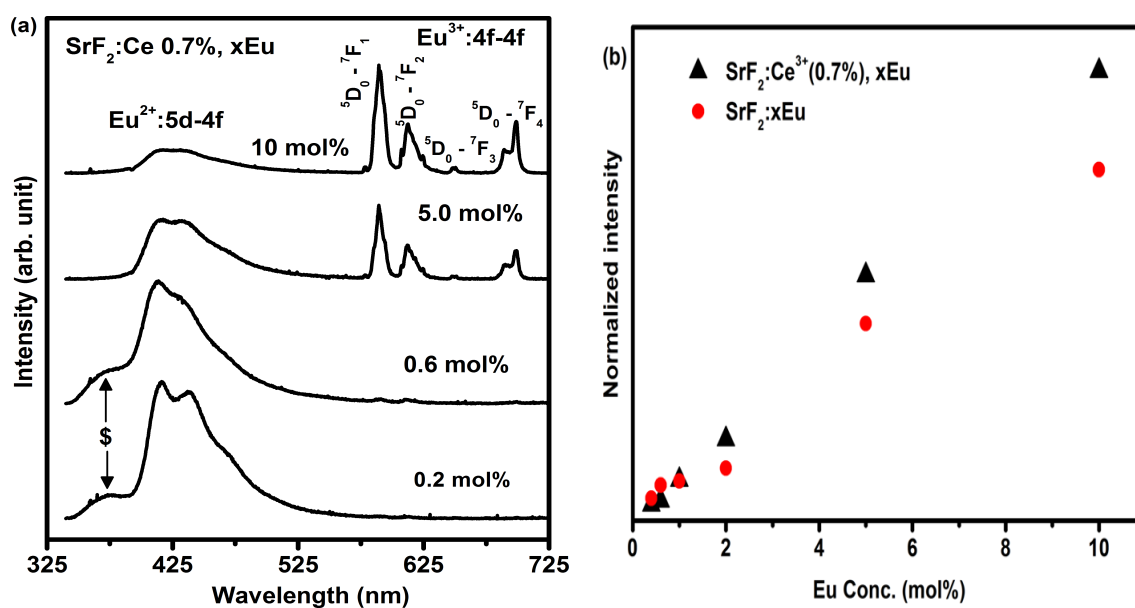


Fig. 6.7: (a) Photoluminescence spectra of $\text{SrF}_2:\text{Ce}^{3+}$ (0.7 mol%), xEu excited by laser system with 325 nm excitation wavelength and (b) $\text{Eu}^{3+} : {}^5\text{D}_0 - {}^7\text{F}_1$ emission intensity ($= 591 \text{ nm}$) of Eu singly and Ce co-doped Eu in SrF_2 matrix as function of Eu concentration excited by 394 nm using the xenon lamp.

More evidence for the energy transfer between Ce^{3+} and Eu ions are reported in fig. 6.8 where the PL emission spectra of the $\text{SrF}_2:\text{Ce}^{3+}$, Eu nano-phosphors excited by 295 nm excitation wavelength are plotted. The broad emission band that is centered at a wavelength of 330 nm (fig. 6.8(a)) is a characteristic of the Ce^{3+} ion which is

in agreement with the emission spectra for Ce^{3+} in fig. 6.6. The emission spectra of Eu^{3+} (fig. 6.8(b)) show the $^5\text{D}_0$ emission line of the Eu^{3+} ions in the SrF_2 crystal [29]. Whereas exciting the $\text{SrF}_2:\text{Eu}$ (1 mol%) sample (without Ce^{3+}) at 295 nm shows no significant emission of the Eu^{3+} ion at this excitation wavelength. From fig. 6.8(b), the Eu^{3+} emissions are enhanced steadily with an increase in Eu concentration under the 295 nm excitation wavelength. In the contrary the Ce^{3+} emission significantly decreased with increasing Eu concentration (fig. 6.8(a)). Fig. 6.8(c) also shows the emission spectra of Ce^{3+} where the Eu^{2+} emission can clearly be seen. The additional broad peak beside the Ce^{3+} emission that was centered at 416 nm is assigned to the Eu^{2+} ions in SrF_2 (clearly shown in the inset graph of fig. 6.8(c)). The Eu^{2+} emission slightly increased before it decreased with increasing Eu concentration. In fig. 6.8(c) the emission spectrum of the $\text{SrF}_2:\text{Eu}$ without Ce excited at 295 nm is also shown. It clearly shows that no Eu^{2+} emission occurred. The presence of Eu^{2+} emission under 295 nm excitation, in the co-doped samples, is therefore evidence of an energy transfer process from Ce^{3+} to Eu^{2+} . This process can occur in such material since the emission of Ce^{3+} overlaps the excitation spectra of Eu^{2+} (fig. 6.9(a); $\text{SrF}_2:\text{Ce}^{3+}$ (0.7 mol%), Eu (0.6 mol%)). Such spectral overlap is a necessary condition for the energy transfer from Ce^{3+} to Eu^{2+} to occur. An efficient energy transfer from Ce^{3+} to Eu^{2+} in a fluoride crystal was previously demonstrated even for a very low concentration [30]. The fact that both Eu^{2+} and Eu^{3+} emissions are observed, under 295 nm (excitation of Ce^{3+} ions), clearly demonstrates that energy transfer from Ce^{3+} to Eu ions occurred in the SrF_2 crystal. From fig. 6.9(b) one can demonstrate that energy transfer from Eu^{2+} to Eu^{3+} is possible but only efficient at high Eu concentration. This is because the emission of Eu^{2+} does not fully overlap the $^7\text{F}_0-^5\text{L}_6$ excitation transition of Eu^{3+} in the SrF_2 crystal. Thus, one can conclude that with 295 nm excitation into Ce^{3+} ions, Ce^{3+} might transfer its energy to the Eu^{2+} ($4\text{f}^65\text{d}$) from where the energy then non-radiatively transfers from Eu^{2+} to the Eu^{3+} ion.

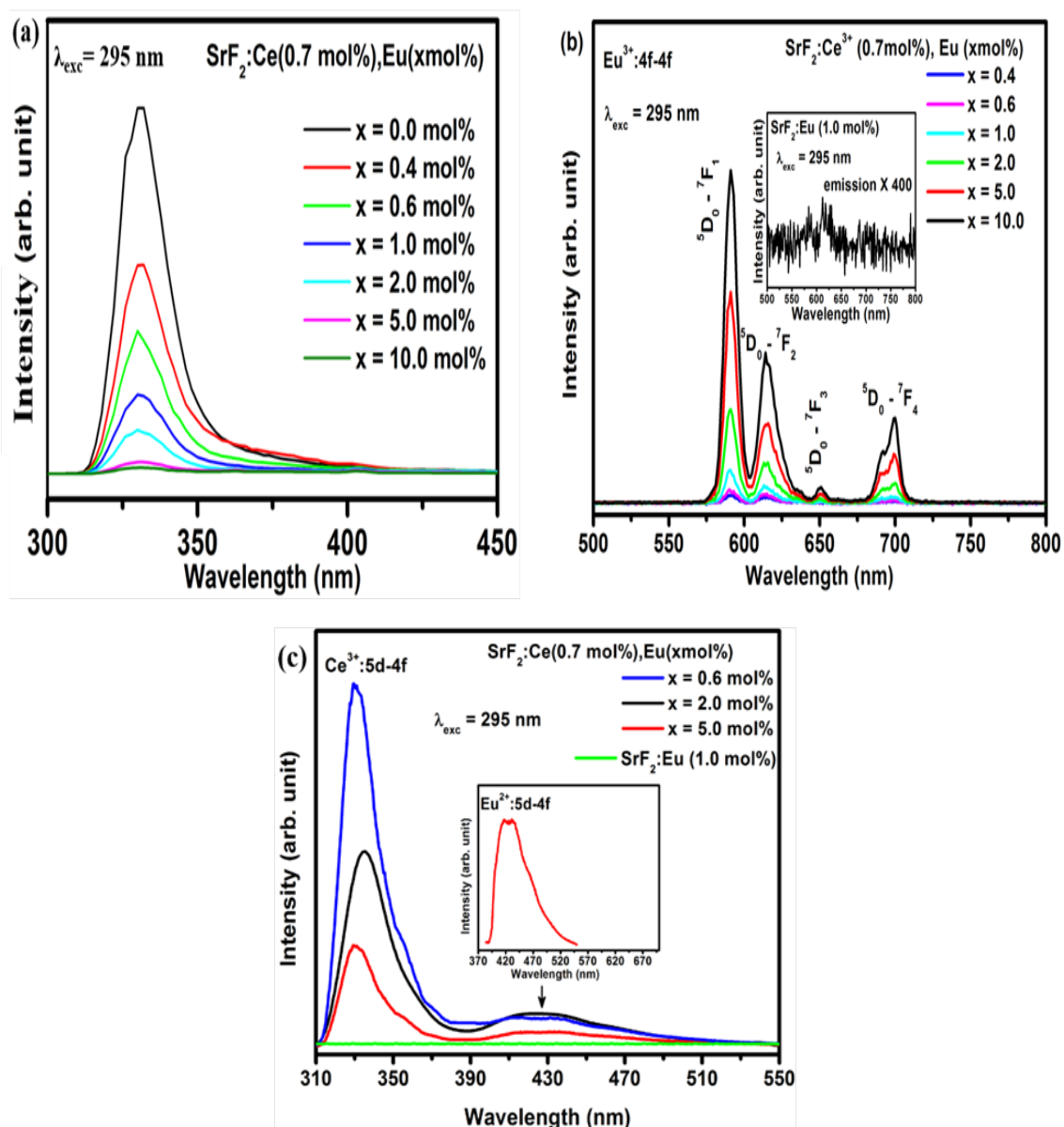


Fig. 6.8: PL emission spectra of (a) Ce^{3+} (b) Eu^{3+} and (c) Ce^{3+} and Eu^{2+} with different Eu doping concentration excited by an excitation wavelength of 295 nm. The inset in (b) is the emission of Eu^{3+} in $\text{SrF}_2:\text{Eu}(1 \text{ mol}\%)$ without Ce^{3+} ions and the inset in (c) is the Eu^{2+} emission from $\text{SrF}_2:\text{Ce}^{3+}(0.7 \text{ mol}\%), \text{Eu}(5.0 \text{ mol}\%)$.

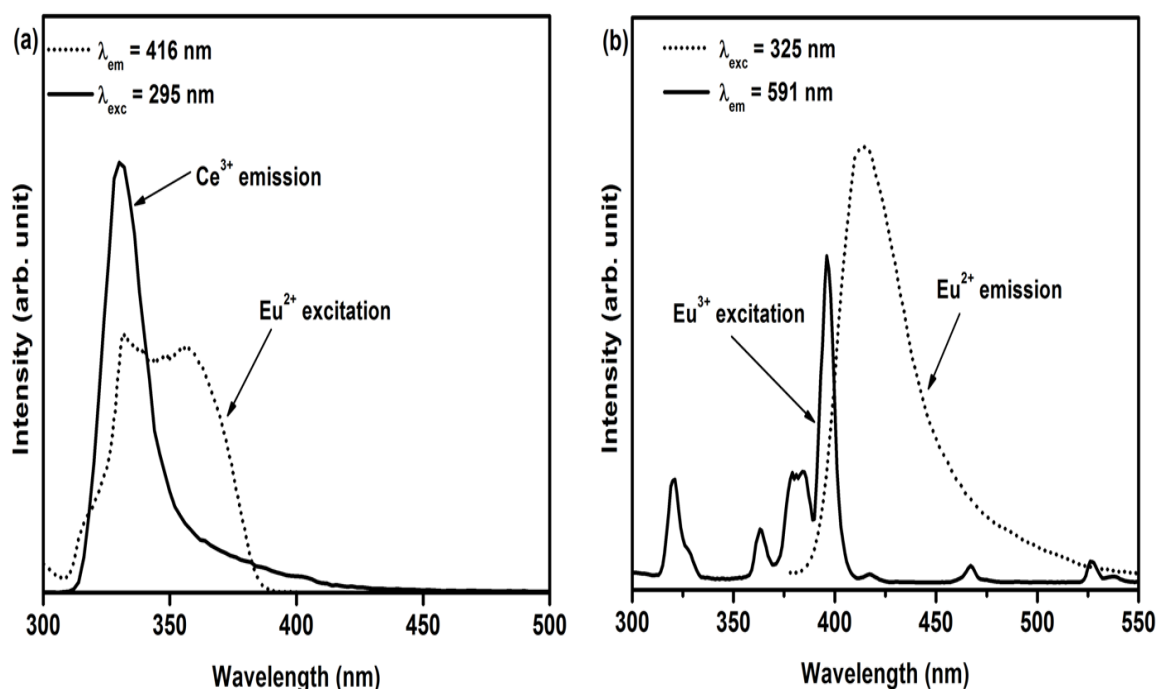


Fig. 6.9: Spectral overlap between (a) Ce^{3+} emission and Eu^{2+} excitation and (b) the Eu^{2+} emission and Eu^{3+} excitation ($\text{SrF}_2:\text{Ce}^{3+}$ (0.7 mol%), Eu (0.6 mol%)).

The room temperature luminescence excitation spectra of $\text{SrF}_2:\text{Ce}^{3+}$ (0.7 mol%), Eu (0.6 mol%) nano-phosphors are plotted in fig. 6.10. The excitation spectrum of Eu^{2+} (dotted line) not only consists of the $\text{Eu}^{2+}:4f^7 \rightarrow 4f^65d$ excitation transition but also the Ce^{3+} excitation band (clearly seen in the inset of the fig. 6.10). Monitoring the Eu^{3+} emission peak at 591 nm yields two kind of excitation bands: a broadband and a number of sharp excitation peaks. The broad excitation band is attributed to the $\text{Eu}^{2+}:4f^7 \rightarrow 4f^65d$ excitation transition. The sharp peaks correspond to the $\text{Eu}^{3+}:4f-4f$ transition. The absence of the Ce^{3+} excitation peak in the excitation spectrum of Eu^{3+} excludes the possibility of direct energy transfer from Ce^{3+} to Eu^{3+} . This result confirmed that under 295 excitation wavelength the absorbed energy transferred from Ce^{3+} (5d band) to Eu^{2+} ($4f^65d$) from where the energy then transferred to the Eu^{3+} ion. This implies that Eu^{2+} ions should act as a bridge between Ce^{3+} and Eu^{3+} ions. This could be true since the emission of Eu^{2+} is slightly increased before it decreased with increasing Eu concentration due to the energy transfer to Eu^{3+} ions (fig. 6.8(c)). The observation of energy transfer from Eu^{2+} to Eu^{3+} in BaF_2 was demonstrated where

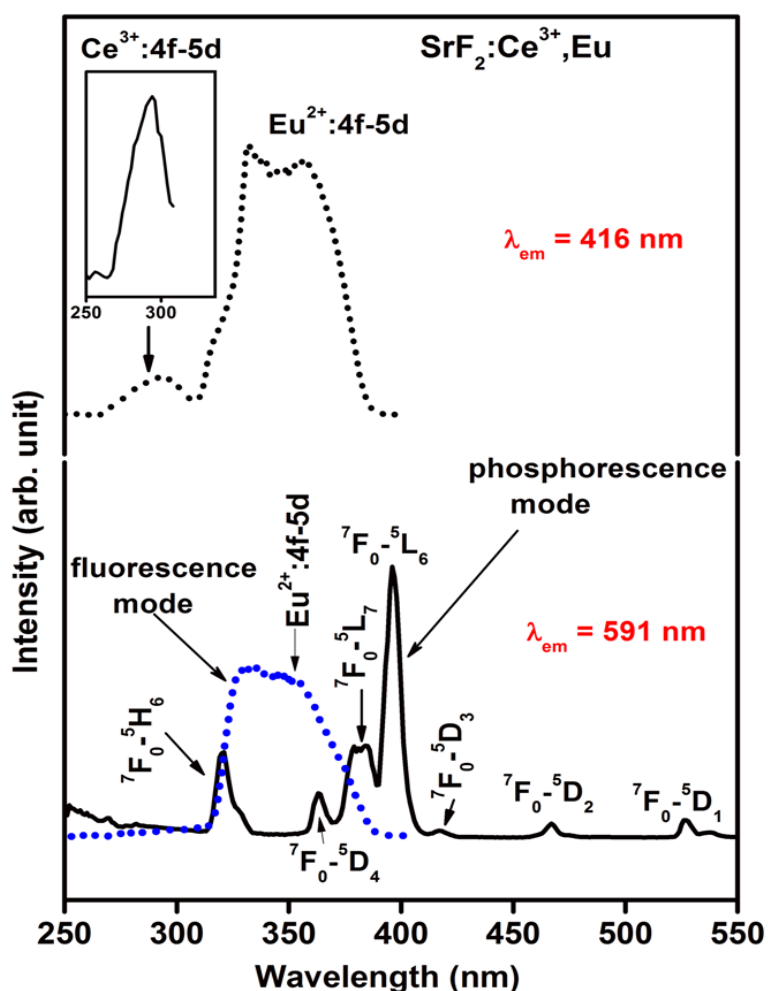


Fig. 6.10: Excitation spectra of $\text{SrF}_2:\text{Ce}^{3+}$ (0.7 mol%), Eu (0.6 mol%) nano-phosphors measured at an emission wavelength of 416 nm and 591 nm. The inset shows the enlarged Ce^{3+} excitation part of the spectrum.

Eu^{2+} emission overlapped the Eu^{3+} excitation [31]. However, the excitation lineshape of Eu^{2+} was found to be dependent on the monitored emission wavelength. When the emission of Eu^{3+} at 591 nm was monitored the excitation spectrum composed of a broadband excitation. While monitoring the Eu^{2+} emission at 416 nm the broadband excitation of Eu^{2+} is separated into two peaks with an additional shoulder at 320 nm (fig. 6.10). This behaviour of Eu^{2+} excitation can be attributed to multisite structures created by the charge compensation of both the Ce^{3+} and Eu^{3+} ions.

6.3.2.3 Decay curve analysis

Results obtained from the luminescence decay curves for Ce^{3+} emission also contributed further to the energy transfer efficiency process with different Eu concentrations. The decay time of the donor ions does not change in the presence and absence of the acceptor ions if the radiative energy is dominant [32]. In the situation of non-radiative energy transfer the decay time of the donor ions gradually decreases with an increase in the acceptor concentration. The PL decay curves of Ce^{3+} with various Eu concentration are shown in fig. 6.11. It can be seen that the decay curve of the Ce^{3+} ions gradually decreased with an increase in the Eu concentration. The luminescence decay curve of Ce^{3+} in SrF_2 nano-particles can well be fitted into a single-exponential function, whereas the decay curve of the entire co-doped concentrations were fitted with a bi-exponential decay model [32, 33]:

$$I(t) = A_1 \exp\left(\frac{-t}{\tau_1}\right) + A_2 \exp\left(\frac{-t}{\tau_2}\right), \quad (6.1)$$

$I(t)$ is the luminescence intensity at time t , A_1 and A_2 are constants, and τ_1 and τ_2 are the short- and long-decay components, respectively. The average lifetime constant (τ^*) can be calculated from the following equation:

$$\tau^* = \frac{A_1 \tau_1^2 + A_2 \tau_2^2}{A_1 \tau_1 + A_2 \tau_2} \quad (6.2)$$

The lifetime of the Ce^{3+} doped SrF_2 is determined to be 77.15 ns. This value is in good agreement with the reported value of Ce^{3+} in SrF_2 [22]. In the Eu ions co-doped system, the average lifetime of the donor ion (Ce^{3+}) decreased up to 8.2 ns at 10 mol% Eu concentration. This results indicate that the excitation energy of Ce^{3+} ions was transferred to the Eu ions (specifically Eu^{2+}) [22]. The lifetime results for the Ce^{3+} ions in the SrF_2 host strongly suggest that the energy transfer from Ce^{3+} to Eu^{2+} was non-radiative. The energy transfer efficiency from Ce^{3+} to Eu is defined by the following expression:

$$\eta_{ET} = 1 - \frac{\tau^*}{\tau_0}, \quad (6.3)$$

where τ^* and τ_0 are the average lifetime of Ce^{3+} in the presence and absence of the Eu ions, respectively. The corresponding lifetime and energy transfer efficiencies are

tabulated in table 6.2. From table 6.2, the energy transfer of Ce^{3+} increased gradually with an increase in the Eu concentration. The maximum energy transfer efficiency is about 89.4% for the sample doped with 0.7 mol% Ce^{3+} and 10 mol% Eu.

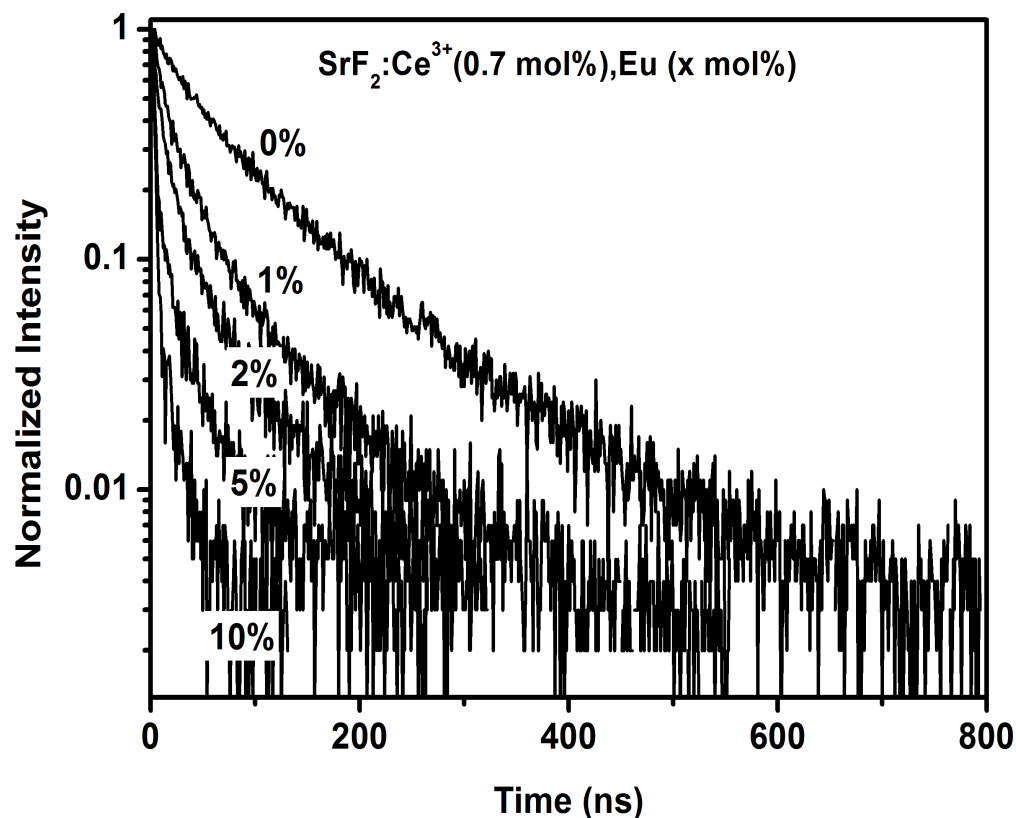


Fig. 6.11: The decay lifetime of Ce^{3+} ions in the SrF_2 host with an increase in Eu concentration. The inset graph shows the decay curve of 0.7% Ce^{3+} in SrF_2 fitted to a single-exponential fitting function.

Eu Conc.(mol%)	τ (ns)	η_{ET} (%)
0	77.15	0
1	46.3	40
2	31.9	58.6
5	16.05	79.2
10	18.2	89.4

Table 6.2: Lifetime of the 5d-4f transition of Ce^{3+} (330 nm) and the Ce^{3+} -Eu energy transfer efficiency (η_{ET}) in SrF_2 matrix.

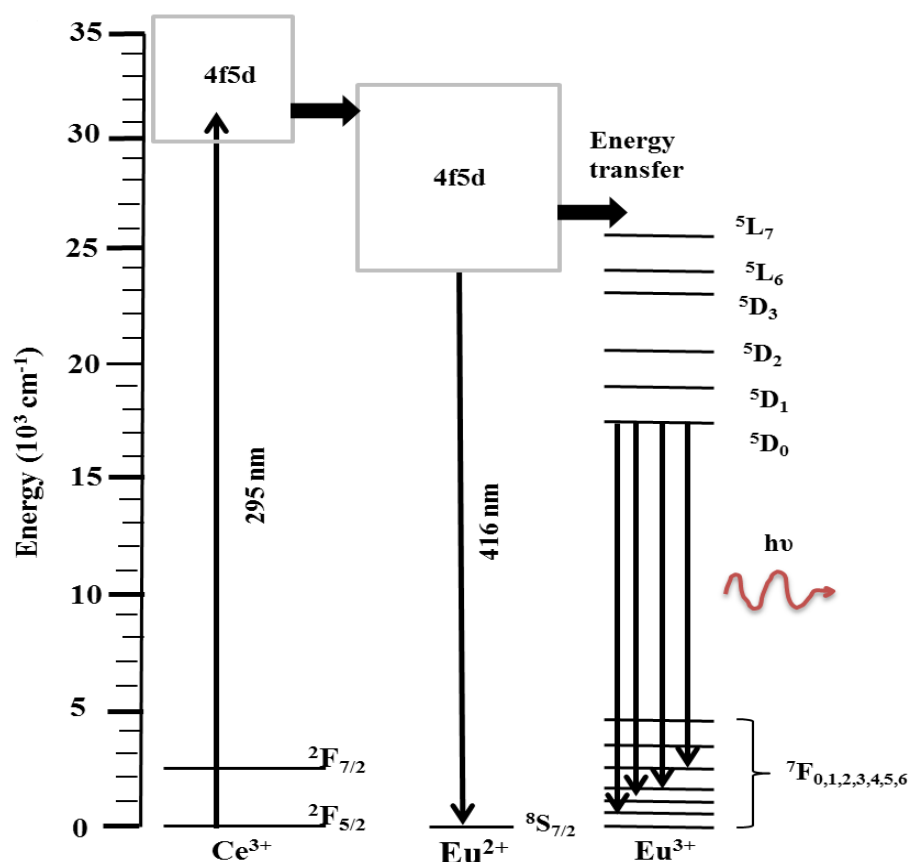


Fig. 6.12: Schematic energy level diagram of Ce³⁺ and Eu with a possible energy transfer between the Ce³⁺ and Eu ions.

To understand the luminescence mechanism in SrF₂:Ce³⁺, Eu nano-phosphor, a simplified energy level diagram of Ce³⁺ and Eu ions is shown in fig. 6.12. Upon 295 nm excitation the absorbed energy is likely to be transferred from Ce³⁺ (5d) to Eu²⁺ (4f⁶5d) from where the energy then non-radiatively gets absorbed by the Eu³⁺ ion. This is a possible reason for the observation of considerable Eu³⁺ emission under Ce³⁺ excitation at 295 nm. Thus, the introduction of Ce³⁺ ions can enhance the absorption and emission of Eu³⁺ ions with a subsequent positive effect on spectral conversion. With this result spectral conversion from 295-550 nm to 570-710 nm can be achieved by co-doping with Ce³⁺ ions. In our previous investigation of SrF₂:Eu we noticed that the Eu²⁺ ion was however found to be unstable when irradiated by the YAG laser. The Eu²⁺ ion's PL emission intensity rapidly decreased with time and this result make

the SrF₂:Eu nano-phosphor an unsuitable candidate for several applications, such as white light-emitting diodes and wavelength conversion films for silicon photovoltaic cells [11]. This might be true for the current samples since they were prepared by the same method as the previous SrF₂:Eu samples.

6.4 Conclusions

As-prepared SrF₂:Eu,Ce nano-phosphors were successfully synthesised with the hydrothermal technique. The average crystallite size that was calculated by using Scherrer's equation was found to be in nanometre scale. Dopant ions were intended to decrease the particle size of the host. The Auger spectra confirmed the presence of Sr, F, Eu and Ce elements in the host matrix. The TOF-SIMS results showed that the dopants were homogeneously distributed over the host matrix. Photoluminescence properties of Ce³⁺ and Eu co-doped SrF₂ nano-phosphor have been investigated and possible energy transfer from Ce³⁺ to Eu ions was demonstrated. From the PL decay curves the energy transfer efficiency was calculated to be 89.4% for the SrF₂: 0.7 mol% Ce³⁺, 10 mol% Eu sample. The results indicate that Ce³⁺ co-doped SrF₂:Eu is beneficial for improving the fluorescence emission and conversion efficiency under broadband excitation.

References

- [1] K. V. Ivanovskikh, V. A. Pustovarov, M. Krim and B.V. Shulgin, *J. Appl. Spectrosc.*, **72** (2005) 564-568.
- [2] B. M. Van der Ende, L. Aarts and A. Meijerink, *Adv. Mater.*, **21** (2009) 3073-3077.
- [3] K. Ivanovskikh, V. Pustovarov, A. Smirnov and B. Shulgin, *Phys. Stat. Sol. C*, **4** (2007) 889-892.
- [4] N. Kristianpoller, D. Weiss and R. Chen, *Radiat. Meas.*, **38** (2004) 719-722.
- [5] R. Shendrik, E.A. Radzhabov and A. I. Nepomnyashchikh, *Radiat. Meas.*, **56** (2013) 58-61.
- [6] R. Shendrik and E. Radzhabov, *Nucl. Sci. IEEE Trans.*, **57** (2019) 1295-1299.
- [7] N. Rakov, R. B. Guimaraes, D. F. Franceschini and G. S. Maciel, *Mater. Chem. Phys.*, **135** (2012) 317- 321.
- [8] C. Oprea, V. Ciupina and G. Prodan, *Romanian J. Phys.*, **53** (2008) 223-230.
- [9] H. A. A. Seed Ahmed, O. M. Ntwaeaborwa and R. E. Kroon, *Curr. Appl. Phys.*, **13** (2013) 1264-1268.
- [10] F. Wang, Y. Han, C. S. Lim, Y. Lu, J. Wang, J. Xu, H. Chen, C. Zhang, M. Hong and X. Liu, *Nature*, **463** (2010) 1061-1065.
- [11] M. Y. A Yagoub, H. C. Swart, L. L Noto, J. H. O'Connell, M. E Lee and E. Coetsee, *J. Lumin.*, **156** (2014) 150-156.
- [12] R. E. Kroon, H. C. Swart, O. M. Ntwaeaborwa and H. A. A. Seed Ahmed, *Physica B*, **439** (2014) 83-87.
- [13] J. T. van Wijngaarden, S. Scheidelaar, T. J. H. Vlugt, M. F. Reid and A. Meijerink, *Phys. Rev. B*, **81** (2010) 155112-155117.
- [14] R. P. Vasquez, *Surf. Sci. Spectra*, **1** (1992) 24-30.

- [15] R. Vercaemst, D. Poelman, L. Fiermans, R. L. Van Meirhaeghe, W. H. Laflere and F. Cardon, *J. Electron. Spectrosc. Relat. Phenom.*, **74** (1995) 45-56.
- [16] D. Lu, M. Sugano, X. Y. Sun and W. Su, *Appl. Surf. Sci.*, **242** (2005) 318-325.
- [17] J. Zhang, M. Yang, H. Jin, X. Wang, X. Zhao, X. Liu and L. Peng, *Mater. Res. Bull.*, **47** (2012) 247-252.
- [18] R. Vercaemst, D. Poelman, R. L. Van Meirhaeghe, L. Fiermans, W. H. Laflere and F. Cardon, *J. Lumin.*, **63** (1995) 19-30.
- [19] R. Lässer, J. C. Fuggle, M. Beyss and M. Campagna, *Physica B*, **102** (1980) 360-366.
- [20] M. Gamza, A. Slebarski and H. Rosner, *Eur. Phys. J. B*, **63** (2008) 1-9.
- [21] B. R. Chakraborty, D. Haranath, H. Chander, S. Hellweg, S. Dambach and H. F. Arlinghaus, *Nano-technol.*, **16** (2005) 1006-1015.
- [22] C. Zhang, Z. Hou, R. Chai, Z. Cheng, Z. Xu, C. Li, L. Huang and J. Lin, *J. Phys. Chem. C*, **114** (2010) 6928-6936.
- [23] Y. C. Li, Y. H. Chang, Y. F. Lin, Y. S. Chang and Y. J. Lin, *J. Alloys Compd.*, **439** (2007) 367-375.
- [24] Y. Jin, W. Qin and J. Zhang, *J. Fluorine Chem.*, **129** (2008) 515-518.
- [25] P. Dorenbos, *J. Lumin.* **104** (2003) 239-260.
- [26] L. L. Noto, S. S. Pitale, M. A. Gusowki, J. J. Terblans, O. M. Ntwaeaborwa and H. C. Swart, *Powder Technol.*, **237** (2013) 141-146.
- [27] P. J. Bendall, C. R. A. Catlow, J. Corish and P. W. M. Jacobs, *J. Solid State Chem.*, **51** (1988) 159-169.
- [28] D. R. Tallent, D. S. Moore and J. C. Wright, *J. Chem. Phys.*, **67** (1977) 2897-2907.

-
- [29] J. Peng, S. Hou, X. Liu, J. Feng, X. Yu, Y. Xing and Z. Su, *Mater. Res. Bull.*, **47** (2012) 328-332.
- [30] U. G. Caldino, C. D. Gruz, G. H. Monoz and J. O. Rubio, *Solid State Commun.*, **4** (1989) 347-351.
- [31] K. Biswas, A. D. Sontakke, R. Sen and K. Annapurna, *J. Fluor.*, **22** (2012) 745-752.
- [32] J. Zhou, Z. Xia, H. You, K. Shen, M. Yang and L. Liao, *J. Lumin.*, **135** (2013) 20-25.
- [33] T. Katsumata, T. Nabae, K. Sasajima, S. Komuro and T. Morikawa, *J. Electrochem. Soc.*, **144** (1997) L243-L245.

Chapter 7

Eu²⁺ enhanced Pr³⁺ photoluminescence by energy transfer in SrF₂ phosphor

This chapter focuses on the possibility of using the Eu²⁺ ion as a sensitizer to Pr³⁺ ion in SrF₂ crystal. The energy transfer between Eu²⁺ and Pr³⁺ phosphor is discussed.

7.1 Introduction

Phosphor materials prepared by doping inorganic hosts with rare-earth ions have brought much attention due to their various applications [1–3]. One of these applications is use of phosphor materials to boost the efficiency of the Si solar cells [3–5]. The major problem that limits the solar cells efficiency is their insensitivity to the whole solar spectrum (see chapter 2). The absorption of high energy photons by solar cells induces the thermalization of the charge carriers, which is so-called thermalization loss [4, 6]. One approach to reduce the thermalization loss is to use the inorganic materials doped lanthanide ions that are capable of converting each high energy photon into two lower energy photons. Both these low photons can then be absorbed by the solar cell. The process of generating or cutting one high energy photon into two lower energy photons is called down-conversion (or quantum cutting) [4, 5].

SrF₂: Pr³⁺-Yb³⁺ is reported as one of the best down-conversion phosphor materials [3, 6]. In SrF₂: Pr³⁺-Yb³⁺, absorption of a blue photon results in feeding two Yb³⁺ ions, which gives rise to the emission of two near infrared photons with an efficiency close to 200% that can be utilized for creating two electron-hole pairs. As mentioned in chapter 1, the major problem that limits the SrF₂: Pr³⁺-Yb³⁺ down-conversion for use in solar cell application is its 4f-4f transition, which characterized by a weak absorption cross-section. In order to enhance the 4f-4f absorption strength, one suggestion to investigate is to add a third sensitizer [3, 7]. Such sensitizer must be able to efficiently absorb all light in UV and visible part of the spectrum and transfer the energy to the

down-conversion couple, e.g. 3P_j levels of Pr³⁺. The requirement must therefore be an ion with allowed absorption transitions. Eu²⁺ could be used as a sensitizer because it shows a broad excitation band that comes from a fully allowed 4f-5d transition [8, 9]. This transition strongly depends on the crystal field of the matrix. The crystal field is very important because efficient energy transfer between a sensitizer and a donor can only occur when the emission band of the sensitizer overlaps the excitation band of the donor. In the SrF₂ host, Eu²⁺ ion emits a broadband emission centred at 416 nm [9], which could make it a suitable to sensitize the 3P_j levels of Pr³⁺ ion.

This chapter therefore examines the possibility of using Eu²⁺ as a sensitizer for Pr³⁺ in the SrF₂ crystal. The phosphors were synthesized by co-precipitation method and their luminescent properties were investigated with PL and time-resolved luminescence measurements. This work serves as a requirement in preparation for the quantum cutting effect in the Pr³⁺-Yb³⁺ couple in the SrF₂ host.

7.2 Experimental section

Analytical grade of Sr(NO₃)₂, Pr(NO₃)₃.6H₂O, Eu(NO₃)₃.6H₂O and NH₄F were used without further purification. Sodium hydroxide was used to adjust the pH of the system, which were 8.5 in this study. For a typical synthesis of SrF₂:Eu²⁺,Pr³⁺, 30 mmol of NH₄F and 0.1 mol/mL of sodium hydroxide were added drop-wise to an aqueous solution containing Sr(NO₃)₂ and Pr(NO₃)₃.6H₂O and Eu(NO₃)₃.6H₂O in a period of about 30 min. After one hour of stirring, the mixture was left for 5 hours. Then, the product was collected by using a centrifugal and washed with water and ethanol. Finally, the product was dried for 48 hours in an oven at 80 °C. The samples were annealed under a reducing atmosphere (Ar 95%/H₂ 5%) in order to reduce Eu³⁺ into Eu²⁺ ions.

The phosphors were characterized by XRD (Bruker Advance D8 diffractometer with Cu K α radiation ($\lambda = 0.154$ nm)) to identify the crystalline structure of the powder. The morphology and elemental composition of the materials were analysed using JEOL JSM-7800F high field emission scanning electron microscope (FE-SEM) equipped with

EDS. High resolution XPS was obtained with a PHI 5000 Versaprobe system. A low energy Ar⁺ ion gun and low energy neutralizer electron gun were used to minimize charging on the surface. A 100 μm diameter monochromatic Al K α x-ray beam ($h\nu = 1486.6$ eV) generated by a 25 W, 15 kV electron beam was used to analyze the different binding energy peaks. The pass energy was set to 11 eV giving an analyzer resolution of ≤ 0.5 eV. Multipack version 8.2 software was utilized to analyze the spectra to identify the chemical compounds and their electronic states using Gaussian-Lorentz fits. Diffuse reflection spectra were measured using a Lambda 950 UV-vis spectrophotometer with spectralon as the reference material. PL spectra were collected using a Cary Eclipse fluorescence spectrophotometer equipped with a xenon lamp. Luminescence decay curves of Eu²⁺ were recorded under pulsed excitation (HORIBA scientific) with 375LH NanoLED diode with a 375 nm excitation wavelength. Whereas, the luminescence decay curves of Pr³⁺ were measured under pulsed excitation using a diode pumped YAG laser with a 335 nm excitation wavelength, power of 1.3 milliwatt and a SR430 Multichannel scalar photomultiplier (Linköping, Sweden). All measurements were performed at room temperature.

7.3 Results and Discussion

The XRD patterns of the SrF₂:Eu²⁺,Pr³⁺ powder phosphor as well as the standard data for SrF₂ (card No. 00-086-2418) are shown in fig. 7.1. The doped samples crystallized into face centred cubic phase with the Fm3m space group and a lattice parameter of 5.794 ± 0.0054 nm. It can also be seen that all observed peaks match well with the reference data, which indicates that there was no obvious influence of the dopants on the crystalline structure of the host.

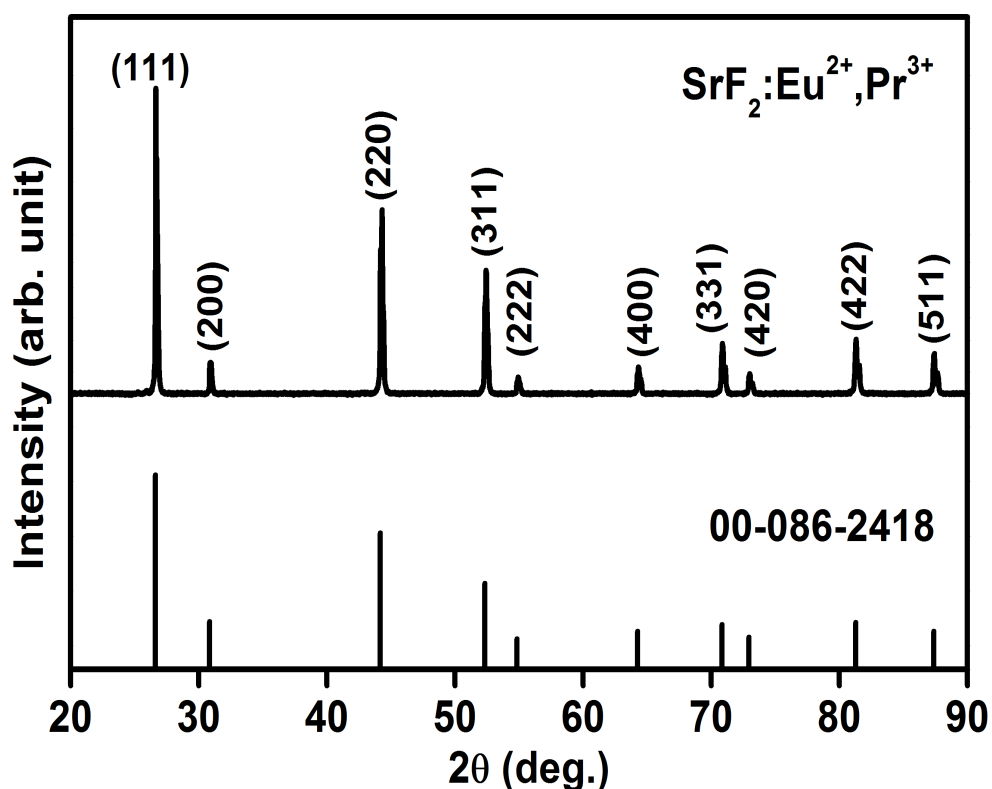


Fig. 7.1: XRD pattern of the SrF₂:Eu²⁺ (1.5 mol%), Pr³⁺ (10 mol%) phosphor powder and the standard data (card No. 00-086-2418).

SEM images were obtained in order to investigate the surface morphology of the phosphors. Fig. 7.2(a) shows the SEM image of SrF₂ co-doped with 1.5 mol% and 4 mol% concentration of Eu²⁺ and Pr³⁺, respectively. The image shows the powder consisted of agglomerated spherical particles with a diameter bigger than 100 nm. Fig. 7.2(b) depicts the elemental analysis of the samples using EDS. Representative peaks associated to F, Eu, Pr and Sr elements are clearly identified. The EDS result confirmed the presence of Sr, F, Eu and Pr in the sample powder. EDS can however not differentiate between the oxidation states of the elements.

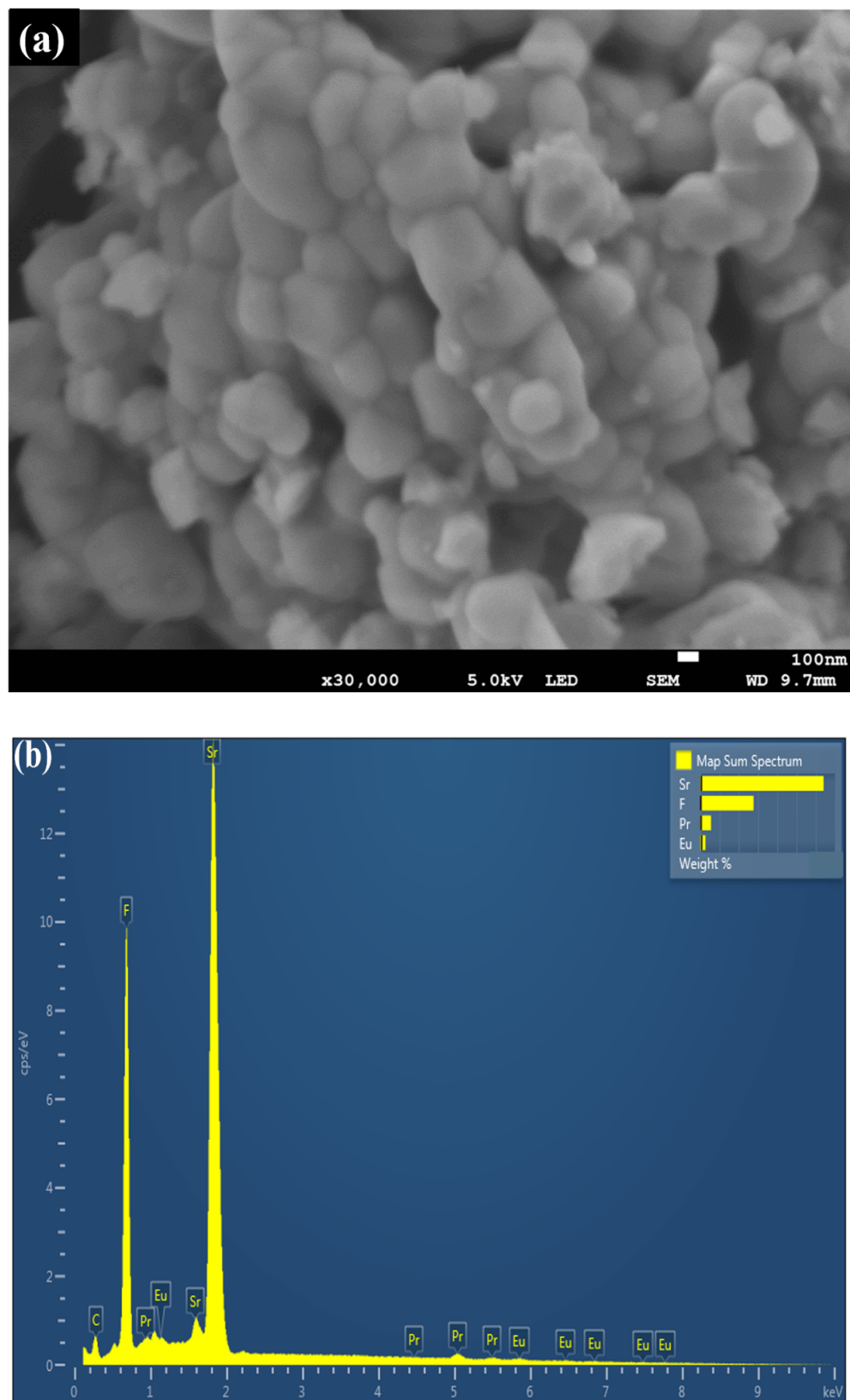


Fig. 7.2: (a) SEM image and (b) EDS spectrum of SrF₂:Eu, Pr phosphor powder.

Eu can occur in the divalent (Eu²⁺) and in the trivalent (Eu³⁺) states, while Pr can occur in the trivalent (Pr³⁺) and tetravalent (Pr⁴⁺) states. Both the oxidation states of Eu are optically active and were detected in SrF₂ host in a study previously done by the authors [9] and it was reported in investigations done by other researchers [10, 11]. In the Pr ions only Pr³⁺ oxidation state is optically active while the Pr⁴⁺ state acts as quenching center on the materials [12]. The XPS technique is a suitable technique to investigate the oxidation states of the lanthanide ions in compounds [13–15]. XPS analysis therefore performed to investigate the conversion of the Eu³⁺ to Eu²⁺ ions as well as the optically active Pr³⁺ ions of Pr. All the Gaussian percentages were assumed to have a combined Gaussian-Lorentzian shape during the deconvolution of the peaks. The high resolution XPS peaks of Pr 3d and Eu 3d are shown in fig. 7.3(a) and (b), respectively. The high resolution XPS peaks of Pr 3d consists of two spin-orbit splitting peaks of 3d_{5/2} and 3d_{3/2}. Peak deconvolution showed the two main peaks, m and m', the shake-down peaks s and s', and an extra peak that exist only at the 3d_{3/2} component, t' [16–18]. The s and s' structures are known to occur from strong mixing of the two final states of 3d⁹4f² and 3d⁹4f³, while the t' structure was claimed to be caused by the multiplet effect [18]. All these peaks are characteristics of the Pr³⁺ ions [16].

Fig. 7.3(b) shows the peak deconvolution for the Eu 3d high resolution XPS peaks. The Eu 3d peak consists of two peaks that originated from the spin-orbit splitting, 3d_{5/2} and 3d_{3/2} of the Eu²⁺ oxidation state [9, 13]. In our previous XPS investigation of as-prepared SrF₂:Eu phosphors powders the Eu showed both the two oxidation states, Eu²⁺ and Eu³⁺ [9]. This result confirms that the conversion process of Eu³⁺ to Eu²⁺ occurred.

Fig. 7.4 shows the excitation and emission spectra of the singly doped Pr³⁺ ions whose charge was compensated locally by the F ions [6, 19, 20]. The excitation spectrum of SrF₂:Pr³⁺ (dotted line) was obtained by monitoring the emission centred at 488 nm (³P₀-³H₄ transition). The observed excitation bands correspond to the transitions of ³H₄-³P_j (j=0, 1, 2) and ¹I₆. All these bands occurred within the 4f-4f transitions of the Pr³⁺ ion [2]. Upon excitation with 439 nm (into ³P₂ energy band), depopulation

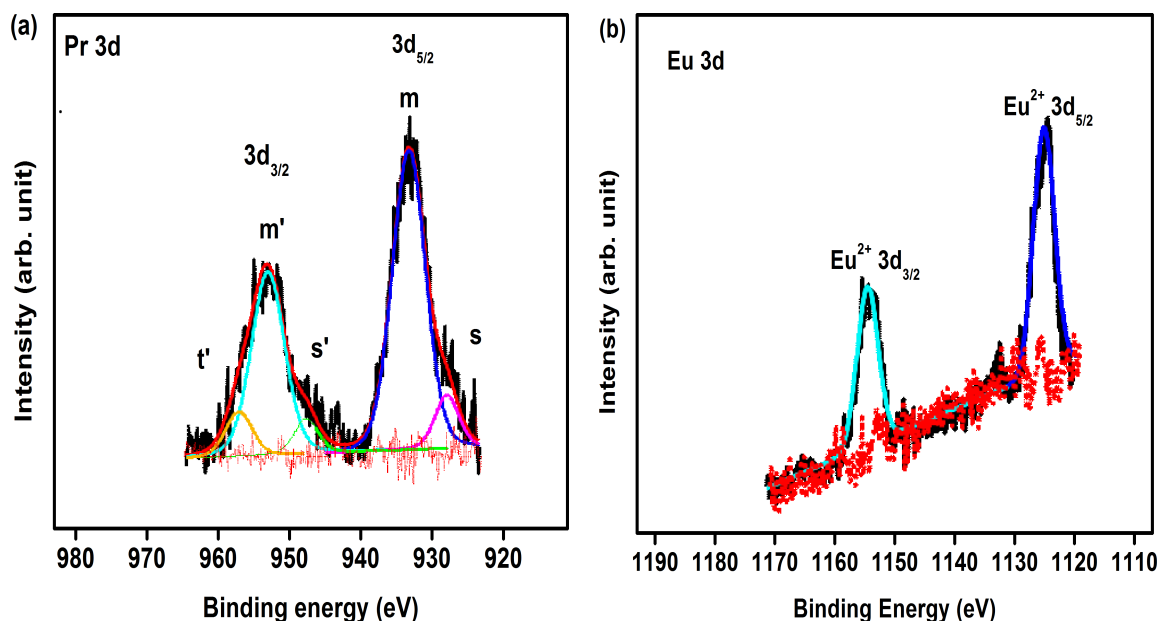


Fig. 7.3: XPS high resolution peaks for the (a) Pr 3d and (b) Eu 3d ions in the SrF₂ phosphor powder.

from higher energy bands occurred to the metastable ³P₀ energy band. The emission bands centred at 488, 524, 605, 638, 715 and 730 nm were due to the ³P₀-³H₄, ³P₀-³H₅, ³P₀-³H₆, ³P₀-³F₂, ³P₀-³F₃ and ³P₀-³F₄ transitions, respectively. All the observed emission peaks originated mostly from the ³P₀ energy level. This demonstrates that the dominant transition in SrF₂ is the ³P₀ transition.

The excitation and emission spectra of Eu²⁺ in SrF₂ are shown in fig. 7.5. The spectra clearly consist of broad excitation and emission bands centred at 332 and 416 nm, respectively. It is well known that such broad excitation and emission bands are mainly originating from the inter-configuration 4f⁶5d¹-4f⁷ allowed transition of Eu²⁺ [8, 9]. The inset graph in fig. 7.5 shows the emission intensity variation as a function of Eu²⁺ concentration. The maximum luminescence intensity occurred for the sample doped with 1.5 mol% and a further increase in concentration resulted in a decrease in Eu²⁺ emission intensity.

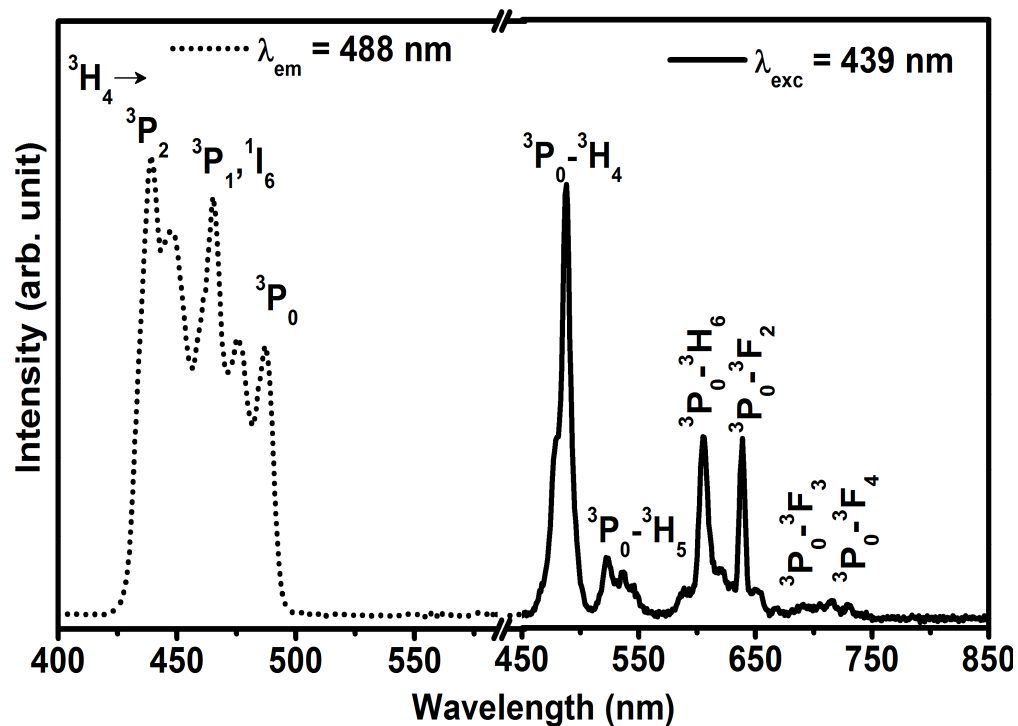


Fig. 7.4: Excitation spectrum (dotted line) and emission spectrum (solid line) of SrF₂:Pr³⁺ 0.3 mol% excited with 439 nm to the ³P₂ energy level.

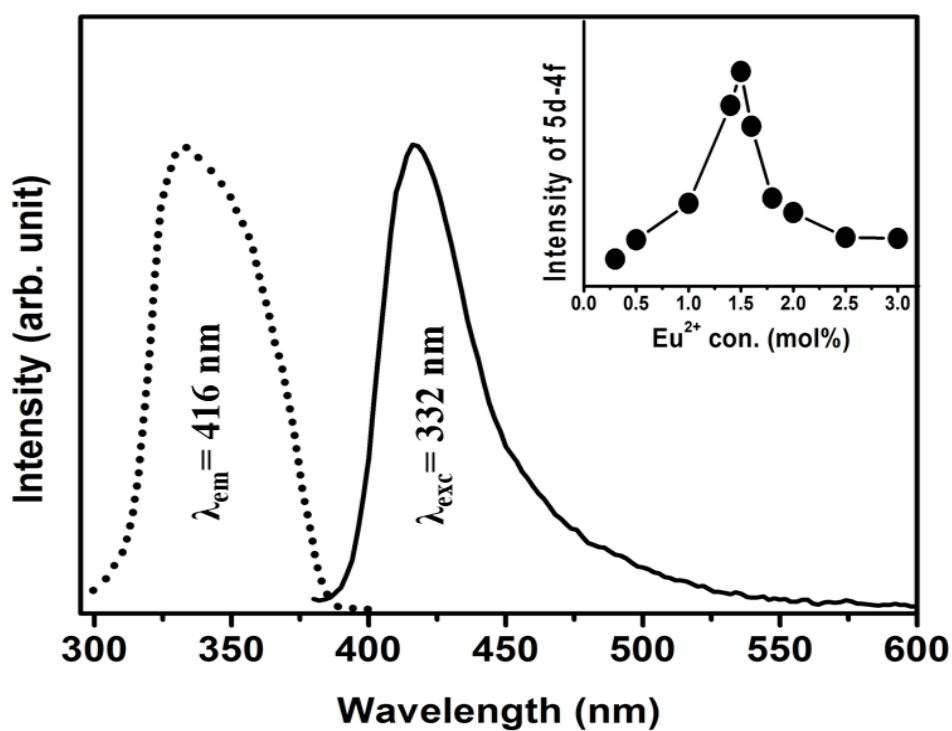


Fig. 7.5: Excitation spectrum (dotted line) and emission spectrum (solid line) of SrF₂:Eu²⁺ 1.5 mol% excited by 332 nm.

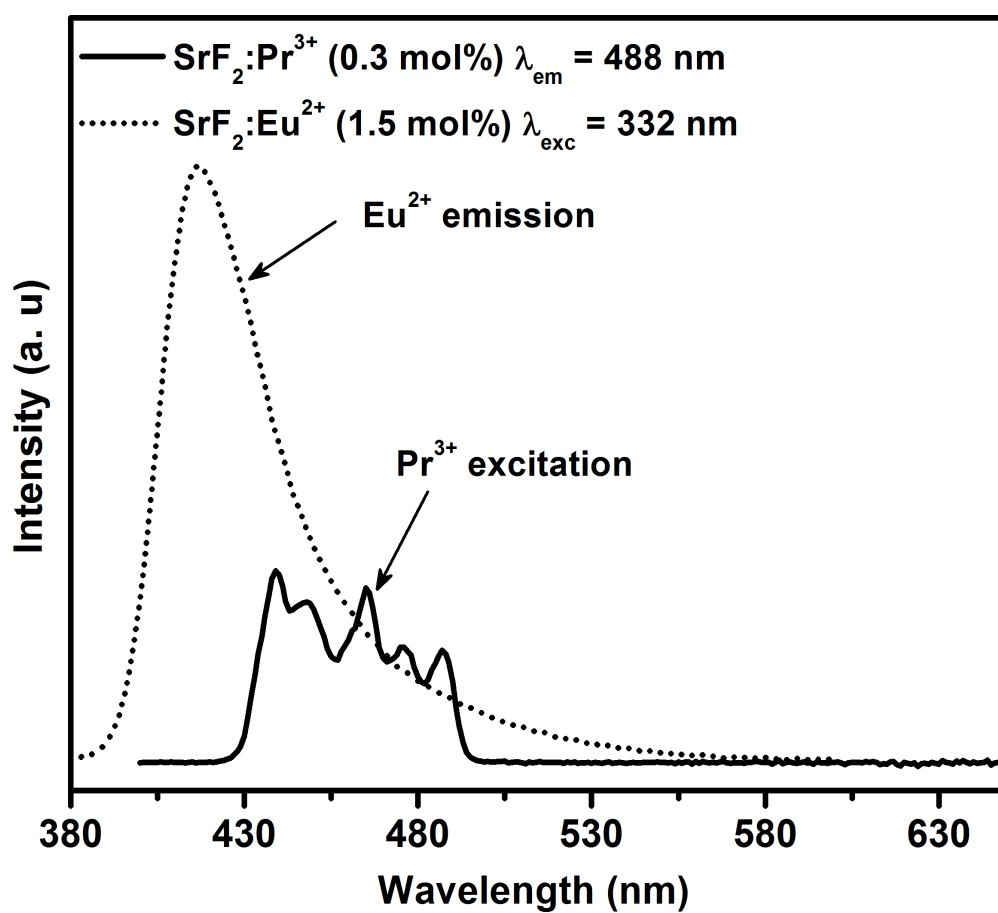


Fig. 7.6: Spectral overlap between Eu²⁺ emission and Pr³⁺ excitation in the SrF₂ crystal structure.

Fig. 7.6 compares the excitation and emission spectra of Pr³⁺ and Eu²⁺ singly doped SrF₂. It is worth noting that the emission band of Eu²⁺ overlap with the excitation band of the ³P_j (j = 0, 1, 2) Pr³⁺ ion. This result is strong evidence to show that the Eu²⁺ ion should be a good sensitizer for Pr³⁺ ion under 332 nm excitation.

To study the energy transfer efficiency for the Eu²⁺-Pr³⁺ couple, a series of powder samples were prepared with 1.5 mol% of Eu²⁺ and various Pr³⁺ (0, 1, 2, 3, 5, 7 and 10 mol%) concentration. In fig. 7.7, the emission spectra of Eu²⁺ (4f⁶5d¹-4f⁷ transition) and Pr³⁺:4f-4f transition with varied Pr³⁺ concentration are shown under identical conditions. The emission spectra of Pr³⁺ co-doped SrF₂, fig. 7.7(b), shows the characteristic ³P₀ emission line of Pr³⁺ that correlates well with the emission spectra for the Pr³⁺ singly doped sample, as was shown in fig. 7.4. From fig. 7.7(a) it can be seen that the Eu²⁺ emission (4f⁶5d¹-4f⁷ transition) decreased significantly with the increased Pr³⁺ concentration. The Pr³⁺ emissions were enhanced steadily with an increase Pr³⁺ concentration. This is shown in the inset of fig. 7.7(b) where the emission spectra of Pr³⁺ (³P₀-³H₄ transition) are plotted as a function of Pr³⁺ concentration. The increase in Pr³⁺ concentration resulted in a concentration quenching effect that occurred at high doping concentrations (around 2 mol%). This can be attributed to the cross-relaxation caused by the interactions between the nearby Pr³⁺ ions. Due to the nature of the Pr³⁺ energy levels the concentration quenching between the Pr³⁺ ions in fluoride and oxide hosts occurs at relatively low Pr³⁺ concentration (maximum 0.4 mol%) [2, 6]. The optimal intensity obtained for the Pr³⁺ doped SrF₂ crystal was 0.4 and 0.2 mol% when prepared by hydrothermal and combustion synthesis techniques, respectively [21]. The Eu²⁺ co-doped SrF₂:Pr³⁺ in the current study enhanced the Pr³⁺ optimal intensity and hence improved the Pr³⁺: 4f-4f absorption strength.

A good estimation of the enhancement is obtained by calculating the ratio of the integrated emission intensity of Eu²⁺ luminescence (between 388 and 550 nm) for a sample without Pr³⁺ to the integrated Pr³⁺ luminescence (between 460-800 nm) for a sample co-doped with Eu²⁺ and Pr³⁺ [6]. The highest value was for samples doped with 2 mol% Pr³⁺, which also indicates that the Pr³⁺ emission intensity was quenched as a result of concentration quenching due to cross-relaxation between the Pr³⁺ ions.

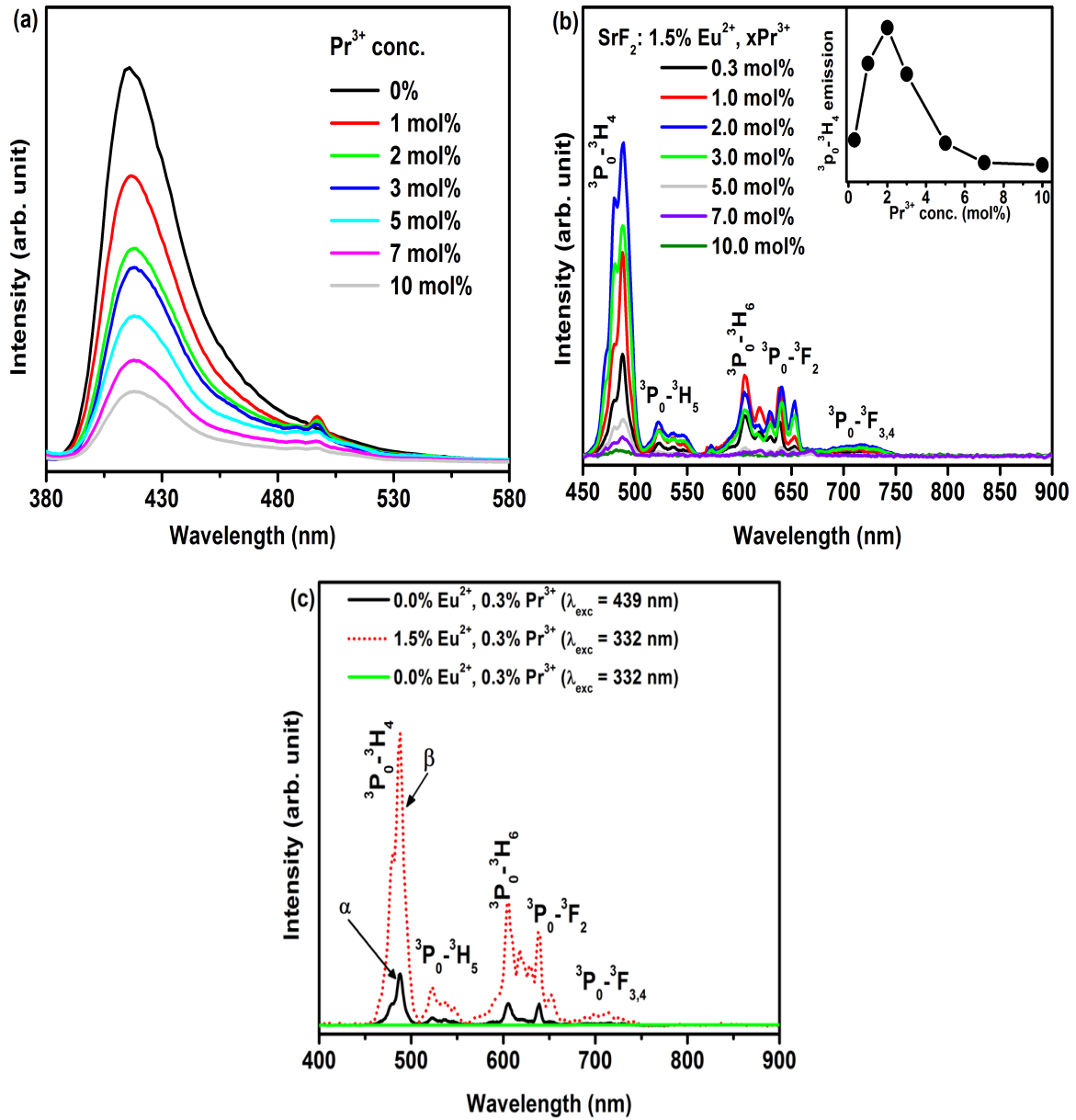


Fig. 7.7: a) Emission spectra of the 1.5 mol% Eu²⁺ in SrF₂ with varied Pr³⁺ concentration, (b) emission spectra of Pr³⁺ in codoped samples with increasing Pr³⁺ concentration and (c) a comparison between Pr³⁺ singly doped (α) and codoped (β) ions in SrF₂. The inset graph in (b) is a variation of Pr³⁺ (³P₀-³H₄) emission intensity as a function of the Pr³⁺ concentration for SrF₂ containing 1.5 mol% Eu²⁺.

Fig. 7.7(c) portrays a comparison between the PL spectra of the SrF₂:Eu²⁺ (1.5 mol%), Pr³⁺ (0.3 mol%) and 0.3 mol% Pr³⁺ singly doped in SrF₂ excited by 332 and 439 nm, respectively. The emission bands of Pr³⁺ in SrF₂ were clearly observed in both spectra. All the Pr³⁺ emission bands were significantly enhanced in the co-doped sample. The biggest enhancement is for the 488 nm band (³P₀-³H₄ transition). A comparison between the total calculated intensity emissions revealed that the Pr bands in the co-doped sample have been enhanced by nearly six times. Fig. 7.7(c) also includes the emission spectrum of the SrF₂:Pr³⁺ (0.3 mol%) without Eu²⁺ excited at 332 nm. It clearly shows that Eu²⁺ well enhanced the emission of Pr³⁺ in the co-doped sample. All these results demonstrate that efficient energy transfer occurred from the Eu²⁺ to the Pr³⁺ ion.

More evidence for the energy transfer between the Eu²⁺ and Pr³⁺ ions are reported in fig. 7.8, where the photoluminescence excitation (PLE) spectra of the Pr³⁺ singly doped and co-doped Eu²⁺ in SrF₂ are plotted. Three excitation bands at 439, 468 and 484 nm were detected for the Pr³⁺ singly doped SrF₂ phosphor when the Pr³⁺ emission wavelength of 488 nm was monitored. These peaks are due to the absorption transition of ³H₄-³P₂, ³H₄-³P₁ and ¹I₆, and ³H₄-³P₀, respectively. These excitation bands were slightly weakened in the Eu²⁺ co-doped phosphor. The co-doped system showed a much broader excitation band, which was attributed to the Eu²⁺:4f⁷-4f⁶5d absorption transition. It can be noticed that the Eu²⁺ co-doping phosphor increases the excitation cross-section of the system compared to that of the Pr³⁺ singly doped phosphor. This could be due to the stronger 4f⁷-4f⁶5d transition than 4f-4f transition of the Pr³⁺ ion and therefore confirms that most of the energy will be absorbed by the Eu²⁺ ion resulting in weakened Pr³⁺ excitation peaks [22]. It might also be one of the reasons that lead to the Pr³⁺ emission enhancement in the co-doped samples.

Luminescence decay curves that were measured for the Eu²⁺ emission 5d energy level contributed further toward the energy transfer efficiency process with different Pr³⁺ ion concentrations. In general, the decay time of the sensitizer ions does not change in the presence and absence of the donor ions if the radiative energy is dominant [23]. Whereas, in case of the non-radiative energy transfer the decay time of sensitizer ions

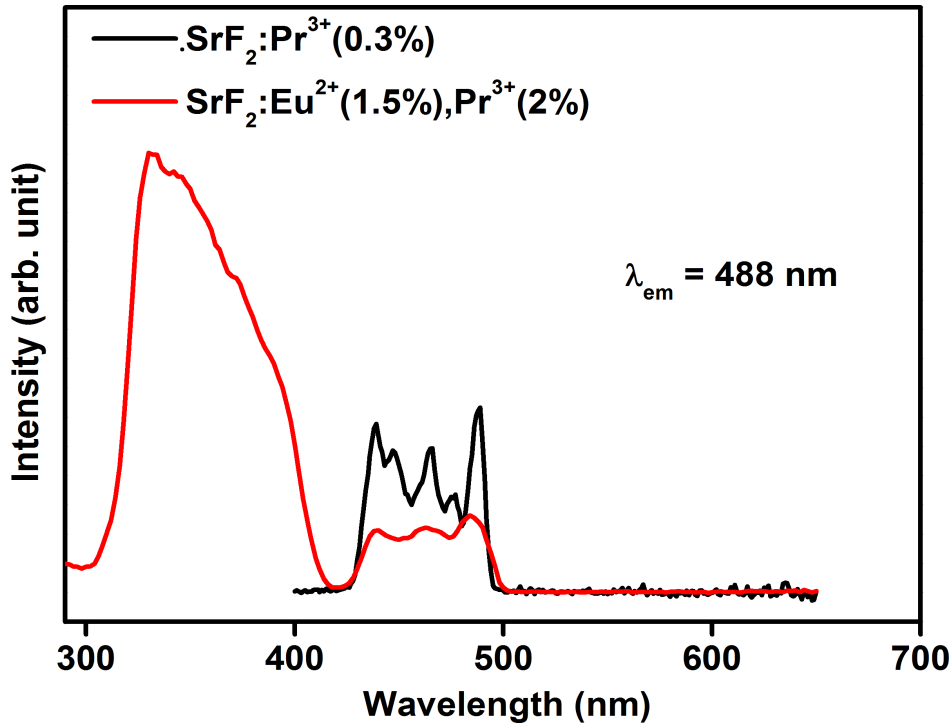


Fig. 7.8: PLE spectra of the SrF₂:0.3 mol% Pr³⁺ and SrF₂:1.5 mol% Eu²⁺, 0.3 mol% Pr³⁺ samples.

gradually decreases with increasing the donor concentration. In fig. 7.9(a), the decay curve are shown for SrF₂:Eu²⁺ (1.5 mol%) codoped with 0, 1, 2, 5, 7 and 10 mol% Pr³⁺. The decay time for the singly doped Eu²⁺ was 435 ns. This decay time was due to radiative decay from the 4f⁶5d¹ (T_{2g}) level, which is in agreement with reported values for the decay time of Eu²⁺ emission [24]. Co-doping with Pr³⁺ induced faster decay, which can be attributed to the energy transfer from Eu²⁺ to Pr³⁺ (fig. 7.9(b)). An estimation for the energy transfer efficiency can be obtained from $\eta_{ET} = 1 - \tau_x/\tau_0$ as outline in reference [23, 25]. Here, τ_x and τ_0 are the corresponding lifetimes of Eu²⁺ in the presence and absent of Pr³⁺, respectively. The corresponding energy transfer efficiencies were 28, 39, 59, 65 and 79% for samples with 1, 2, 5, 7 and 10 mol%, respectively. This shows that the Eu²⁺-Pr³⁺ energy transfer was efficient at high Pr³⁺ concentrations, but that the Pr³⁺ emission was quenched due to concentration quenching. The luminescence decay curves of Pr³⁺ revealed further details into the cross-relaxation between Pr³⁺ ions. In fig. 7.9(b), the decay curves for Pr³⁺ in the co-doped samples with 0.3, 1, 2, 5 and 10 mol% Pr³⁺ are plotted. It can be seen that

the decay curve for 0.3 and 1 mol% are identical and nearly single exponential decay, which demonstrates that up to this doping level there is no interaction between the Pr³⁺ ions. The Pr³⁺ ion started to interact at around 2 mol% and that can be seen in the decay curve for 2 mol%, which has a little bit faster decay. Higher concentrations, however, demonstrated that the concentration quenching of Pr³⁺ emission intensity occurred due to the cross-relaxation between the Pr³⁺ ions.

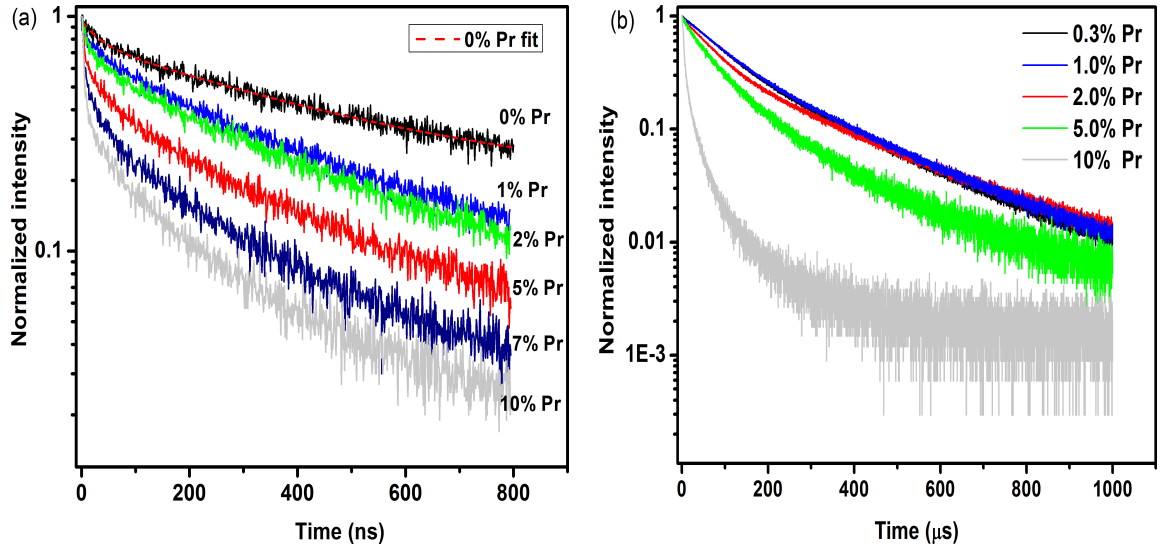


Fig. 7.9: Decay curves of (a) Eu²⁺ 5d (monitoring 416 nm emission) under 355 nm excitation and (b) Pr³⁺ ³P₀-³H₄ (monitoring 488 nm emission) under 375 nm excitation.

A detailed energy transfer processes from Eu²⁺ to Pr³⁺ and the possible cross-relaxation mechanism that may occur between the Pr³⁺ ions are schematically shown in fig. 7.10. Upon 332 nm excitation, one can demonstrate that the absorbed UV photon energy is likely transferred to excited states of Pr³⁺ (¹I₆ and ³P_{*j*}, *j* = 0, 1, 2) by resonant energy transfer via energy migration from Eu²⁺ (4f⁶5d) to Pr³⁺ (³P₂). The other energy transfer pathway is due to the cross-relaxation process between the Eu²⁺ to Pr³⁺ energy levels: [4f⁶5d, ³H₄] → [4f(⁸S_{7/2}), ³P₂]. These two energy transfer pathways result in enhanced Pr³⁺ emission via the ³P₂-¹I₆ and ³P_{*j*} (*j* = 0,1) non-radiative process. This process has been reported recently by W. Xu et. al. [22] for GeS₂-GeS₃-CsCl chalcoc-halide glasses co-doped with Pr³⁺ and Eu²⁺. However, we propose two cross-relaxation processes that are mostly responsible to reduce the ³P₀ emission intensity of Pr³⁺ ions in the SrF₂ matrix. The first cross-relaxation possibility is [³P₀, ³H₄] → [³H₆, ¹D₂] as in-

indicated in fig. 7.10 (pathway 1). The [³P₀,³H₄]→[³H₆,¹D₂] cross-relaxation process is a suggestion taken from literature for Pr³⁺-doped yttrium aluminium garnet (YAG) and gadolinium gallium garnet (GGG) [26, 27]. Another de-activating pathway within a Pr-Pr pair is the [³P₀,³H₄]→[¹G₄,¹G₄] cross-relaxation process as is shown in fig. 7.10 (pathway 2). This pathway was also a suggestion taken from literature for a Pr³⁺ doped KYb(WO₄)₂ crystal [28].

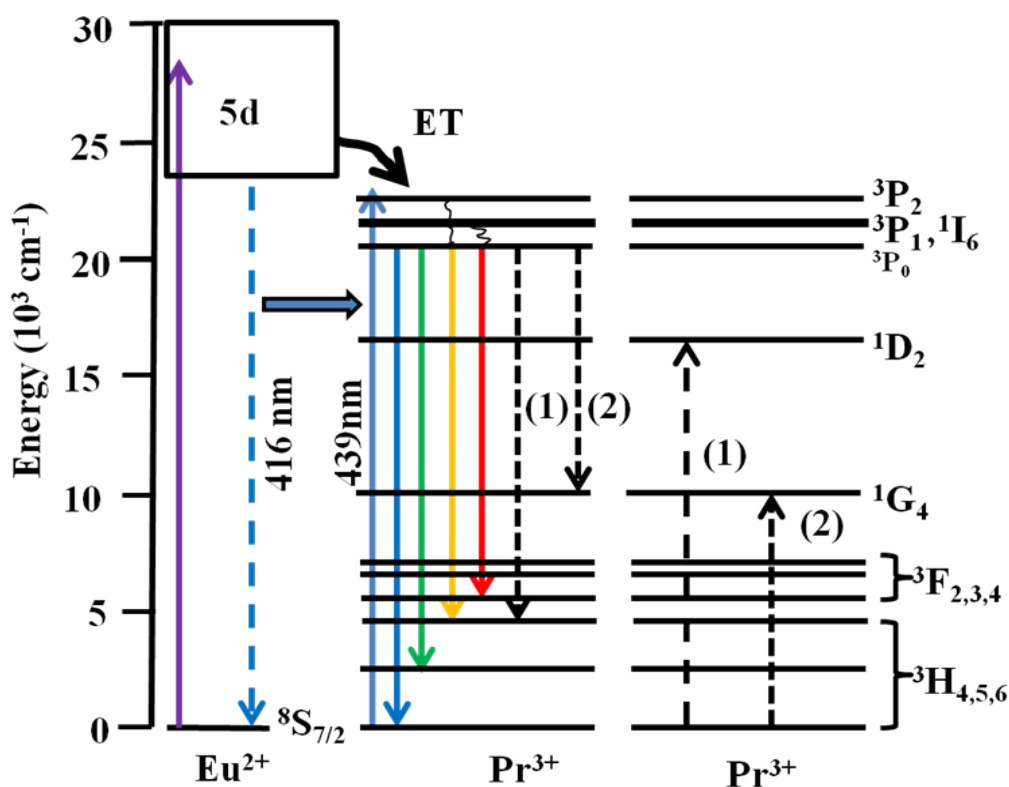


Fig. 7.10: Simplified energy level diagram of Eu²⁺ and Pr³⁺ showing a possible energy transfer between Eu²⁺ and Pr³⁺ ions, and a possible cross-relaxation mechanism between the Pr³⁺ ions.

The present results showed efficient energy transfer from Eu²⁺ to Pr³⁺. The ³P₀ emission intensity has increased and then decreased. The decreased intensity of Pr³⁺ emission bands at higher Pr³⁺ concentration was due to the cross-relaxation process between Pr³⁺ ions. Y. Chen et al. [29] demonstrated the efficient energy transfer between the Eu²⁺ and Pr³⁺ couple in LiSrPO₄ powder that resulted in NIR emission from ¹D₂ and ¹G₄ levels of Pr³⁺. A. Guille et al. [7] demonstrated energy transfer between the Ce³⁺-Pr³⁺ couple in CaYAlO₄ powders and thin film. The energy transfer followed by

a cross-relaxation process that involves the 4f levels of the Ce³⁺ ion, lead to sensitize the ¹D₂ level of the Pr³⁺ ion. The difference was explained by the fact that the Ce³⁺ donor has two 4f energy states (²F_{5/2} and ²F_{7/2}) separated with the same energy as the energy level of Pr³⁺ (³P₀ and ¹D₂). As a result, the cross-relaxation Pr³⁺: [³P₀-¹D₂] → Ce³⁺: [²F_{5/2}-²F_{7/2}] populates the ¹D₂ level of the Pr³⁺ ion. They conclude that the energy transfer from this level to the Yb³⁺ ion is possible but it would not lead to the quantum cutting process. This reduces their potential for application in solar cell. In this study it was shown that the energy transfer from the Eu²⁺ to Pr³⁺ ions lead to sensitized the transition from the ³P₀ level of the Pr³⁺ ion where the quantum cutting process towards the Yb³⁺ ion via resonance and cross-relaxation energy transfer is likely to occur. Therefore, Eu²⁺ can be used as an efficient sensitizer to feed the Pr³⁺ ions and therefore it might improve the NIR absorption of the Pr³⁺-Yb³⁺ couple in SrF₂ for solar cell application. Further investigations on Eu²⁺ sensitized the Pr³⁺-Yb³⁺ couple in SrF₂ is therefore described in chapter 9.

7.4 Conclusions

It was successfully demonstrated that efficient energy transfer occurred from the 5d band of the Eu²⁺ ions toward the ³P_j levels of the Pr³⁺ ion. The energy transfer was likely to be followed by a cross-relaxation process between the Pr³⁺ ions. The Eu²⁺ ions could be an efficient sensitizer to the Pr³⁺ ions and hence increased the excitation cross-section of the Pr³⁺ ions. This might then resulted in a quantum cutting process for the Pr³⁺-Yb³⁺ ion in the SrF₂ crystal.

References

- [1] X. Zhang, J. Zhang, Z. Dong, J. Shi and M. Gong, *J. Lumin.*, **132** (2012) 914-918.
- [2] L. L. Noto, S. S. Pitale, M. A. Gusowki, J. J. Terblans, O. M. Ntwaeaborwa and H. C. Swart, *Powder Technol.*, **237** (2013) 141-146.
- [3] B. M. Van der Ende, L. Aarts and A. Meijerink, *Phys. Chem. Chem. Phys.*, **11** (2009) 11081-11095.
- [4] T. Trupke, M. A. Green and P. Würfel, *J. Appl. Phys.*, **92** (2002) 1668-1674.
- [5] X. Huang, S. Han, W. Huang and X. Liu, *Chem. Soc. Rev.*, **42** (2013) 173-201.
- [6] B. M. Van der Ende, L. Aarts and A. Meijerink, *Adv. Mater.*, **21** (2009) 3073-3077.
- [7] A. Guille, A. Pereira, G. Breton and A. Bensalah-ledoux, B. Moine, *J. Appl. Phys.*, **111** (2012) 043104-043108.
- [8] P. Dorenbos, *J. Lumin.*, **104** (2003) 239-260.
- [9] M. Y. A Yagoub, H. C Swart, L. L Noto, J. H. O'Connell, M. E Lee and E. Coetsee, *J. Lumin.*, **156** (2014) 150-156.
- [10] R. Vercaemst, D. Poelman, L. Fiermans, R. L. Van Meirhaeghe, W. H. Laflere and F. Cardon, *J. Electron. Spectrosc. Relat. Phenom.*, **74** (1995) 45-56.
- [11] S. P. Kowalczyk, N. Edelstein, F. R. McFeely, L. Ley and D. A. Shirley, *Chem. Phys. Lett.*, **29** (1974) 491-495.
- [12] L. L. Noto, W. D. Roos, O. M. Ntwaeaborwa, M. Gohain, M. Y. A. Yagoub, E. Coetsee, and H. C. Swart, *Sci. Adv. Mater.*, **7**(6) (2015) 1197-1206.
- [13] R. Vercaemst, D. Poelman, R. L. Van Meirhaeghe, L. Fiermans, W. H. Laflere and F. Cardon, *J. Lumin.*, **63** (1995) 19-30.
- [14] D. Lu. M. Sugano, X. Y. Sun and W. Su, *Appl. Surf. Sci.*, **242** (2005) 318-325.
- [15] J. Zhang, M. Yang, H. Jin, X. Wang, X. Zhao, X. Liu and L. Peng, *Mater. Res. Bull.*, **47** (2012) 247-252.

- [16] H. Ogasawara, A. Kotani, R. Potze, G. A. Sawatzky and B. T. Thole, *Phys. Rev. B*, **44** (1999) 5465-5469.
- [17] J. Gurgul, M. T. Rinke, I. Schellenberg and R. Pottgen, *Solid State Sci.*, **17** (2013) 122-127.
- [18] S. W. Han, J. D. Lee, K. H. Kim, H. Song, W. J. Kim, S. J. Kwon, H. G. Lee, C. Hwang, J. L. Jeong and J. S. Kang, *J. Korean Phys. Soc.*, **40** (2002) 501-510.
- [19] P. J. Bendell, C. R. A. Catlow, J. Corish and P. W. M. Jacobs, *J. solid state Chem.*, **51** (1984) 159-169.
- [20] D. R. Tallant, D. S. Moore and J. C. Wright, *J. Chem. Phys.*, **67** (1977) 2897-2907.
- [21] M. Y. A. Yagoub, H. C. Swart and E. Coetsee, *Opt. Mater.*, **42** (2015) 204-209.
- [22] W. Xu, Q. Yan, Jing Ren and G. Chen, *J. Lumin.*, **134** (2013) 75-78.
- [23] J. Zhou, Z. Xia, H. You, K. Shen, M. Yang and L. Liao, *J. Lumin.*, **135** (2013) 20-25.
- [24] Q. Luo, X. Qiao and X. Fan, *J. Am. Ceram. Soc.*, **93** (2010) 2684-2688.
- [25] T. Katsumata, T. Nabae, K. Sasajima, S. Komuro and T. Morikawa, *J. Electrochem. Soc.*, **144** (1997) L243-L245.
- [26] R. Naccache, F. Vetrone, A. Speghnini, M. Bettinelli and J. A. Capobianco, *J. Phys. Chem. C*, **112** (2008) 7750-7756.
- [27] X. Wu, W. M. Dennis and W. M. Yen, *Phys. Rev. B*, **50** (1994) 6589-6595.
- [28] P. J. Deren, A. Bednarkiewicz, R. Mahiqu and W. Streck, *Mol. Phys.*, **101** (2003) 951-960.
- [29] Y. Chen, J. Wang, C. Liu, J. Tang, X. Kuang, M. Wu and Q. Su, *Opt. Express*, **21** (2013) 3161-3169.

Chapter 8

NIR quantum cutting of Na^+ and Eu^{2+} - Yb^{3+} couple activated SrF_2 crystal

In this chapter, the influence of the Na^+ ions on the photoluminescence of $\text{SrF}_2:\text{Eu}^{2+}$ - Yb^{3+} is studied. The cooperative energy transfer process from Eu^{2+} to Yb^{3+} ion is also discussed.

8.1 Introduction

Near-infrared (NIR) quantum cutting materials are luminescent materials that convert one high energy (i.e. UV/visible) photon into two NIR photons through lanthanide ions [1–3]. Recently, the use of luminescent materials based on lanthanide ions to boost the efficiency of the Si solar cells have been suggested [2–5]. Most of the quantum cutting materials are based on the Ln^{3+} - Yb^{3+} couple [2]. The low absorption cross-section of the 4f-4f transition of the quantum cutting materials based on the Ln^{3+} - Yb^{3+} couples limit the implementation of such application [1]. Ideal NIR quantum cutting materials for Si solar cells should efficiently convert the UV/Vis broadband part of the solar spectrum into ~ 1000 nm NIR photons. Much attention have lately been paid to the broadband NIR quantum cutting that occurred in the Yb^{3+} ion by using a broadband excitation ions as sensitizers [1, 6–9]. The 4f-5d transition of the broadband strongly depend on the crystal field of the host. The Eu^{2+} ion in SrF_2 emits a blue photon centred at 416 nm [10] which is approximately twice the single excited state's ($^2\text{F}_{5/2}$)value of the Yb^{3+} ion. This makes Eu^{2+} ion an efficient sensitizer for Yb^{3+} through cooperative energy transfer. It is therefore quite meaningful to investigate the Eu^{2+} - Yb^{3+} couple co-doped in SrF_2 for its application in photovoltaic cells.

The SrF_2 crystal is one of the widely used hosts in various applications [2, 11–13]. The photoluminescence properties of SrF_2 doped by Ln^{3+} ions have been extensively investigated in which charge compensation for the substitution of Ln^{3+} for Sr^{2+} is required.

This gives rise to a rich multisites structure, which leads to broad absorption and emission bands. The disadvantage of such charge compensation (fluorine interstitial) is that it would reduce the quantum efficiency of the system [14]. A new class of charge compensation that is based on monovalent impurity ions that exist along with Ln³⁺ ions into the fluorite hosts have been reported [14–16]. Co-doping Yb³⁺ with Na⁺ as a charge compensator decreases the multisite of Yb³⁺ since Yb³⁺-Na⁺ complexes are expected to dominate the system [14].

8.2 Experimental

Analytical grade of Sr(NO₃)₂, Eu(NO₃)₃·5H₂O, Yb(NO₃)₃·5H₂O, NaOH and NH₄F were used without further purification. For a typical synthesis of SrF₂:Eu²⁺, Yb³⁺ by using the co-precipitation process, 30 mmol of NH₄F and 0.1 mol/mL of NaOH were added drop-wise to an aqueous solution containing Sr(NO₃)₂, Yb(NO₃)₃·5H₂O and Eu(NO₃)₃·5H₂O in periods of about 30 min. After one hour of stirring, the mixture was left for 5 hours. Then, the product was collected by using a centrifugal and washed with water and ethanol. Finally, the product was dried for 48 hours in an oven at 80 °C. The samples were annealed under a reducing atmosphere (Ar 96%/H₂ 4%) in order to reduce Eu³⁺ into Eu²⁺ ions.

The structure of the prepared samples was characterised by XRD using a Bruker Advance D8 diffractometer (40 kV, 40 mA) with Cu K α x-rays ($\lambda = 0.154$ nm). UV-Vis-NIR diffuse reflection spectra were measured using a Perkin Elmer Lambda 950 spectrophotometer with an integrating sphere and using spectralon as the reference material. PL spectra were collected by using a Cary Eclipse fluorescence spectrophotometer equipped with a xenon lamp. The NIR PL spectra were collected with a He-Cd laser PL system with a 325 nm excitation wavelength and a 2 mm InGaAs photodiode detector. Luminescence decay curves of Eu²⁺ were recorded under pulsed excitation (HORIBA scientific) with a 375LH NanoLED diode with a 375 nm excitation wavelength. All measurements were performed at room temperature.

8.3 Results and discussion

It is worth mentioning that the Na⁺ concentration was fixed to 0.5 mol% throughout this study. Fig. 8.1 shows the XRD patterns of singly doped Eu²⁺ and co-doped Eu²⁺-Yb³⁺ ions in the SrF₂ crystal. For Eu²⁺ singly doped SrF₂, the pattern crystallized into the cubic structure of SrF₂ (card 00-086-2418). Co-doping with low concentrations of Yb³⁺ ions (up to 3 mol%) with the Na⁺ ions in the SrF₂:Eu²⁺ (1.5 mol%) structure did not cause any change in the XRD patterns. With increased Yb³⁺ ion's concentrations, the XRD patterns of the samples can be indexed as a mixture of the cubic phases for SrF₂ and NaYbF₄ (JCPDS 77-2043). The schematic structure of pure SrF₂ is shown in fig. 8.2(a). The Sr²⁺ sub-lattice is face-centered cubic, the F⁻ sub-lattice is simple cubic where each second cube contains Sr²⁺ ion (others are empty). The divalent (Eu²⁺) ion easily substitutes for the central Sr²⁺ ion, leaving it in a crystalline environment. In general, when Yb³⁺ ions are co-doped in the system, the extra positive charge of the Yb³⁺ relative to the Sr²⁺ ion makes some type of charge-compensation mechanism necessary, which is required to maintain the electrical neutrality of the crystal. The O_h (cubic) symmetry of the Sr²⁺ site would be changed to the lower symmetries, tetragonal (C_{4v}) and trigonal (C_{3v}), respectively [14, 17]. Fig. 8.2(b) shows the possible F⁻ interstitial sites. Co-doping with Yb³⁺ and Na⁺ ions in the SrF₂ crystals can also cause the Na⁺ ions to compensate with the extra charge of the Yb³⁺ ion. The Na⁺ ions can therefore enter in substitutional or interstitial positions near the Yb³⁺ ions and then result in a modified C_{3v} symmetry (fig. 8.2(b)) [15]. Some of the possible sites for Na⁺ ions in the SrF₂ host are shown in fig. 8.2(b). The cubic NaYbF₄ system is a fluorite structure (SrF₂) with the Sr²⁺ sites randomly occupied by Na⁺ and Yb³⁺ ions [18]. Thus, the presence of Na⁺ ions with increased Yb³⁺ concentration in the SrF₂ structure gradually lead to the formation of mixed cubic structure between SrF₂ and NaYbF₄.

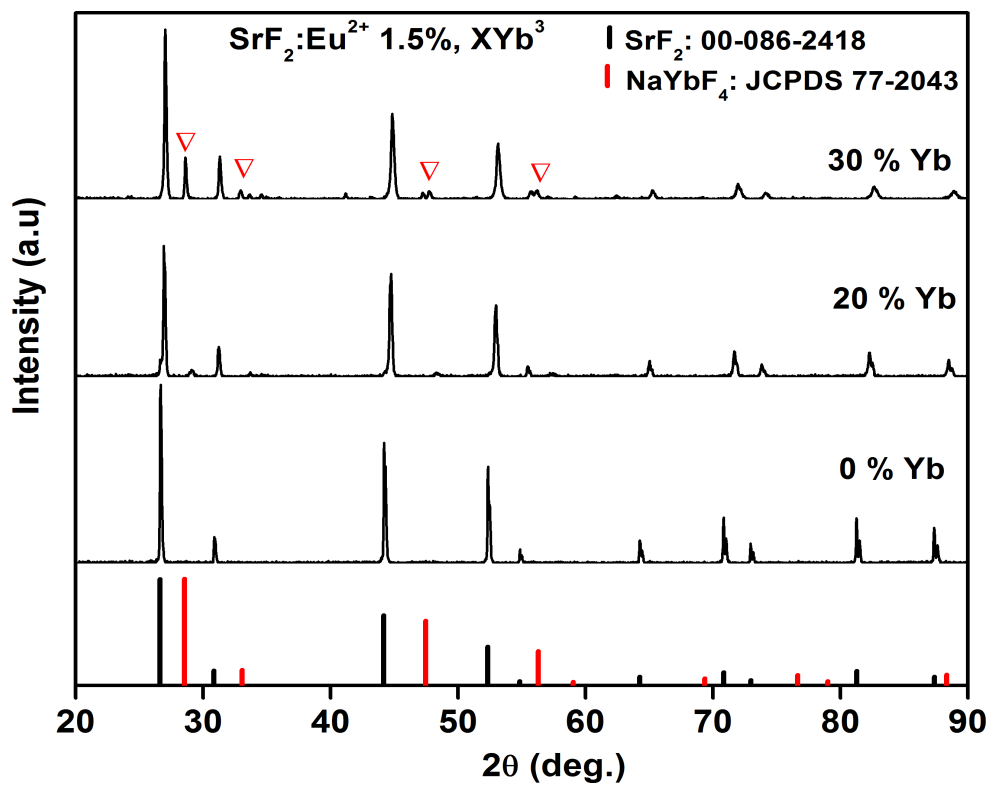


Fig. 8.1: XRD patterns of the $\text{SrF}_2:\text{Eu}^{2+}$ (1.5 mol%) crystals and a mixture of the SrF_2 and NaYbF_4 XRD patterns obtained after co-doping with high Yb^{3+} concentration (0.5 mol% Na). The peaks marked with a triangle refer to the cubic-phase of NaYbF_4 . The SrF_2 and NaYbF_4 standard XRD patterns are also shown.

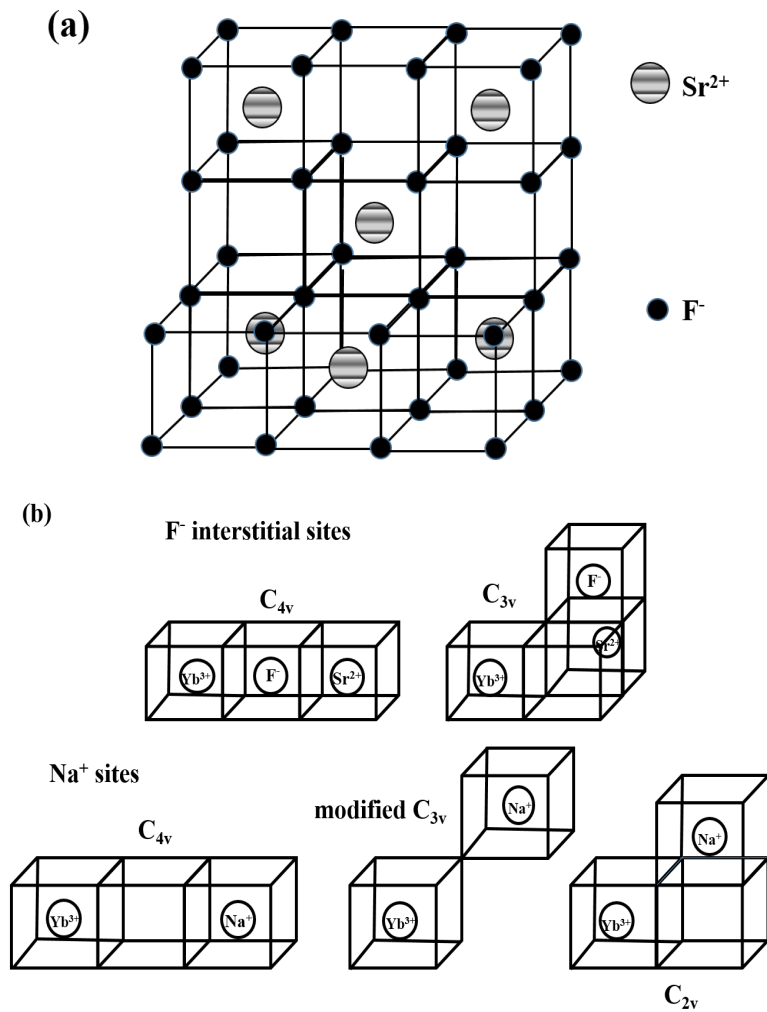


Fig. 8.2: (a) A pure SrF_2 structure showing that every second simple cubic of the F^- sub-lattice contains a Sr^{2+} ion, (b) Schematic pictures of some Yb^{3+} ions' charge compensation pairs (i.e. both the Na substitutional sites and the F interstitial sites).

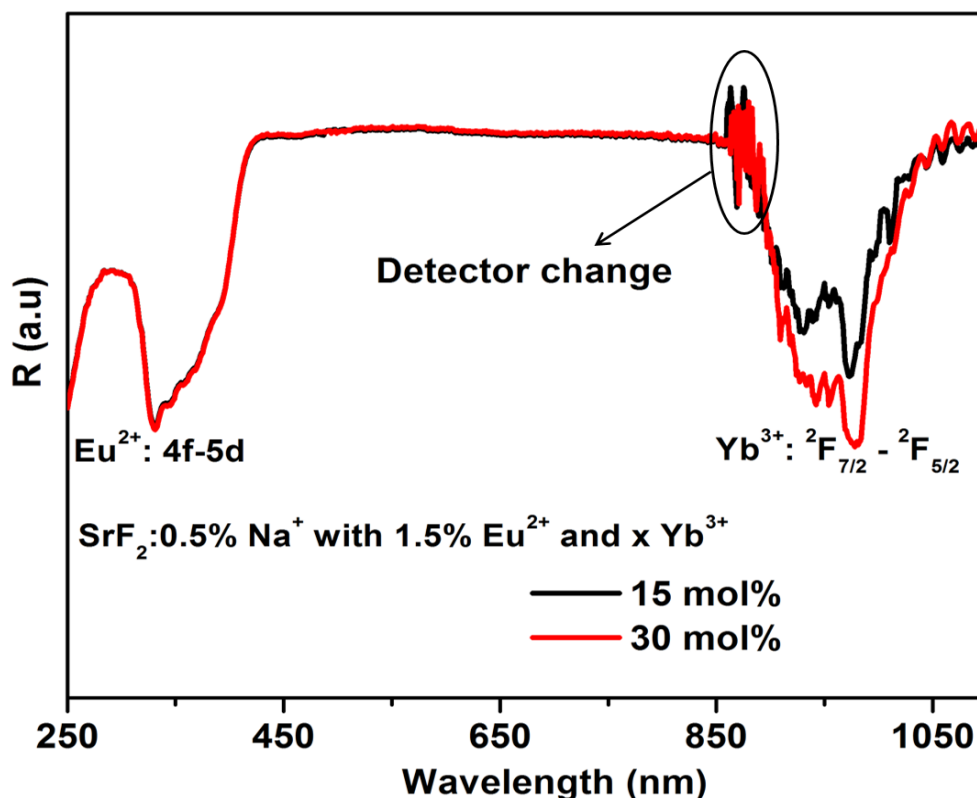


Fig. 8.3: Diffuse reflectance spectra of Eu^{2+} and Yb^{3+} ions co-doped in SrF_2 : 0.5 mol% Na^+ with 15 and 30 mol% Yb^{3+} ions' concentrations.

Fig. 8.3 depicts the diffuse reflectance spectra of 1.5 mol% Eu^{2+} co-doped with 15 and 30 mol% Yb^{3+} concentration in the $\text{SrF}_2:\text{Na}^+$ (0.5 mol%) to confirm the existence of europium in the divalent state. The broad absorption band located between 275 and 400 nm is a result of the strong absorption of the Eu^{2+} ($4f^7-4f^65d$) ion. It can be seen that the absorption strengths for the peaks corresponding to Eu^{2+} ions have similar absorption strength for the two samples, which demonstrates that the Eu^{2+} is equally incorporated in the SrF_2 crystal. The absorption peak in the NIR part with a maxima at 976 nm is assigned to the $4f-4f$ transition of the Yb^{3+} ion. The weak sensitivity of our system in the NIR region results in a weak and noisy intensity signal for the low Yb^{3+} concentration. As expected, the intensity of the NIR absorption band increased with increasing Yb^{3+} doping concentration. It is well known that the interstitial fluorine sites induce broad excitation bands to trivalent rare-earth ions-doped SrF_2 due to a rich multisite structure of several types of charge compensation (nearest neighbor ($\text{C}_{4\nu}$),

next nearest neighbor (C_{3v}) or no local site (O_h) and various clusters) [14, 17]. If Na⁺ ions also present in fluoride host it leads to narrow absorption and emission bands of the Ln³⁺ ions [16]. Due to the weak sensitivity of our UV-Vis system in the NIR region no significant change has been observed in the NIR absorption spectra for both the F⁻ and Na⁺ sites.

The excitation and emission spectra of Eu²⁺ in SrF₂ are reported in chapter 7, fig. 7.5. The spectra clearly showed broad excitation and emission bands centred at 332 and 416 nm, respectively. The maximum luminescence intensity occurred for the sample doped with 1.5 mol% and a further increase in concentration resulted in a decrease in Eu²⁺ emission intensity.

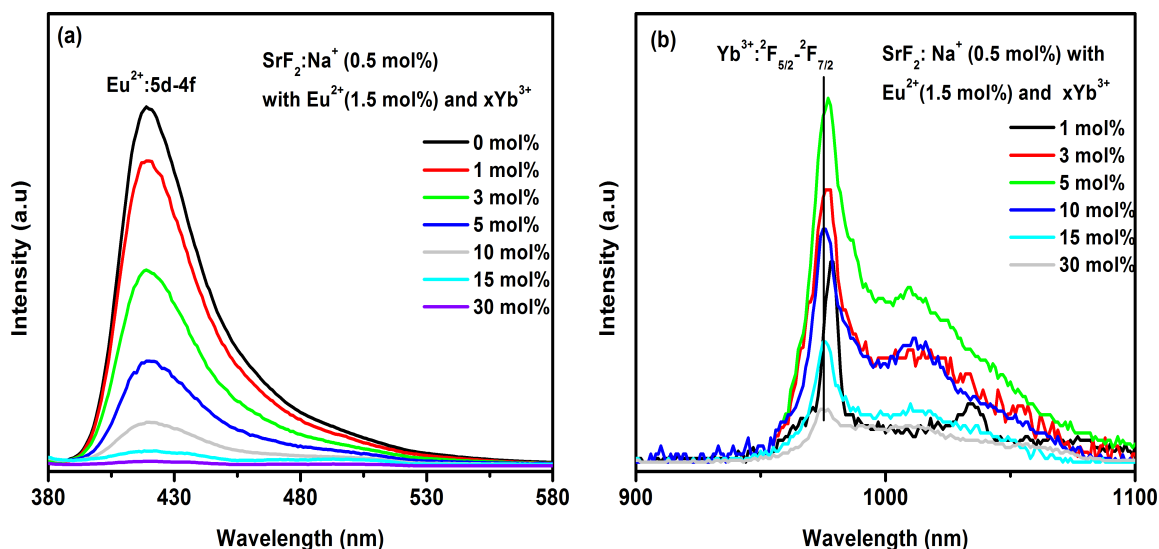


Fig. 8.4: (a) Eu²⁺ emission intensity as a function of Yb³⁺ concentration, and (b) NIR emission spectra as a function of Yb³⁺ concentration excited by a He-Cd laser system with a 325 nm excitation wavelength.

To study the energy transfer in the Eu²⁺-Yb³⁺ couple as well as the influence of Na⁺ on Yb³⁺ emission, a series of powder samples were prepared with 0.5 mol% Na⁺, 1.5 mol% of Eu²⁺ and various Yb³⁺ concentrations under identical condition. In fig. 8.4(a) and (b), the emission spectra for the visible region of the Eu²⁺ and NIR of Yb³⁺ with fixed Eu²⁺ and varied Yb³⁺ concentrations are shown. Under UV excitation the PL spectra of Eu²⁺ clearly showed the broad emission band centred at 416 nm, which is similar to that in the Eu²⁺ singly doped SrF₂ crystal. The NIR emission spectra that are shown

in fig. 8.4(b) correspond to the Yb³⁺ ions' transitions from the ²F_{5/2} excited state to ²F_{7/2} ground state. The Yb³⁺ emission is strongly affected by the Na⁺ impurity ions. One can see that the emission intensity of Yb³⁺ at 1 mol% (fig. 8.4(b)) is relatively different from the other spectra. It consists of two narrow peaks centered at 978 and 1035 nm. With increased Yb³⁺ concentration, the shape and position of these two peaks were significantly changed. The peak at 1035 nm strongly blue shifted whereas the peak at 978 nm gradually blue shifted and broadened. The influence of Na⁺ on the absorption and emission of the Yb³⁺ ions has been reported previously [14, 15, 17]. All these previous studies agreed that the Na⁺ ions give rise to narrow and clearly resolved, small blue shifted, emission and absorption spectra of the Yb³⁺ ions. In this study, one can conclude that the Na⁺ impurity ions strongly influence the Yb³⁺ spectra at low Yb³⁺ concentrations. This is because at low Yb³⁺ concentration the Na⁺ sites are abundant whereas an increase in the Yb³⁺ concentrations gradually transformed the structure to a mixture of the two cubic phases of SrF₂ and NaYbF₄ with fluorine interstitial sites.

From fig. 8.4(a) it can be seen that the Eu²⁺ (1.5 mol%) emission (4f⁶5d-4f⁷ transition) gradually decreased until it is almost totally quenched at the highest Yb³⁺ concentration. On the contrary the Yb³⁺ emissions are enhanced steadily with increased Yb³⁺ concentration (up to 5 mol%). This is shown in fig. 8.4(b) where the NIR emission of Yb³⁺ are plotted with varied Yb³⁺ concentrations. The increase in the Yb³⁺ concentration resulted in a concentration quenching effect that occurred to the Yb³⁺ emissions at higher (higher than 5 mol%) concentrations. This can be attributed to the concentration quenching caused by the interactions between the nearby Yb³⁺ ions. The decrease in the Eu²⁺ emission indicates that there most likely exists an energy transfer from Eu²⁺ to Yb³⁺.

Fig. 8.5 shows the decay curves of Eu²⁺:4f⁶5d¹-4f⁷ (416 nm) with varied Yb³⁺ concentration. The decay times of Eu²⁺ in the singly doped and co-doped samples are listed in table 8.1. The decay time for the singly doped Eu²⁺ was 435 ns. This decay time was due to radiative decay from the 4f⁶5d¹ (T_{2g}) level, which is well in agreement with a reported value for the decay time of Eu²⁺ emission in SrF₂ [19]. Co-doping

with Yb³⁺ ion induced faster decay, which can be attributed to the energy transfer from Eu²⁺ to Yb³⁺. An estimation of energy transfer efficiency can be obtained from $\eta_{ET,x\%Yb} = 1 - \tau_x / \tau_0$ as outline in literature [20, 21]. Here, τ_x and τ_0 are the corresponding average lifetimes of Eu²⁺ in the presence and absent of Yb³⁺, respectively. From table 1, the energy transfer efficiency of Eu²⁺ increased gradually with an increase in the Yb³⁺ concentration. The energy transfer efficiency for the sample doped with 1.5 mol% Eu²⁺ and 10 mol% Yb³⁺ is about 89 %. This shows that the Eu²⁺-Yb³⁺ energy transfer is completed at these higher concentrations. For concentration higher than 10 mol% Yb³⁺, the decay curves of Eu²⁺ however seem to remain constant. This might be attributed to the decrease of the Eu²⁺ lifetime less than the pulsed duration of the laser system, which was used to measure the Eu²⁺ PL decay curves. The Yb³⁺ emission was quenched due to concentration quenching at the higher concentrations. The energy transfer between Eu²⁺ and Yb³⁺ has been reported to occur through cooperative quantum cutting energy transfer [7, 8]. The energy transfer based on cooperative quantum cutting has been realized in different lanthanide ion couples [7, 22, 23]. The quantum cutting energy transfer is based on two different models for the interaction between the donor and acceptor centers, i.e. first order energy transfer and second-order energy transfer. In the first order energy transfer, the emission spectrum of the donor should overlap with the excitation spectrum of the acceptor. In the case where the overlap between the donor's emission and acceptor's absorption spectra is absent, second-order down-conversion may become the dominant relaxation process [22]. The resonance condition occurs when the sum of the energy of the absorption transitions of the two acceptor centers approximately equals the energy of the donor's emission. The first order energy transfer can be excluded to occur in the Eu²⁺-Yb³⁺ couple, since energy overlap does not exist. Hence, the energy transfer between Eu²⁺ and Yb³⁺ couple occurred through cooperative quantum cutting energy transfer, where one Eu²⁺ photon splits to excite two Yb³⁺ ions.

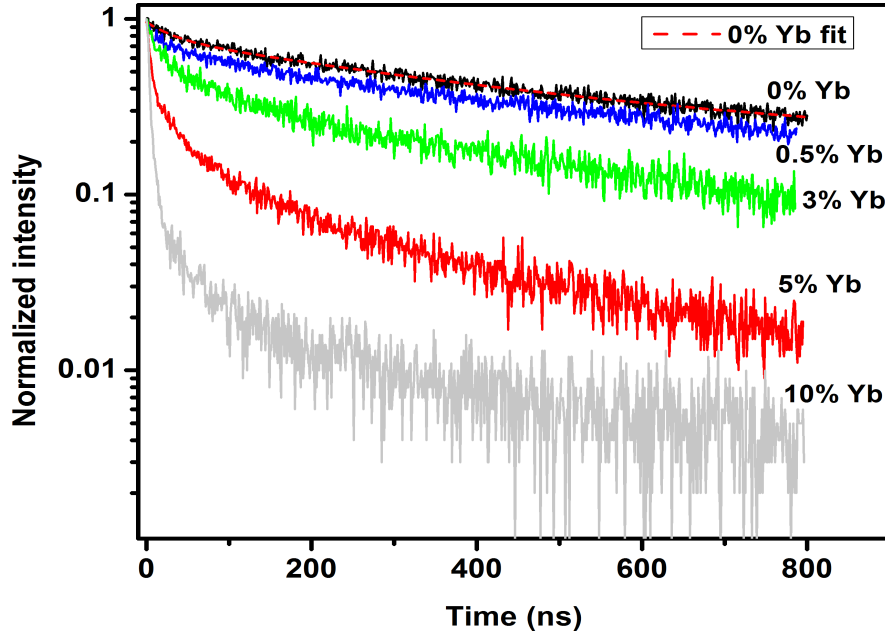


Fig. 8.5: Normalized decay curves of the Eu²⁺ emission at 416 nm as a function of the Yb³⁺ concentration.

Yb ³⁺ conc.(mol%)	τ (ns)	$\eta_{ET,x\%Yb}$
0	435	0
0.5	383	12
3	4243	44
5	105	76
10	47	89

Table 8.1: The average decay lifetime (τ (nm)) of the 5d-4f transition of Eu²⁺ (416 nm) and the Eu²⁺-Yb³⁺ energy transfer efficiency ($\eta_{ET,x\%Yb}$).

The total quantum efficiency of the SrF₂:Eu²⁺, Yb³⁺ is defined as the ratio between the total number of photons emitted by Eu²⁺ to the number of the photons absorbed by Yb³⁺, and can be calculated as a function of Yb³⁺ concentration by [24]:

$$\eta = \eta_{Eu}(1 - \eta_{ET,x\%Yb}) + 2\eta_{Yb}\eta_{ET,x\%Yb}, \quad (8.1)$$

where η_{Eu} and η_{Yb} are the quantum efficiency of Eu²⁺ and Yb³⁺ luminescence, respectively, which are set to unity [24, 25]. Considering only the Eu²⁺ energy transfer, the

highest quantum efficiency, 189 %, was obtained for samples co-doped with 10 mol%. However, the actual quantum efficiency is lower due to the concentration quenching and other non-radiative decay processes for Yb^{3+} or due to other quenching sites originating from material defects.

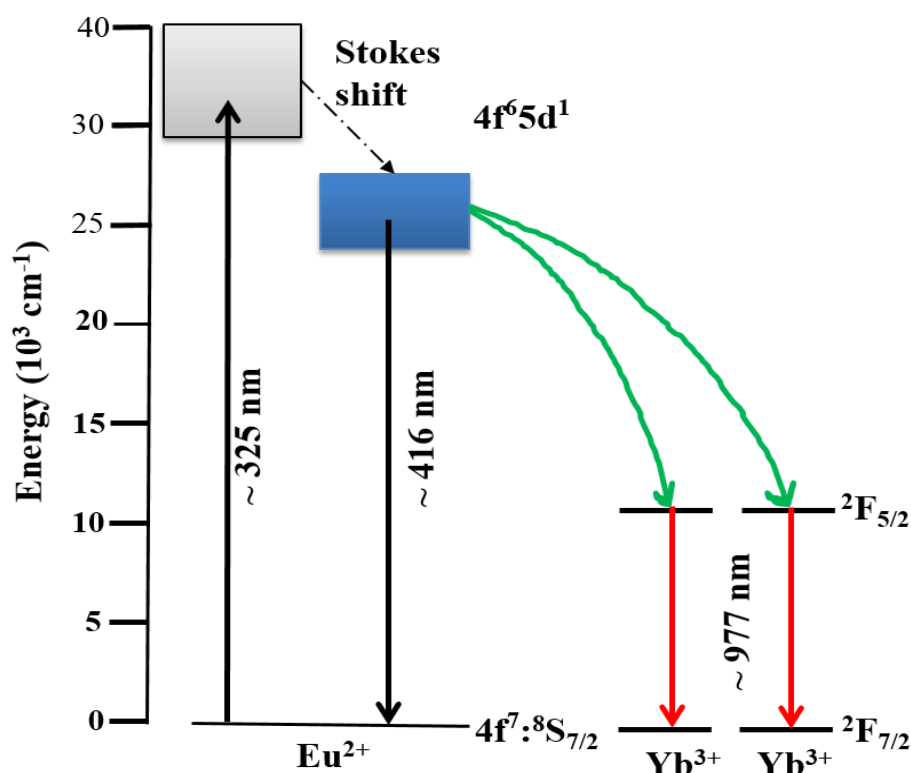


Fig. 8.6: Schematic energy level diagrams of Eu^{2+} and Yb^{3+} in SrF_2 and possible energy transfer process between Eu^{2+} and Yb^{3+} .

The schematic energy levels with the electronic transitions, which may be involved in the cooperative energy-transfer process between one of the Eu^{2+} ions and two of the Yb^{3+} ions in the SrF_2 crystal are shown in fig. 8.6. The emission energy of the $\text{Eu}^{2+}:\text{4f}^6\text{5d}^1\text{-4f}^7$ transition is approximately twice that of the $\text{Yb}^{3+}:\text{2F}_{5/2}\text{-2F}_{7/2}$ transition. Upon 325 nm excitation, Eu^{2+} ions emit at 416 nm due to the $\text{4f}^6\text{5d}^1\text{-4f}^7$ transition, which activates two NIR photons due to the $\text{Yb}^{3+}:\text{2F}_{5/2}\text{-2F}_{7/2}$ transition. The present results suggested that Eu^{2+} can be used as an efficient sensitizer to enhance the Yb^{3+} NIR emission through the a cooperative quantum cutting process.

8.4 Conclusions

Various Yb³⁺ ions' concentrations and Na⁺ (0.5 mol%) co-doped in SrF₂:Eu²⁺ (1.5 mol%) were prepared by the co-precipitation method. XRD results showed a mixture of the two cubic phases of SrF₂ and NaYbF₄ at high Yb³⁺ concentrations. At low Yb³⁺ concentrations, the NIR emission was strongly effected by the Na⁺ sub-situational sites. Cooperative energy transfer from Eu²⁺ to Yb³⁺ ions was demonstrated. The broad emission band of Eu²⁺ (4f⁶5d-4f⁷) leads to efficient NIR emission from Yb³⁺ through the quantum cutting process. The broad UV-Vis energy excitation photons that was efficiently converted into NIR photons corresponded well with the energy of the bandgap of Si. We therefore conclude that the material studied in this work might have practical application possibilities for raising the efficiency of c-Si solar cells.

References

- [1] B. M. Van der Ende, L. Aarts and A. Meijerink, *Phys. Chem. Chem. Phys.*, **11** (2009) 11081-11095.
- [2] X. Huang, S. Han, W. Huang and X. Liu, *Chem. Soc. Rev.*, **42** (2013) 173-201.
- [3] Q.Y. Zhang and X. Y. Huang, *Prog. Mater. Sci.*, **55** (2010) 353-427.
- [4] B. M. Van der Ende, L. Aarts and A. Meijerink, *Adv. Mater.*, **21** (2009) 3073-3077.
- [5] D. Serrano, A. Braud, J.-L. Doualan, P. Camy, A. Benayad, V. Ménard and R. Moncorgé, *Opt. Mater.*, **33** (2011) 1028-1031.
- [6] F. You, A. J. J. Bos, Q. Shi, S. Huang and P. Dorenbos, *J. Phys.: Condens. Matter*, **23** (2011) 215502-215508.
- [7] Q. Yan, J. Ren, Y. Tong and G. Chen, *J. Am. Ceram. Soc.*, **96** (2013) 1349-1351.
- [8] J. Zhou, Y. Teng, G. Lin, X. Xu, Z. Ma and J. Qiu, *J. Electrochem. Soc.*, **157** (2010) B1146-B1148.
- [9] Y. Teng, J. Zhou, X. Liu, S. Ye and J. Qiu, *Opt. Express*, **18** (2010) 9671-9676.
- [10] M. Y. A Yagoub, H. C Swart, L. L Noto, J. H. O'Connell, M. E Lee and E. Coetsee, *J. Lumin.*, **156** (2014) 150-156.
- [11] K. V. Ivanovskikh, V. A. Pustovarov, M. Krim and B.V. Shulgin, *J. Appl. Spectrosc.*, **72** (2005) 564-568.
- [12] K. Ivanovskikh, V. Pustovarov, A. Smirnov and B. Shulgin, *Phys. Stat. Sol. C*, **4** (2007) 889-892.
- [13] N. Kristianpoller, D. Weiss and R. Chen, *Radiat. Meas.*, **38** (2004) 719-722.
- [14] L. Su, J. Xu, H. Li, W. Yang, Z. Zhao, J. Si, Y. Dong and G. Zhou, *Opt. Express*, **30** (2005) 1003-1006.
- [15] I. Nicoara and M. Stef, *Eur. Phys. J. B*, **85** (2012) 180-186.

-
- [16] D. W. Pack, W. J. Manthey and D. S. McClure, *Phys. Rev. B*, **40** (1989) 9930-9944.
- [17] L. Su, J. Xu, H. Li, L. Wen, W. Yang, Z. Zhao, J. Si, Y. Dong and G. Zhou, *J. Cryst. Growth*, **277** (2005) 264-268.
- [18] F. Wang, Y. Han, C. S. Lim, Y. Lu, J. Wang, J. Xu, H. Chen, C. Zhang, M. Hong and X. Liu, *Nature lett.*, **463** (2010) 1061-1065.
- [19] Q. Luo, X. Qiao and X. Fan, *J. Am. Ceram. Soc.*, **93** (2010) 2684-2688.
- [20] J. Zhou, Z. Xia, H. You, K. Shen, M. Yang and L. Liao, *J. Lumin.*, **135** (2013) 20-25.
- [21] T. Katsumata, T. Nabaie, K. Sasajima, S. Komuro and T. Morikawa, *J. Electrochem. Soc.*, **144** (1997) L243-L245.
- [22] H. Wen and P. A. Tanner, *Opt. Mater.*, **33** (2011) 1602-1606.
- [23] B. Fan, C. Point, J. L. Adam, X. Zhang and X. Fan, *J. Appl. Phys.*, **110** (2011) 113107-113114.
- [24] P. Vergeer, T. J. H. Vlugt, M. H. F. Kox, M. I. den Hertog, J. P. J. M. van der Eerden and A. Meijerink, *Phys. Rev. B*, **71** (2005) 014119-014129.
- [25] Q. Y. Zhang and G. F. Yang, *Appl. Phys. Lett.*, **91** (2007) 051903-051905.

Chapter 9

Eu²⁺ sensitized Pr³⁺-Yb³⁺ quantum cutting couple in a SrF₂ crystal

In this chapter the possibility of using the broadband excitation of Eu²⁺ ion as a sensitizer for Pr³⁺-Yb³⁺ couple in SrF₂ is discussed.

9.1 Introduction

In chapter 7, we demonstrated excellent sensitization effects of Eu²⁺ on the luminescence properties of the Pr³⁺ ion. The luminescence intensities of the Pr³⁺ ion greatly enhanced with the co-doping of Eu²⁺. In this chapter, we investigated however to what extent the NIR emission of the Pr³⁺-Yb³⁺ couple in SrF₂ crystal can be affected by using the broadband excitation of Eu²⁺ ion as a sensitizer. The phosphors were prepared by the co-precipitation process. The energy transfer mechanism is demonstrated by the decrease of Eu²⁺ and Pr³⁺ related photoluminescence and by lifetime measurements with increasing Yb³⁺ concentration.

9.2 Experimental

A detail descriptions of the co-precipitation synthesis method can be found in chapter 7. Analytical grade of Yb(NO₃)₃·5H₂O was used as source for the Yb³⁺ dopant.

The diffuse reflection spectra were measured using a Perkin Elmer Lambda 950 spectrophotometer with an integrating sphere and using spectralon as the reference material. PL spectra were collected by using a Cary Eclipse fluorescence spectrophotometer equipped with a xenon lamp as well as the He-Cd laser PL system with a 325 nm excitation wavelength. NIR PL measurements were collected with a He-Cd laser PL system with a 325 nm excitation wavelength and 2 mm InGaAs photodiode detector.

Luminescence decay curves of Eu²⁺ were recorded under pulsed excitation (HORIBA scientific) with 375LH NanoLED diode with a 375 nm excitation wavelength. The luminescence decay curves of Pr³⁺ were measured under pulsed excitation using a diode pumped YAG laser with a 335 nm excitation wavelength, power of 1.3 milliwatt and a SR430 Multichannel scaler photomultiplier (Linköping, Sweden). All measurements were performed at room temperature.

9.3 Results and discussion

Fig. 9.1 shows the absorption bands observed in the diffuse reflectance spectra of Eu²⁺ sensitized Pr³⁺-Yb³⁺ couple in the SrF₂ crystal. The sharp small bands centred at 440, 466, 482, 588 nm are ascribed to the 4f-4f transition from the ³H₄ ground state to the ³P₂, ³P₁, ³P₀ and ¹D₂ excited states of the Pr³⁺ ion (labelled in fig. 9.1), respectively [1]. The broad absorption band below 400 nm represents the strong absorption of the Eu²⁺ (4f⁶5d-4f⁷) ion. The Eu²⁺ and Pr³⁺ ions' absorption include a large part of the UV and Vis regions ranging from 310 to 590 nm. The additional absorption peak in the NIR part with a maxima at 976 nm is assigned to the 4f-4f transition of the Yb³⁺ ion. The weak sensitivity of our system in the NIR region results in weak intensity and noise for all the samples below 5 mol% Yb³⁺ concentration and this also influenced the intensity of the samples with high Yb³⁺ concentration. All the Pr³⁺ ion's absorption bands in the NIR region were also not observed due to the system's sensitivity [2]. As expected, the intensity of the Yb³⁺:²F_{7/2}-²F_{5/2} absorption increased with increasing Yb³⁺ doping concentration. The diffuse reflectance results confirmed that the Eu ion is in the divalent state and all the dopants were successfully incorporated in the host material.

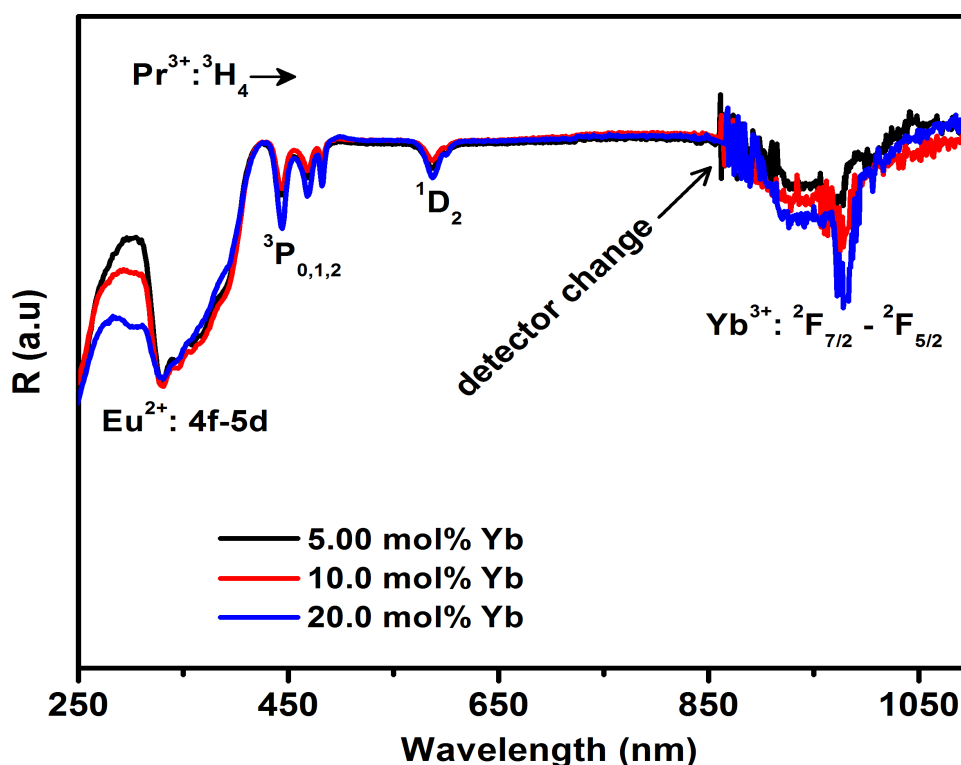


Fig. 9.1: Diffuse reflectance spectra of the Eu²⁺ sensitized Pr³⁺-Yb³⁺ couple in SrF₂ with different Yb³⁺ concentrations.

Fig. 9.2 shows the emission of singly Eu²⁺ and co-doped Pr³⁺ in the SrF₂ crystal excited by 325 nm. The spectrum of singly Eu²⁺ doped crystal shows only the emission of inter-configuration 4f⁶5d1¹-4f⁷ allowed transition of Eu²⁺ [3, 4]. The co-doped spectrum consists of emission from both the Eu²⁺ and Pr³⁺ ions. The strong broad emission band in the co-doped spectrum is the characteristic emission of Eu²⁺:4f⁶5d1¹-4f⁷ allowed transition. The narrow emission bands centred at 488, 524, 605, 638, 715 and 730 nm were assigned to the Pr³⁺:4f-4f transitions (³P₀-³H₄, ³P₀-³H₅, ³P₀-³H₆ and ³P₀-³F₂), respectively [1, 5]. The strong emission of Eu²⁺ suppressed the weak emission bands of the Pr³⁺ ion. In fig. 9.2 the emission spectrum of the SrF₂:Pr³⁺ without Eu²⁺ excited at 325 nm is also shown. It clearly shows no Pr³⁺ emission has occurred. The presence of Pr³⁺ emission under 325 nm excitation, in the co-doped samples, indicates therefore that there most likely exists an energy transfer from Eu²⁺ to Pr³⁺, as can be seen in chapter 7.

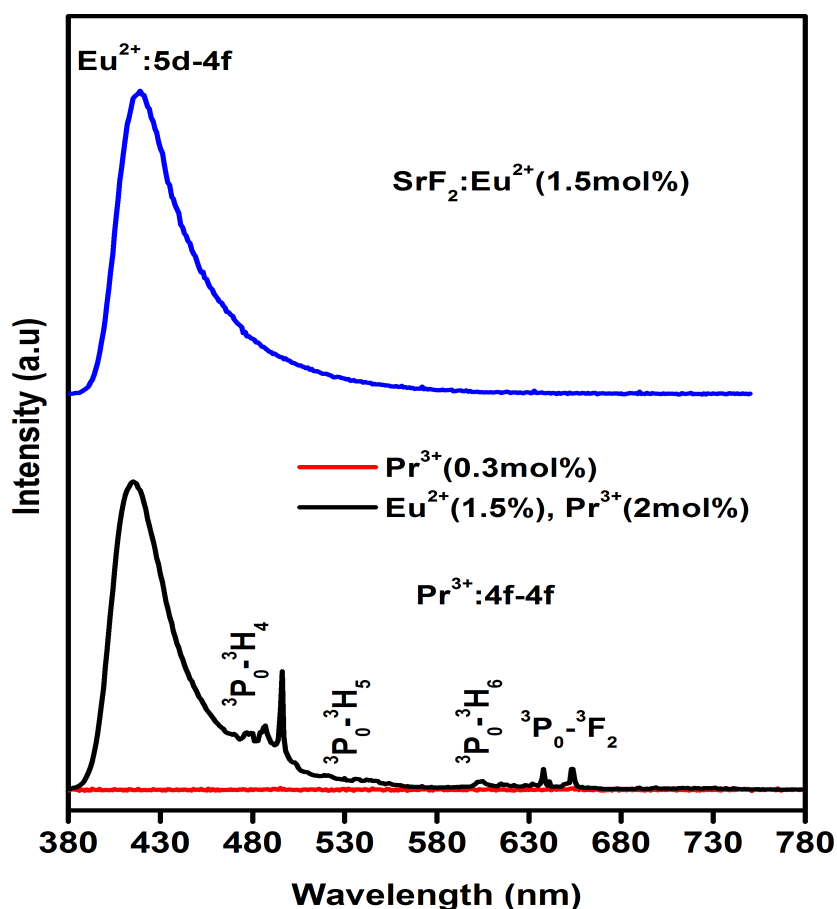


Fig. 9.2: Visible emission of Eu²⁺ and Pr³⁺ ions in the SrF₂ host excited by the He-Cd laser system with 325 nm excitation wavelength.

To study the influence of the Eu²⁺ on NIR quantum cutting emission of Pr³⁺-Yb³⁺, a series of crystalline powder samples with fixed Eu²⁺ and Pr³⁺ and with different Yb³⁺ ions' concentrations were prepared. In fig. 9.3(a) and (b), the emission spectra of 1.5 mol% Eu²⁺ (4f⁶5d¹ → 4f⁷ transition) and 2 mol% Pr³⁺ with varied Yb³⁺ concentration are shown under identical conditions. The broad emission band of Eu²⁺ originates from the inter-configuration 4f⁶5d¹-4f⁷ allowed transition of Eu²⁺ [3, 4]. The additional sharp peak centred at 488 nm is assigned to the Pr³⁺:³P₀-³H₄ transition. The PL spectra of Pr³⁺-related emissions as a function of Yb³⁺ concentration are shown in fig. 9.3(b). The emission spectra of Pr³⁺ show the characteristic ³P₀ emission line of Pr³⁺ [1, 5]. The 4f⁶5d¹-4f⁷ allowed transition of Eu²⁺ is however characterized by a fast emission rate, which is the so-called fluorescence emission. The 4f-4f emission of Pr³⁺ is classified as a phosphorescence emission that arises from the triplet excitation states in which

the electron in the excited state has the same spin orientation as the ground state electron. Such transitions are forbidden and the emission rates are slow. By using our Cary Eclipse PL system (designed to separate the fluorescence and phosphorescence emissions) the 4f-4f emission should be measured in phosphorescence mode, while the Eu²⁺ emission should be measured in fluorescence mode. The observed 4f-4f emission of Pr³⁺ in fluorescence mode can be explained by a decrease in the emission rates of Pr³⁺ emission with increasing Yb³⁺ concentration.

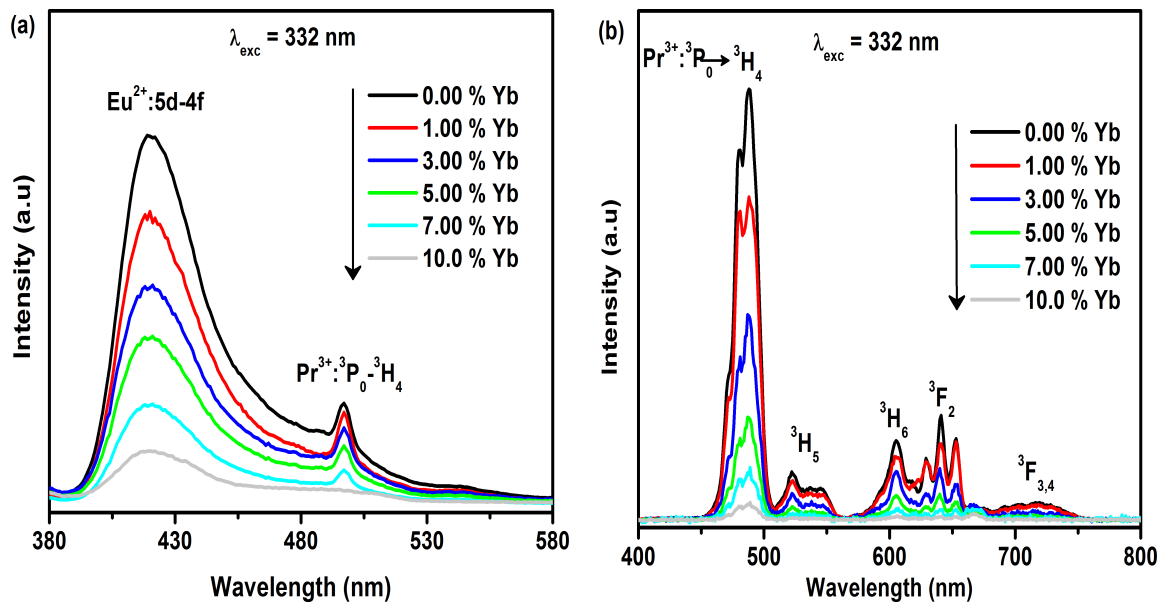


Fig. 9.3: Visible PL emission of (a) Eu²⁺ and (b) Pr³⁺ as a function of Yb³⁺ concentration, excited by 332 nm.

From fig. 9.3(a) it can be seen that the Eu²⁺ emission (4f5d¹ → 4f⁷ transition) decreased with the increased the Yb³⁺ concentration. This indicates there may exist other quenching site since the Pr³⁺ concentration (2 mol%) is fixed in all the samples with different Yb concentrations. The inset graph in fig. 9.4 represents the emission of Yb³⁺ sensitized by Eu²⁺ in the SrF₂ system excited by 325 nm. The emission shows the characteristic ²F_{5/2}-²F_{7/2} transition line of Yb³⁺ that correlates well with the emission spectra for the Yb³⁺ ion in literature [6]. The Yb³⁺ ion has a single excited state (²F_{5/2}) approximately 10000 cm⁻¹ above the ²F_{7/2} ground state. The absence of the energy levels above the excited state (²F_{5/2}) allows Yb³⁺ to absorb energy packages of 10000 cm⁻¹ and emits photons around ~1000 nm. The presence of Yb³⁺ emission

under Eu²⁺ excitation indicates that an energy transfer from Eu²⁺ to Yb³⁺ occurred. The decrease in the Eu²⁺ emission intensity can therefore be attributed to the energy transfer between the Eu²⁺ and Yb³⁺ ions through cooperative quantum cutting energy transfer [7]. The detail investigations of energy transfer between Eu²⁺ and Yb³⁺ was discussed in chapter 8.

The PL spectra of Pr³⁺-related emissions as a function of Yb³⁺ concentration is shown in fig. 9.3(b). All the Pr³⁺ in SrF₂ emission bands were significantly enhanced in the co-doped sample. The biggest enhancement was found for the 488 nm band (³P₀ → ³H₄ transition)¹. From fig. 9.3(b) it can be seen that all bands for the Pr³⁺ emission decreases significantly with increasing the Yb³⁺ concentration. A drastic decrease in intensity can be seen in the sample with 10 mol% of Yb³⁺. This result shows the efficient energy transfer from Pr³⁺ to the Yb³⁺ ion.

PL of the NIR spectra are shown in fig. 9.4. For the sample co-doped with Eu²⁺ (1.5 mol) and Pr³⁺ (2 mol%) (shown in fig. 9.4 as 0.0% Yb), a number of NIR bands can be observed. The emission band centered at 993 nm with small shoulders at 1004 and 1015 nm is ascribed to the transition of the lowest Stark level of ¹G₄ in Pr³⁺ to different Stark levels of the ground state of ³H₄ [8]. The other peaks located at 1057, 1080 and 1307 nm are assigned to the transitions of ¹D₂-³F₃, ¹D₂-³F₄ and ¹G₄-³H₅ in Pr³⁺, respectively. The observation of emission bands originating from the ¹D₂ level implies that cross-relaxation between the Pr³⁺ ions pairs occurred since the multi-phonon relaxation process from ³P₀ to ¹D₂ level is negligible [5]. After doping with Yb³⁺ ions a sharp and small PL peak appears at 977 nm, which is attributed to the 4f-4f transition of Yb³⁺:²F_{5/2}-²F_{7/2} [9]. By increasing the Yb³⁺ concentration the Yb³⁺ emission gradually appeared. At 10 mol% Yb³⁺, the Pr³⁺:¹G₄-³H₃ emission is completely quenched hence the Yb³⁺ emission can clearly be observed. This indicates that the energy transfer between the Pr³⁺ and Yb³⁺ ions occurred efficiently. Although the energy transfer occurred between Pr³⁺ and Yb³⁺ ions, the Yb³⁺ emission intensity is relatively weak. This can be attributed to the concentration quenching between Yb³⁺ ions at high Yb³⁺ concentration. The relatively weak emission of Yb³⁺ at low

¹You can also see chapter 7 for more details.

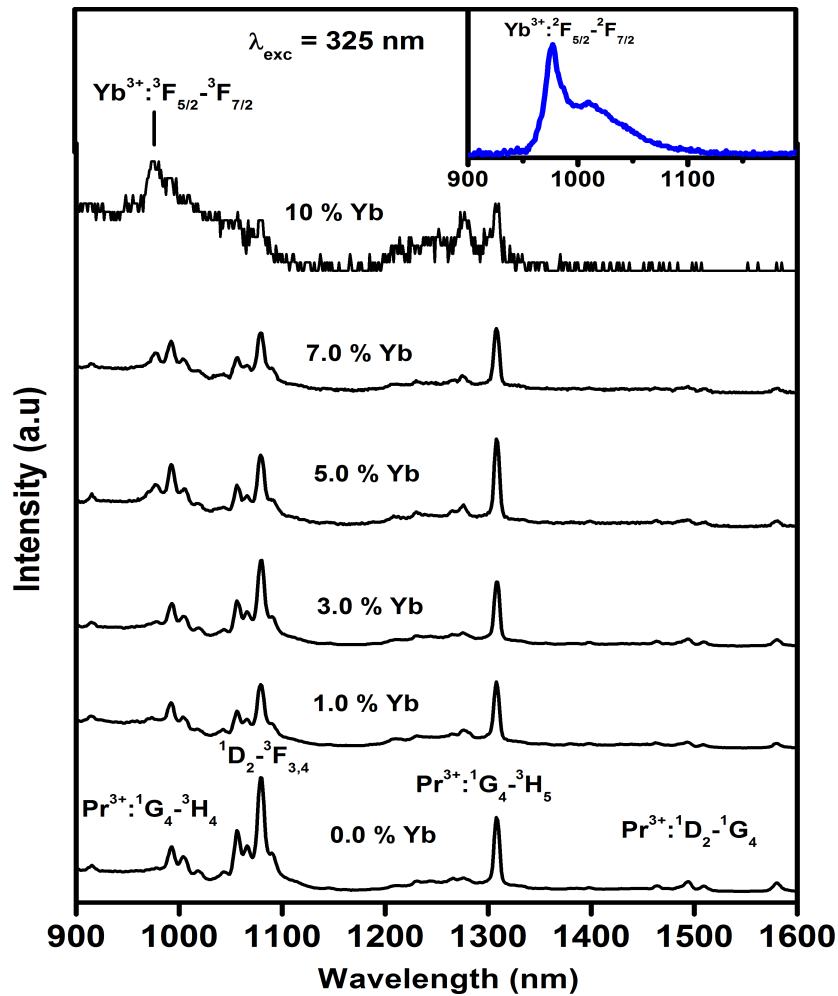


Fig. 9.4: NIR emission spectra of Eu²⁺ and the Pr³⁺-Yb³⁺ couple as a function of Yb³⁺ concentration. The 10 % Yb spectrum is drawn with a different scale.

Yb³⁺ concentration may be due to the strong emission of the Pr³⁺:4f-4f band that overlaps with Yb³⁺ emission. This is suggesting that the spectral effect of Yb³⁺ in the current system is small. The overall conclusion is however intense NIR emission occurred under Eu²⁺ sensitization.

Results obtained from the luminescence decay curves for Eu²⁺ and Pr³⁺ emission also contributed to the discussion about the energy transfer process that occurred with different Yb³⁺ concentrations. Fig. 9.5(a) shows the decay curves of the Eu²⁺:4f⁶5d¹-4f⁷ at 416 nm emission. The decay time for the singly doped Eu²⁺ was 435 ns. This decay time was due to radiative decay from the ⁶5d¹ (*T*_{2g}) level, which is in agreement with reported values for the decay time of Eu²⁺ emission in SrF₂ [10]. Co-doping with

2 mol% of Pr³⁺ induced faster decay, which can be attributed to the energy transfer from Eu²⁺ to Pr³⁺. Adding 1 mol% of Yb³⁺ to the Eu²⁺-Pr³⁺ couple dramatically decrease the Eu²⁺ decay lifetime. The decay curve of Eu²⁺-Yb³⁺ is also shown in fig. 9.5(a). The bi-exponential decay curve of 1.5 mol% Eu²⁺ and 1 mol% Yb³⁺ confirmed that energy transfer from Eu²⁺ to Yb³⁺ was occurred. An estimation of energy transfer efficiency can be obtained from $\eta_{ET} = 1 - \tau_x / \tau_0$ as outlined in literature [7, 11]. Here, τ_x and τ_0 are the corresponding average lifetimes of Eu²⁺ in the presence and absent of an acceptor, respectively. The corresponding energy transfer efficiency are 31, 39 and 62 % for B, C and D (labelled in fig. 9.5(a)) respectively.

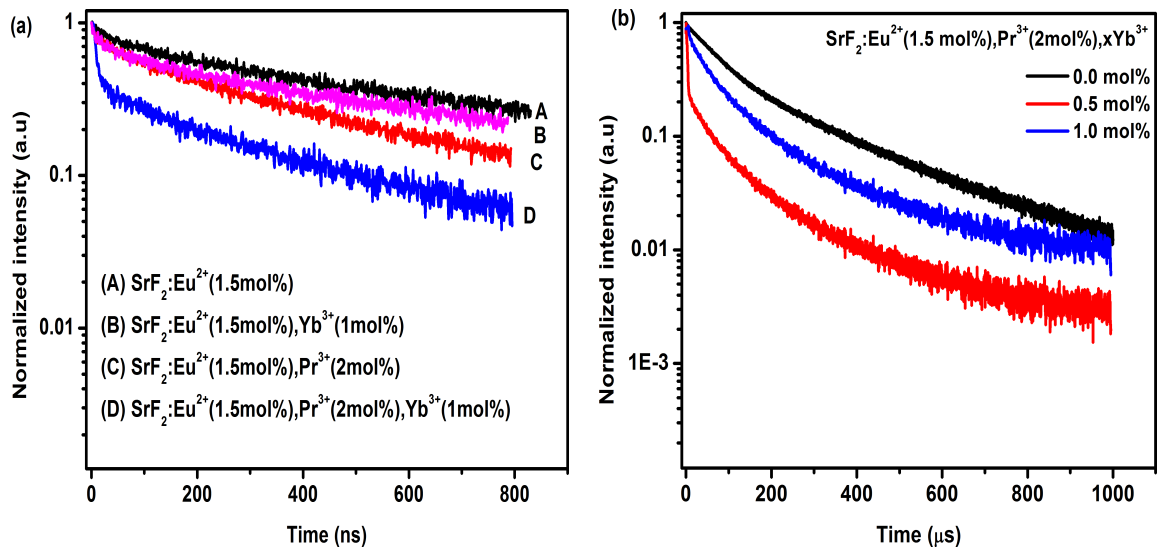


Fig. 9.5: (a) Normalized decay curves of the Eu²⁺ emission at 416 nm of SrF₂:Eu²⁺, SrF₂:Eu²⁺, Pr³⁺ and SrF₂:Eu²⁺, Pr³⁺, Yb³⁺. (b) Normalized decay curves of the Pr³⁺ emission at 488 nm for SrF₂:Eu²⁺, Pr³⁺ and with 0.5 and 1 mol% Yb³⁺.

The luminescence decay curves for the Pr³⁺ related transition ³P₀-³H₄ is shown in fig. 9.5(b). The decay time for Pr³⁺ rapidly decreased when the system was co-doped with Yb³⁺. This indicates an additional decay pathway, i.e, the energy transfer between Pr³⁺ and Yb³⁺. There is a fast decay curve in the Pr³⁺ curve with increasing Yb³⁺ concentration. For 0.5 and 1 mol% Yb³⁺ concentration, the energy transfer efficiency values are 35 and 60%, respectively. This result is not in good agreement with the decrease in the Pr³⁺ emission with increasing Yb³⁺ concentration (see fig. 9.3(b)). Therefore, the fast decay curve is not fully understood and is still under investigation.

At higher Yb³⁺ concentrations, the decay curves seem to remain constant. This might be attributed to the decrease in the Pr³⁺ lifetime towards nanoseconds and this exceeded the pulsed duration of the YAG laser system (in microseconds), which was used to measure the Pr³⁺ PL decay curves. This is in good agreement with our assessment where the ³P₀-³H₄ emission is observed in the fluorescence spectra along with Eu²⁺, see fig. 9.3(a).

Recently quantum-cutting based on the Pr³⁺-Yb³⁺ couple has been clearly demonstrated in SrF₂ crystal [9]. It consists of two steps resonance energy transfer process as shown in fig. 9.6. The ³P₀ level from the Pr³⁺ ion is populated after absorption of blue photons. The two steps resonance energy transfer process between Pr³⁺ and Yb³⁺ with the ¹G₄ level of the Pr³⁺ ion acting as the intermediate level: Pr³⁺: [³P₀-¹G₄, ¹G₄-³H₄ → 2×Yb³⁺: [²F_{7/2}-²F_{5/2}]) can then occur [9, 12]. G. Gao et al. [13] however investigated the quantum cutting of Pr³⁺-Yb³⁺ couple in LaBO₃ glass ceramics. They have concluded that energy transfer between Pr³⁺ and Yb³⁺ could occur through both the ³P₀ and ¹D₂ levels. In this study, the Yb³⁺ emission is a results of combination of energy transfer from both the Pr³⁺ and Eu²⁺ to the Yb³⁺ ion. The energy transfer between Eu²⁺ and Yb³⁺ has been reported to occur through cooperative quantum cutting energy transfer [7, 14]. The schematic diagram of quantum cutting process between Eu²⁺ and Yb³⁺ is sketch in fig. 9.6 (pathway 2). The ³P₀-¹G₄ transition has weak dipole oscillator strength [12]. Therefore, the absence of ³P₀-¹G₄ emission (fig. 9.4) and the weak intensity of Yb³⁺ in NIR region suggested that the cooperative energy transfer process between Pr³⁺ and Yb³⁺ cannot be neglected (pathway 1 in fig. 9.6).

It is well known that the ³H₄-³P_j transition of the Pr³⁺ ion is parity forbidden and therefore it has a low absorption cross-section. On the contrary, the 4f-5d transition of the Eu²⁺ ion is a fully allowed transition. Absorption by the Eu²⁺ ions is therefore strong and most of the incident energy will then be absorbed by the Eu²⁺ ions. The energy can then be transferred to the Pr³⁺ ions. Thus, the light yield is much more significant in the Eu²⁺ co-doped Pr³⁺-Yb³⁺ couple systems than in the Pr³⁺-Yb³⁺ couple. The practical action for enhancing the excitation cross-section of Pr³⁺-Yb³⁺ couple has been done by A. Guille et. al. [15] in CaYAlO₄ thin film and bulk co-

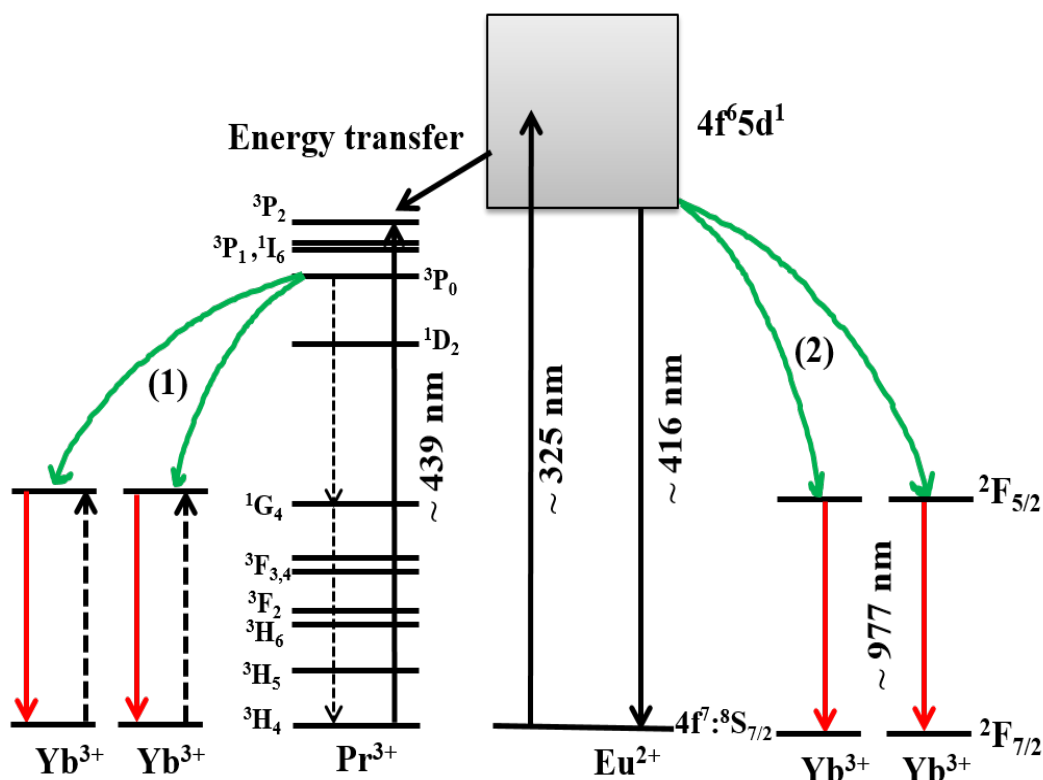


Fig. 9.6: (Color online) schematic diagram energy level and down-conversion mechanism for the Eu²⁺ sensitized Pr³⁺, Yb³⁺ couple. The diagram shows the cooperative energy transfer and first-order energy transfer between the Pr³⁺ and Yb³⁺.

doped with Pr³⁺ and Ce³⁺ ions, where the Ce³⁺ ions feed the ¹D₂ level of Pr³⁺. They concluded that the energy transfer from the ¹D₂ level of the Pr³⁺ ion to the Yb³⁺ ion is only possible via photon assistant energy transfer and hence it would not lead to a quantum cutting process. The present results showed that the energy transfer from Eu²⁺ to Pr³⁺ lead to an enhancement in the NIR emission. The quantum cutting process from Pr³⁺ to Yb³⁺ occurred but the strong emission for Pr³⁺:4f-4f in the NIR region suppressed the weak intensity of Yb³⁺ ion. The weak Yb³⁺ emission was clearly observed at high concentration where the intensity of Pr³⁺:¹G₄-³H₄ is quenched. The Yb³⁺ induced faster decay times to both the Eu²⁺ and Pr³⁺ ions but the Yb³⁺ emission intensity is however significantly low. This might be due to the concentration quenching and other non-radiative decay processes for Yb³⁺ or another quenching sites originating from the material defects.

9.4 Conclusions

The energy transfer process between Eu²⁺ and the Pr³⁺-Yb³⁺ couple was studied. The PL and lifetime measurements showed that the Eu²⁺ (4f⁶5d¹-4f⁷) emission band leads to efficient energy transfer from Eu²⁺ to the Pr³⁺ ions. Excitation into the Eu²⁺ bands revealed extensive NIR emission. Pr³⁺ emits strongly in the NIR region where it overlaps with the Yb³⁺ emission. Emission from Yb³⁺ was only observed at high Yb³⁺ concentration after the Pr³⁺ emission was quenched. The results suggested that the Eu²⁺ ions well sensitized the Pr³⁺-Yb³⁺ couple in the current system.

References

- [1] L. L. Noto, W. D. Roos, O. M. Ntwaeaborwa, M. Gohain, M. Y. A. Yagoub, E. Coetsee, and H. C. Swart, *Sci. Adv. Mater.*, **7**(6) (2015) 1197-1206.
- [2] Y. Katayama and S. Tanabe, *Mater.*, **3** (2010) 2405-2411.
- [3] M. Y. A. Yagoub, H. C. Swart, L. L. Noto, J. H. O'Connell, M. E. Lee and E. Coetsee, *J. Lumin.*, **156** (2014) 150-156.
- [4] P. Dorenbos, *J. Lumin.*, **104** (2003) 239-260.
- [5] M. Y. A. Yagoub, H. C. Swart, L. L. Noto and E. Coetsee, *Proceeding od SAIP2013: the 58th Annual Conference of the South African Institute of Physics*, edited by Roelf Botha and Thulani Jili (2013), pp. 205-210. ISBN:978-0-620-62819-8. Available online at <http://events.saip.org.za>.
- [6] S. Hraiech, A. Jouini, K. Jin Kim, Y. Guyot, C. Goutaudier, A. Yoshikawa, M. Trabelsi-Ayadi and G. Boulon, *Ann. Phys. Fr.*, **32** (2007) 59-61.
- [7] T. Katsumata, T. Nabae, K. Sasajima, S. Komuro and T. Morikawa, *J. Electrochem. Soc.*, **144** (1997) L243-L245.
- [8] L. B. Shaw, B. B. Harbison, B. Cole, J.S. Sanghera and I. D. Aggarwal, *Opt. Express*, **1** (1997) 87-96.
- [9] B. M. Van der Ende, L. Aarts and A. Meijerink, *Adv. Mater.*, **21** (2009) 3073-3077.
- [10] Q. Luo, X. Qiao and X. Fan, *J. Am. Ceram. Soc.*, **93** (2010) 2684-2688.
- [11] J. Zhou, Z. Xia, H. You, K. Shen, M. Yang and L. Liao, *J. Lumin.*, **135** (2013) 20-25.
- [12] J. T. van Wijngaarden, S. Scheidelaar, T. J. H. Vlugt, M. F. Reid and A. Meijerink, *Phys. Rev. B*, **81** (2010) 155112-155117.
- [13] G. Gao and L. Wondraczek, *Opt. Mater. Express*, **3** (2013) 633-644.
- [14] Q. Yan, J. Ren, Y. Tong and G. Chen, *J. Am. Ceram. Soc.*, **96** (2013) 1349-1351.

- [15] A. Guille, A. Pereira, G. Breton, A. Bensalah-ledoux and B. Moine, *J. Appl. Phys.*, **111** (2012) 043104-043108.

Chapter 10

Conclusions and future work

This chapter contains the general conclusion of the results obtained as well as future work for this research study.

10.1 Conclusions

The work described in this thesis deals with the synthesis, characterization, and investigation of the effect of the broadband excitation ions on the NIR emission of the Pr^{3+} - Yb^{3+} down-conversion couple as well as the red emission of Eu^{3+} downshifting ion for solar cell application.

Initially, the effect of different synthesis techniques on the concentration quenching of Pr^{3+} ions was investigated. $\text{SrF}_2:\text{Pr}^{3+}$ powder was synthesised by two method, namely hydrothermal and combustion methods. PL results demonstrated that both samples exhibit blue-red emission from 4f-4f transition under 439 nm excitation wavelength. The optimum Pr^{3+} doping level for maximum emission intensity was 0.4 and 0.2 mol% for the hydrothermal and combustion samples, respectively. The reduction of Pr^{3+} emission intensity was a result of the Pr^{3+} clustering in SrF_2 due to charge compensation. The dipole-dipole interactions between the nearby Pr^{3+} ions are responsible for the concentration quenching of Pr^{3+} intensity in the SrF_2 crystal in both methods. This result showed that optimizing the synthesis condition does not improve the emission intensity of the Ln^{3+} lanthanide ions (4f-4f transition) to an acceptable level. $\text{SrF}_2:\text{Eu}$ nano-phosphors were synthesised and extensive research was done on their surface, structural and optical properties. The average crystalline size of the phosphor was calculated and found to be in nano-metre scale. From PL and XPS results, it was found that Eu was in both the Eu^{2+} and Eu^{3+} valance states. Photoluminescence measurements showed that at low Eu concentrations the emission from Eu^{2+} centered at 416 nm was more dominant. While the narrow band of Eu^{3+} emission intensity

increased with an increase in the Eu concentration. The presence of both Eu oxidation states therefore significantly enhanced the absorption response of Eu^{3+} to UV excitation. The results indicated that Eu concentrations of more than 5 mol% of Eu were beneficial for improving fluorescence emission of Eu^{3+} and conversion efficiency under the broadband excitation. TOF-SIMS results suggested that the energy transfer from Eu^{2+} to Eu^{3+} is likely to be dominant. The Eu^{2+} ion was however found to be unstable when irradiated by the YAG laser. The Eu^{2+} ion's PL emission intensity rapidly decreased with time and this result make this $\text{SrF}_2:\text{Eu}$ nano-phosphor an unsuitable candidate for applications such as a downshifting layer to enhance the response of photovoltaic cells.

The effect of Ce^{3+} ions on the Eu emission in SrF_2 was investigated. Ce^{3+} and Eu ions were successfully incorporated into SrF_2 nano-phosphors. Dopant ions were intended to decrease the particle size of the host. The AES spectra confirmed the presence of Sr, F, Eu and Ce elements in the host matrix. Photoluminescence properties of Ce^{3+} co-doped Eu in SrF_2 nano-phosphor suggested a possible efficient energy transfer from Ce^{3+} to Eu ions. The spectral conversion from 295-550 nm to 570-710 nm was achieved. Upon 295 nm excitation into Ce^{3+} ions, the absorbed energy transferred from Ce^{3+} (5d band) to Eu^{2+} ($4f^65d$) from where the energy then non-radiatively transferred to the Eu^{3+} ion. From the PL decay curves the energy transfer efficiency was calculated to be 89.4% for the $\text{SrF}_2: 0.7 \text{ mol}\% \text{ Ce}^{3+}, 10 \text{ mol}\% \text{ Eu}$ sample. The results indicate that Ce^{3+} co-doped $\text{SrF}_2:\text{Eu}$ is beneficial for improving the fluorescence emission and conversion efficiency under broadband excitation.

The effect of Eu^{2+} on the emission of $\text{Pr}^{3+}-\text{Yb}^{3+}$ down-conversion couple and Yb^{3+} ion was also studied. The samples of interest were successfully synthesized by the coprecipitation method. XPS confirmed that all Eu ions were in the Eu^{2+} oxidation state. Initially, the effect of Eu^{2+} on the Pr^{3+} absorption strength was investigated. Efficient energy transfer occurred from the 5d band of Eu^{2+} ions to the $^3\text{P}_j$ levels of Pr^{3+} in $\text{SrF}_2:\text{Eu}^{2+}, \text{Pr}^{3+}$ system. The emission intensity of Pr^{3+} ion was greatly enhanced in the co-doped system. The energy transfer was followed by a cross-relaxation process between the Pr^{3+} ions. The results showed that the Eu^{2+} could be an efficient sensitizer

to Pr^{3+} and hence it increases the absorption strength of the $\text{Pr}^{3+}:4f-4f$ transition under broadband excitation.

The combination of $\text{SrF}_2:\text{Eu}^{2+}$ (1.5 mol%) co-doped with Na^+ (0.5 mol%) and various concentrations of Yb^{3+} in SrF_2 showed a mixture of cubic phase of SrF_2 and NaYbF_4 at high Yb^{3+} concentration. The broad emission band of Eu^{2+} ($4f^65d-4f^7$) leads to efficient NIR emission through cooperative quantum cutting process with Yb^{3+} ion. At low Yb^{3+} concentration, the NIR emission strongly effected by the influenced of Na^+ substitutional sites. The NIR photons match well with the bandgap of c-Si. The investigated system might have practical application possibilities for raising the efficiency of c-Si solar cells.

Eu^{2+} ions and $\text{Pr}^{3+}-\text{Yb}^{3+}$ couple were successfully incorporated into the SrF_2 crystal. The energy transfer process between Eu^{2+} ions $\text{Yb}^{3+}-\text{Pr}^{3+}$ couple was studied. The PL and lifetime measurements showed that the Eu^{2+} ($4f^65d \rightarrow 4f^7$) emission band leads to efficient energy transfer from Eu^{2+} to the Pr^{3+} ions and also towards the quantum cutting process with Yb^{3+} . Excitation into the Eu^{2+} bands revealed extensive NIR emission. Pr^{3+} emits strongly in the NIR region where it overlap with the Yb^{3+} emission. Emission from Yb^{3+} was only observed at high Yb^{3+} concentrations after the Pr^{3+} emission was quenched. The results also demonstrated that quantum cutting from both Eu^{2+} and Pr^{3+} to Yb^{3+} occurred in Eu^{2+} sensitized $\text{Pr}^{3+}-\text{Yb}^{3+}$ couple. The results suggested that the Eu^{2+} ions well sensitized the $\text{Yb}^{3+}-\text{Pr}^{3+}$ couple in the current system and can be used as a solar spectral down-converter for the c-Si solar cells application.

10.2 Future work

This work serve as the required investigation of spectral down-conversion and down-shifting layers to be coated with the solar cell. Some additional investigations need to be done before the investigated materials will be applied.

- Further studies can be made to solve the Eu^{2+} stability in SrF_2 host. This might be done by synthesizing the $\text{SrF}_2:\text{Eu}$ material in different chemical conditions.

Further investigations also need to be done on the effect of these synthesis conditions on the $\text{Eu}^{2+}/\text{Eu}^{3+}$ ratio in the SrF_2 host.

- The study showed Eu^{2+} efficiently enhanced Pr^{3+} emission intensity under UV excitation. Accordingly, the Pr^{3+} ion strongly emits in the NIR region, which contrasted all the previously reported studies on Pr^{3+} - Yb^{3+} couple doped fluoride crystals. Hence, the luminescence properties of Eu^{2+} - Pr^{3+} in the NIR region require more investigation.
- Upon sensitized with broadband excitation ions, the issue of concentration quenching of NIR emission still remains. Therefore, the Eu^{2+} sensitized Pr^{3+} - Yb^{3+} can be prepared by other preparation methods. This might optimized the NIR emission to acceptable level.

Appendix A

Publications

This thesis is based on the following publications. The help of co-authors in preparing these publications is gratefully acknowledged:

- M. Y. A. Yagoub, H. C. Swart, L. L. Noto, J. H. O'Connell, M. E. Lee, E. Coetsee. The effect of Eu-concentrations on the luminescent properties of SrF₂:Eu nanophosphor, *J. Lumin.* **156** (2014) 150-156.
- M. Y. A. Yagoub, H. C. Swart, E. Coetsee. Concentration quenching, surface and spectral analyses of SrF₂:Pr³⁺ prepared by different synthesis techniques, *Opt. Mater.* **42** (2015) 204-209.
- M. Y. A. Yagoub, H. C. Swart, L. L. Noto, P. Bergman, E. Coetsee. Surface characterization and photoluminescence properties of Ce³⁺ co-doped SrF₂:Eu down-shifting nano-phosphor, *Materials* **8** (2015) 2361-2375.
- M. Y. A. Yagoub, H. C. Swart, P. Bergman, E. Coetsee. Eu²⁺ enhanced Pr³⁺ photoluminescence by energy transfer in SrF₂ phosphor, submitted.
- M. Y. A. Yagoub, H. C. Swart, M. S, Dhlamini, E. Coetsee. Near infrared quantum cutting of Na⁺ and Eu²⁺-Yb³⁺ couple activated SrF₂ crystal, submitted.

A.1 Conference proceedings:

- M. Y. A. Yagoub, H. C. Swart, L. L. Noto, E. Coetsee. Proceeding of SAIP2013, the 58th annual conference of the South African institute of Physics, 8-12 July 2013, Richards Bay, University of Zululand, South Africa.
- M. Y. A. Yagoub, H. C. Swart, E. Coetsee. Proceeding of SASEC2014, the 2nd Southern African Solar Energy Conference, 27-29 January 2014, PortElizabeth, South Africa.

- M. Y. A. Yagoub, H. C. Swart, E. Coetsee. Proceeding of SASEC2015, the 3rd Southern African Solar Energy Conference, 11-13 May 2015, Kruger National Park, South Africa.

A.2 Presentations at national and international conferences/workshops:

- 3rd Southern African Solar Energy Conference, 11-13th May 2015, Kruger national park, South Africa.
- The 4th workshop Linköping, Sweden, PortElizabeth/Bloemfontein, South Africa, 15-18th June 2014, Karlskrona, Sweden.
- Annual Conference of the Nordic Microscopy Society, 10-14th June 2014, Linköping, Sweden.
- 2nd Southern African Solar Energy Conference, 27-29th January 2014, PortElizabeth, South Africa.
- 6th African Laser Centre Student Workshop, 21-23th November 2013, Zevenwacht, Stellenbosch, South Africa.
- ICTP regional workshop on material science for solar energy conversion 4-8th November 2013, IThemba labs. Cape Town, South Africa.
- The 58th Annual Conference of the SA Institute of Physics, 8-12th July 2013, University of Zululand, South Africa.